Nshii, Chidi Christopher (2011) *Tunable mid-infrared light sources based on intersubband transitions.*
PhD thesis.

UNIVERSITY OF GLASGOW

Tunable Mid-Infrared Light Sources Based on Intersubband Transitions

by

Chidi Christopher Nshii

A thesis submitted for the
degree of Doctor of Philosophy (Ph.D.)

in the
School of Engineering
UNIVERSITY OF GLASGOW

May 2011

Declaration of Authorship

I, Chidi Nshii, declare that this thesis titled, 'Tunable Mid-Infrared Light Sources Based on Intersubband Transitions' and the work presented in it are my own. I confirm that:

- This work was done wholly or mainly while in candidature for a research degree at this University.
- Where any part of this thesis has previously been submitted for a degree or any other qualification at this University or any other institution, this has been clearly stated.
- Where I have consulted the published work of others, this is always clearly attributed.
- Where I have quoted from the work of others, the source is always given. With the exception of such quotations, this thesis is entirely my own work.
- I have acknowledged all main sources of help.
- Where the thesis is based on work done by myself jointly with others, I have made clear exactly what was done by others and what I have contributed myself.

Signed: CNshii

Date: 12/05/2011

UNIVERSITY OF GLASGOW

Abstract

School of Engineering
UNIVERSITY OF GLASGOW

Doctor of Philosophy

by Chidi Christopher Nshii

This thesis describes how for the first time, unidirectional operation and coupled ring tuning were realised on a quantum cascade laser material; specifically on a new strain compensated $In_{0.7}Ga_{0.3}As/AlAs_{0.6}Sb_{0.4}$ grown on InP substrate and operates in pulsed mode in the 3-4 μm hydrocarbon absorption region.

Unidirectional ring lasers have the advantages that, in the favoured emission direction, they can have up to double the quantum efficiency of bidirectional lasers and they do not suffer from spatial hole burning. In this work, this operation was realised by incorporating an "S"-crossover waveguide into the ring cavity in a manner that it introduces non reciprocal loss and gain in the counter-clockwise (CCW) and clockwise (CW) directions respectively. The measured result showed higher quantum efficiency in the CW. In fact at 1.5 times the threshold current. 90 % of the light was emitted in the favoured CW.

On the other hand, the coupled ring quantum cascade laser showed nearly single mode operation, with side mode suppression ratio ~22 dB. Continuous wavelength tuning of about 13 nm was observed from one of these devices, at a tuning rate of approximately 0.4 nm/mA.

Publications

1. C. C. Nshii, C. N. Ironside, M. Sorel, T. J. Slight, S. Y. Zhang, D. G. Revin, and J. W. Cockburn, “A unidirectional quantum cascade ring laser”, *Applied Physics Letters*, vol. 97, no. 23, p. 231107, 2010.
2. C. C. Nshii, C. N. Ironside, M. Sorel, T. J. Slight, S.Y. Zhang, D. G. Revin and J. W. Cockburn, “Quantum Cascade Ring Lasers: Unidirectional Operation and Coupled Ring Tuning”, Accepted for publication by the European Conference on Lasers and Electro-Optics (CLEO-EUROPE), 2011

Acknowledgements

My sincere gratitude goes to my supervisor, Prof. Charles Ironside for his unrelenting support and supervision. Also many thanks to Dr. Marc Sorel and Prof. Douglas Paul for their advice and guidance.

Many thanks to the QCSENSE group members: Prof. John Cockburn and his group from Sheffield University for the wafer; Andy Mckee, Wyn Meredith, Iain, Henry Sinclair from Compound Semiconductor Technologies for the ICP etching.

Special thanks to Dr. Thomas Slight and Dr. Corrie Farmer for teaching me how to operate the FTIR spectrometer and helping me out with the measurements. Also to be remembered here is Dr. Garbor Mesozi for his great help. To my colleagues in the office: Leo, Andy, Jason, Kamil, Dr. Antonio, Peppe, Piotr, I appreciate your contributions and will greatly miss you all.

To the technicians in JWNC: Eve, Helen, Mary, Donald and a host of others, I appreciate.

Last, and not least, my love and thanks go to my family and friends for the support. Above all, special thanks to my parents for making funds available for this research.

To my Wife and Son (Jason), I love you.

Contents

List of Figures

List of Tables

Acronyms

MMI multimode interference

SRL semiconductor ring laser

QCL quantum cascade laser

CCW counter-clockwise

CW clockwise

QCRL quantum cascade ring laser

FP Fabry Perot

EFC evanescent field coupler

SEM scanning electron microscope

MIR mid-infrared region

DFB distributed feed back

DBR distributed Bragg reflector

OPO optical parametric oscillator

SSL semiconductor superlattice

WSL Wannier-Stark ladder

HBT heterostructure bipolar transistor

NDR negative differential resistance

I-V current-voltage

QW quantum well

QSE quantum size effect

MBE molecular beam epitaxy

SHB spatial hole burning

EBL electron beam lithography

FSR free spectral range

SMSR sidemode suppression ratio

QC quantum cascade

THz terahertz

TM transverse magnetic

FIR far infrared

ASE amplified spontaneous emission

FWHM full width at half maximum

TE transverse electric

LO longitudinal optical

FTIR fourier transform infrared

BTC bound to continuum

LED light emitting diode

CR-QCL coupled ring quantum cascade laser

PECVD plasma enhanced chemical vapour deposition

SPA semiconductor parameter analyser

RIE reactive ion etching

ICP-RIE inductively coupled reactive ion etching

IPA Isopropyl alcohol

LOR Liftoff resist

RPM revolution per minute

CWSR counter propagating wave suppression ratio

UQCRL unidirectional quantum cascade laser

CRQCL coupled ring quantum cascade laser

L-I light-current

GaAs gallium arsenide

BPM beam propagation method

Chapter 1

Introduction

The research reported here is on investigation of semiconductor light sources based on intersubband transitions (i.e transition between energy levels contained in a band, typically the conduction band)[1] in quantum wells and superlattices. These sources have evolved over the years as likely candidates for mid-infrared region ($\lambda \sim 3 - 14\mu$m) optical spectroscopy. This region, known as the molecular fingerprint region of the spectrum, is very important for spectroscopy [2]. Most substances, molecules and trace gasses of interest have tell-tale absorption features due to vibro-rotational transition in this wavelength region as can be seen from figure 1.1

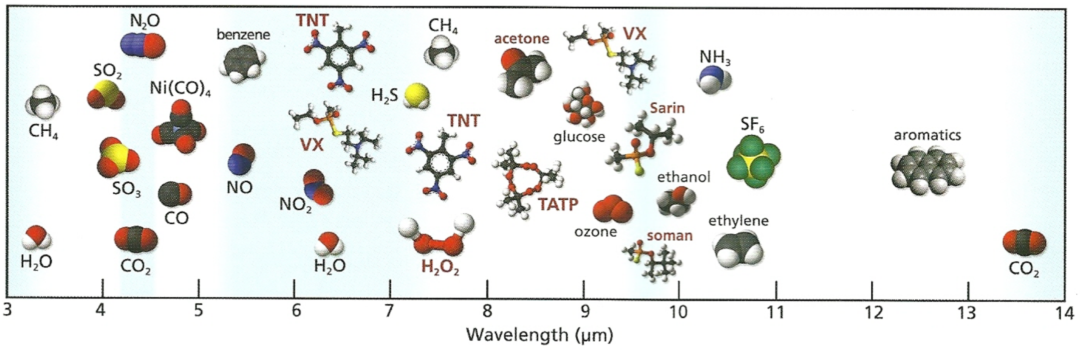

FIGURE 1.1: Some of the molecules of interest and their absorption wavelengths in the mid-infrared region of the spectrum
[3]

A tree diagram showing how this research is structured is shown in figure 1.2. The first project undertaken in this work, was the SuperTune project. This was a novel widely tunable ($\lambda \sim 5 - 13 \mu$m) mid-infrared incoherent source, based on earlier work by Scarmacio *et al* [4].

In this project, we redesigned the original wafer by including waveguides, in order to increase the output power from $\sim n$Watts reported in Ref. [4] to μ- or milli-Watts, suitable for spectroscopy (with sensitivities of several parts per billion by volume). Other changes made to the original wafers to achieve our target include, fabricating SuperTune as a ridge waveguide device (instead of mesas), replacing the semiconducting substrate with a lightly doped (i.e conducting) substrate which offered better thermal management and a less complicated fabrication. Also the cap layer was excessively doped (5x10^{19} cm^{-3}) compared to (5x10^{18} cm^{-3}) reported for the original wafer, to encourage plasma assisted waveguiding, especially in the longer wavelength [5]. These devices, as will be discussed later in chapter 7, rely on both inter and intra- Wannier-Stark ladder (WSL) transitions in the conduction band of the superlattice active region for its operation, with the later controlling its tunability. Furthermore, the wide tunability expected from this devices can be achieved by mere tuning of the applied voltage from 7 - 14 V. This project is covered in **chapter 7**.

The 3 - 4 μm wavelength range is of key technological importance for a wide range of applications. Many important hydrocarbon species, for example ethane, methane, acetone, formaldehyde and butane and other molecules such as hydrogen halide have their strongest absorption features in this region. This leads to many potential applications in areas such as clinical diagnostics (breath analysis), process monitoring, control of outdoor and indoor pollution, and remote detection of oil and gas deposits.

Quantum cascade laser based sensing (QCSENSE) project was initiated to develop a highly sensitive state of the art quantum cascade laser (QCL)[6]-based detection system, operating at the ethane first absorption band, 2954 cm^{-1}[7], (i.e $\lambda \sim$ 3.385 μm) and suitable for detecting traces of ethane naturally escaping from oil reservoir underground. A new QCL material system based on strain compensated AlAsSb/InGaAs/InP[8], was developed for this project.

Although light sources based on interband antimonide [9] and lead-salts [10] have been demonstrated in the $\lambda \sim 3 - 4$ μm region, they require cryogenic cooling for operation [11], unlike the QCL reported here which operates reasonably well at room temperature. Other advantages of QCLs over lead-salt lasers in the 3-4 μm range include:

1. higher operating temperatures [12]
2. higher output power [12, 13]; 400 mW peak power compared [14] to $\sim$ 1mW reported for a lead-salt laser operating at 3.5 μm [15]
3. compact size
4. better single mode behaviour [12] with Single-mode continuous tunability of $\sim$ 15 cm^{-1} [14] from a distributed feed back (DFB) operating at 3.35 μm compared to $\sim$ 1 cm^{-1} reported for a lead-salt laser operating at 3.5 μm [15]

The overall performance of quantum cascade lasers make them excellent candidates for ultra sensitive trace gas sensing in the 3-5 μm and 8-13 μm atmospheric window.

The theory of QCLs relevant to the undertaken research is detailed in **chapter 2** while the material and device design considerations are covered in **chapter 3**. The fabrication techniques employed to overcome key challenges in the device processing are discussed in **chapter 4**

In the QCSENSE project, we investigated a new approach to achieving tunable single mode QCLs. This technique which have been investigated and demonstrated in the communication wavelength (1.55 μm) by Choi *et al* [16], Segawa *et al* [17], Liu *et al* [18] is based on coupled ring effect. Coupled ring lasers have the potential of achieving M times the tuning range of a single ring laser, where M is the Vernier effect tuning enhancement factor associated with coupled waveguide [19]. The tuning enhancement factor is responsible for wide tunability observed in coupled ring lasers. Coupled ring QCLs offer many advantages over DFB-QCLs. These include; ultra wide wavelength tuning range, narrower band-width, higher sidemode suppression ratio (SMSR), low frequency chirp, lower fabrication tolerance and simpler fabrication and ability to tune over wide wavelength range ($<$ 50 nm) with small injected current (<7 mA). [17]. This investigation is reported fully, in **chapter 6**

Also, investigated under the QCSENSE project was the possibility of a unidirectional operation in QCL [20]. Though not particularly related to sensing application, it finds relevance in mode-locked operation, as unidirectional lasers do not suffer from spatial hole burning (SHB) which is a source of noise and has recently been shown to be a limitation on modelocked operation of QCLs, as SHB deteriorates pulse quality [21]. In addition, unidirectional lasers have the advantage that, in the favoured emission direction, they can have up to double the quantum efficiency of bidirectional lasers. In this project, we designed, fabricated and characterised the first unidirectional quantum cascade ring lasers (with 90% emission in the favoured direction) [20] by incorporating an "S"-cross arm waveguide into the ring cavity in a manner that it introduces, respectively, a non-reciprocal loss and gain to the unwanted and the favoured emission direction [22]. This project is described in **chapter 5**.

1.1 Research Aims

The aim of this research work was to investigate new types of light emitting devices, operating in the mid-infrared region (MIR), based on intersubband transitions in superlattices and quantum wells.

1.2 Research Objectives

The objective of this research was to investigate and develop tunable MIR light sources suitable for detecting one or more species shown in figure 1.1.

1.3 Thesis Outline

The thesis is structured this way:

Chapter2 discusses the theory of QCLs relevant to the undertaken research,

Chapter3 details the material and device design consideration employed in this work,

Chapter4 describes the processing techniques used to produce the devices reported in this work.

Chapters 5 and 6 cover the work carried out on the unidirectional quantum cascade ring lasers and the coupled ring quantum cascade lasers respectively.

Finally the SuperTune work is detailed in chapter 7

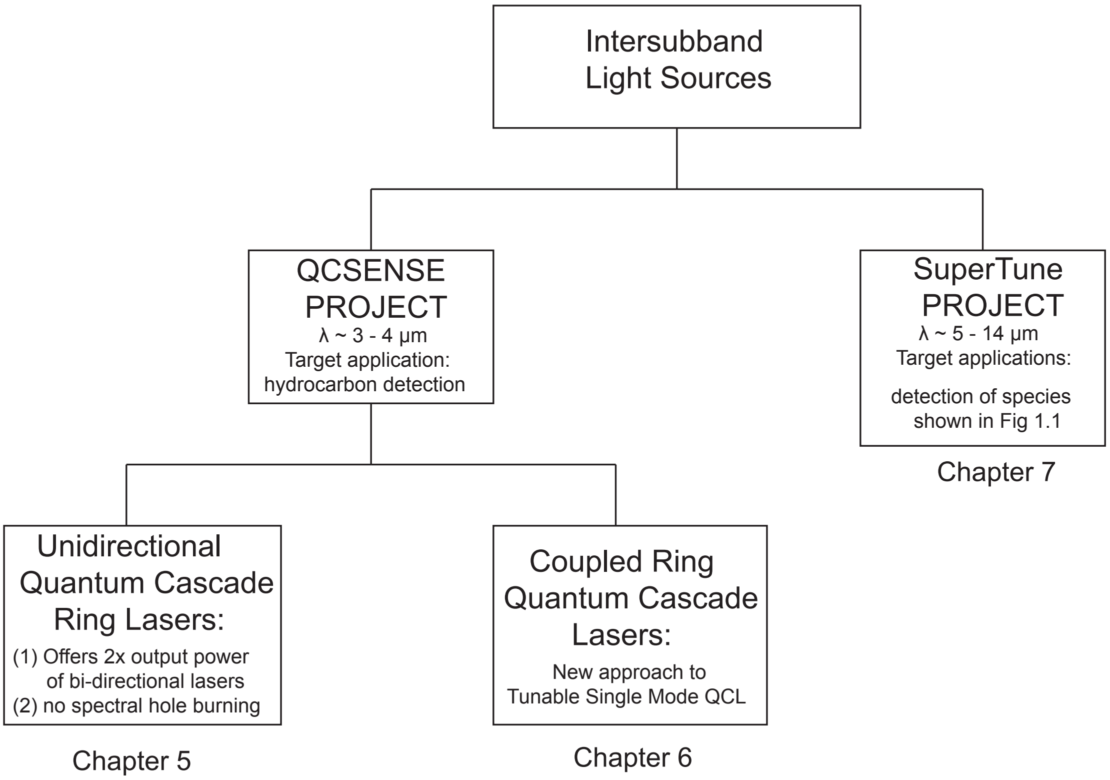

FIGURE 1.2: The structure of the work undertaken in this research

Chapter 2

Quantum Cascade Laser Theory

2.1 Introduction

This chapter presents an overview of the basic concepts of quantum cascade laser (QCL) operation and design. Recent developments in this field with regards to improvements in the active region design is also reviewed together with recent progress towards high performance short wavelength QCLs operating in the technologically important 3-5 μm region. A brief history of QCL development is given in section2.2. The basic operational principle of QCLs are detailed in section 2.4, while section 2.6 covers its active region designs.

2.2 Brief history of Quantum Cascade Lasers

Stimulated emission based on intersubband transitions (a unique feature of QCLs) was postulated in the early 1970's by Kazarinov and Suris[23] and Esaki and Tsu[24]. While working on superlattices, they predicted that transition between ground and excited states in adjacent quantum wells could be accompanied by photon emission, if appropriate bias is applied.

But it was not until the mid nineties that the first QCL was invented. First demonstrated in Bell Laboratories in USA by Jerome Faist and co-workers [6], in 1994, following extensive research in the field of bandstructure engineering and advancement in molecular beam epitaxy (MBE) growth technology. Since then, QCLs have evolved into a state of the art light source covering the scientifically-important mid- and far infrared as well as the terahertz (THz) regions of the spectrum.

The first QCL was based on $\mathrm{Al_{0.48}In_{0.52}As/\ Ga_{0.47}In_{0.53}As}$ heterojunction material system lattice-matched to InP, operating on $\lambda \sim 4.3\mu$m at 88 K under pulsed condition. The following year (i.e 1995) witnessed the operation of the first continuous wave laser with maximum operating temperature of 80 K[25]. Extensive research in these structures, especially on its carrier transportation mechanisms, led to the demonstration of a QCL operating above room temperature under pulsed condition, in 1996[26]. In 2002, the first QCL operating under continuous wave above room temperature was demonstrated[27]. For more milestone achievements in this field and in-depth knowledge of the physics and development of QCLs, the reader is referred to the review paper by Gmachl *et al*[28].

2.3 General QCL Concepts

Quantum cascade lasers are intersubband lasers operating in the mid-infrared region (MIR), far infrared (FIR) and THz region of the spectrum. These lasers differ from conventional interband in many aspects:

1. In complete contrast to interband transition as observed in conventional lasers, QCLs rely on intersubband transition for photon generation. A schematic illustration of interband and intersubband transitions are shown in figure 2.1

   In interband transition [figure 2.1(a)], electrons injected into the conduction band recombine with holes in the valence band emitting photons which

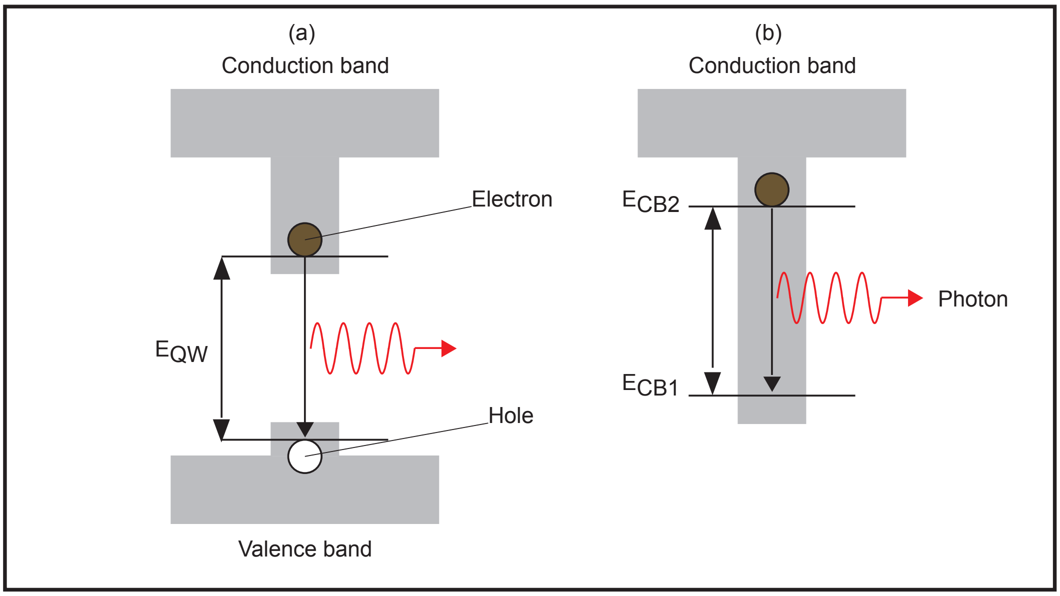

Figure 2.1: Schematic illustration of (a) interband transition i.e photon emission through electron-hole recombination (b) intersubband transition i.e transition between two energy levels in a quantum well

wavelength corresponds to the bandgap energy of the semiconductor material. On the other hand, in intersubband transition [figure 2.1(b)], injected electrons are scattered from higher energy level (E$_{CB2}$) in the conduction band to a lower energy level (E$_{CB1}$) in the same conduction band, emitting photons corresponding to the energy difference between the two subbands (E$_{CB2}$-E$_{CB1}$). Also because the whole transition occurs in the conduction band without electron annihilation (as observed in interband transition), injected electrons can be made to undertake more than one transitions (recycling) by cascading multiple quantum wells (QWs) in the active region with a mechanism in place for extracting and re-injecting electrons into adjacent QWs. The only limiting factor to the number of cascades in a QCLs is the operational voltage.

2. In conventional interband lasers, the emission wavelength is solely a function of the material bandgap, meaning that different semiconductor materials are required for different emission wavelength. This is not the case in intersubband lasers. Here, the emission wavelength does not depend on the bandgap

and can be tailored over a wide range of wavelength (using the same semiconductor), by carefully varying the QW thickness and the electron effective mass in the material.

3. Interband lasers are bipolar devices because they rely on two types of carriers (electrons and holes) for its operation. Intersubband lasers on the contrary, are unipolar devices because only one type of carrier (electrons) is needed for its operation. Based on this, carrier spreading in QCLs are minimised by etching through the active region with no significant effect to its operation. In interband lasers, etching through the active region causes performance deterioration due to non radiative recombination sites introduced by etching active region.

4. In intersubband lasers, the emitted photons are transparent to the quantum cascade (QC) material unlike in interband lasers. This happens because the energy of the emitted photons are far less than the bandgap energy and thus are not absorbed.

5. The dominant scattering mechanism in interband laser is photon emission radiation while in intersubband, phonon scattering mechanism dominates and it is linearly dependent on temperature.

6. Population inversion in interband lasers is obtained by current injection and naturally sustained by the bandgap energy difference between conduction and valence band but in intersubband lasers, population inversion must be established by a suitable design of the active region. This is achieved by manipulating the thicknesses of the QWs and barriers and band offsets in the active region in order to obtain the required energy level separations, carrier scattering rates, optical dipole matrix elements, tunneling times, etc.

2.4 Operation of QCLs

The operation of QCLs is demonstrated using the schematic illustration shown in figure 2.2. The structure is made up of two components: the active region and the injection region. The active region is where optical gain occurs and it consists of undoped QWs. The energy levels in the QWs (E_1, E_2 and E_3) are tailored by bandgap engineering. The energy difference between the upper laser state (E_3) and the lower laser state (E_2) determines the wavelength of operation in the material. The energy difference between E_2 and E_1 is tailored to be in resonance with the longitudinal optical (LO) phonon energy in the material. The E_2 state is rapidly depopulated into E_1 level by very short electron-LO phonon scattering time ($\tau_2 \sim 0.6$ ps) [6] compared to $\sim$ 4.3 ps for the optical-phonon-limited relaxation time(τ_{32}) between E_3 to E_2. The unbalanced scattering rate leads to population inversion (i.e more electrons in E_3 than in E_2) between the two laser states. This condition is necessary for lasing action to be obtained.

The injection region which consists of doped superlattices (described in section 7.4.3) serves as a bridge between two active regions. This region helps to remove accumulated electrons in the ground state (E_1) of the active QWs to avoid backfilling of carriers into E_2 which would affect the laser operation. Extracted electrons are relaxed through a miniband of allowed states within the injection region to ensure that the carriers are at the right energy for injection into the next active region downstream. Also, the minigap (i.e region of no allowed states in a superlattice energy band) helps prevent electrons escaping from E_3 into continuum thus lengthens the electron lifetime in E_3 and improves population inversion.

In summary, when electrons are injected into the first active region on the left, they undergo transition from E_3 to E_2 emitting photons with energy corresponding to E_3 - E_2. In E_2 state, the carriers are rapidly scattered to E_1 via LO phonon interaction. The electrons in E_1 are then extracted via tunneling by the injectors with extremely short time ($\leq$ 0.5 ps) The extracted carriers are relaxed, re-energised and re-injected into E_3 of the adjacent active region and the process repeats itself till the electrons exit the QC material.

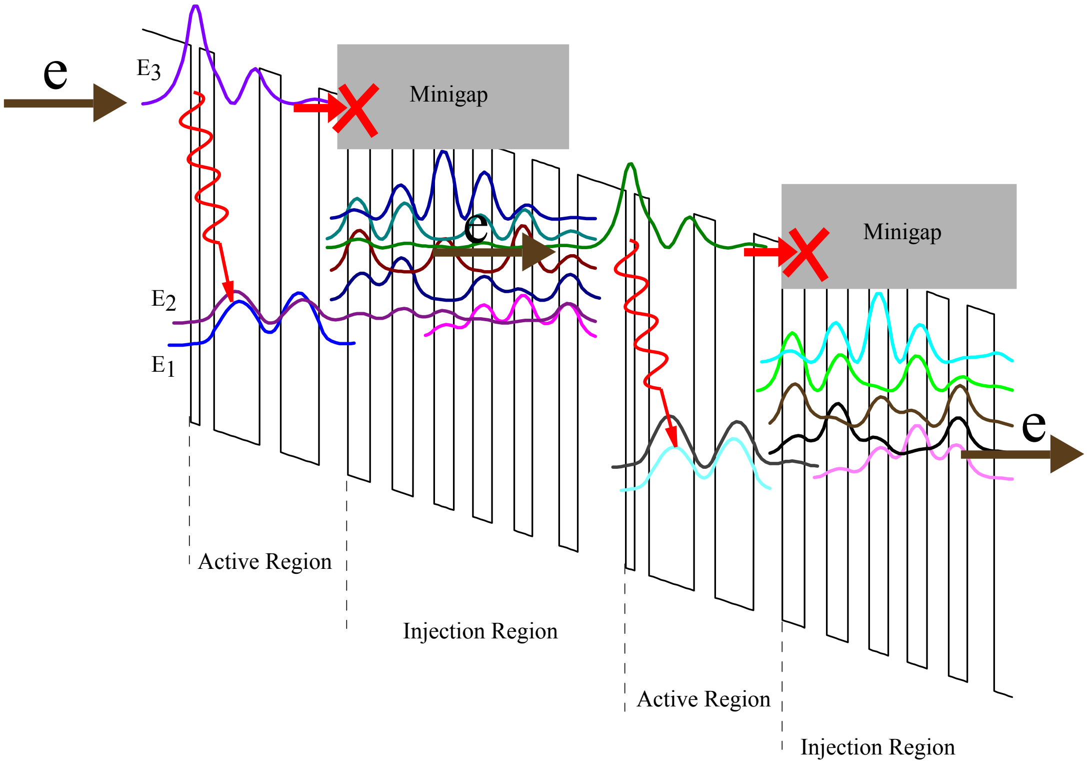

FIGURE 2.2: Schematic of conduction band energy profile used to illustrate the operating principle of quantum cascade laser. The multi-quantum well is under bias with moduli-squared wavefunctions of selected quantum confined energy levels shown. Image taken from Ref [29]

2.5 Population Inversion in QCL

Unlike in conventional interband lasers where population inversion is naturally sustained by the energy separation (bandgap energy) between the electrons in the conduction band and holes in the valence, population inversion in intersubband lasers (e.g QCLs) must be artificially engineered due to the joint density of states of the transition energy levels. Population inversion in QCLs is achieved by manipulating the electron life times and scattering rates in the upper and lower laser levels by using the combination of quantum mechanical tunneling and quantum confinement effect. In its most basic state, a QCL is a simple three energy level system, as illustrated schematically in figure 2.3. Where n_1, n_2 and n_3 are respectively the population of electrons in E_1, E_2 and E_3 states. The direction of scattering is indicated by the arrows; upwards pointing arrow means absorption and vice versa.

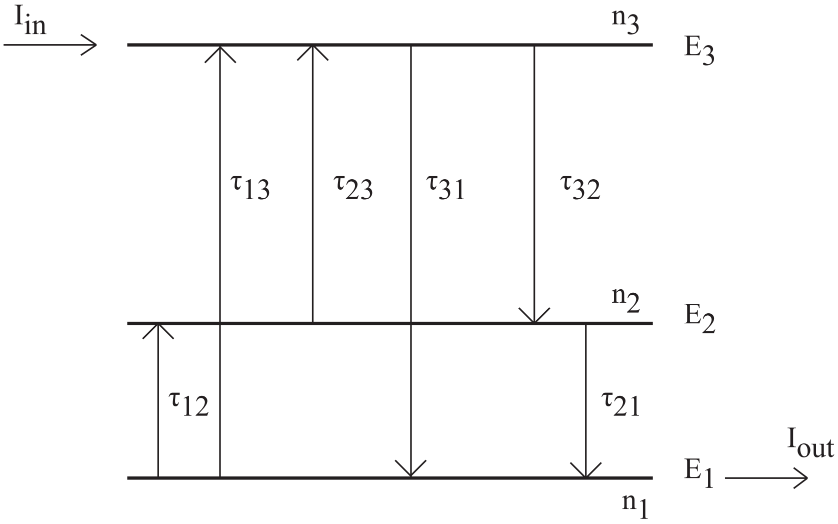

FIGURE 2.3: A schematic illustration of the scattering process in a three energy level quantum cascade laser active region

The rate equations for the population of electrons at each level are given as,

$$\frac{dn_3}{dt} = I_{in} + \frac{n_1}{\tau_{13}} + \frac{n_2}{\tau_{23}} - \frac{n_3}{\tau_{32}} - \frac{n_3}{\tau_{31}} \tag{2.1}$$

$$\frac{dn_2}{dt} = \frac{n_1}{\tau_{12}} + \frac{n_3}{\tau_{32}} - \frac{n_2}{\tau_{21}} - \frac{n_2}{\tau_{23}} \tag{2.2}$$

$$\frac{dn_1}{dt} = \frac{n_3}{\tau_{31}} + \frac{n_2}{\tau_{21}} - \frac{n_1}{\tau_{12}} - \frac{n_1}{\tau_{13}} - I_{out} \tag{2.3}$$

where I_{in} represents the injection rate (i.e the number of electrons per unit time), which in the steady state condition, is equal to the electron extraction rate, I_{out} (as shown in figure 2.3).

Ignoring absorption rates (i.e by assuming a relatively low temperature of operation) and at the same time considering the population of the second level, where in the steady state, the net rate of change is zero, then;

$$\frac{n_3}{\tau_{32}} = \frac{n_2}{\tau_{21}} \tag{2.4}$$

Finally, if we assume that $\tau_{21} > \tau_{32}$, then $n_3 < n_2$, meaning no population inversion. On the other hand, if $\tau_{21} < \tau_{32}$, then $n_3 > n_2$, i.e. a population inversion will exist between levels E_2 and E_3, thus satisfying a necessary condition for stimulated emission. In practice the energy difference E_2-E_1 is designed to be in resonance with the phonon energy in the well.

In quantum cascade lasers, the barriers through which electrons enter the excited laser state (i.e injection barrier) and ones through which relaxed electrons exit the active region into the injector (i.e exit barriers) region are critical to sustaining population inversion and laser operation, even after satisfying equation 2.4. The injection barriers should be thick enough to prevent loss of oscillator strength between the laser states (E_3 and E_2), which would reduced the spatial confinement of E_3 within the first active well. But on the other hand should be thin enough to allow sufficient tunneling of electrons into the upper state of the adjacent well. The exit barrier, unlike the injection barrier should be thin enough to allow for qualitative resonant tunneling from E_1 to the miniband injector but should also not be too thin to allow for carrier escape from E_3 into continuum.

2.6 Quantum Cascade Laser Active Region Design

The material gain coefficient for the active core of a QCL designed for laser emission between an upper subband i and a lower subband f is given by [26];

$$g = (n_i - n_f)\frac{4\pi q^2}{\epsilon_0 n_{eff}\lambda}\frac{z_{if}^2}{2\gamma_{if}L_p} \tag{2.5}$$

where z_{if} is the dipole matrix element, $2\gamma_{if}$ is the full width at half maximum (FWHM) of the lineshape gain function, which is taken as the spontaneous emission linewidth, λ the wavelength and L_p the length of the period (i.e. one active rgion + one injector region), q is the electronic charge and ϵ_0 is the free space permittivity.

From equation 2.5, the material gain coefficient g is proportional to both the intersubband population inversion $n_i - n_f$ (where n_i and n_f are the electronic sheet densities for the upper and lower subbands respectively) and the square of the intersubband dipole matrix element, expressed as

$$z_{if} = |\langle \psi_f | z | \psi_i \rangle|, \tag{2.6}$$

where ψ_f and ψ_i are the z-direction envelope functions. It is possible to tailor the dipole matrix element to some degree through choice of active region design such that a large dipole matrix can be realised, as increased dipole matrix means increased gain in the material. This can be attained by localising the initial and the final wavefunction in the same well and by the utilisation of materials systems with low electron effective mass in the quantum wells. However, localising the two wavefunctions, reduces the non-radiative lifetime of the upper state. To these effect, different types of active regions have been proposed and realised in QCLs; these are detailed in sections below.

2.6.1 Design of the Lower Laser Levels

Sustaining population inversion, as discussed in section 2.5 requires depopulating the lower laser level at a faster rate than the upper laser level. To achieve this, the quantum wells with the two lower states are designed in a manner that energy separation between them is in resonance with the LO phonon energy in the wells, under the application of an appropriate electric field. An illustration of the principles involved in the design of the lower laser levels are shown in figure 2.4, at different applied electric fields.

E_1 and E_2 are the ground state levels of QW1 and QW2 respectively. In this system, E_2 is tailored to be slightly higher than E_1 at zero bias, by making QW1 slightly thicker than QW2. Also the barrier between the two wells is thin enough to allow for strong coupling between the two wavefunctions. This asymmetry breaks the degeneracy of the two confined states and results in the lower energy state of the two being more localised in QW1 and the higher energy state being more localised in QW2.

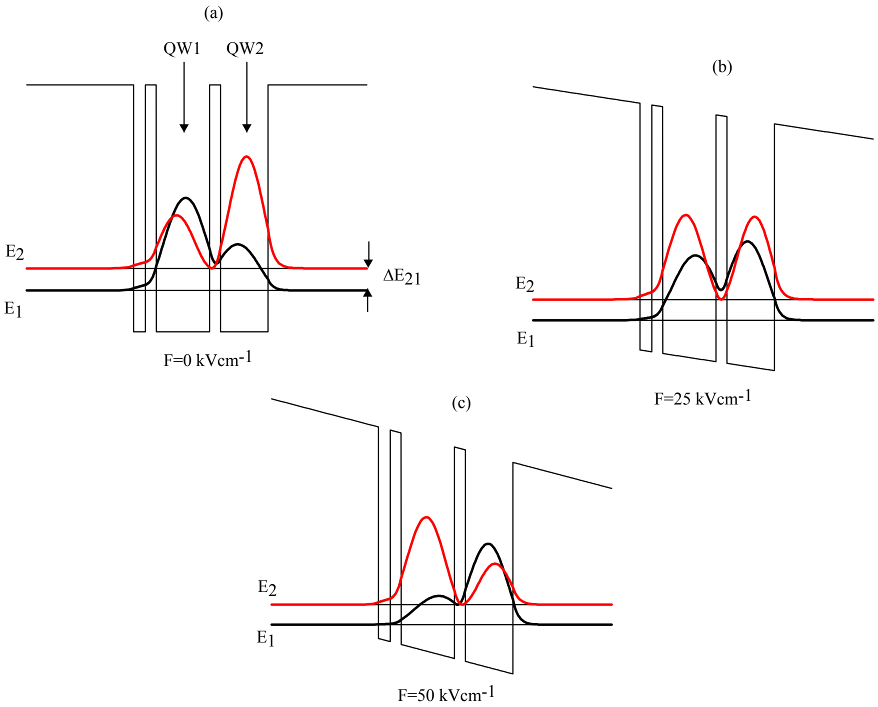

FIGURE 2.4: Conduction band profile showing the two energy levels E_2 and E_1 and the moduli squared of the wavefunctions at (a) F = 0 kV/cm, (b) F = 20 kV/cm; anticross is observed at this point as the wavefunctions begins to switch QWs of localisation, and (c) F = 50 kV/cm. The layer sequence from left to right are *1.2*/***1.1***/*5.4*/***1.1***/4.8 *n*m (normal italics denote GaAs and bold italics denote $Al_{0.45}Ga_{0.55}As$ layers)

On application of an electric field, QW1 increases in potential, while the potential in QW2 decreases, thus the energy levels are brought together. To understand the physics behind this behaviour, the energy offset between the two wavefunctions (ΔE_{21}) were numerically computed (using the 1-band self consistent Poisson-Schr*ö*dinger solver which includes exchange interactions but in the present case no doping was added) as a function of applied electric fields. The result of this calculation is shown in figure 2.5.

As can be observed from the figure, the two energy levels are brought closer together, and as the field increases, ΔE_{21} which initially was decreasing linearly, reaches a minimum value at F=20 kV/cm and then increases again. At the minimum separation, E_1 which was originally localised in QW1, switches and becomes localised in QW2 and vice versa as shown in figure 2.4(b). The phenomena is known as *anti-crossing*.

ΔE_{21} remains closely matched to E_{phonon} over the operating field range (40-60 kVcm^{-1}).

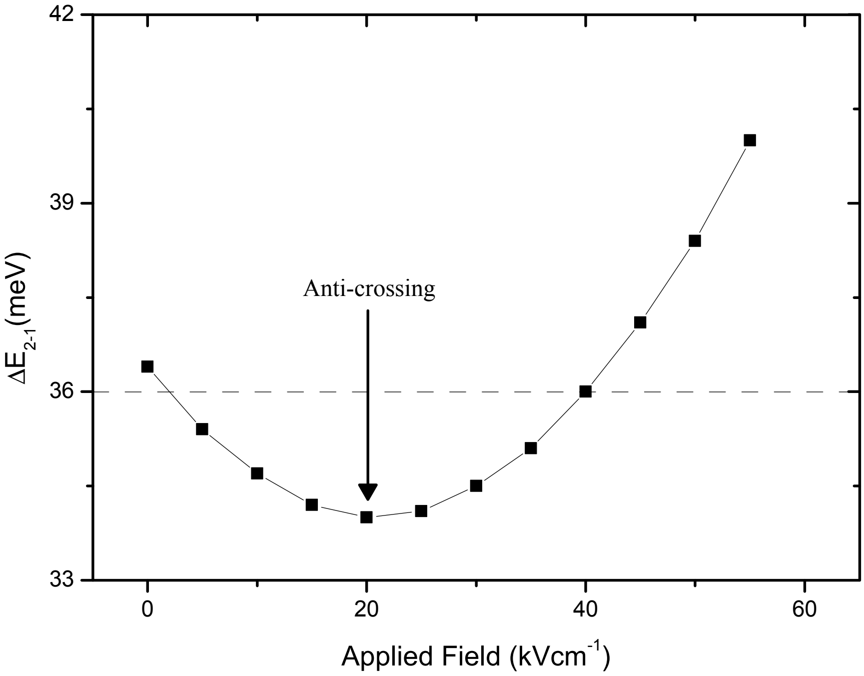

FIGURE 2.5: Energy difference (E_2-E_1) as a function of applied electric field. Dashed line is the calculated LO phonon energy of the well (GaAs)

2.6.2 Vertical Transition Active Region

In two well vertical transition active region (figure 2.6), optical transition occurs between two energy level (E_3 to E_2) localised in the same quantum well (QW1). The two lower levels E_2 to E_1 are designed to have (1) energy gap of about one LO phonon energy and (2) strong coupling between the two wavefunctions, as discussed earlier in section 2.6.1, to maintain population inversion within the operating field regime.

As can be seen in figure 2.6, the application of electric field simultaneously pushes E_2 and E_1 wavefunctions from their original wells under zero applied field to QW1 and QW2 respectively, at 50 kVcm^{-1}. These leads to stronger coupling between E_2 and E_1 wavefunctions and at the same time increases the spatial overlap between E_3 and E_2 wavefunctions. The increase in the spatial overlap between the two laser

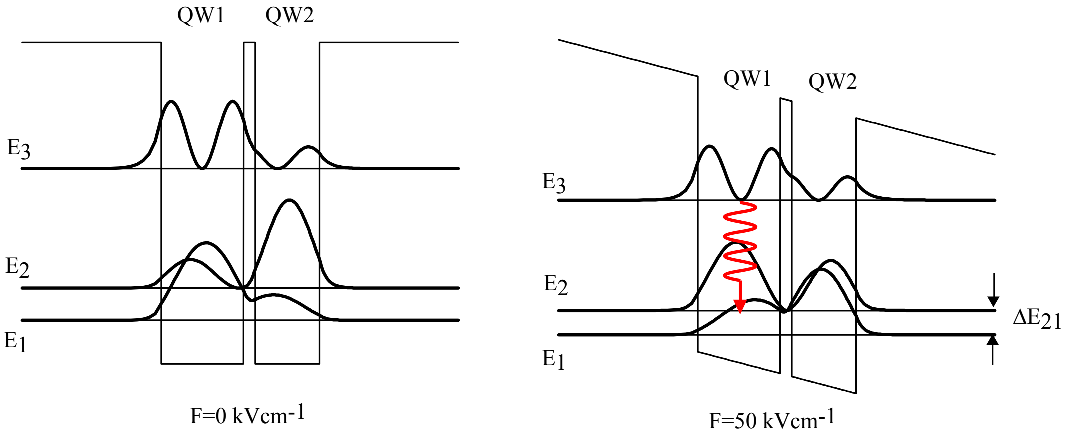

FIGURE 2.6: Conduction band profile of a two well vertical transition active region, the layer structure from left to right starting from QW1 is *6.4*/***0.9***/*5.0* nm (normal italics denote GaAs and bold italics denote $Al_{0.45}Ga_{0.55}As$ layers). Also shown are the moduli-squared wavefunctions of the laser subbands and optical transition denoted by wavy red arrow [30].

states results in a large dipole matrix element for the E_3 to E_2 optical transition and according to equation 2.5, would lead to increased gain coefficient in the material. The calculated dipole matrix element in the above design is $z_{32} \sim 2.2$ nm [30]. The LO phonon assisted intersubband scattering times calculated for this structure are: $\tau_{32} \sim 2.1$ ps, $\tau_{31} \sim 3.4$ ps and $\tau_{21} \sim 0.4$ ps , giving τ_3 1.3 ps [29]‘.

However, this type of design suffers from a reduced upper state E_3 lifetime [31], due to direct scattering by LO phonon emission from E_3 to E_1 (because $q_{32} \approx q_{31}$), in addition to the preferred E_3 to E_2, thus reducing the overall E_3 lifetime according to equation 2.7

$$\tau_3 = \frac{\tau_{31}\tau_{32}}{\tau_{31} + \tau_{32}} \tag{2.7}$$

Other merits of this type of active region include, operational less sensitivity to interface roughness and impurity fluctuations, narrower gain spectrum and thus lower threshold [31].

2.6.3 Diagonal Transition Active Region

The very first quantum cascade laser, by Faist *et al* [6], was based on *interwell* or *photon-assisted tunneling* (i.e diagonal) transition active region. In this type of active region, optical transition takes place between two energy levels localised in adjacent wells, which is in complete contrast to *intrawell* (i.e vertical) transition discussed in section 2.6.2. Shown in figure 2.7, the diagonal transition system consists the upper laser level (E_3), lower laser level (E_2) and the ground state (E_1). As indicated by the red wavy arrow, optical transition occurs between E_3 in QW1 and E_2 in QW2. The energy gap between E_2 and E_1 is tailored to match one LO phonon energy in the well, as discussed in section 2.6.1, to rapidly depopulate the E_2, thus ensuring population inversion between E_3 and E_2.

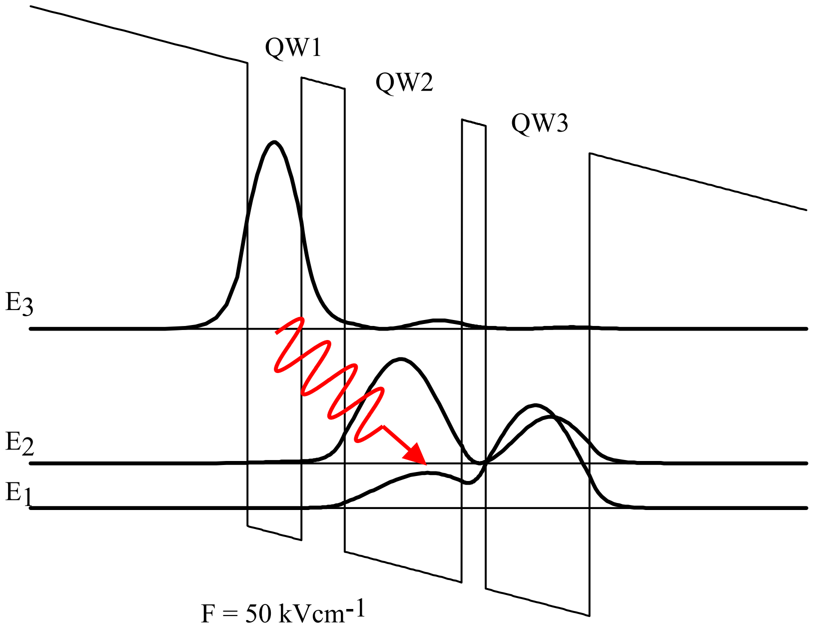

Figure 2.7: Conduction band profile of a diagonal transition quantum cascade active region design. The layer sequence from left to right is *2.5*/***2.0***/*5.4*/***1.1***/*4.8* nm (normal italics denote GaAs and bold italics denote $Al_{0.45}Ga_{0.22}As$ layers. The moduli squared wavefunctions of the laser subbands are shown, the red wavy arrow denotes optical transition

The spatially indirect nature of diagonal optical transitions results in reduced spatial overlap between E_3 and E_2 wavefunctions. A reduced spatial overlap translates into reduced dipole matrix element for the transition. This according to equation 2.5 would lead to a reduction in the material gain coefficient and a wider gain width (compared to vertical transition) due to interface scattering. However, the reduction in spatial overlap leads to an increase in the non-radiative scattering lifetime of the upper level, thereby enhancing population inversion in the system. This by far remains the most important feature of diagonal transition. Also QCLs devices based on this design display a strong voltage induced Stark-shift (see section 7.4.6) of the emission wavelength which allows some degree of wavelength tunability, unlike in vertical intersubband transition (where energy spacing is bias independent) [32]. The calculated parameters for ($Al_{0.33}Ga_{0.67}As$ /GaAs) diagonal active region at 77 K are $z_{32} \sim 0.35$ nm, $\tau_{32} \sim 2.4$ ps, $\tau_2 \sim 0.3$ ps, $\tau_3 \sim 1.5$ ps [33] $2\gamma \approx 35$ meV ([34] p.1560)

2.6.4 Bound to Continuum Active Region

The bound to continuum (BTC) active region [35], shown in figure 2.8 was designed to encompass efficient resonant tunneling injection feature of the 3QW design (e.g inter-/intrawell active region) and effective electron extraction efficiency of the superlattice active region design [36], to eliminate backfilling. In this design the active region spans the whole period and consists of a chirped superlattice with a tilted lower miniband. The upper state is created in the first minigap by a small well adjacent to the injection barrier.

Optical transition occurs in this case between this discrete upper level (E_u) and the tilted lower miniband of states formed within the chirped superlattice active/bridging region.

Because of the quasi-continuum nature of the lower states, the BTC design has a homogeneously broadened gain spectrum that can be used as the basis for QCLs that are tunable over a relatively wide MIR wavelength range. The calculated

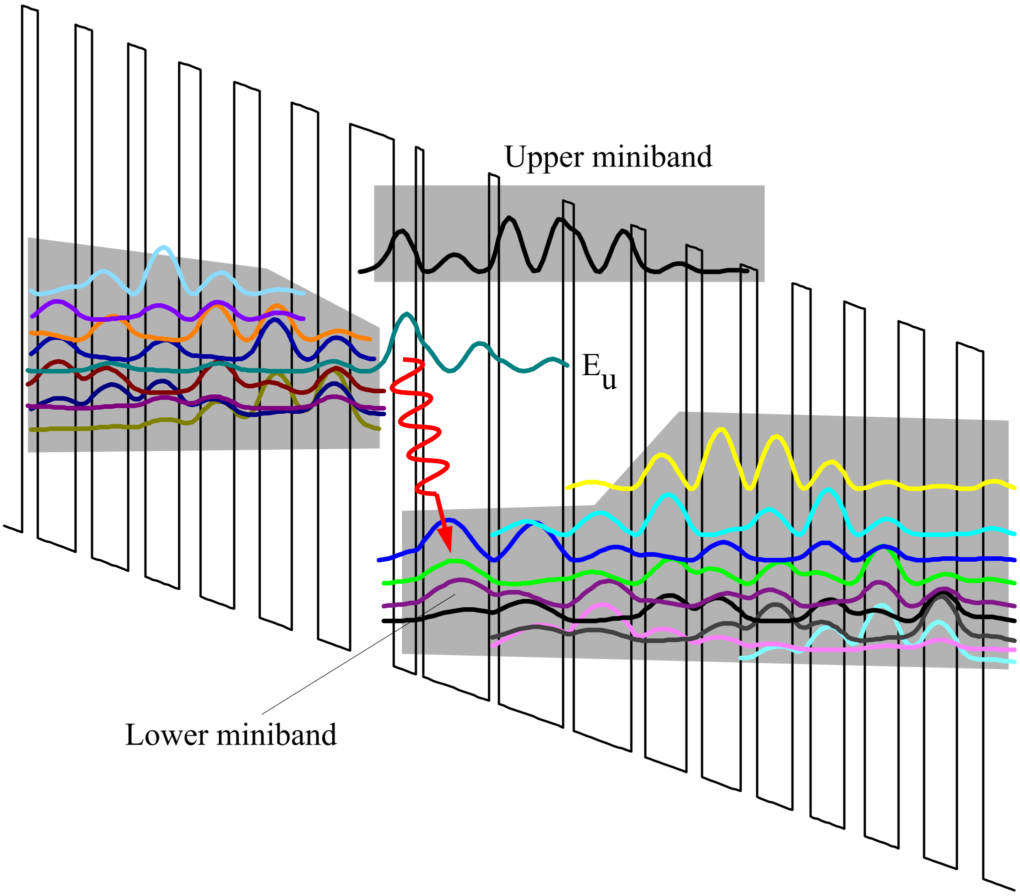

FIGURE 2.8: Conduction band diagram of one stage of the bound to continuum structure under an applied electric field of 35 kV/cm. The moduli squared of the relevant wavefunctions are shown [35].

parameters for ($Al_{0.48}In_{0.67}As$ /$In_{0.53}Ga_{0.47}As$) bound to continuum active region at 300 K are $z_{32} \sim 1.6$ nm, $\tau_{32} \sim 2.4$ ps, $\tau_2 \sim 0.2$ ps, $\tau_3 \sim 1.5$ ps [35]

Other types of QC active region not discussed here, due to time constraint, but are found in literature (e.g double phonon and superlattice active region) can be found in Ref. [37] and Ref. [36] respectively.

2.6.5 Conclusion

There exists a trade off between the two major classes of active region designs (i.e vertical and diagonal). While diagonal transition active region offers longer non-radiative lifetime for electrons in E_3 (i.e increased lasing oppurtunity), it suffers from reduced spatial overlap between the two laser wavefunctions, reduced dipole moment, reduced oscillation strength and interface scattering (leading to broadened gain spectrum). On the other hand the reverse is the case for vertical transition region. Though it offers stronger probability of optical transition due to increased dipole matrix element, it suffers from reduced non-radiative lifetime of electrons in the upper laser state. In conclusion, the choice of active region type is a trade-off between wavelength and confinement.

2.7 Injector Region

In quantum cascade structure, the injection region is used to bridge/ connect two active regions together. To understand its role, we first considered a situation where two active regions were directly connected without an injector, as shown in figure 2.9 With application of appropriate field, electrons injected into the upper lasers state of active region 1, E_{3^1} will be scattered to E_{2^1} and finally to E_{1^1} where they accumulate. Non of the electrons is injected into the upper laser level of active region 2 (i.e E_{3^2}) downstream because E_{1^1} is not aligned to E_{3^2}. To achieve the required energy alignment and very fast sweeping of electrons, superlattice injectors are sandwiched between the two active regions (see figure 2.2). The superlattice miniband which consists of closely spaced energy levels helps extract the electrons from the lower level of active region 1, relax and inject into the upper lasing state of active region 2. To enhance the injection efficiency, the superlattice is designed so that the wavefunction corresponding to the lowest energy state becomes selectively localised in the last two or three periods adjacent to the injection barrier [38]. This is realised in practical terms by progressively decreasing and increasing the QWs and barrier thicknesses respectively, in the direction of current flow. The central part of the injector is selectively n-type doped to prevent the formation of electric field domain that would occur if electrons were directly injected from the contact region.

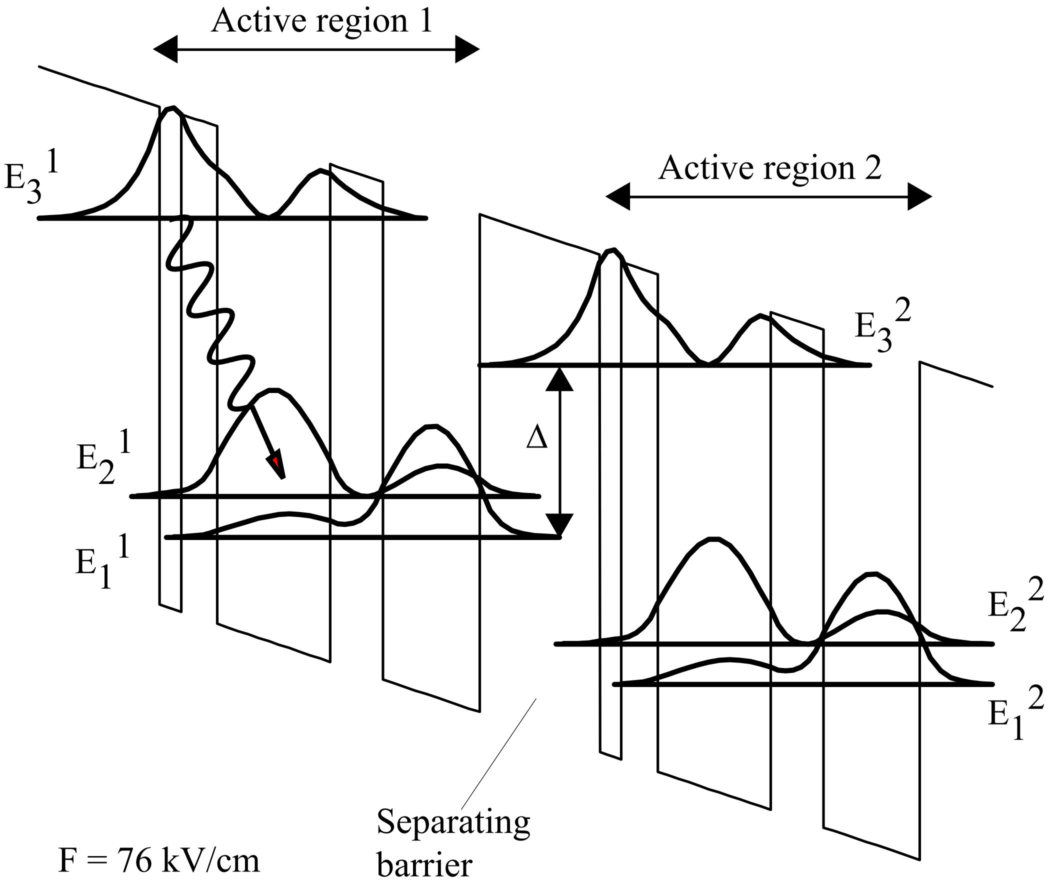

Figure 2.9: Conduction band profile under an electric field of 75 kV/cm to illustrate the requirement for an injector region to connect consecutive active regions. Here two active regions are connected back to back with 5.0 nm central barrier. The optical transition is denoted by the wavy arrow.

Chapter 3

Material and Device Design Considerations

3.1 Introduction

This chapter describes the material and device design consideration, plus the basic integrated optic components that were used in the work reported here on quantum cascade lasers (QCLs). An important part of the QCLs is the semiconductor optical waveguide. Different types of the waveguide have been reported in the literature based on the application requirement. Ring laser optical waveguide are considered in this work, owing to some of its properties needed in this work. This is detailed in (section 3.6). Ring laser optical waveguide are configured in various ways depending on the choice and nature of output coupler required. The theory and design considerations of various output couplers employed in this work are detailed in (section 3.5.1). Amongst the couplers discussed are evanescent field couplers (EFCs) (section 3.5.1.1), multimode interferences (MMIs) (section 3.5.1.2) and Y-couplers (section 3.5.1.3).

3.2 Material Design

3.2.1 Material Aspect of III-V Semiconductors

QCLs consists of hundreds of epilayers of alternating semiconductor materials, typically in the range of a few nanometer thick grown by molecular beam epitaxy (MBE) on either a GaAs or InP substrate [39]. Usually, good epitaxial growth of multiple different semiconductor layers is limited by the need for the lattice constants of the constituent materials to match. To ensure high quality pseudomorphic QCL structure, only a small lattice mismatch (typically $< 1\ \%$) between the alternating layers is accommodated. The lowest energy gap as a function of lattice constant for some commonly encountered III-V compound semiconductors and their ternary alloys at low temperature are shown in figure 3.1. Understanding this relationship is vital to designing and growing complex epilayer structures like the QCL material without compromising on device performance.

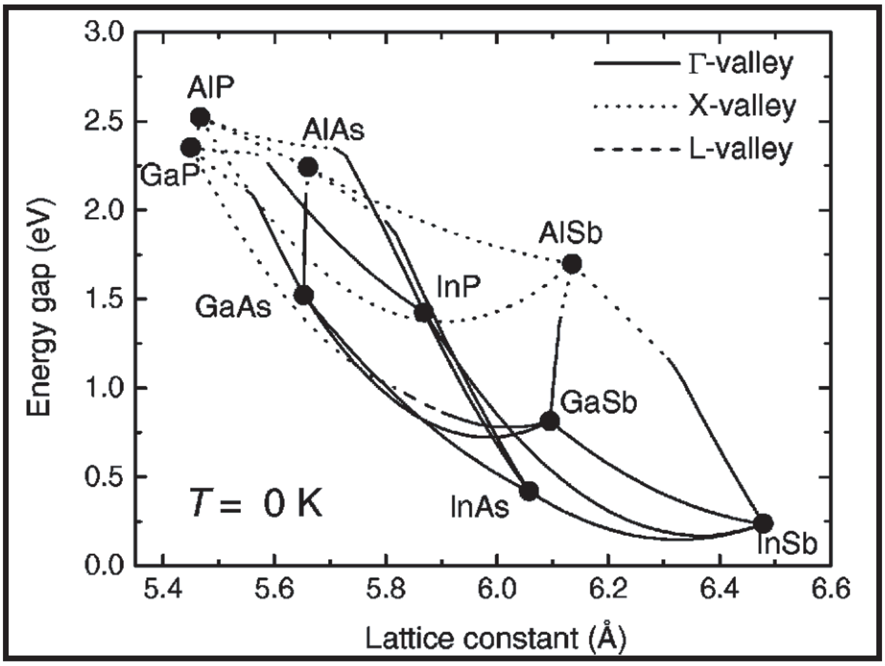

FIGURE 3.1: Energy gaps of III-V semiconductors as a function of lattice constants at low temperature.
Figure courtesy of ref. [40]

3.2.2 Strain in Quantum Wells

The effects of strain are of particular interest in multiple quantum well (QW) structures like QCLs used in this research. Strains, which arise as a result of lattice mismatch between the components of the epilayer structure, could be said to have both negative and positive effects on laser performance. On the former, strains lead to formation of defects and imperfection in the crystal lattice, which deteriorates or completely destroy the device performance. On the other hand, strains can be positively engineered in epitaxial layers to change the crystal lattice geometry, i.e to perturb its size and symmetry. This results in a change of the electronic structure, in particular, a modification of the conduction and valence band edges [41].

In QCLs, the conduction band edge-shift, implies an equivalent change in the barrier heights (i.e larger or lesser conduction band offset) and therefore a corresponding shift in energy levels localised in the QWs. In addition, strain influences the energy difference between sub-bands so introducing a shift in intersubband transition energies. This implies that strain engineering could be used to reach desired emission wavelengths otherwise not attainable, especially in the technological important 3-5 μm atmospheric window. In 1998, Faist *et al* [42] demonstrated a QCL operating at a wavelength of $\lambda \sim 3.4$ μm based on a strain compensated InGaAs/AlInAs material system, in which the band offset, ΔE_c was increased from ~0.51 eV for $In_{0.47}Ga_{0.48}As/Al_{0.48}In_{0.52}As$ lattice matched to an InP substrate to ~0.74 eV for strain compensated $In_{0.7}Ga_{0.3}As/Al_{0.6}In_{0.4}As$ i.e is about 20% increase in ΔE_c.

In 2009, Zhang *et al* [43] demonstrated room temperature operating ($\lambda \sim 3.1$ μm) QCL based on strain compensated $In_{0.8}Ga_{0.2}As/AlAs_{0.67}Sb_{0.33}/InP$ material system. Compared to a similar active region design based on lattice matched $In_{0.53}Ga_{0.47}As/AlAs_{0.56}Sb_{0.44}/InP$ material system reported earlier by Revin *et al* [44], the former showed greater performance characteristics; e.g. lower threshold current density(~3.6 kA/cm^2 at 80 K compared to ~ 12 kA/cm^2 at 20 K). Also while the lattice matched devices suffered from limited operating current range with pronounced roll-over behaviour at high applied field, due to intervalley scattering, such behaviour was not observed in the strained devices probably due to higher intervalley separation ($\Gamma - L$).

If a thin epitaxial layer is deposited on a much thicker substrate, then the lattice constant (a_l) in the growth plane (i.e perpendicular to the growth direction) of the layer will be forced to change to try and equal the lattice constant of the substrate (a_0). As a consequence, the crystal lattice is put under biaxial stress along the growth interface and, while no force is applied along the growth direction, the crystal is able to freely relax along that direction. Growth which allows the lattice constant of the epitaxial layer to fully match the substrate is usually referred as *pseudomorphic growth*. In such case the in-plane strain can be easily calculated as [41]:

$$\epsilon_{\|} = \frac{a_0 - a_l}{a_l} \tag{3.1}$$

The lattice constant of the epitaxial layer can be either larger or smaller than

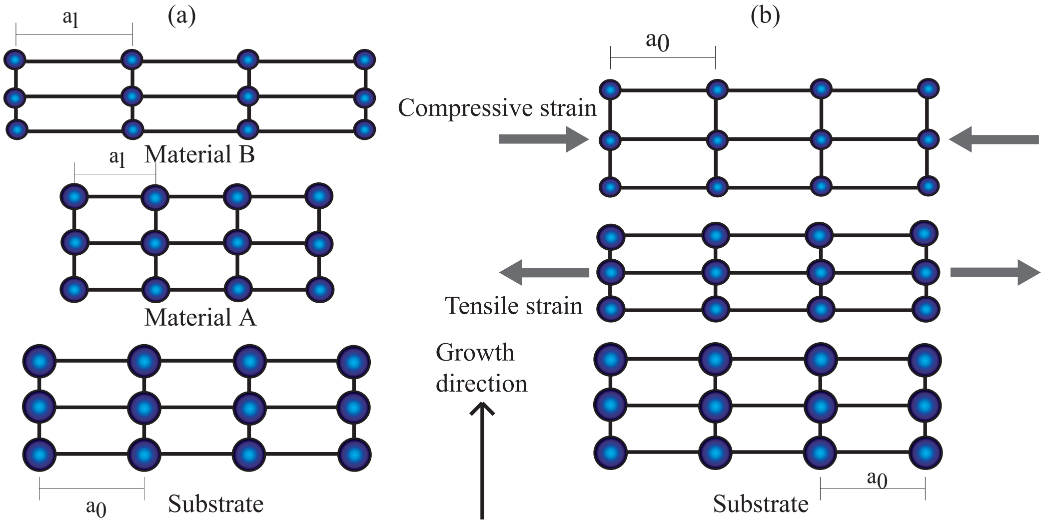

Figure 3.2: Schematic illustration of a substrate with two mismatched layers, (a) shows the individual unstrained layers with lattice constants $a_l < a_0$ (material A) and $a_l > a_0$ (material B), where a_0 is the substrate lattice constant and (b) shows the situation when either of the material is grown on the substrate. As can be seen, material A is under tensile strain while material B is under compressive strain as their lattice constants are forced to match that of the substrate.

the lattice constant of the substrate (see figure 3.2) defining a compressive ($\epsilon_{\|} < 0$ because $a_l > a_0$) or a tensile ($\epsilon_{\|} > 0$ because $a_l < a_0$) strain, respectively. A compressive strain will therefore force the lattice constant in the plane to shrink (see material B in figure 3.2(b)), on the contrary, tensile strain will force it to expand (see material A in figure 3.2(b)).

While lattice matching is generally necessary in order to ensure crystallinity and defect-/imperfection-free interface which could affect the performance of QCL devices, it is possible to incorporate some degree of mismatch, provided that (1) the width of the mismatch layer is not greater than the *critical thickness* and (2) the resultant strain is compensated for by the adjacent materials. The critical thickness is the layer thickness at which the force exerted by the misfit strain balances the force due to the overall tension in the dislocation line. It is given by the expression [45],

$$h_C = \frac{b}{2\pi f}\frac{(1-\nu\cos^2\alpha)}{1+\nu\cos\lambda}\left(\ln\frac{h}{b}+1\right) \tag{3.2}$$

where b is the length of the dislocation, f is 2 times the maximum value of strain, ν is the Poisson ratio, λ is the angle between the strained interface normal and the slip plane and α is the angle between the dislocation line and its Burgers vector.

Beyond this thickness, the force exerted by misfit strain exceeds the overall tension in the line. This causes the dislocation to move thereby destroying the coherence of the interface leading to formation of strain.

3.2.2.1 Strain Compensation in QWs

In order to ensure pseudomorphic growth of multiple layers of QWs, a technique called *strain-compensation* or *strain-balancing* is commonly employed. This involves balancing out the effect due to strain in the whole epilayer structure (i.e achieving zero-stress condition). In strained QCL materials,
(e.g $\text{In}_x\text{Ga}_{1-x}\text{As}/\text{Al}_y\text{In}_{1-y}\text{As}$), the compressive strain introduced (by pseudomorphicaly increasing x beyond the lattice matched condition i.e x >53%) in the QWs, can be compensated by introducing an opposite strain (i.e tensile strain) of the same magnitude in the barriers by pseudomorphicaly increasing y beyond

the lattice matched condition i.e y >48% [42]. The overall result is a net strain-neutral heterojunction which can have a significantly higher ΔE_c than the lattice matched system. This satisfies the zero-stress condition required to achieve strain balancing, provided the thickness of individual layers does not exceed the critical layer thickness.

3.2.3 QCLs Operating in ($\lambda \sim$ 3-5 μm) Atmospheric Window

The ($\lambda \sim$ 3-5 μm) transparent atmospheric window is particularly important for spectroscopy. Most gases and molecules of interest have finger-print like absorption signatures in this region.

The fundamental requirement for QCLs operating in this region is that the QWs in the active region must be:

1. deep enough to provide not only the high conduction band offset (e.g $\Delta E_c \sim$ 740 meV [42] for $\lambda \sim$ 3.6 μm operation at 280 K) required but also limit the escape of electrons from the upper laser state into continuum, which is a source of concern for devices operating at high temperatures and/or applied field.
2. thin enough to support the high transition energy spacing between the upper and lower laser states as required.

In fact as a rule of thumb, a ΔE_c of about twice the laser transition energy is required for room temperature pulsed operation at a particular wavelength, with higher multiples required for maximum power, efficiency and temperature operation.

However, the thin nature of the QWs in the active region, means that significantly higher electric fields are demanded for short wavelength operation due to the large energy spacing between the two laser states. Example, F = 67 kV/cm for a $\lambda \sim$5.4

μm [46] device compared to 35 kV/cm for a $\lambda \sim 9$ μm [47] device of the same bound to continuum (BTC) active region design described in section 2.6.4. This means that as the operating wavelength decreases, the required electric field increases. These fields, increasingly produces triangular tunneling barrier (see figure 3.3), thereby increasing the probability of electrons escaping into the continuum, from the upper laser state. To minimise the escape of electrons at very high applied field and/or high temperature, the upper laser state should be positioned far away from the region of triangular barriers by using higher barrier height materials.

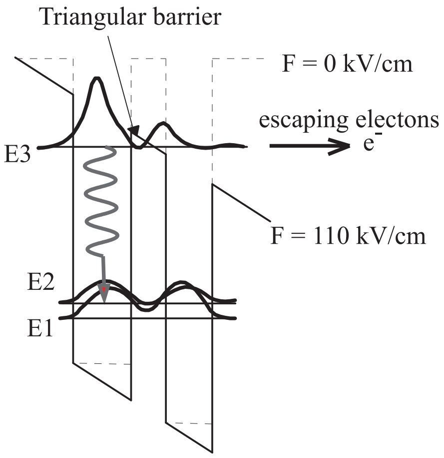

Figure 3.3: Schematics showing formation of triangular barrier and its effect on intersubband population inversion. At high applied field, due to severe band bending, the width of the barrier at the top becomes narrower than the rest of the barrier thereby encouraging tunneling of electrons to the band of continuum

In addition, the narrow quantum wells required for short wavelength operation also place significantly greater demands on crystal growth, since fluctuations and growth mis- calibrations on a monolayer scale have a proportionally greater effect on confinement energies than is the case for wider well devices.

Apart from deep QWs required for short wavelength operation, a critical factor to consider when selecting QCL material is the effect of conduction band satellite valleys on the intersubband population inversion dynamics. Interestingly, even in devices where performance is not limited by barrier height, the energy of the lowest satellite valley minimum in the well may set an approximate lower limit on the emission wavelength possible within a given material system.

Shown in figure 3.4 are some materials of interest for short-wavelength QCLs. Also shown are the satellite valleys and their energy spacings. The first material shown in figure 3.4(a) is $Al_{0.45}Ga_{0.55}As/GaAs$ with maximum $\Delta E_c(\Gamma - \Gamma) \sim 390$ meV, corresponding to the shortest wavelength of about 7 μm, according to the rule of thumb described earlier and corroborated by findings by Gao *et al* [48, 49] on this material system. This effectively renders this material system unsuitable for short wavelength operation. In fact, the shortest wavelength reported for $Al_{0.45}Ga_{0.55}As/GaAs$ QCL at room temperature, was ~9 μm [50].

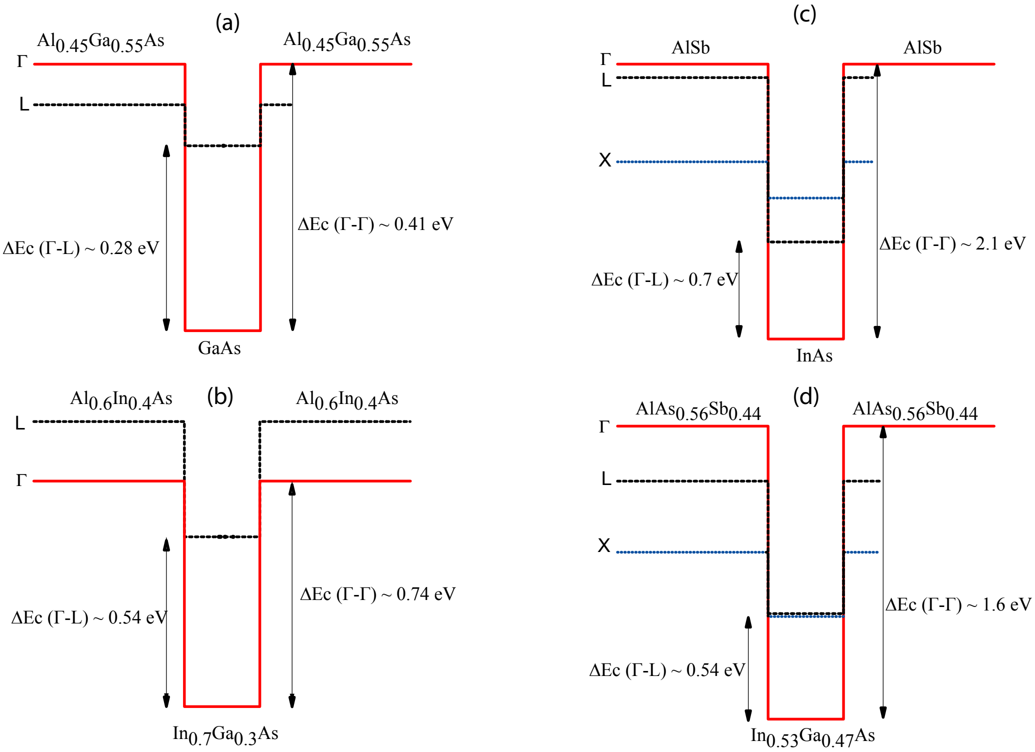

FIGURE 3.4: Some heterostructure systems of interest for short-wavelength QCLs: (a) $Al_{0.45}Ga_{0.55}As/GaAs$ grown on GaAs substrate, this system is only included to explain the basic requirement for short-wavelength operation, (b) Strain compensated $Al_{0.6}In_{0.4}As/In_{0.7}Ga_{0.3}As$ grown on InP substrate, (c) AlSb/InAs grown lattice matched on either GaSb or InSb, (d)$AlAs_{0.56}Sb_{0.44}/In_{0.53}Ga_{0.47}As$ grown on InP substrate . Calculations were done with [51], based on parameters from Ref. [40]

The $Al_yIn_{1-y}As/In_xGa_{1-x}$ material system, lattice matched to InP substrate, has a $\Delta E_c(\Gamma - \Gamma) \sim 520$ meV [52], which is slightly insufficient to support efficient operation in the λ ~3-5 μm region. In fact the shortest emission wavelength reported for this material is $\lambda \sim 5$ μm (i.e photon energy of about 250 meV [29]). The bandgap offset can be improved by applying the strain compensation technique, discussed earlier in (section 3.2.2.1), to the material. To this effect, the $\mathrm{In}_x\mathrm{Ga}_{1-x}As$ QWs are compressively strained with respect to the InP substrate by increasing the fraction of indium beyond the lattice match condition (i.e. $x > 0.52$), while keeping the well width below the critical thickness to avoid formation of defects and misfits. This reduces the bandgap of the QWs (see figure 3.1), thus increasing the ΔE_c. On the other hand, to compensate for the strain introduced into the wells, the fraction of aluminum in the pairing barriers is pseudomorphicaly increased beyond the lattice match condition (i.e y >0.48), thereby introducing tensile strain of equal magnitude but opposite in sense to the compressive strain in the wells. This results in a net strain-neutral material with significantly higher $\Delta E_c(\Gamma - \Gamma) \sim 740$ meV [42] (for $x \sim 0.7$ and $y \sim 0.6$), as shown in figure 3.4(b). Based on the strain-compensated material design discussed here, Faist and co workers demonstrated the shortest wavelength ($\lambda \sim 3.6$ μm) of operation in this material, although at a very high threshold current density ($J_{th} \sim 20$ kA/cm^2). The high threshold could be traced to intervalley scattering at high temperatures, as the upper laser state is slightly lying above the L satellite valley in the quantum wells. This rapidly deteriorates intersubband population inversion in the material leading to high current injection in order to attain lasing operation.

The most promising QCL material (in terms of ΔE_c) for short wavelength operation is the AlSb/InAs shown in figure 3.4(c). This material system, grown lattice matched to either GaSb or InAs substrate, has $\Delta E_c(\Gamma - \Gamma) \sim 2.1$ eV and $\Delta E_c(\Gamma - L) \sim 700$ meV, which is equivalent to the $\Delta E_c(\Gamma - \Gamma) \sim 740$ meV of the strain compensated $\mathrm{Al}_{0.6}\mathrm{In}_{0.4}\mathrm{As}/\mathrm{In}_{0.7}\mathrm{Ga}_{0.3}$ As material system discussed earlier. In addition, the small effective mass of InAs QWs ($m^* = 0.023m_0$) increases the dipole matrix element and reduces non-radiative relaxation rate, both of which are expected to lower the threshold current density of devices from this material [53].

The limiting factors to the shortest possible wavelength of operation in the material are; the position of the lowest satellite minima (L) in the quantum well, which is about 0.7 eV above the InAs conduction band minima and hole generation effects in the low gap InAs associated with 'Zener tunneling' at the high electric fields required for short wavelength devices [53].

Other limitation to the operation of devices from this material system include;

- The inability to grow this material lattice matched to mature GaAs or InP based technology.
- The requirement for very thin barriers (typically$\sim$ 0.6 nm) [54] to ensure efficient resonant tunneling between electronic states in adjacent wells. And according to Ref. [55], the control of the thickness of these layers is crucial for proper operation of the structure because it strongly affects the position of the upper laser level, thereby changing the laser emission wavelength and the resonant alignment of the injector to the upper laser level. The later, according to Ref. [54] is responsible for negative differential resistance (NDR) observed in their devices. NDR, which is associated with breakdown in resonant tunneling (i.e misalignment in energy between the ground state of an injector and the upper laser state) condition, is reported to limit the maximum operating temperature of QCLs based on InAs/AlSb material system.
- the existence of confined states above the upper laser states is another issue to contend with in the development of intersubband lasers in material systems with high conduction band offset. These states can absorb some of the emitted radiation and thus contribute to optical loss. This is the remote cause of high threshold current density observed from these devices at room temperature [55].

The shortest wavelength QCL, so far demonstrated is in the AlSb/InAs material system, emitting at 2.95 - 2.97 μm [56] in pulsed mode. This information was correct at the point of writing this thesis.

3.2.3.1 $AlAs_{0.56}Sb_{0.44}/In_{0.53}Ga_{0.47}As/InP$ quantum cascade (QC) Material

$AlAs_{0.56}Sb_{0.44}/In_{0.53}Ga_{0.47}As/InP$ material system, shown in figure 3.4(d), is one of the most sought-after QC material for short wavelength operation because of the relative large depth of the QWs. The compatibility of the material with established InP device processing and waveguide technology, combined with large conduction band offset ($\Delta E_c \sim 1.6$ eV), particularly makes this material interesting. In addition, the high thermal conductivity of InP (0.68 $Wcm^{-1o}C^{-1}$)[57] improves the thermal management of the devices thus maximises the potential for the realization of high duty cycle or continuous wave short wavelength QCLs.

A particular concern in designing QCLs based on this material system is the position of the lowest satellite valley in the $In_{0.53}Ga_{0.47}As$ QW, which is calculated to be about 520 meV above the Γ position [40]. This was suggested to limit the shortest wavelength operation of QCLs to about 3.7 μm [58] because below this wavelength, the upper laser level is calculated to be above the energy of the lowest satellite valley (L or X) in the well. Such a situation might be expected to lead to a reduction in injection efficiency and intersubband population, due to intervalley scattering, hence restrains laser action.

However, laser action at slightly shorter wavelength was demonstrated by Revin *et al* [44], although at higher threshold current densities, lower maximum operating temperatures and lower output powers compared to longer wavelength devices of similar design. In order to improve the performance of these devices, a larger energy separation between the lowest satellite valley and the Γ level in the QW is needed. This can be achieved by highly straining the the InGaAs well, as discussed in section 3.2.2.1. This strain compensated system is of interest for QCLs operating at wavelengths less than 3.5 μm [59]. It provides increased energy separation between the Γ and L or X conduction band minima in the quantum wells, thus decreasing carrier leakage from the upper laser levels by intervalley scattering and hence improves laser performance.

For QCLs with $In_{0.7}Ga_{0.3}As$ wells, like the ones reported in this thesis, the commonly accepted value for the lowest satellite L valley minimum is 620 meV above the Γ valley band edge [40].

3.3 Wafer Structure

The QC structure employed in this research work is a highly strained $AlAs_{0.56}Sb_{0.44}/In_{0.53}Ga_{0.47}As/InP$ material system (see section 3.2.3.1), with active region design based on *slightly diagonal* [60] bound to continuum (section 2.6.4) technique, operating at $\lambda \sim 3.5$ μm at room temperature and have been previously reported in Ref. [61].

The epi-layer structure of the QC material is shown in figure 3.5 and the computed conduction band profile shown in figure 3.6

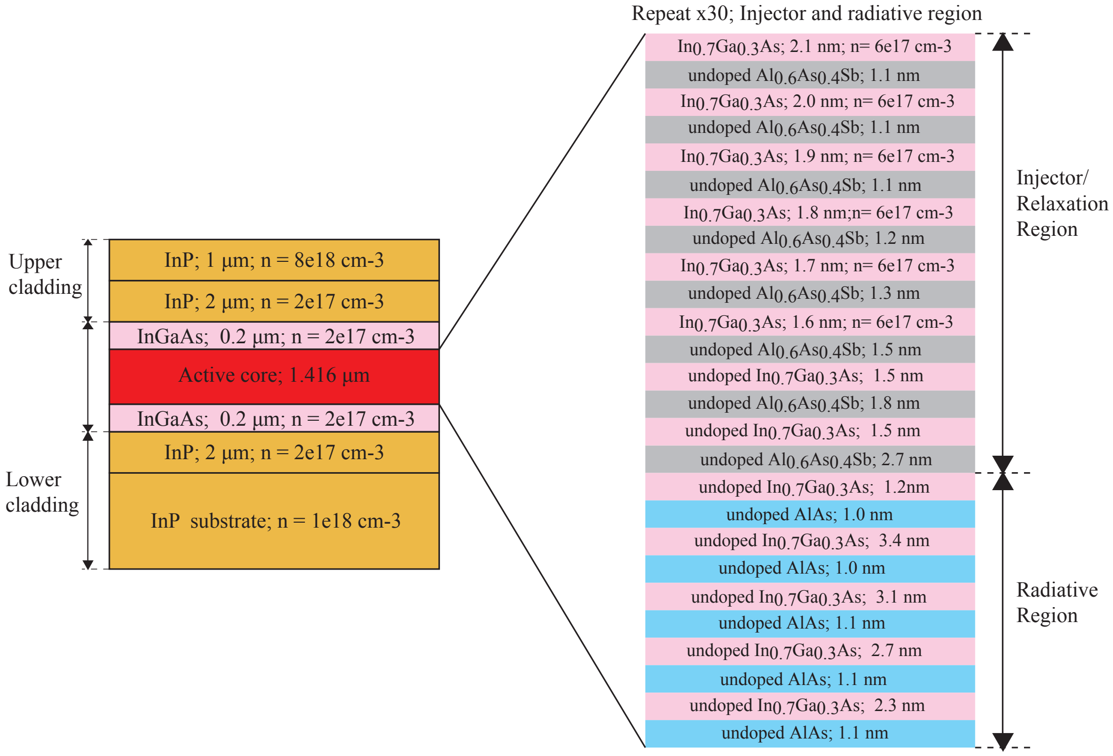

FIGURE 3.5: Epi-layer structure of the QC material used in this research [61]

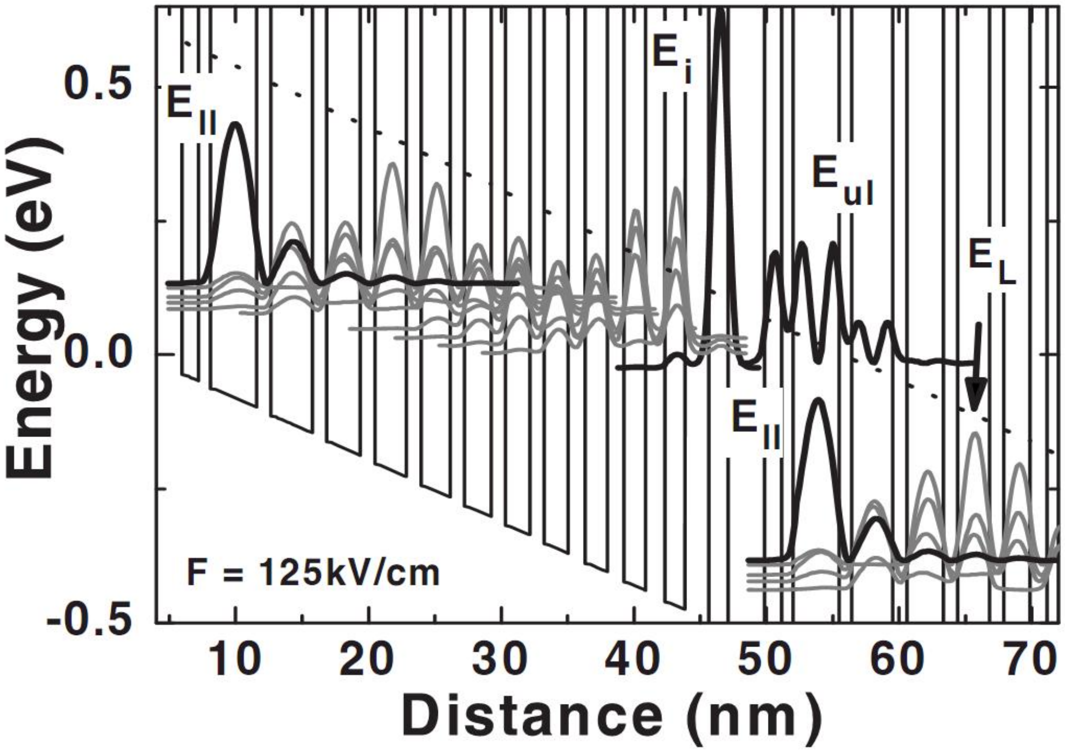

FIGURE 3.6: Calculated conduction band profile for $AlAs_{0.6}Sb_{0.4}/In_{0.7}Ga_{0.3}As/InP$ QC material system under applied bias of F=125 kV/cm for part of the core region. Also shown are the moduli squared of the relevant wavefunctions. E_i, E_{ul} and E_{ll} indicate the injector, upper laser and lower laser energy levels respectively. The energy of the lowest lying satellite energy (E_L) in the well is also shown at a value of about 620 meV above the Γ minimum in the well [61]

The QC material contains 30 periods of strain compensated $In_{0.7}Ga_{0.3}As/AlAs$ active region and $In_{0.7}Ga_{0.3}As/AlAs_{0.6}Sb_{0.4}$ injector regions, grown by MBE, while the lower and upper InP claddings were grown by metal organic vapour phase epitaxy. AlAs barriers were employed in the active regions to improve interface quality and reduce interface scattering.

3.4 Optical waveguide

Optical waveguide is a critical part of a laser responsible for confining or guiding the photons generated in the gain medium, as it propagates along the cavity thereby helping maintain high optical density and hence gain along the device length. In semiconductor lasers, this is achieved by sandwiching the gain region between two semiconductor layers (cladding) with lower refractive index. Optical feedback required for lasing is provided by placing mirrors at the two ends of the cavity; practically this is achieved by cleaving the waveguide in the (101) i.e x-z crystal plane. This configuration allows photons to travel back and forth along the cavity thereby causing more and more stimulated emission until the optical gain overcomes the absorption loss in the material and lasing commences. The index difference at the interface of the semiconductor materials reduces the fraction of light escaping in the growth (z) direction, through a process known as *total internal reflection.* The most common type of waveguide in literature is the ridge waveguide shown in figure 3.7. Ring waveguide used in this work and shown in figure 3.8 is a special type of ridge waveguide developed for chip integration. In these waveguides, optical guiding in the lateral direction (x) is achieved by

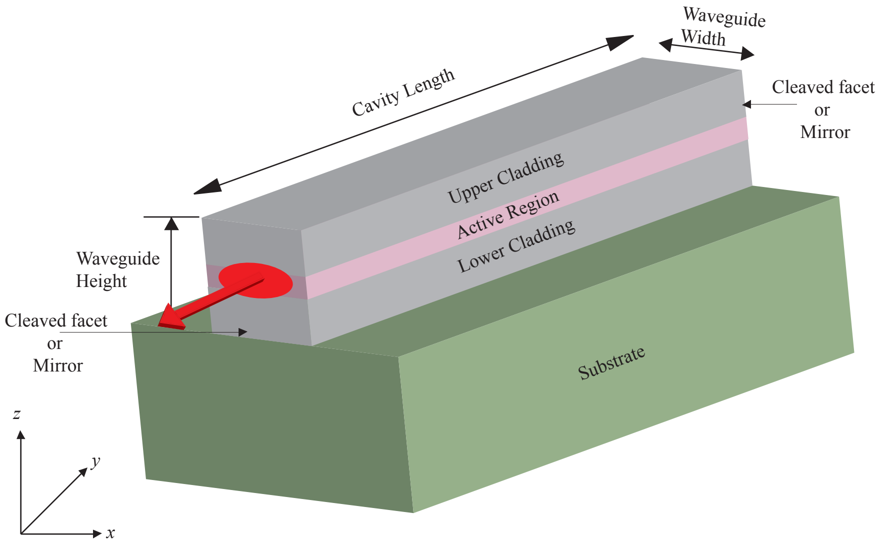

Figure 3.7: Schematic diagram of a ridge waveguide (Fabry-Perot) quantum cascade laser. In this structure, vertical (z) confinement is achieved with the aid of the cladding, while the ridge structure helps confine the photons on the horizontal (x) direction

removing parts of the semiconductor on either side of the ridge through a process known as *etching*. An index difference is introduced at the semiconductor-air interface, thus minimising optical loss on the horizontal direction. This confines the propagating modes within the active region with the exponentially decaying tails (i.e the evanescent filed) overlapping with the cladding.

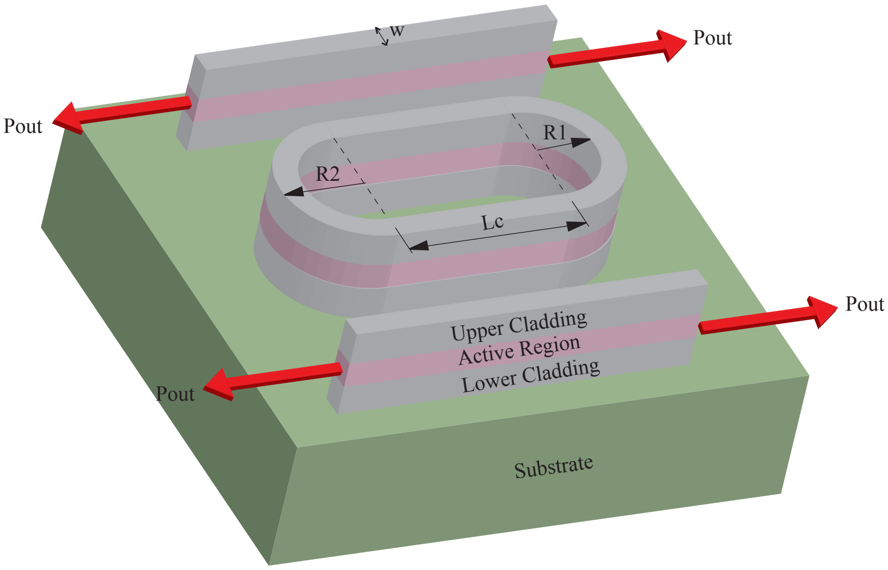

FIGURE 3.8: Schematic diagram of a racetrack ring quantum cascade laser. R1 and R2 are the inner and outer radius of the circular part of the racetrack; *Lc* and *w* are the length of the straight waveguide and the width of the waveguides respectively.

3.4.1 Waveguide Modeling

Waveguide modeling was carried out to select the most suitable waveguide parameters for the devices in this work. Prior to waveguide modeling, the refractive indices and absorption coefficients of the epilayer structure of the QC material presented in figure 3.5 were calculated using equations 7.6, 7.9, 7.10 and 7.11, given in section 7.6.1 and data given in ref. [62]. The calculated optical parameters are shown in table 3.1

Using the parameters in table 3.1, the effective refractive index and the fundamental mode profile of the waveguide structure were calculated using both analytical

Table 3.1: Calculated refractive indices and absorption coefficients of the layers of the QC material at $\lambda \sim 3.5$ μm using equations 7.6, 7.9, 7.10 and 7.11

Layer	Semiconductor	Dop. Conc. (cm^{-3})	Index	$\alpha(cm^{-1})$	Thickness
6	InP	$N=8.10^{18}$	2.917	61.05	$1\mu m$
5	InP	$N=2.10^{17}$	3.101	1.436	$2\mu m$
4	InGaAs	$N=2.10^{17}$	3.39	1.14	$0.2\mu m$
3	InGaAs/AlAsSb	undoped	3.33	0.91	$1.46\mu m$
2	InGaAs	$N=2.10^{17}$	3.39	1.14	$0.2\mu m$
1	InP	$N=2.10^{17}$	3.101	1.436	$2\mu m$
0	InP	10^{18}	3.082	7.22	

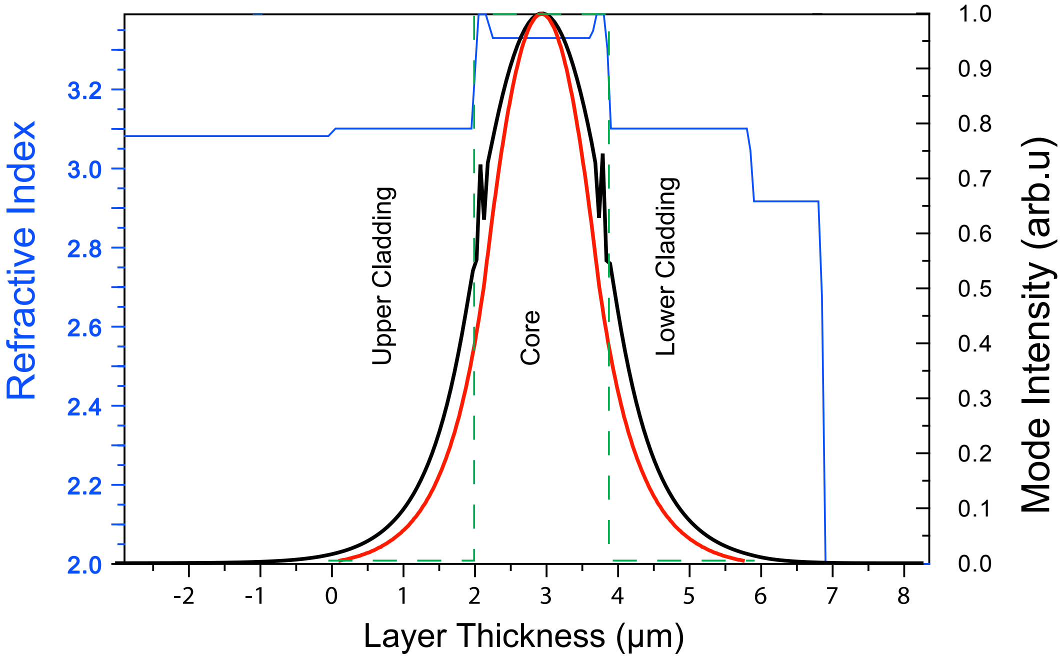

Figure 3.9: Computed index (blue colour) and fundamental mode profile (black colour) of the waveguide structure, using the parameters in table 3.1 in BeamProp

method [63] and beam propagation method [64]. The results are shown in figure 3.9.

3.4.1.1 Analytical calculation

To undertake analytical calculation of the effective index and the mode profile, we further reduce the five-layer structure shown in table 3.1 to a three-layer slab waveguide shown in table 3.2 to simplify the mode calculation and analysis. To achieve this we collapsed layers 2, 3 and 4 in table 3.1 into layer 2 in table 3.2, while layers 1 and 5 being the lower and upper cladding in table 3.1 become layers 1 and 3 in table 3.2, respectively. The cap layer i.e. layer 6 was omitted because the cladding layers are thick enough that only negligible part of the mode overlap with the cap. The analytical mode profile for the fundamental transverse magnetic (TM) mode is calculated from the expression [63],

TABLE 3.2: Reduced waveguide structure used for the analytical calculation of the effective index and the fundamental mode profile

Layer	Semiconductor	Dop. Conc. (cm^{-3})	Index	$\alpha(cm^{-1})$	Thickness
3	InP	N=2.10^{17}	3.101	1.436	2μm
2	InGaAs/AlAsSb	undoped	3.34	0.94	1.86μm
1	InP	N=2.10^{17}	3.101	1.436	2μm
0	InP	10^{18}	3.082	7.22	

$$\phi(y) = \begin{cases} Acos(\kappa y), & \text{for } \mid y \mid \ \leq \text{d}/2 \\ Bexp[-\gamma(\mid y \mid - d/2)], & \text{for } \mid y \mid \ \geq \text{d}/2 \end{cases} \tag{3.3}$$

where, $d = 1.86\ \mu$m,

$$\kappa = k_0(n_2 - n_{eff})^{1/2} \tag{3.4}$$

$$\gamma = k_0(n_{eff} - n_1)^{1/2} \tag{3.5}$$

and n_{eff}=3.26, n_2=3.34 and n_1=3.101 and are the effective index, refractive indices for the active and cladding layers respectively. $k_0 = 2\pi/\lambda$ and $\lambda = 3.5\ \mu$m.

For even TM modes (e.g. the fundamental mode), the continuity of ϕ and $d\phi/dy$ at $\mid y \mid = d/2$ requires that,

$$B = Acos(\kappa d/2) \tag{3.6}$$

$$\gamma B n_2^2 = \kappa n_1^2 A cos(\kappa d/2) \tag{3.7}$$

If we divide equation 3.7 by equation 3.6 we obtain the eigenvalue equation

$$\gamma n_2^2 = n_1^2 tan(\kappa d/2), \tag{3.8}$$

whose solutions yield the effective mode index ($n_{eff} = 3.26$)

In figure 3.9 the analytical mode profile is shown in red colour, while the refractive index profile used for the calculation is shown in green (dotted).

3.4.1.2 Numerical Computation

The TM fundamental mode profile was numerically calculated using the beam propagation method in BeamProp [64]. Using the data in table 3.1, the mode profile was computed. The blue and black plots in figure 3.9 are the computed refractive index and mode profile.

The mode profiles look identical with the exception of the kinks in the numerically computed mode profile. These kinks, which were due to layers 2 and 4 (see table 3.1) with refractive index higher than that of the core, were not present in the analytical index profile used for the mode profile calculation.

3.5 Constitutional Component design

3.5.1 Couplers

The closed optical-path nature of a ring or racetrack laser requires a means of coupling power out from them. Available power coupling techniques, such as evanescent field couplers [65], Y-junction couplers [66], and MMI [67], have been reportedly used to out-couple power from ring lasers. Not only do couplers extract light from the ring cavities, studies and experimental works on the impact of output coupler configuration on the operating characteristics of semiconductor ring lasers, conducted by Krauss *et al* [68], have shown that the dynamics of ring lasers are affected by output couplers. Some of the factors to consider when selecting the appropriate coupler configuration include: back reflection to the cavity, flexibility in choosing coupling ratios, fabrication tolerance and tunability.

3.5.1.1 Evanescent field couplers

This is an important device used to couple light into and out of a ring laser. It consists of at least two waveguides placed in a manner (see Fig.3.12) that the evanescent (tail) part of the field propagating in one waveguide overlaps and gets coupled into the second waveguide over a certain length, known as *coupler length* (L_c). Shown in figure 3.11 is an scanning electron microscope (SEM) of the vertical cross-sectional view of the fabricated EFC. As outlined in Table 3.3 evanescent field couplers are less complex to fabricate and there is great flexibility in the amount of power that could be coupled from one waveguide to another, unlike in other types of coupler. The later is the most fascinating feature of this coupler. One of its draw back is its operational sensitivity to slight change (in nm scale) in etchdepth and coupling space (see Fig.3.10) which makes it difficult to produce a given coupling ratio, accurately and reproducibly.

To gain an insight into the coupling mechanism of an EFC, we make reference to solution of couple-mode equations described by [69] for a field coupler shown in Fig.3.12; The power propagating in waveguide 1 and 2 can be calculated from eqn.3.9 and eqn.3.10 respectively.

$$P_1(l) = P_0 \frac{|C_{21}|^2}{S^2} \sin^2(Sl) \tag{3.9}$$

$$P_2(l) = P_0 \left[\frac{(\Delta(k))^2}{2S} \sin^2(Sl) + \cos^2(Sl) \right] \tag{3.10}$$

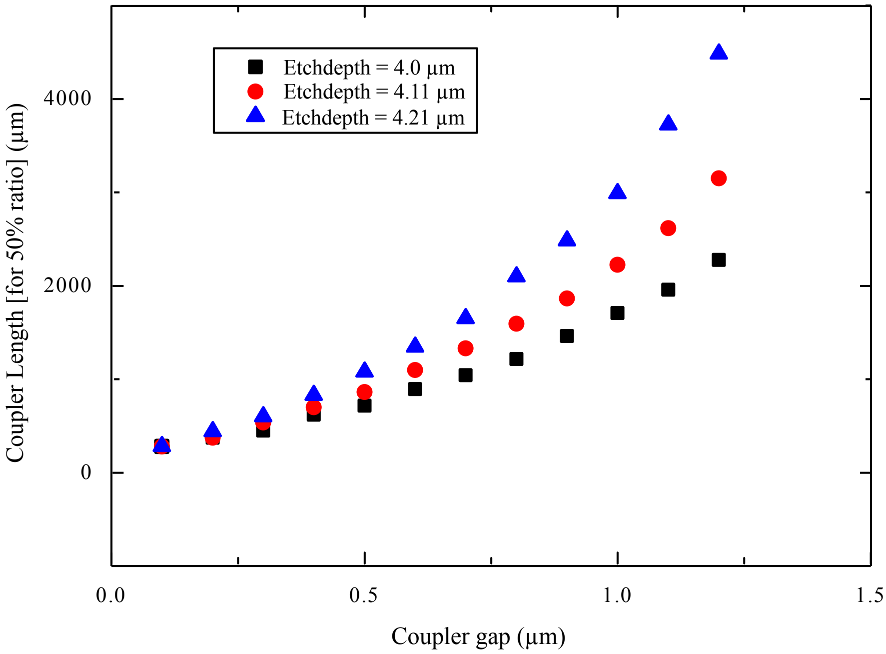

FIGURE 3.10: A plot of coupler length (for 50% coupling) as a function of etch depth and coupler gap in a 5 μm waveguide; calculated using BeamProp [64] at λ~3.5 μm

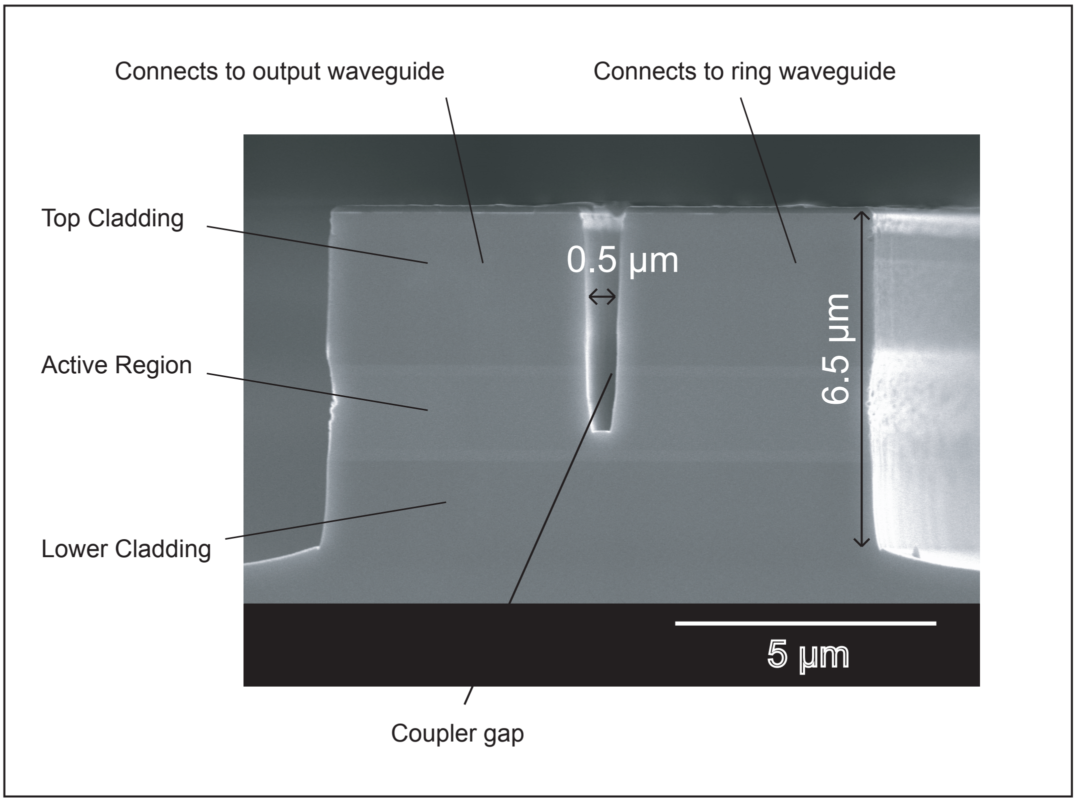

FIGURE 3.11: Cross-sectional view SEM of the fabricated evanescent field coupler

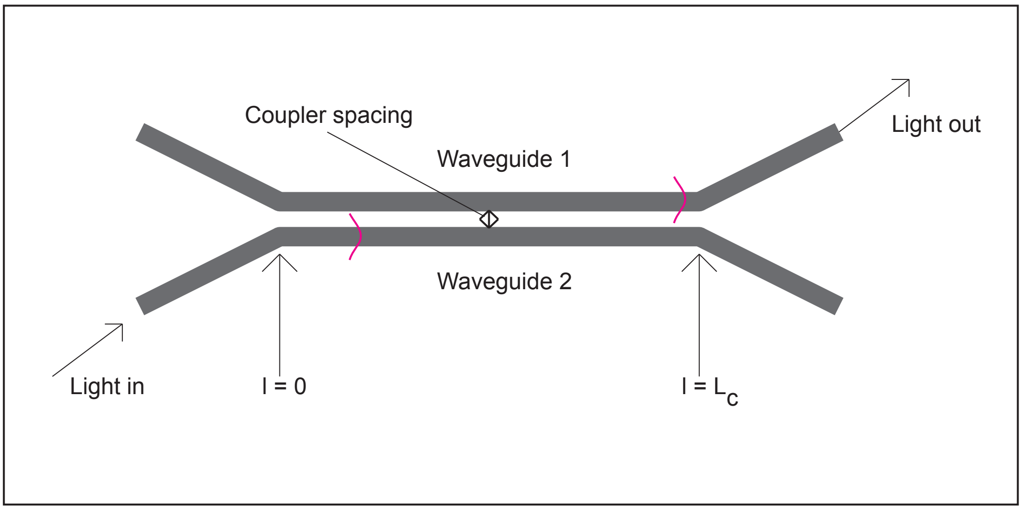

FIGURE 3.12: Top view schematic of a simple evanescent field coupler

where P$_0$ represent the initial power injected into waveguide 2, $S = \sqrt{\frac{(\Delta(k))^2}{2} + C_{21}C_{12}}$ is the phase coupling coefficient and C$_{21}$, C$_{12}$ and $\Delta(k)$ are coupling coefficient from waveguide 2 to 1, coupling coefficient from waveguide 1 to 2 and phase difference between the two waveguides respectively. Under phase-matched condition as it is in our case (waveguides 1 and 2 are identical), $\Delta(k) = 0$ and $C_{21} = C_{21}$ ≡(C); eqn. 3.9 and eqn. 3.10 are reduced to eqn. 3.11 and eqn. 3.12 respectively.

$$P_1(l) = P_0 \sin^2(Cl) \tag{3.11}$$

$$P_2(l) = P_0 \cos^2(Cl) \tag{3.12}$$

Under phase-matched condition, according to eqn. 3.11 and eqn. 3.12, power is periodically coupled between the two waveguides, along the propagation direction l.

In this work, evanescent field couplers were used to out-couple light from some of the ring lasers, unidirectional laser and the coupled ring lasers. To ascertain the optimum length of the couplers for this work, BeamPROP was used to compute the coupling coefficient as a function of coupler spacing using the following data (coupler etchdepth = 4.0 μm and gap = 0.5 μm). The result is shown in figure 3.13;

coupler length = 670 μm can be deduced from the plot for a 50:50 coupling ratio.

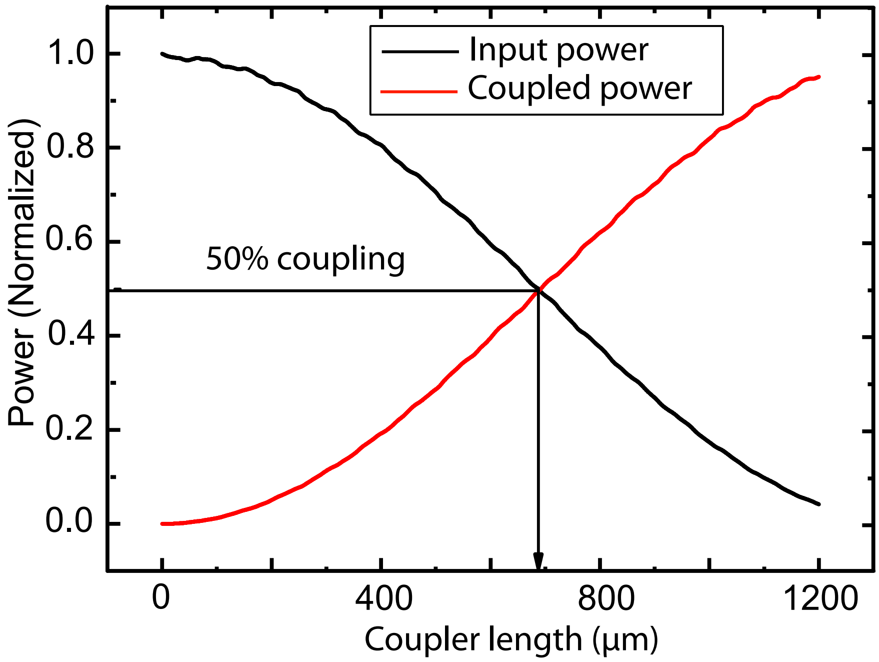

FIGURE 3.13: A plot of coupled power against coupler length for a coupler gap, d = 0.5 μm and 4.0 μm etch depth. This computation was done using BEAMPROP.

3.5.1.2 Multimode Interference Couplers

The operation of optical MMI is based on the principle of self-imaging, a property of multimode waveguides, where an input field profile is reproduced in single or multiple images (see Fig.3.14) at periodic intervals along the propagation direction of the waveguide [70].

From the graphical representation shown in Fig.3.14, an input field, Ψ(x,y), injected into the MMI at a point where x= -W$_e$/6 and y = 0 is split into two equal fields (50% coupler) between x= -W$_e$/6 and x= W$_e$/6 at y = 1/2(L$_m$). At point y = L$_m$, the field is completely coupled from the input x position (x= -W$_e$/6) to x= W$_e$/6 (100% coupler). Point y = 3/2(L$_m$) is a mirror image of what was obtained at point y = 1/2(L$_m$) (i.e 50:50 coupler) and finally the original image is repeated at point y = 2(L$_m$) (i.e 0% coupler). Where W$_e$ known as the effective width is

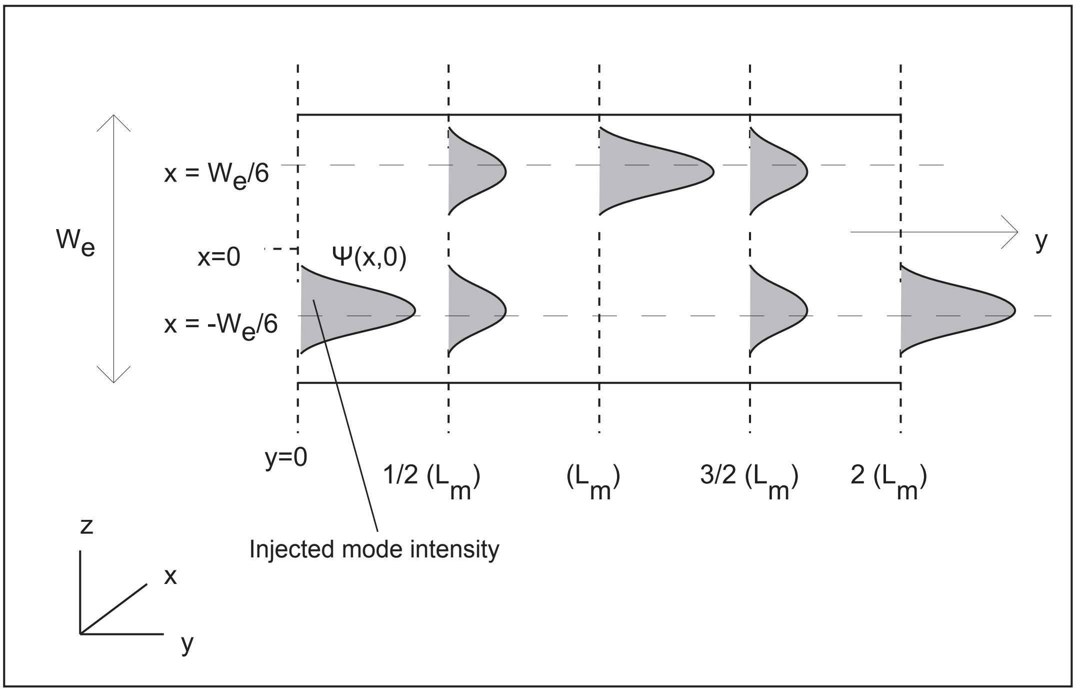

FIGURE 3.14: Graphical representation of the imaging properties in the multimode waveguide with an input field injected at x=-W$_e$/6

calculated from the expression [70];

$$W_e = W_m + \left(\frac{\lambda_0}{\pi}\right)\left(\frac{n_c}{n_{eff}}\right)^2 (n_{eff}^2 - n_c^2)^{-(1/2)} \tag{3.13}$$

where λ_0 is the free-space wavelength, n$_c$ is the refractive index of the cladding (i.e air), n$_{eff}$ is the effective index of the waveguide and W$_m$ is the physical width of the waveguide. On the other hand, L$_m$ (the beat length of two lowest order modes) can be calculated from the expression [70];

$$L_m = \left(\frac{4 n_{eff} W_e^2}{3\lambda_0}\right) \tag{3.14}$$

In this research, only 3dB (50:50) 2x2 MMI couplers were used. Two suitable mechanisms of self imaging in multi-mode waveguides appear for this case; (1) N x N general interference mechanism and (2) 2xN restricted paired interference mechanism (where N is the number of inputs/outputs). In the former, the images are independent of the launch-field input position but in the latter, the reverse is the case. In general self imaging couplers, as shown schematically in Fig.3.15(a)

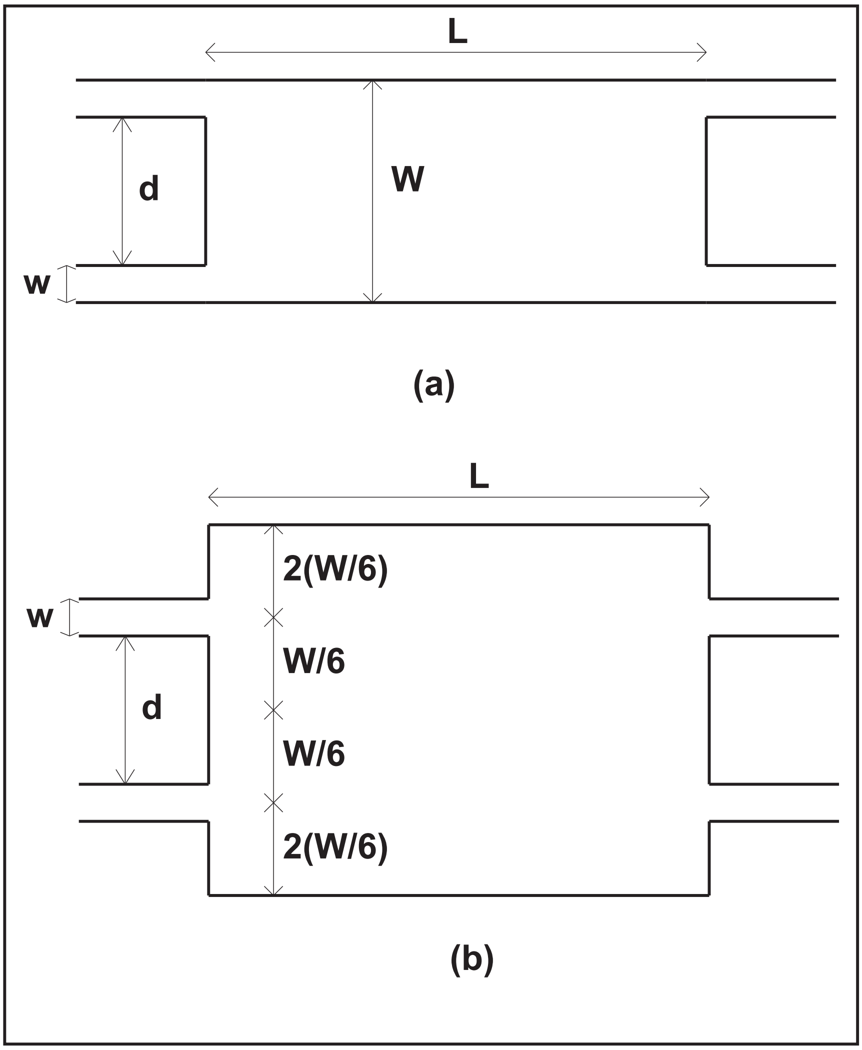

FIGURE 3.15: Schematic layouts of (a) a 2 x 2 general interference MMI coupler and (b) 2 x 2 restricted pair interference MMI

where N=2, the first single image distance is found at 3L_m with the first N-fold image being found at:

$$L = \frac{3L_m}{N} \tag{3.15}$$

Compared to the restricted paired case, as shown in Fig.3.15(b), where the first single image may be found at L_m and the first N-fold image at;

$$L = \frac{L_m}{N} \tag{3.16}$$

In Fig.3.15(a) and (b) a realistic distance, d, is maintaned between the two access waveguides; (1) to ensure no field coupling between the access waveguides, prior to launching into the multimode waveguide, (2) to ensure no RIE lag effect (Ref.[71]) during fabrication. For the devices reported in this thesis, $d = 3$ μm was chosen. With this value, a minimum width is forced on the two MMIs; minimum width attainable with general interference mechanism and restricted interference mechanism are calculated from eqn.3.17 and eqn.3.18 respectively. With w $=$ 5 μm, W$_{min}$g $=$ 15 μm and W$_{min}$r $=$ 24 μm; i.e general interference mechanism give shorter MMI than MMI based on restricted interference mechanism. Although for a certain number of modes (say 6) the MMI width will be same for both and as such, according to equations 3.15 and 3.16, restricted interference MMI will give shorter MMI. Other advantages of general MMI over restricted interference MMI include; non-dependence of the imaging properties on the position and shape of input fields and non-dependence of operational condition on modal excitation requirement [72]. On the other hand, general MMI suffer from reduced image resolution compared to restricted interference MMI [70]. Based on this facts, we chose MMI based on restricted interference mechanism, as image quality is very crucial in our device operation.

$$W_{min}g = 2w + d \tag{3.17}$$

$$W_{min}r = 3(w + d) \tag{3.18}$$

In order to allow for as many modes as possible in the multi-mode guide for increased image resolution, a physical width of 24 μm was chosen. By inserting n_c=1.0, n$_{eff}$=3.25, W_m=24 μm and λ_0=3.5μm into eqn.3.13 and eqn.3.14, W_e is calculated to be approximately 24 μm and L$_m$ equal to 704 μm; with these values, the MMI length that yields 2-self images at the coupler output was calculated to be 352 μm, using equation 3.16.

To verify these results, a 3-D BPM simulation was carried out using a circuit layout, schematically shown in Fig.3.16.

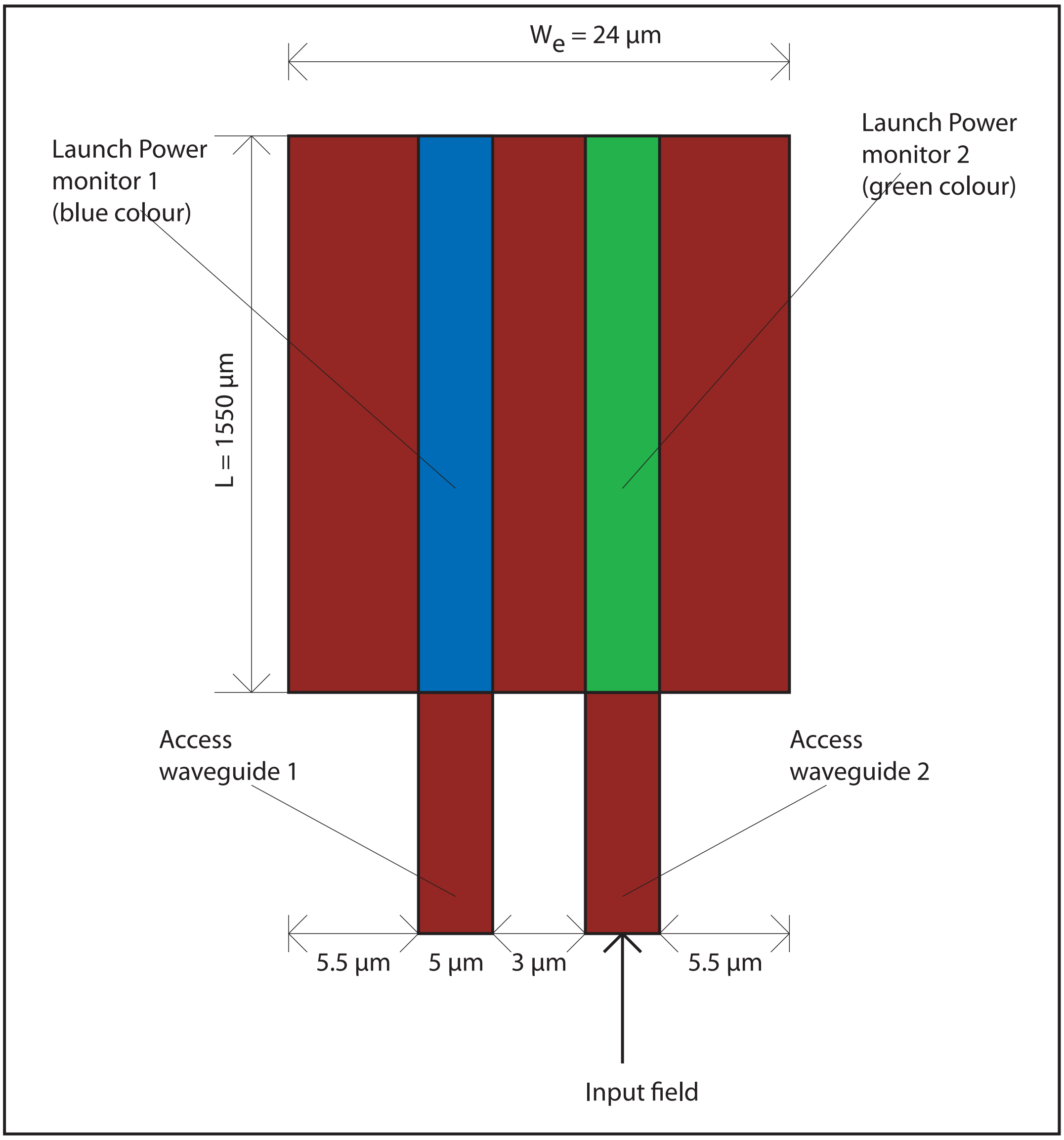

FIGURE 3.16: Schematic of the circuit layout used for the BPM simulation

Shown in Fig.3.17 is the simulation result i.e the simulated power monitor values of the output waveguides, that were placed at x=$\pm\left(\frac{W_e}{6}\right)$=4 μm, as a function of coupler length.

From this figure the 3 dB (50:50) coupling length appears at 374 μm, thus making the simulated coupler length 22 μm more than the calculated value.
The simulated coupler length was chosen for the final design. To investigate the

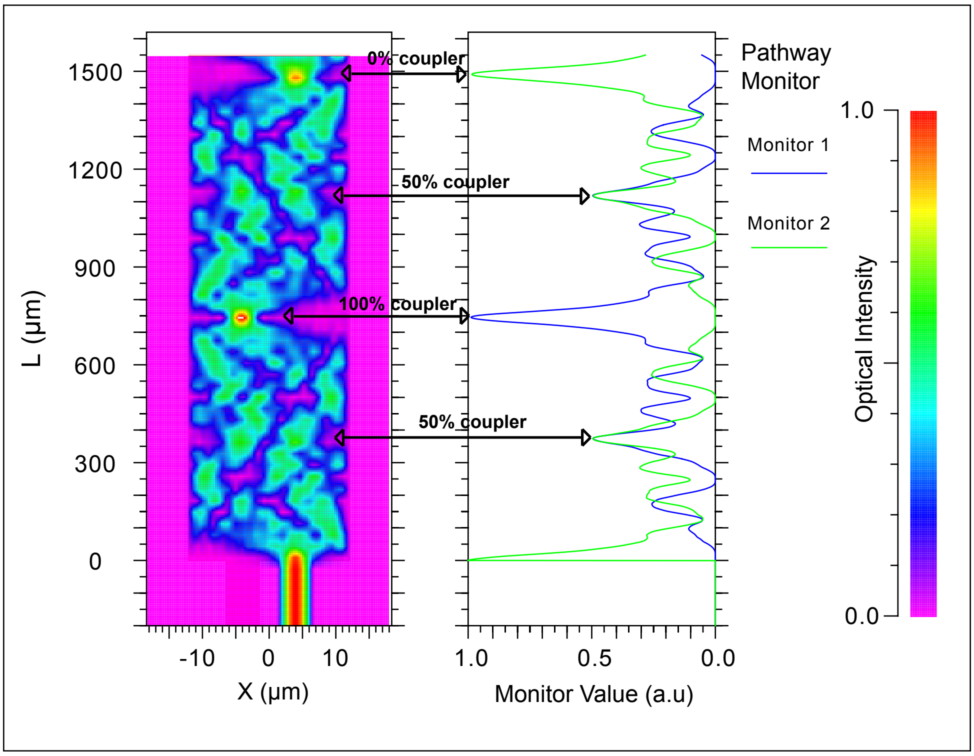

Figure 3.17: 3-D BPM simulation of the restricted paired coupler with a physical width of 24 μm. The 3 dB coupling length appears at 374 μm

positioning of the beams at the coupler output (i.e at L=374 μm), a cross-sectional view of the transverse field profile (see Fig.3.18) was acquired during the simulation process and it shows good power splitting (49.5 % : 49.5 %) with less than 1 % loss.

Another critical factor that must be considered in MMI couplers design is *back reflections* arising from the coupler itself [72]. Hanfoug *et al* [73]have shown that by chamfering out (or tapering) any of the right angled edges of the coupler corners, suppression of the back refections by more than 10 dB is achievable.

This approach has also been taken into the design of the MMI couplers here. To ascertain the effect of the tapering angle on the MMI performance, a BPM simulation was carried out for tapering angles ranging from 0-90 degrees. The result is shown in Fig.3.19; it shows that the divergence angle of the beam is about 20 degrees. To ensure no power loss in the MMI due to tapering, We chose tapering angle (30 degree) greater than the beam divergence angle (20 degree).

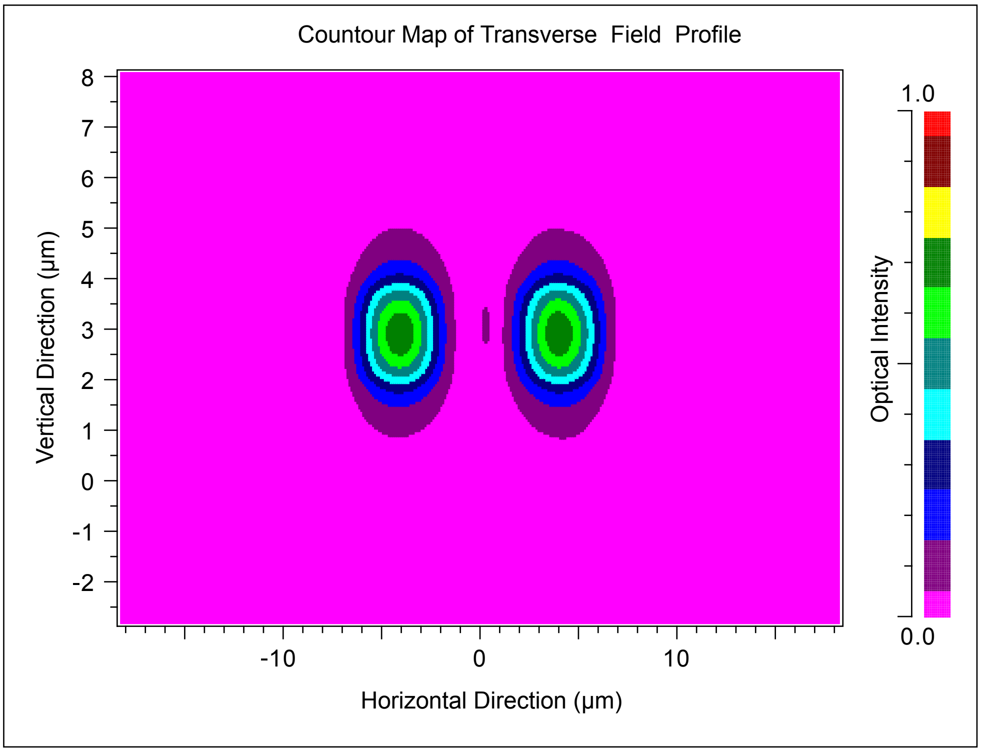

FIGURE 3.18: The cross-sectional view of the transverse field profile acquired during the MMI simulation at L = 374 μm

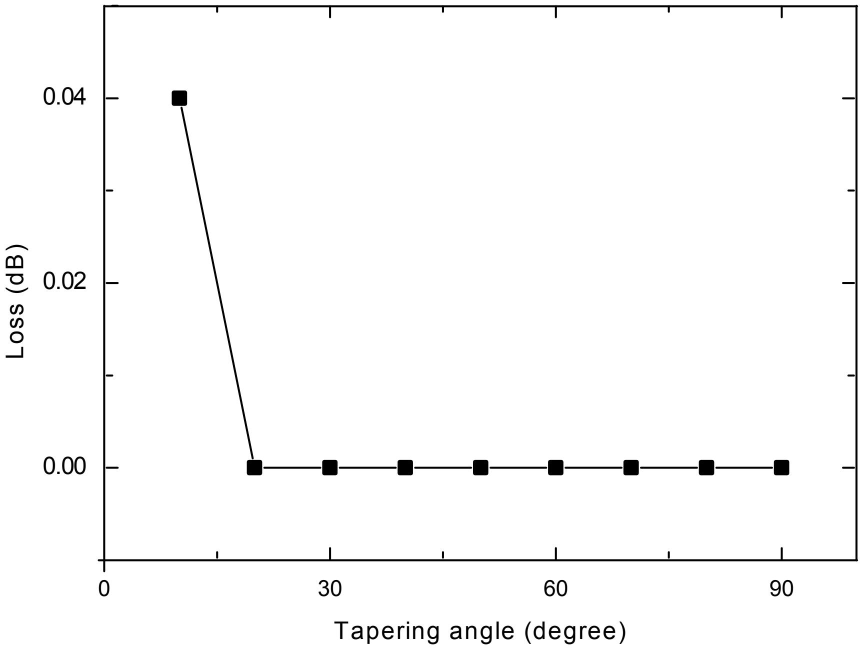

FIGURE 3.19: Plot of tapering angle vs power loss in the MMI

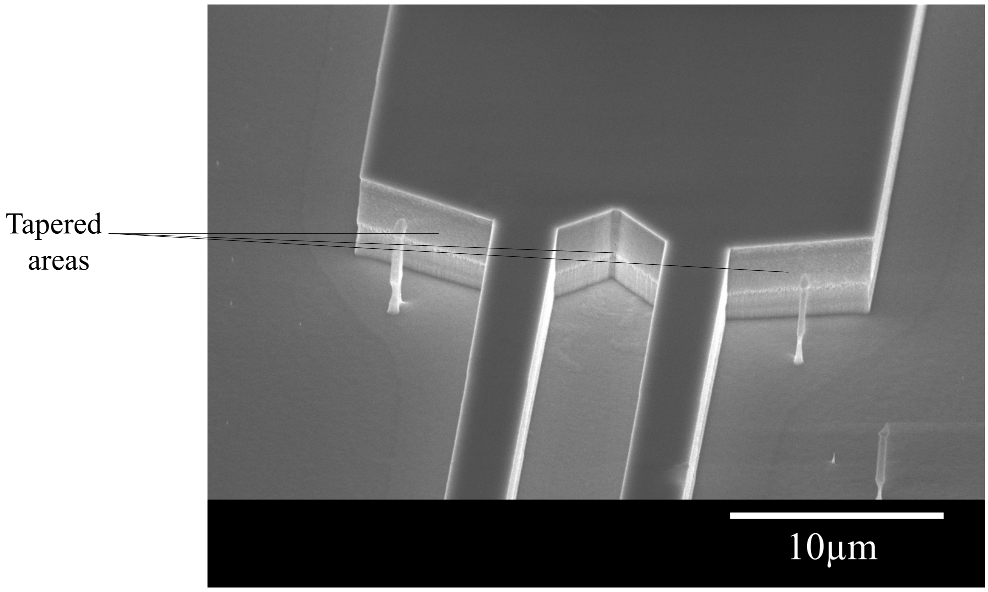

FIGURE 3.20: An SEM of a restricted pair interference MMI tapered to suppress backreflections from the MMI

An SEM of one of the restricted pair interference MMI fabricated using this tapering technique is shown in Fig.3.20.

3.5.1.3 Y-Junction Couplers

Just as the name implies, Y-junction couplers have the structure of a letter Y. It consists of one input waveguide and two output guides (as in the case of a splitter) or two input guides and one output guide (as in the case of a combiner). This coupler was among the first ring laser couplers used owing to its design simplicity. In ring lasers, Y-couplers are formed by joining a tangential waveguide to a circular resonator, as schematically shown in Fig.3.21. Theoretically, Y-couplers split incoming beam into two output beams but practically, the input beam is split into three components; feedback (i.e fraction coupled back into the ring), output (i.e fraction outputted) and radiation (i.e fraction lost at the junction due to modal mismatch)[68]. The last component present the greatest burden with Y-couplers. Radiation loss up to 3 dB has been reported in Ref.[74].

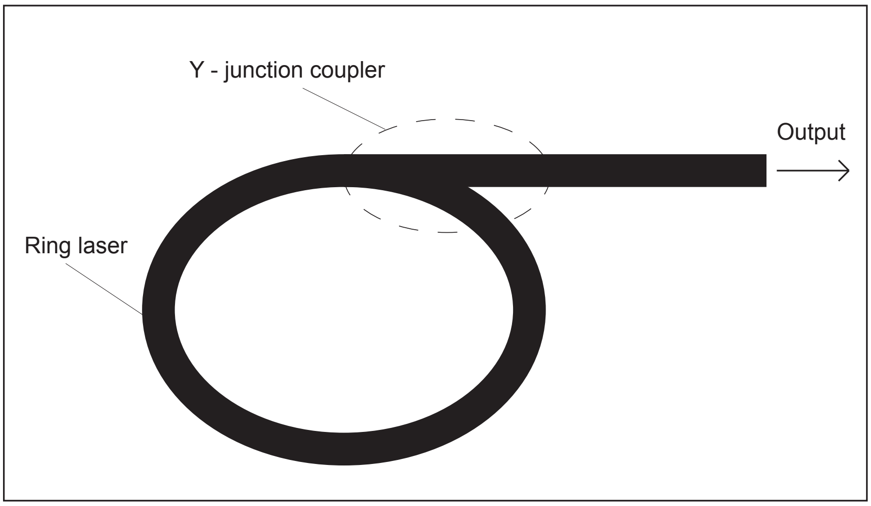

FIGURE 3.21: Schematic of a ringlaser utilising Y-coupler

TABLE 3.3: Comparison of the three available coupling techniques used in this work

Coupling type	Y-junction	MMI	Evanescent field
Intracavity backrecflection	strong	weak	negligible
Coupling ratio	weak	strong	variable
Fabrication tolerance error	insensitive	less sensitive	very sensitive
Size	very short	long	coupling dependent
Tunability	not available	not available	available

In order to calculate the splitting ratio for the coupler used in this work, the Y-junction was modeled using BPM method. The result of this simulation is shown in Fig.3.22. The splitting power between output, feedback and radiation loss appear to be 1:1:0 respectively. To investigate modal position in the structure, we acquired the sectional view of the transverse mode profile at (a) a point before the junction [see Fig.3.23(a)], (b) right in the junction [see Fig.3.23(b)] and (c) after the junction [see Fig.3.23(c)]. The expected modal mismatches can be seen in this figures.

Table 3.3 [68] compares the merits and demerits of the three couplers described in this work.

Based on information given in table 3.3, evanescent field couplers where specifically used in this project for interring coupling in coupled ring quantum cascade lasers (CRQCLs) because the coupling ratio can be tuned (e.g. by altering the coupler

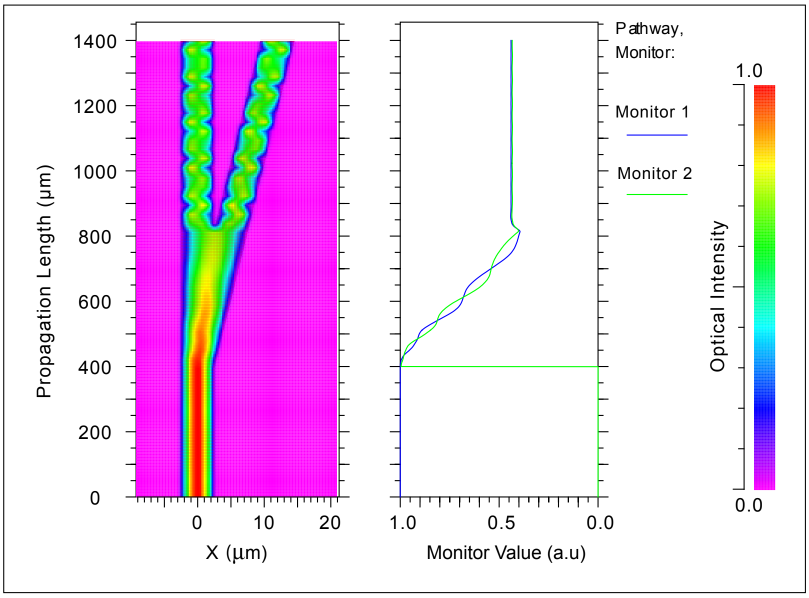

Figure 3.22: 3-D BPM simulation carried out on a Y-junction coupler to calculate the fraction of the beam, outputted, feedback and lost to radiation

gap), unlike in MMI and Y-couplers. In some devices, evanescent couplers were used as output power couplers out of curiosity. MMI were only used as output power couplers because according to table 3.3, they are more robust in deeply etched devices and are less sensitive to fabrication errors than evanescent field couplers. Y-couplers, on the other hand, were only used in the unidirectional laser design because neither MMI nor evanescent field coupler could fit into the design.

3.6 Semiconductor Ring Lasers

These type of lasers utilise a closed path waveguide (e.g. racetrack structure, shown in figure 3.25) as a lasing cavity. First demonstrated in 1980 by Liao *et al* [66], SRLs exhibit several advantages over their Fabry-Perot (FP) counterpart, for example, they do not require cleaved mirror facets or gratings for optical feedback, thus are less complex to fabricate. Secondly, they can operate in bi- or uni-directional regime due to mode competition between the two counter propagating modes [75].

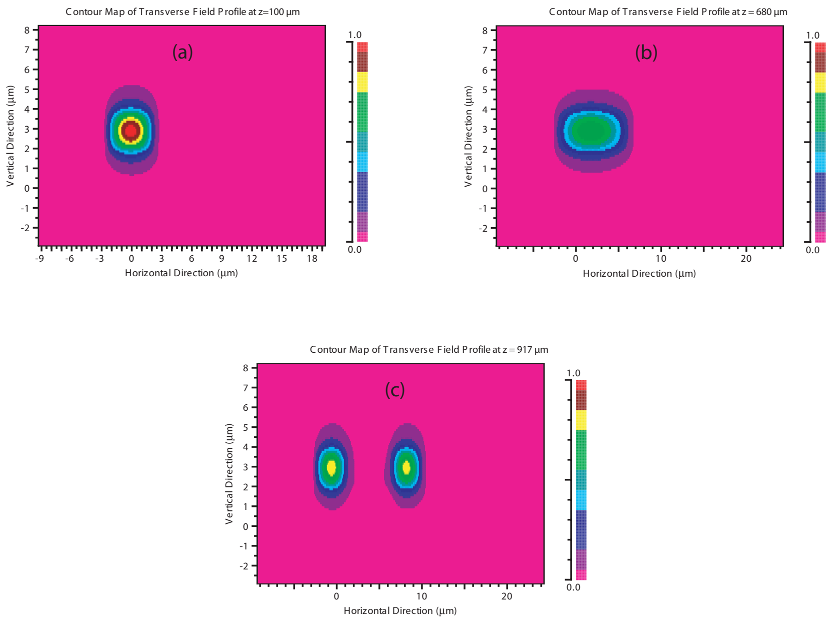

FIGURE 3.23: Sectional view of the transverse field profile in the coupler at (a) z = 100 μm i.e before the Y-junction, (b) z = 680 μm, i.e right in the junction and (c) z = 917 μm, i.e after the junction

3.6.1 Mode Competition

An elementary example of mode competition is observed in ring lasers, where there are two potential modes having the same resonance frequency but travelling in opposite directions around the ring. The mode traveling in the clockwise direction is *the clockwise propagating mode (CW)* and the one traveling in the opposite direction is *counter-clockwise propagating wave (CCW).* The two modes will compete for available population inversion (gain) in the laser. Oscillation in one mode will generally reduce the gain available for another mode, and in some situations may suppress the other mode entirely.

3.6.1.1 Two-Mode Competition Analysis

To describe the competition between two potentially oscillating modes in a gain medium, we begin by writing the rate equations, or intensity growth equations, for the two assumed modes as,[75]

$$\frac{dI_1}{dt} = [g_1 - \beta_1 I_1 - k_{12} I_2] I_1 \tag{3.19}$$

$$\frac{dI_1}{dt} = [g_2 - \beta_2 I_2 - k_{21} I_1] I_2 \tag{3.20}$$

where g_i is the unsaturated gains minus losses in the i^{th} mode, β_i and k_{ij} the self- and cross-saturation coefficients. $i = j = 1, 2$.

Steady state solutions to eqn.(3.19-3.20) require either that the saturated gain factor, $g_i - \beta_i I_i - k_{ij} I_j = 0$ or that the corresponding intensity $I_i = 0$. Then the condition for zero saturated gain for each mode is given by one of the linear relations

$$I_1 = \left(\frac{g_1}{\beta_1}\right) - \left(\frac{k_{12}}{\beta_1}\right) I_2 \tag{3.21}$$

and

$$I_2 = \left(\frac{g_2}{\beta_2}\right) - \left(\frac{k_{21}}{\beta_2}\right) I_1 \tag{3.22}$$

and each of these relations can in turn be represented by a straight line in the I_1, I_2 plane, as illustrated in Fig.3.24(a) These two lines may or may not intersect in the first quadrant of the I_1, I_2 plane, as shown in Fig.3.24(b) and Fig.3.24(c) where points $O_1 \equiv g_1/\beta_1$ and $O_2 \equiv g_2/\beta_2$ are the origin of these lines; $T_1 \equiv g_1/k_{12}$ and $T_2 \equiv g_2/k_{21}$ are the points where the two lines intercept the opposite axis.

Understanding the conditions required for stable operation of the modes under steady-state condition calls for enhanced perturbation stability analysis; to evaluate this we expanded the intensities $I_1(t)$ and $I_2(t)$ about the steady-state intensities in the form

$$I_1(t) = g_1/\beta_1 + \epsilon_1(t) \tag{3.23}$$

$$I_2(t) = g_2/\beta_2 + \epsilon_2(t) \tag{3.24}$$

and looking for the linearised growth or decay rates of the the small perturbations $\epsilon_1(t)$ and $\epsilon_2(t)$ about each potential steady-state operating point.

Starting with single-mode operating point at O_1, where mode-1 is oscillating alone

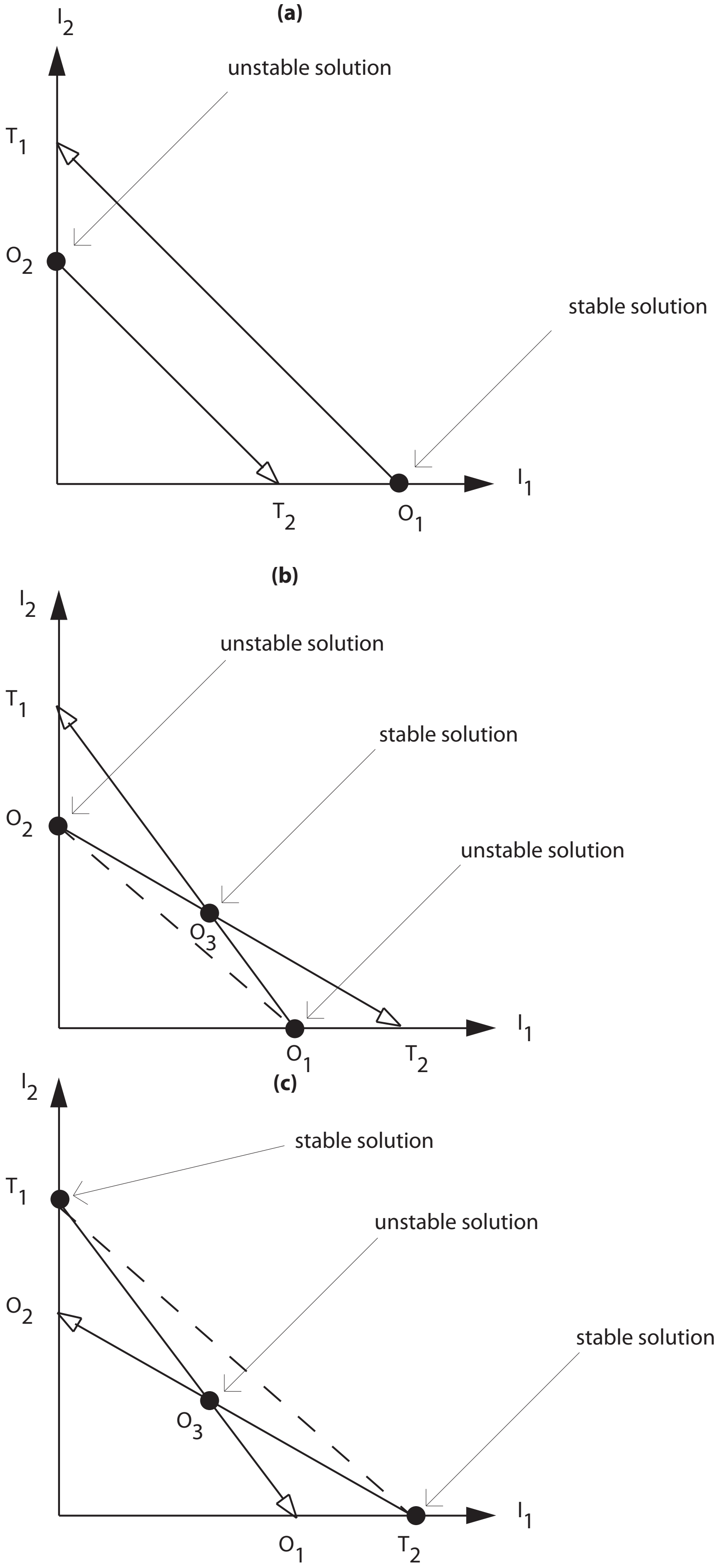

FIGURE 3.24: (a) single-mode coupled-oscillator conditions (b) weakly coupled oscillator modes (C<1) showing simultaneous oscillation (c)Strongly coupled oscillator modes (C>1) indicating bistable oscillation [75]

with intensity $I_1 = g_1/\beta_1$, the linearised differential equations for the signal perturbations about this point then become

$$\frac{d\epsilon_1(t)}{dt} \approx -g_1\epsilon_1(t) - \frac{k_{12}g_1}{\beta_2}\epsilon_2(t) \tag{3.25}$$

and

$$\frac{d\epsilon_1(t)}{dt} \approx \left[g_2 - \frac{k_{21}g_1}{\beta_1}\right]\epsilon_2(t) \tag{3.26}$$

The requirement that mode-2 remains stable at zero amplitude at this operating point is clearly determined by the stability criterion that

$$\frac{k_{21}g_1}{\beta_1 g_2} > 1 \tag{3.27}$$

In geometric terms, this condition says that

$$\frac{O_1}{T_2} = \frac{g_1\beta_1}{g_2/k_{21}} > 1 \tag{3.28}$$

That is, for single-mode stability the origin O_1 of the zero-gain line for mode-1 must be farther out on the I_1 intensity axis than the tip T_2 of the zero-gain line for mode-2.

Geometrically, it is clear that if the two zero-gain lines do not intercept, as in Fig.3.24(a), the origin of the outermost of the two vectors (vector I_1 to T_1 in this illustration) is the stable solution. The laser oscillates only in mode-1 and this mode completely suppresses the less favoured mode-2.

But when the two zero-gain vectors overlap (intersect), as in Fig.3.24(b) and (c), two quite different situations can occur. Firstly, if the origins O_i of both vectors lie inside the tips T_j of the opposite vectors on the I_i axes, as shown in Fig.3.24(b), then by the criteria, (see equation 3.27) neither of the single-mode solutions O_1 or O_2 can be stable. Hence, the dual-mode solution O_3 must be the only stable solution. The mathematical criterion for this is that

$$\frac{O_1}{T_2}\frac{O_2}{T_1} = \frac{k_{12}k_{21}}{\beta_1\beta_2} \equiv C < 1 \tag{3.29}$$

This is generally referred to as *weak coupling* between the two oscillating modes.

According to equation 3.29, the product of the cross saturation coefficients ($k_{12}k_{21}$) between the two modes is less than the product of their self saturation coefficients ($\beta_1\beta_2$). Physically, this means that gain competition between the modes is very weak because of the weak coupling between the modes. In other words, the gain medium is inhomogeneously broadened. To attain single mode behaviour, the coupling between the modes must be improved and one of the ways to do that in semiconductor ring lasers is to incorporate an "S"-crossover waveguide into the ring [76]. This introduces non reciprocal gain and loss respectively to the favoured and unfavoured modes respectively, thereby introducing gain competition needed to attain single mode operation.

For *strong coupling* (Figs.3.24(a) and 3.24(c)), shown in equation 3.30 both of the single-mode solutions O_1 or O_2 are stable.

$$C \equiv \frac{k_{12}k_{21}}{\beta_1\beta_2} = \frac{O_1}{T_2}\frac{O_2}{T_1} > 1 \tag{3.30}$$

From equation 3.30, the product of the cross saturation coefficients ($k_{12}k_{21}$) between the two modes is greater than the product of their self saturation coefficients ($\beta_1\beta_2$). This means that mode #1 cross-saturates mode #2 more than it self-saturates and vice versa. In order words, the coupling between the two modes is very high, leading to strong gain competition between the two modes.

In conclusion, competition between two modes as observed in ring lasers may lead to stable single-mode operation (strongly coupled modes) or dual-mode operation (as in weakly coupled modes).

3.6.2 Regimes of operation

Three operational regimes have been reported for semiconductor ring lasers (SRLs) [77, 78]. They include: (1) bidirectional continuous wave regime; this is the first regime and occurs immediately after threshold. In this regime the two counter-propagating modes are active and operate in continuous wave. The two modes were also reported to be phase-locked [78], (2) bidirectional with alternate oscillations regime; This regime precedes the bidirectional continuous wave regime. Here the intensities of the two counter-propagating modes are modulated by harmonic sinusoidal oscillations, the modulation is out-of-phase, for the two modes. (3) unidirectional regime; this is the last of the three regimes and occurs immediately after bidirectional-with- alternate-oscillations regime. In this regime, only one of the two modes is active as the second mode is completely suppressed, leading to higher output (2x) power from the preferred direction. This kind of behaviour can also be forced on the ring, at all injection current by introducing a non-reciprocal loss in one of the propagating modes [76].

For more theories on the operating regimes and the dynamics of the two counter-propagating modes in these regimes, the reader is referred to Ref. [77, 78].

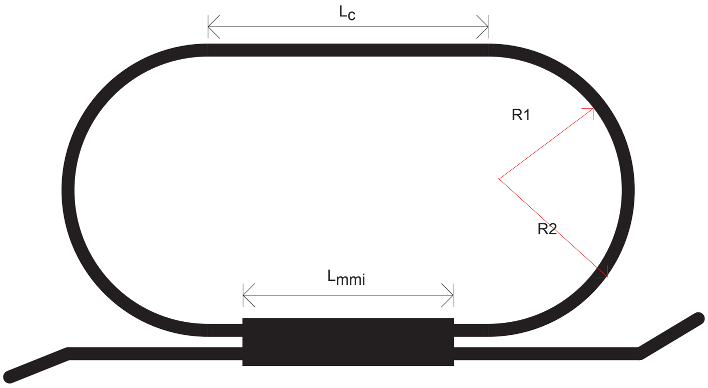

FIGURE 3.25: Schematic diagram of a racetrack laser coupled to an MMI coupler

3.6.3 Free Spectral Range

Free spectral range (FSR) is one of the main performance characteristics of ring lasers and is defined as the frequency spacing between the longitudinal modes supported by the ring resonator. Mathematically, it is expressed as:

$$FSR = \frac{\lambda^2}{n_g L} \tag{3.31}$$

In a racetrack ring lasers (see figure 3.25),

$$FSR = \frac{\lambda^2}{n_g(2\pi R_{eff} + 2L_c)} \tag{3.32}$$

where $R_{eff} = R1 + R2/2$, n_g is the group index of the semiconductor material, L_c is the length of the coupler and λ is the free space wavelength.

3.6.4 Bending Losses in Ring Waveguides

Bending loss, just as the name implies, is the loss in the propagating optical power associated with a bend in the waveguide. In this structures, the propagating mode looses symmetry and is pushed towards the outer radii. The magnitude of the loss varies inversely with the bending radius and index difference between the core and the cladding [79]. In waveguide with little index difference (i.e. shallow etched waveguides), bending losses are higher. On the contrary, deeply etched waveguides (e.g QCLs) possess stronger optical confinement due to the large index contrast at the semiconductor/air interface, thus lower bending loss.

Bending losses calculation in curved optical waveguides have been accomplished using analytical method [80], computational intensive methods such as effective index, and conformal based methods [81], and numerical simulation using a three dimensional (3D) beam propagation method (BPM) [82] feature in BeamPROP simulation software [64].

3.6.4.1 Numerical Computation of Bend Loss

To ascertain the minimal bending radius (critical radius) beyond which optical power losses due to bend in the waveguide become negligible, a commercially available design tool, BeamPROP [64], based on Beam Propagation Method (BPM) was used to model the bend losses at bend radii ranging from 0-320 μm at emission wavelength of 3.4 μm. Waveguide (5 μm wide and 6 μm deep) was used for the modeling. Figure 3.26 shows the bending loss as a function of the bend radius for the fundamental transverse magnetic (TM) mode. From Fig. 3.26, it is evident that as the bend radius increases, the bending loss decreases exponentially until it gets to the point (critical radius =180 micron) where it flattens. Beyond this point the bending loss becomes negligible (~0 dB/m).

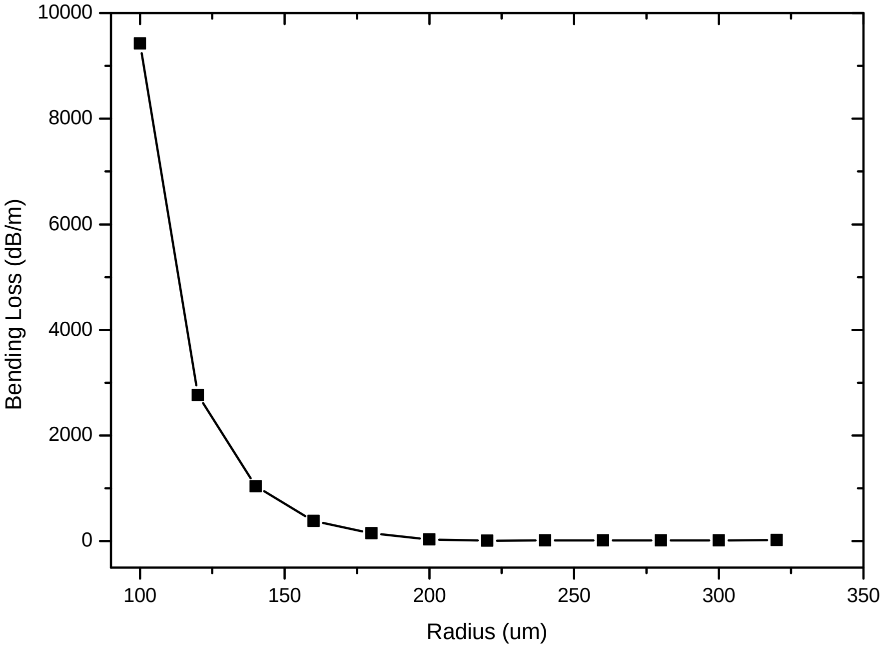

FIGURE 3.26: Computed BPM bending loss as a function of bend radius for a 5 μm wide waveguide with 4.1 μm etch depth.

To demonstrate the validity of the numerically modelled solutions, the bend loss was analytically calculated as described in section 3.6.4.2.

3.6.4.2 Analytical Calculation of Bend Loss

The attenuation of optical guided waves propagating along a section of curved waveguide depends exponentially on the bending radius R and index contrast between the core and the cover material (in this case PECVD SiO_2). The attenuation coefficient for the fundamental TM mode of the curved waveguide is given to a good approximation by, [80]

$$\alpha(m^{-1}) = \frac{u^2}{av^2(\sqrt{\pi wR/a})} exp\left[\frac{-4w^3R}{3v^2a}\frac{\Delta n}{n}\right] \tag{3.33}$$

where $a = 2.5$ μm is half the waveguide width, R is the bend radius. The index contrast is given by the expression,

$$\frac{\Delta n}{n} \equiv \frac{n_2 - n_1}{n_2} \tag{3.34}$$

where $n_1 = 1.46$ is the cover index and $n_2 = 3.34$ is the core index.

The quantity v can be computed from the waveguide parameters as

$$v = \frac{2\pi}{\lambda_0} n_2 a \sqrt{2\frac{\Delta n}{n}} \tag{3.35}$$

where $\lambda_0 = 3.46$ μm is the free space wavelength.
The parameters

$$u = \sqrt{1 + 2ln(v)} \tag{3.36}$$

and

$$w = \sqrt{v^2 - u^2} \tag{3.37}$$

The bending loss in dB/m is therefore,

$$Loss_{bend} = -10log(e^{-\alpha L}) \tag{3.38}$$

where L = 1 m is the propagation length.

Solving equations 3.33 - 3.38 in Matlab we obtained the bend loss as a function of bend radius for index contrast $\Delta n/n \sim 0.57$ (i.e. the index contrast of the QC material reported in this work) shown in figure 3.27.

The analytical result shown in figure 3.27, equally exhibit exponential decrease in bend loss with increasing radius like the numerical result shown in figure 3.26. However while the numerical result flattens at $\sim$ 180 μm, the analytical result flattens $\sim$ 2 μm.

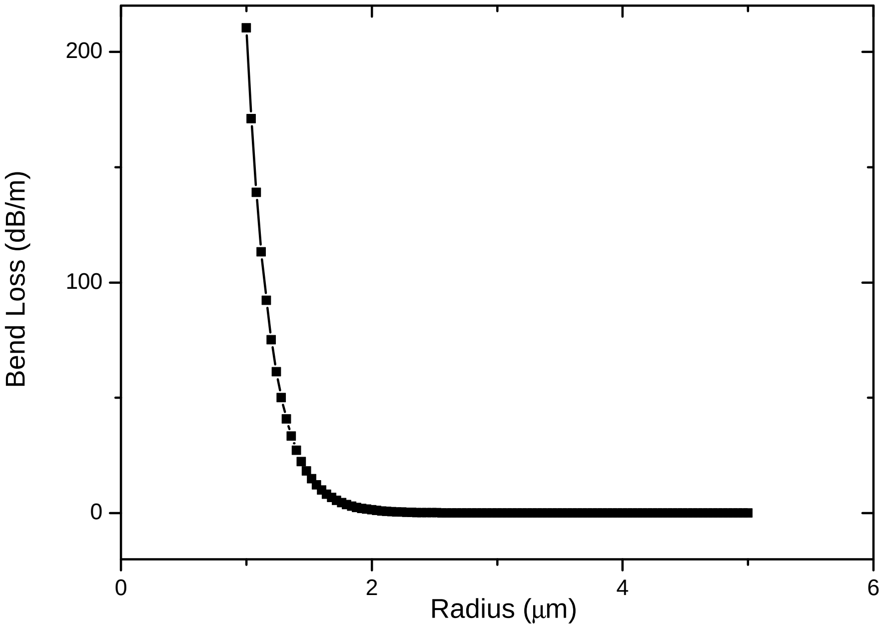

FIGURE 3.27: Bending loss (dB/m) as a function of bend radius at $\Delta n/n \sim 0.57$ for bend radii 1-5 μm, calculated analytically by solving equations 3.33 - 3.38 in Matlab

To understand the great difference between the critical radii, we tried to match the numerical result to the closest analytical results. A comparison plot between the numerical result and the closest analytical results are shown in figure 3.28.

From figure 3.28, we could observe that the critical radius of the numerical result matched with that from the analytical result at $\Delta n/n \sim 0.028$. However the numerical bend loss appears steeper than the analytical results.

The validity of the bending loss computed numerically using BeamProp could not be proven by the analytical calculation. In fact, the analytical calculation seems to give a more accurate result than the numerical result.

The best option would have been to measure the bend losses, experimentally but this could not be done as there was not enough material for the research.

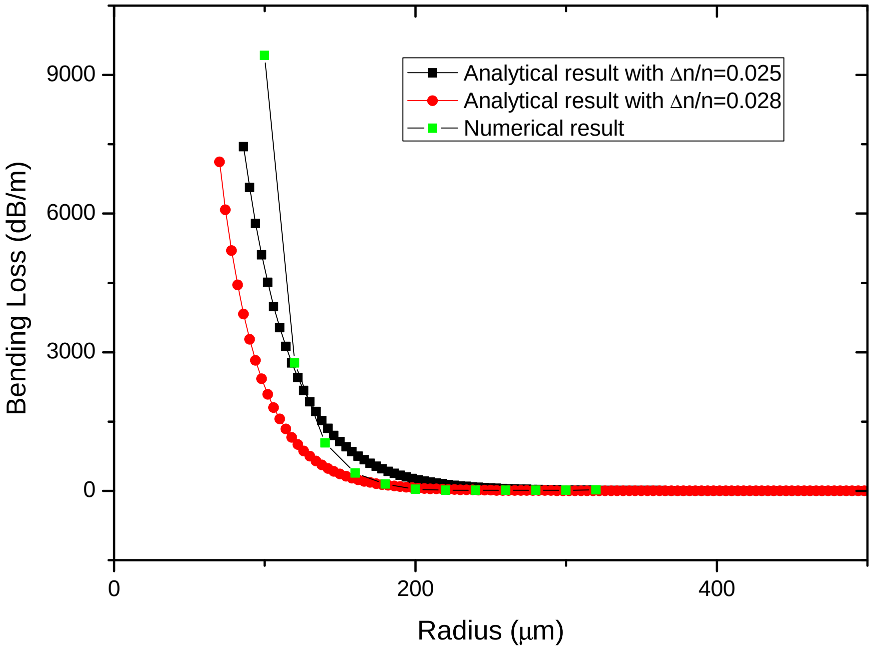

FIGURE 3.28: Comparison between numerically computed bend loss (dB/m) and analytically calculated bend loss at $\Delta n/n \sim 0.025$ and 0.028, as a function of bend radius

3.6.5 Instability of Laser Operation Caused by Facet Reflections

The facet reflectivity of laser diodes, which is determined by the value of the refractive index of the semiconductor material, is approximately 30 %. The performance of the ring laser deteriorates as a result of instability of the laser operation (feedback noise) which is induced by light reflected back into the cavity. Since this instability occurs even when the level of feedback light is less than 0.01 %, facet reflection must be strongly suppressed.

In all the devices described in this work, the facets of the output couplers were tilted at an angle of 7 degrees to the waveguide normal, to minimize back-reflections [83].

3.6.6 Ring Laser Design

The ring lasers described in this thesis were designed with the parameters shown in table 3.4

Table 3.4: Parameters used to design the ring laser

Parameter	Dimension
Waveguide width (μm)	5
Inner ring radius (μm)	249
Outer ring radius (μm)	254
Effective ring radius (μm)	252
MMI length (μm)	374
MMI width (μm)	24
Length of the straight waveguide (μm)	528
Etch-depth (μm)	6.5
Effective length of waveguide (μm)	2640
FSR (nm)	1.4
Output power coupling (%)	50

An SEM of the fabricated single racetrack waveguide and its corresponding MMI coupler is shown in Fig.3.29 below.

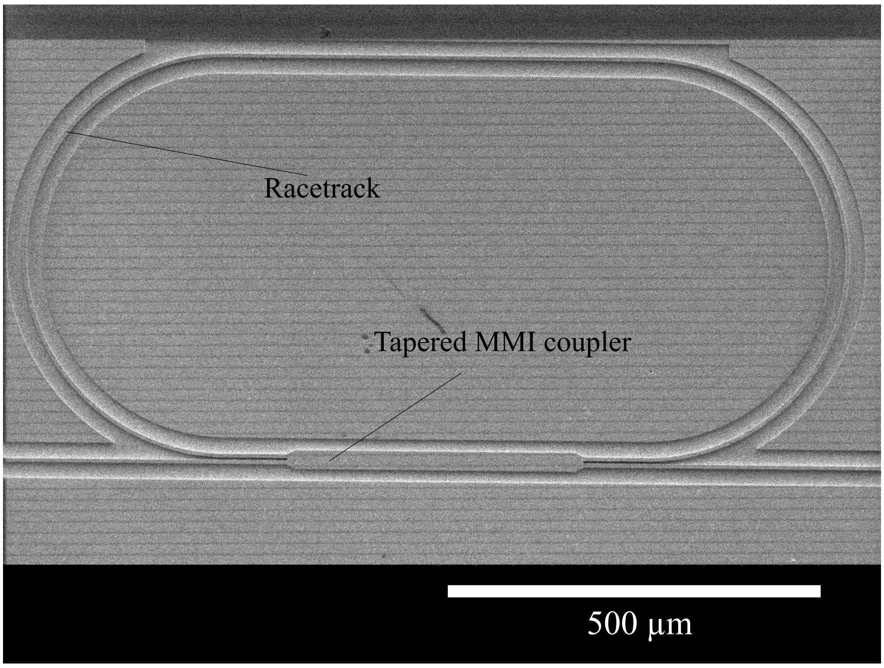

Figure 3.29: SEM image of the fabricated racetrack waveguide and its corresponding tapered MMI coupler

3.6.7 Ring Laser Result

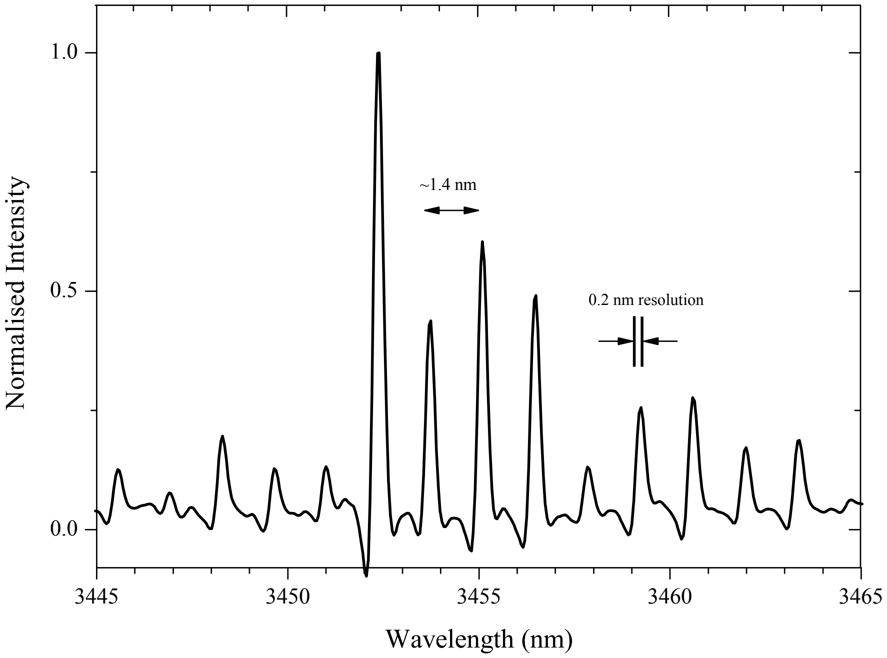

FIGURE 3.30: Acquired emission spectrum of the quantum cascade ring at 1.3 x I$_{th}$, measured at 200 K with FTIR resolution of 0.2 nm

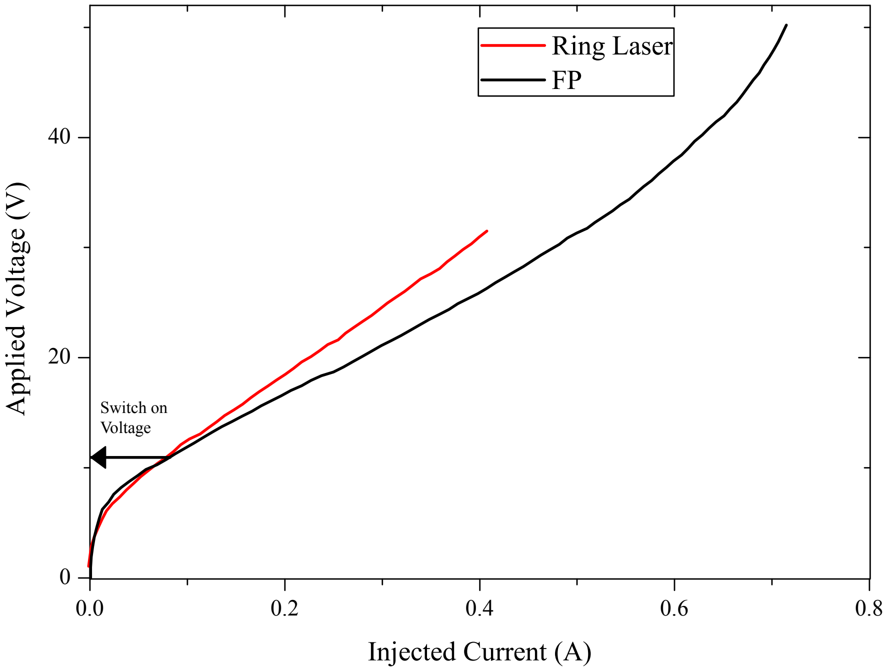

FIGURE 3.31: Current- Voltage curves of the ring laser and a FP of the same dimension measured at 200 K

Shown in figure 3.30 is the spectra acquired from the ring laser at 1.3 x I$_{th}$. In figure 3.32 the normalised optical power versus current curve of the ring laser

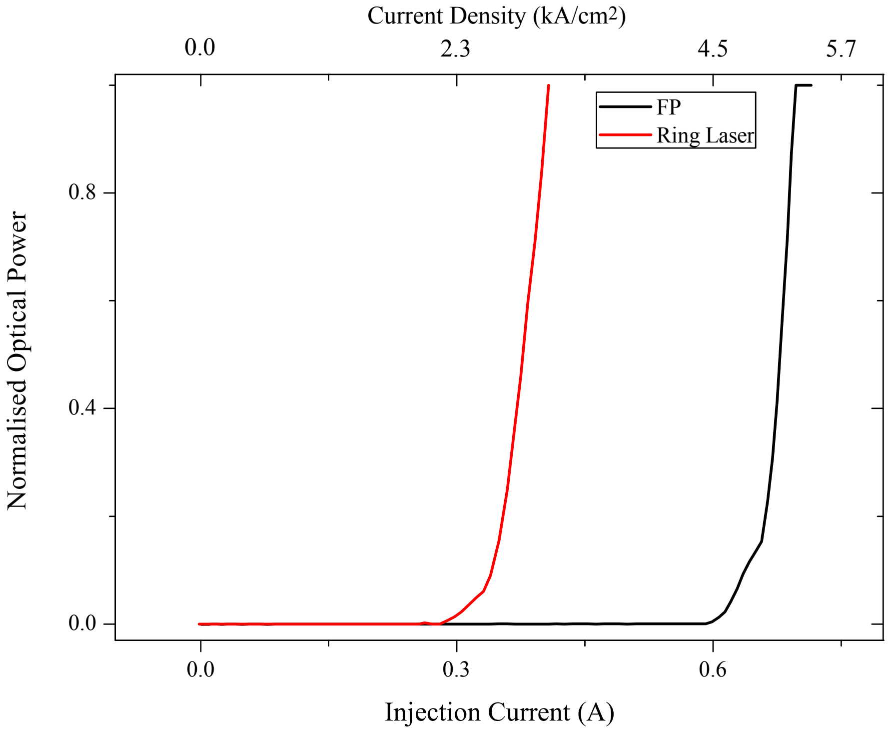

FIGURE 3.32: Normalised Optical power - Current curves of the ring laser and a FP of the same dimension measured at 200 K

and a FP quantum cascade laser from the same wafer and comparable dimensions are shown. In figure 3.31, the current-voltage curve of the ring laser and a FP are shown. The turn on voltage for the two devices occurs at $\sim$ 11 V, which corresponds to the design voltage (i.e $\sim$ 350 meV times the number of cascades, 30). The ring laser has a threshold current density of approximately 2 times less than that of the FP laser (2.6 kA/cm^2 compared to 5.3 kA/^{2}) because the ring laser has less transmission loss. Threshold current density of about 2.5 kA/^{2} have been in this material system at 300 K by Commin *et al* using FP with high reflection coatings [61].

3.7 Conclusion

This chapter has described in details the material system, device design considerations and compositional components employed to realise the coupled quantum cascade ring lasers and unidirectional quantum cascade lasers discussed in chapters 6 and 7 respectively.

Chapter 4

Quantum Cascade Ring Laser Fabrication

4.1 Fabrication Process Overview

An overview of the basic fabrication steps employed to produce the quantum cascade ring lasers reported in this thesis is shown in figure 4.1.

4.1.1 Introduction/ Key fabrication challenges

Here we describe how for the first time ring lasers (conventional rings, unidirectional rings and coupled rings) were fabricated in the short wavelength $\sim$ 3-4 um, antimony (Sb) containing quantum cascade laser material $\mathrm{In_{0.7}Ga_{0.3}As/AlAs_{0.6}Sb_{0.4}}$ designed and grown at Sheffield University.

The Sb-based QC material was very hard to get hold of. Infact I only had 2x2 cm piece of material for this research work. This was clearly not enough supply to do sufficient number of processing test.

The major key challenges in this fabrication were;

- developing dry etch recipe for this material system.

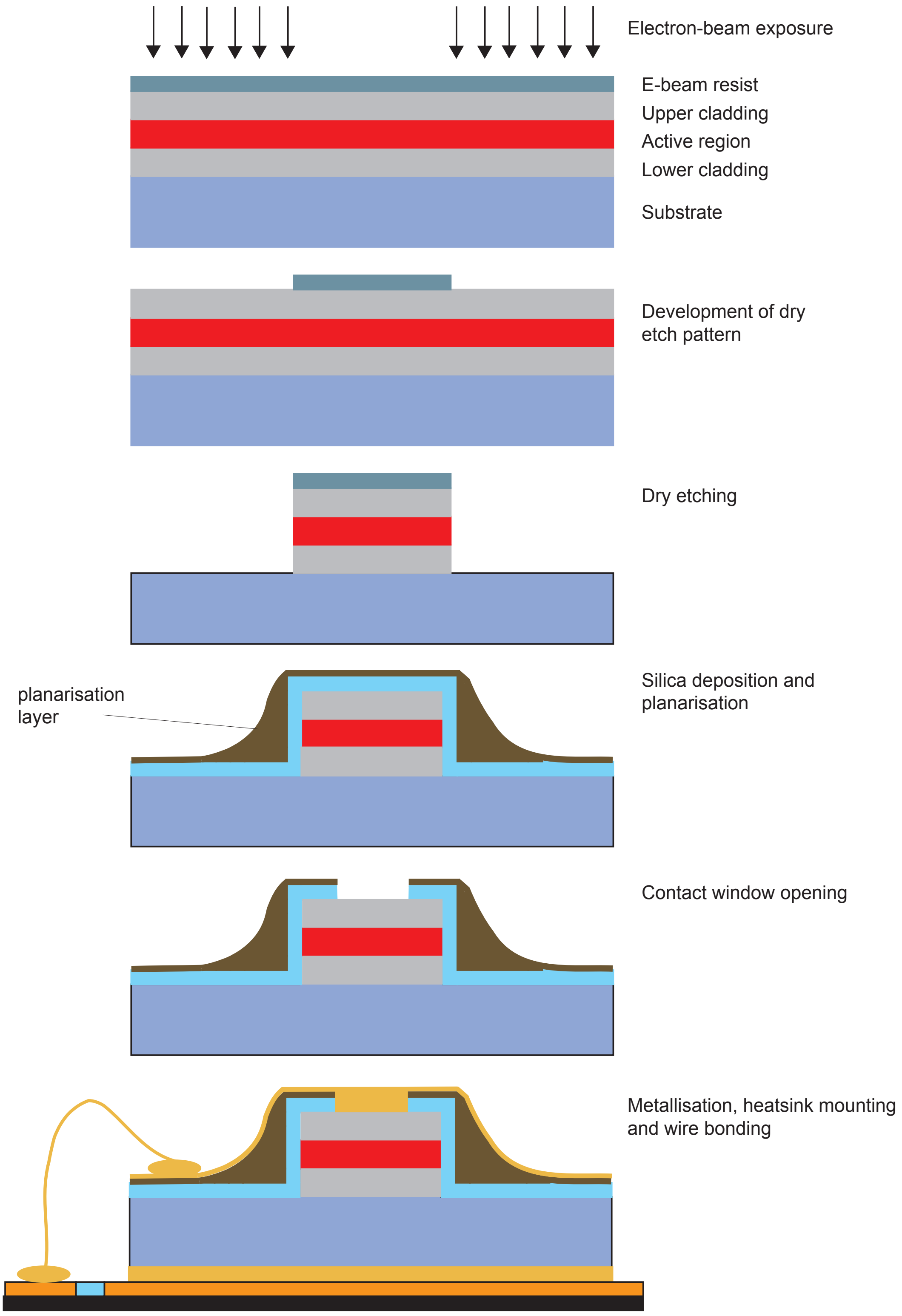

FIGURE 4.1: The basic fabrication steps taken to fabricate the quantum cascade ring lasers reported in this thesis

- achieving separate control of waveguide etch depth and directional coupler etch depth using one etch step.
- how to electrically isolate the two rings (in the case of coupled rings) or the ring cavity and "S"-crossover waveguide (in the case of unidirectional rings) using metal-liftoff technique.
- developing dielectric layer composition to hold off high voltages expected from this short wavelength devices.

How these problems were solved are described in this section. Also described, are other standard fabrication processes, that were relevant in the processing.

All the fabrication work was done in the James Watt Nanofabrication Centre (JWNC) situated in the electrical department of Glasgow university, with exceptions of waveguide etching. Waveguide etching was done in CST, a research collaborator, as the inductively coupled reactive ion etching (ICP-RIE) machine in the department was not available for this work.

4.2 Dielectric Deposition

In the life of this research work, dielectrics (SiO_2 and Si_3N_4) were used for three different purposes:

1. As hardmask for waveguide etching. Quantum cascade laser waveguides are defined by deep etching (i.e etched through the active region). The nature of etching requires a highly resistant mask to protect the unexposed area during etching. SiO_2 have been extensively used for this purpose in the micro-fabrication industry. In this processing, a 500 nm SiO_2 was used as the hardmask for dry etching.
2. For electrical isolation. SiO_2 and Si_3N_4 were used as electrical insulator so that injected electrons only pass through the ohmic contact to the active

region. This helps reduce injected current leakage at the side of the waveguide.

3. As optical buffer. Covering the waveguide with dielectric layers reduces overlap between the propagating modes and the metal contact, especially in the space separating the two couplers, thus reducing optical loss in the structure.

SiO_2 and Si_3N_4 were deposited by a plasma enhanced chemical vapour deposition (PECVD) process. This type of dielectric deposition is conformal, i.e dielectric thickness on the vertical side wall and on the horizontal (flat) surface are almost equal. Other desirable properties of PECVD include: good surface adhesion, low pin hole density [84].

4.3 Lithography

Lithography in semiconductor processing is a technique used for transfering patterns to samples. Lithography is accomplished with the aid of an energy sensitive chemical (resist) which decompose (positive resist) or hardens (negative resist) on exposure to energy. The nature of the exposure energy determines the type of lithographic process. For example, when the resist exposure is accomplished by using light, the lithographic process is called *photolithography* and when accomplished with electron beam, it is known as *e-beam lithography*. In this work, electron beam lithography (EBL) was only used to define patterns for waveguide etching while contact window and metal liftoff patterns were defined using photolithography.

ZEP520A [85], a positive e-beam resist with high resolution and great dry etch resistance (1:5 ZEP520a:SiO_2) was used to define the ring-waveguide patterns on the silica (SiO_2) hardmask.

4.4 Dry etch

Dry etching techniques [86] are those that rely on plasma-driven chemical reactions or energetic ion beams to remove semiconductor materials; specifically developed to achieve anisotropic etching (i.e greater etch rate in the vertical direction than in the horizontal direction), critical for high fidelity pattern transfer. In this work, reactive ion etching (RIE) and ICP-RIE were respectively, used for shallow etching (e.g silica hardmask and contact window opening) and deep etching (in this case the ring waveguide structures)

Some of the benefits of ICP over conventional RIE include: higher etch rate (due to higher ion density ($>10^{11}$ cm^3) compared to ($>10^9$ cm^3) for RIE), higher etch selectivity and reduced physical damage (obtained by using low ion energy), high process flexibiliy (due to separate control over Inductively Coupled Plasma and electrode RF) [87].

4.5 Fabrication Process Flow

This section concisely describes step by step processes utilised in the device fabrication.

4.5.1 Sample Preparation

Prior to processing, the grown wafer was scribed and cleaved into 1 cm x 1 cm sizes. The samples were given thorough solvent cleaning in an ultrasonic bath, using the the following steps: 5 minutes in opticlear, 5 minutes in acetone, 5 minutes in methanol and 5 minutes in Isopropyl alcohol (IPA). The samples were thoroughly and properly rinsed with deionised water before being blow-dried with dry nitrogen. After blow-drying, the samples were put in a Plasmafab oxygen asher and ashed for 180 seconds to remove residues that were not completely removed by solvent cleaning.

4.5.2 Silica (hardmask) deposition and etching

500 nm PECVD silica was deposited on the sample as a hard mask material. ZEP520A was spin-coated on the sample at spin speed of 2000 revolution per minute (RPM) for 60 seconds (this gives resist thickness of about 500 nm). Sample was baked in oven at 180 ^{o}C for 40 minutes. Ring waveguide patterns were transferred to the sample using EBL. After patterning, the sample was developed in o-xylene at 23 ^{o}C for 60 seconds and properly rinsed in IPA by dipping for 20 seconds. Developed sample was transferred to plasmalab 80 plus system for reactive ion etching. Firstly, oxygen etching (RF power = 10 W, gas flow = 10sccm and process pressure = 50 mT) was carried out for 30 seconds to descum the sample and further remove any residue or remnants of the resist on the patterned areas. Using a mixture of CHF_3+Ar, the sample was dry-etched (RF power = 200 W, gas flow = 25/18 sccm and process pressure = 30 mT) for 17 minutes (etch rate = 30 nm/min) to completely remove silica on the patterned area. Etch depth before resist stripping and after resist stripping measured with a Dektak profilometer were 0.95 micron and 0.5 micron respectively. This gives etch selectivity of 1:10 between ZEP520A and silica. The scanning electron microscope (SEM) image of part of the etched hardmask is shown in Figure 4.2.

4.5.3 Effect of RIE lag

To fabricate the devices investigated in this research work, with the exception of devices using multimode interference (MMI) as output coupler, two etch depths were needed; evanescent field coupler etch depth ($D_{coupler}$) and waveguide etch depth ($D_{waveguide}$) as shown in figure 4.3. Based on the epi-layer structure of the wafer used in this work and shown in Figure 3.5, the minimum etch depth required to define the waveguide is $\sim$ 6.4 μm (i.e from the upper cladding down to the lower cladding). Quantum cascade lasers are fabricated by etching deep through the active region. Because they are unipolar devices, they do not suffer from the effect of surface recombination and non-radiative recombination sites

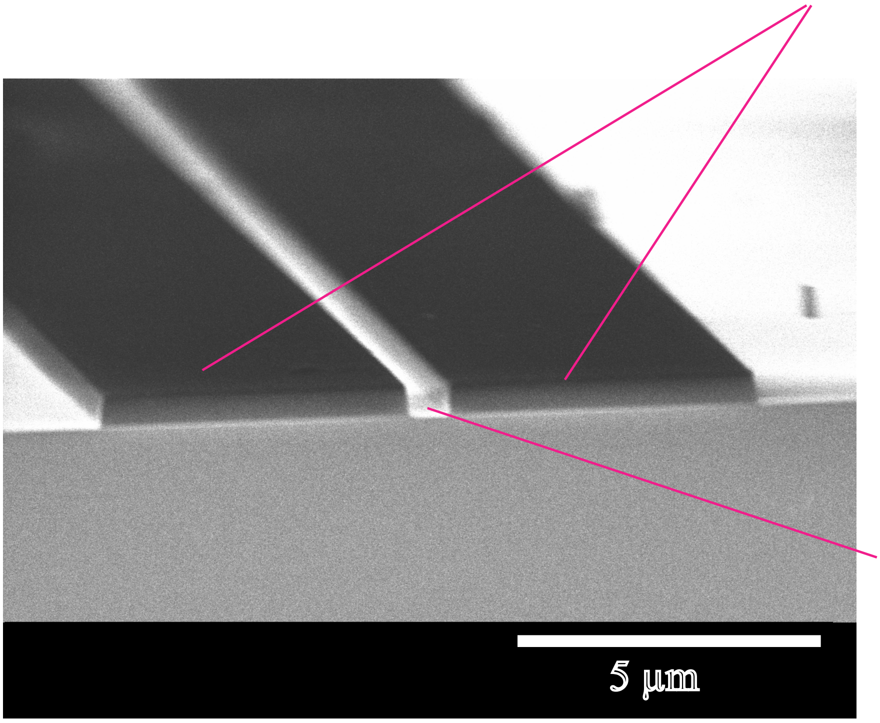

Unetched silica
(used to define couplers in final etching)

Etched area
(to define coupler
spacing in the
final etching)

FIGURE 4.2: SEM image of part of the etched RIE hardmask (showing couplers, i.e area covered by silica, and coupler spacing, i.e etched area)

created by etching through the active region as is observed in bipolar interband lasers. In this work waveguides were defined by etching trenches before and after the waveguide regions (see Fig.4.5)

Furthermore, the etch depth of the coupler together with the coupler gap determine the length of the coupler needed (see Fig.3.10); deeper etch depth means lower coupling between the waveguides, thus longer coupler length. On the contrary, shallower etch depth, for the same coupler spacing, means higher coupling coefficient, thus shorter coupler length. For a robust coupler operation, the two waveguides that make up the coupler must be optically isolated. To ensure this, at the same time keeping optimum coupler length, the coupler has to be etched down to a maximum etch-depth of about 4.2 μm and minimum of about half the waveguide height. Below this region, the coupler length becomes too long and above this region, the coupler length become undesirable very short.

In order to obtain etch-depth of not less than 4.0 μm in the coupler and at least

6.4 μm in the waveguide trenches, using a single etch step, we took advantage of RIE lag effect.

RIE lag, otherwise known as aspect ratio dependent etching, becomes a critical problem when etching small features with high aspect ratios using RIE etching. The rate at which features are etched varies along the sample and depends on the feature sizes. Bigger-sized features experience higher etch rate and smaller features, lower etch rate leading to a lag in etch depth between the latter and former. According to [88], slower etch rate in smaller features, could be attributed to depletion of reactive species (ions) in these areas, and caused by restrictions in angular trajectories of incident ions.

In this work, RIE lag effect was positively utilised in the fabrication. This effect offered separate control of etched waveguide depth (i.e trench depth) over etch-depth of the coupler. While the waveguide depth is controlled solely by the etch parameters, coupler etch-depth is controlled by etch parameters and RIE lag effect. To investigate this effect and possible coupler gap to settle for in the design, an etch test was carried out. Patterns with coupler spacing ranging from 600 nm to 1400 nm were transferred using EBL to the sample. Also on the sample were 20,000 nm wide trench features used to define the waveguides; these parts were equally used for etch-depth profiling during etching as the coupler gaps were two narrow for the stylus of the profilometer (12 μm in diameter).

Fig. 4.4 shows a plot of etch depth ratio (EDR = $D_{coupler}/D_{waveguide}$) as a function of coupler gap d at etch times of 8 and 11 minutes. From the plot it is evident that the longer the etch time the lower the etch-depth ratio (i.e higher RIE lag) and on the other hand, the wider the coupler spacing, the higher the etch-depth ratio (meaning lower lag between the two trenches). Also from the plots, it is observed that the effect of RIE is critical below 1.2 μm and negligible beyond this point as the etchdepth ratio begin to flatten. To take advantage of RIE lag effect in the waveguide etching, the coupler gaps must not be wider than 1100 nm. 500 nm gap was chosen for this work because it gives the optimum coupler length (670 μm)

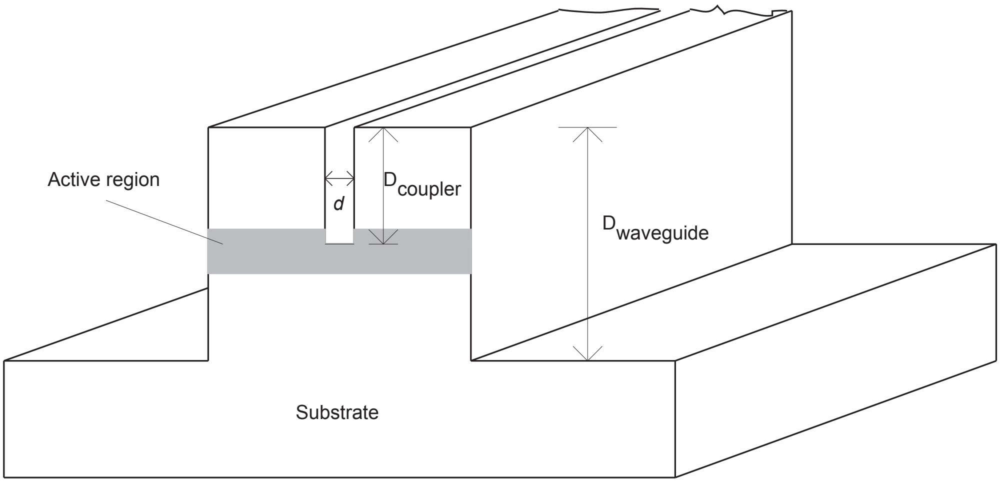

FIGURE 4.3: Schematic diagram illustrating etchdepth difference between coupler etchdepth ($D_{coupler}$) and waveguide etchdepth ($D_{waveguide}$) caused by RIE lag.

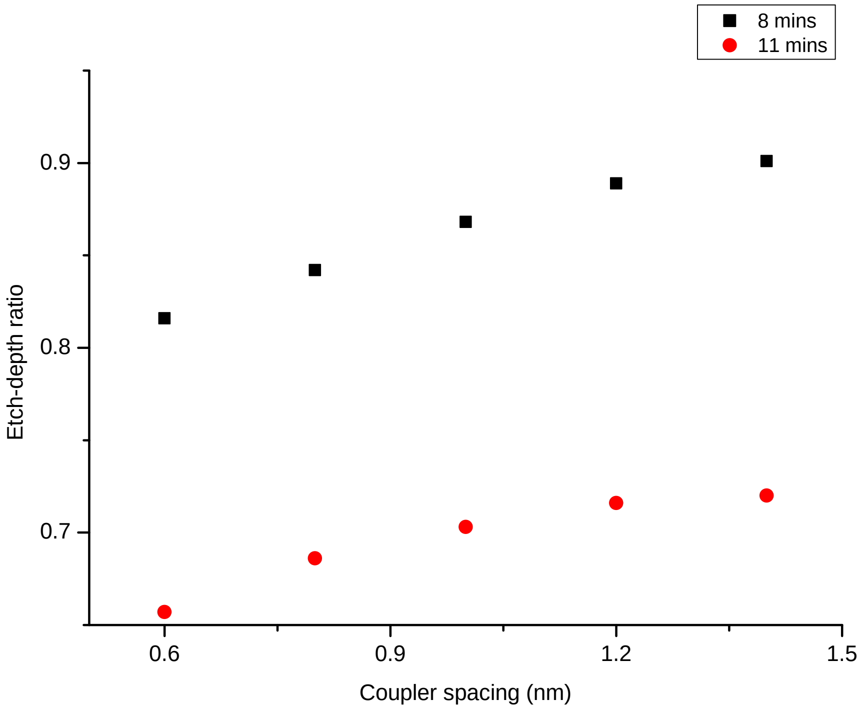

FIGURE 4.4: Plot of etchdepth ratio vs. coupler gap, at etch times of 8 minutes and 11 minutes

Table 4.1: Fitting parameters for calculating etch-depth ratio

y_0	A_1	t_1
0.374	0.21682	-3143.83

An exponential fit to figure.4.4, yields the equation below

$$y = y_0 + A_1 exp^{\frac{-x}{t_1}} \tag{4.1}$$

where y equals etch-depth ratio (EDR), and x is the coupler spacing. Using eqn.4.1 and the fitting parameters in table 4.1, with x=500 nm, EDR value was calculated to be 0.623. With EDR = 0.623 and $D_{coupler}$ fixed at 4.0 μm, $D_{waveguide}$ was calculated to be about 6.4 μm. These values were used for the final waveguide etching.

4.5.4 Ring Waveguide etching

After the hardmask etching, the sample was taken to CST (Glasgow) for ICP-RIE etching of the waveguides. The waveguides were etched (Cl_2/(N_2) etch chemistry for 10.3 minutes. Shown in figure 4.5(a) is the top view SEM image showing two ICP etched coupled rings and their coupler and figure 4.5(b) is an SEM image of the cross-sectional view of one of the couplers.

4.6 Planarisation

The nature of the etched ring waveguides (etch-depth = 6.4 μm and ridge width = 5 μm) means that electrical contact cannot be made directly on the ridges. Even when the ridge area is large enough for wire bonding, direct bonding on the waveguide is avoided in other not to break the fragile waveguide. Planarisation and side wall passivation are used to provide good electrical connection to devices and bondpads, and they help to reduce current leakage through the side walls in deep etched devices. The essence of planarisation was to form a kind of ramp connecting

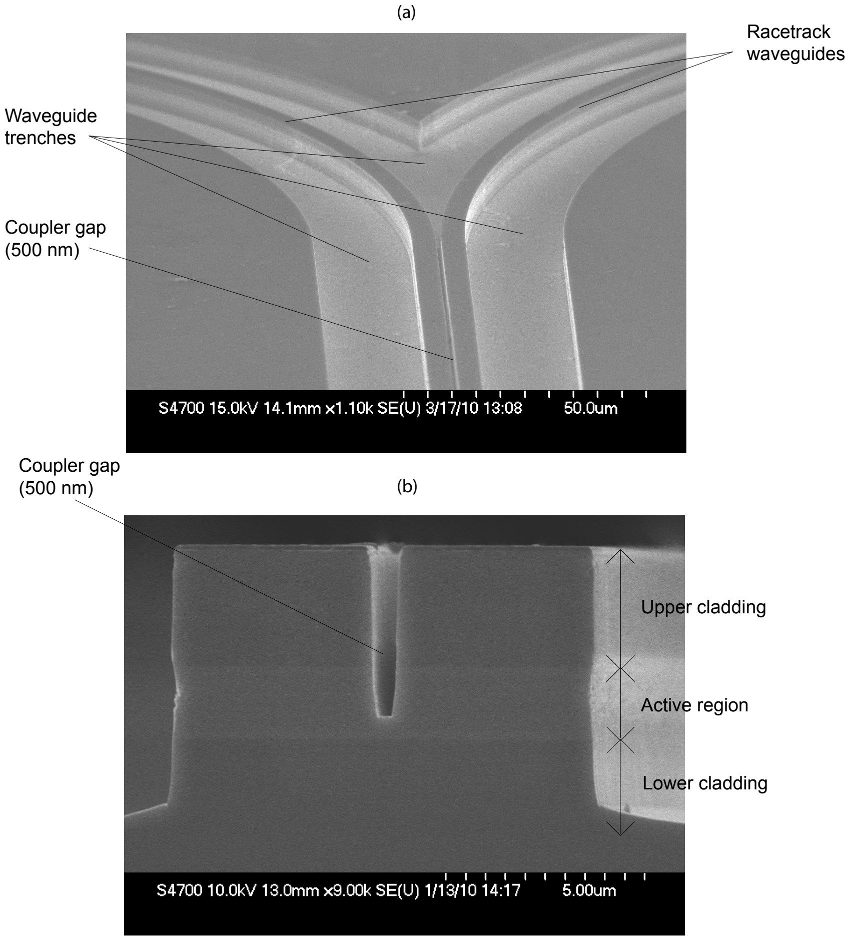

FIGURE 4.5: (a) top view SEM image showing two ICP etched coupled rings and their coupler (b) SEM image of the cross-sectional view of the coupler

the foot of the waveguide to the top (see fig. 4.6). With this in position, metal contact can be evaporated on the device without recourse to metal sputtering, which makes liftoff a bit difficult. In this work, side-wall passivation was achieved by, conformally, depositing 500 nm PECVD nitride on the etched waveguides. On the other hand, waveguide planarisation was carried out using flowable oxide 16 (FOX 16) [89], a spin-on dielectric HSQ, due to its fluidity. This method has been reportedly used for III-V semicondutor devices by Zegaoui *et al* [90]. FOX 16 was spin-coated on the sample at 2000 RPM for 60 seconds, giving thicknesses of $\sim$ 600 nm, 1600 nm and 150 nm on flat surface, waveguide trench and ridge top respectively. The spun sample was then placed in a 180 ^{o}C oven for 60 minutes to transform HSQ into silica. Finally, 200 nm PECVD silica was deposited on the planarised surface to smoothen the surface, thus providing good adhesion for contact metals.

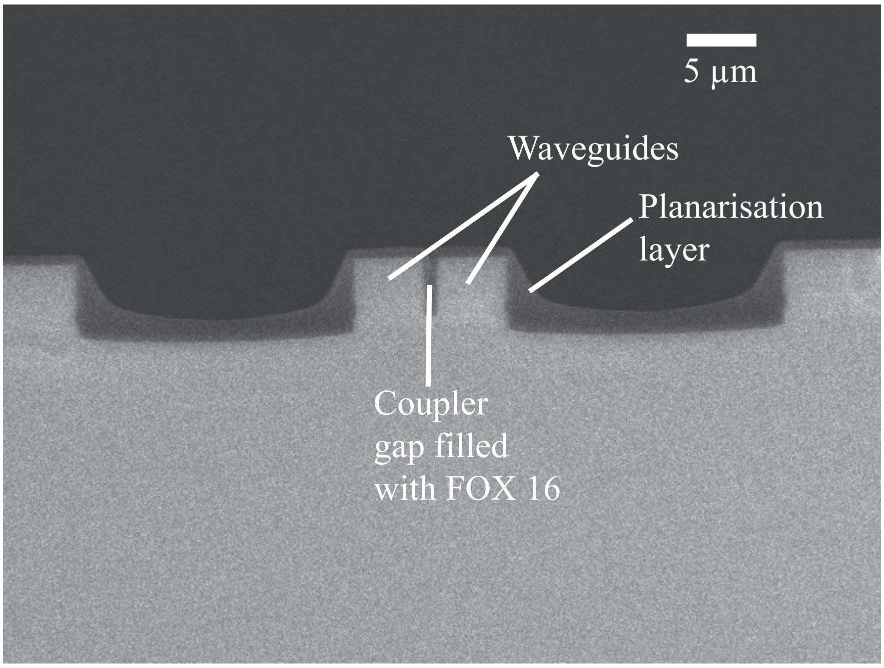

Figure 4.6: SEM of a planarised waveguide using the method described in this section (4.6).

4.7 Contact window opening

Contact windows were opened through the dielectric layers to the semiconductor cap layer to enable current injection into these devices. Because of three layers of dielectric (200 nm SiO_2 + 150 nm FOX 16 and 500 nm Si_3N_4) overlaying the waveguide, two dry etch chemistries were used for the contact window opening. These include;

- CHF_3+Ar for etching SiO_2 and FOX 16, with 29 nm/min and 21 nm/min etch rates respectively.
- CHF_3+O_2 for Si_3N_4 etching, etch rate is about 40 nm/min

Oxford Plasmalab RIE80 plus machine and Shipley S1818 photoresist was used for the process. Etch selectivity of 1:3 was observed between the photoresist and the dielectrics.

4.8 Liftoff Pattern

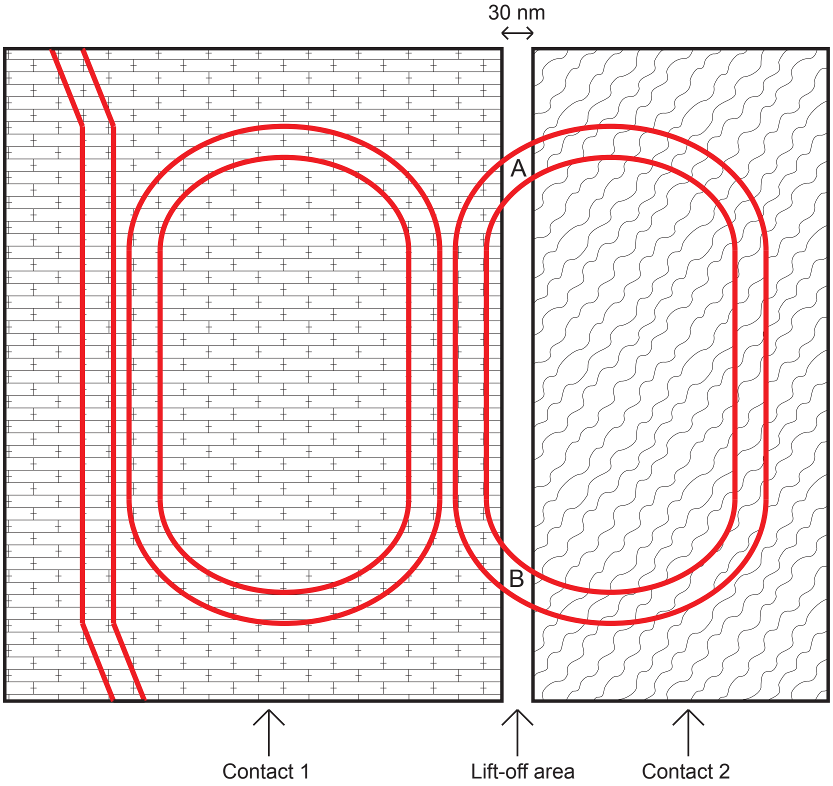

FIGURE 4.7: Top view schematic showing how the coupled ring devices were isolated electrically

Electrical isolation of the two rings (in the case of coupled rings) or the ring and S-waveguide (in the case of unidirectional rings) using standard metal-liftoff technique was not possible in this work. One of the greatest challenges encountered in the course of this research work was realising metal liftoff pattern across the waveguides (particularly at points A and B shown in figure 4.7).

Two approaches were taken to solve this problem. Liftoff resist, Michrochem LOR10A [91], was used as a sacrificial resist, in the two approaches to get undercut required for metal lift-off.

In the first approach the waveguides were not planarised. Four layers of LOR10A were spun on the sample and baked in an 180 ^{o}C oven to drive away the solvent. S1818 photoresist was spun at 4000 RPM for 30 seconds and pre-baked on a hot plate at 115 ^{o}C for 50 seconds. Liftoff pattern was transferred onto the sample using photolithography process. The exposed sample was developed in a 1:1 mixture of water and microposit developer. Developed sample was given 2 minutes oxygen ashing before being post-baked in an 120 ^{o}C oven for 30 minutes. Sample was developed in CD 26 developer solution to dissolve the Liftoff resist (LOR) thus giving useful undercut. The issue with this approach was that the resist thickness in the waveguide trenches were thicker than the resist on the ridges and the sidewalls. During development, LOR resist on the ridges and sidewalls dissolve faster than those in the trenches and on flat surfaces. Thus causing the overlaying resist (S1818) to collapse on the ridges. To encourage faster and a more uniform resist development, the beaker containing the sample and developer solution was placed in ultrasonic bath for 3 seconds. This process worked, but came at a price. The agitation from ultrasonic bath caused parts of some ring waveguides to snap. An SEM image of a liftoff done using this technique is shown in figure 4.8.

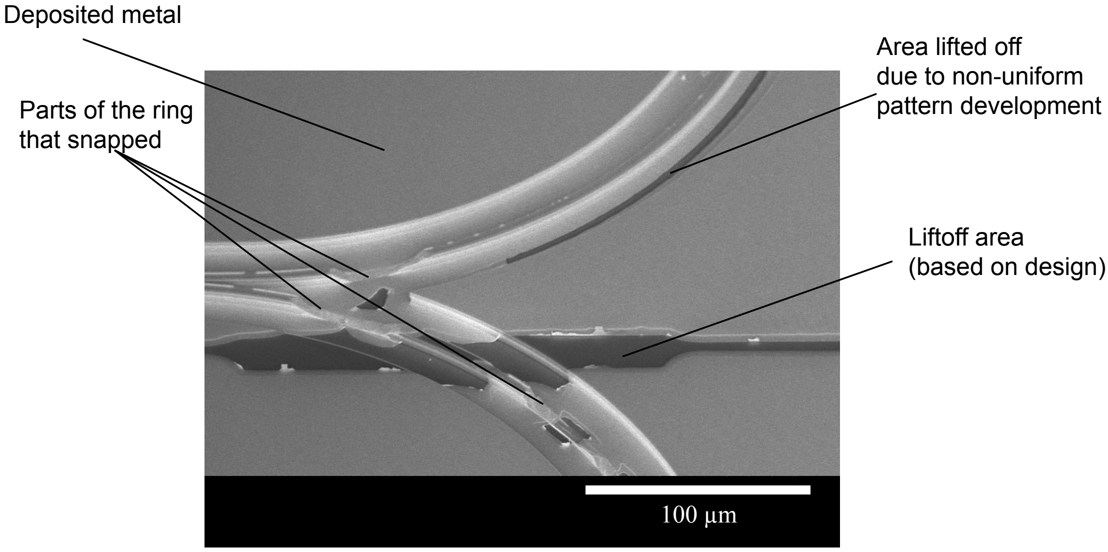

Figure 4.8: SEM image of metal liftoff on a coupled ring done using first approach

In the second approach, the waveguides were first planarised using the method described in section 4.6. The same process used in the first approach was repeated here. Liftoff pattern development was very uniform and no collapsed patterns were observed. Unlike the first approach, the second method is highly repeatable with better yield. A micrograph image of devices fabricated using this technique is shown in figure 4.9

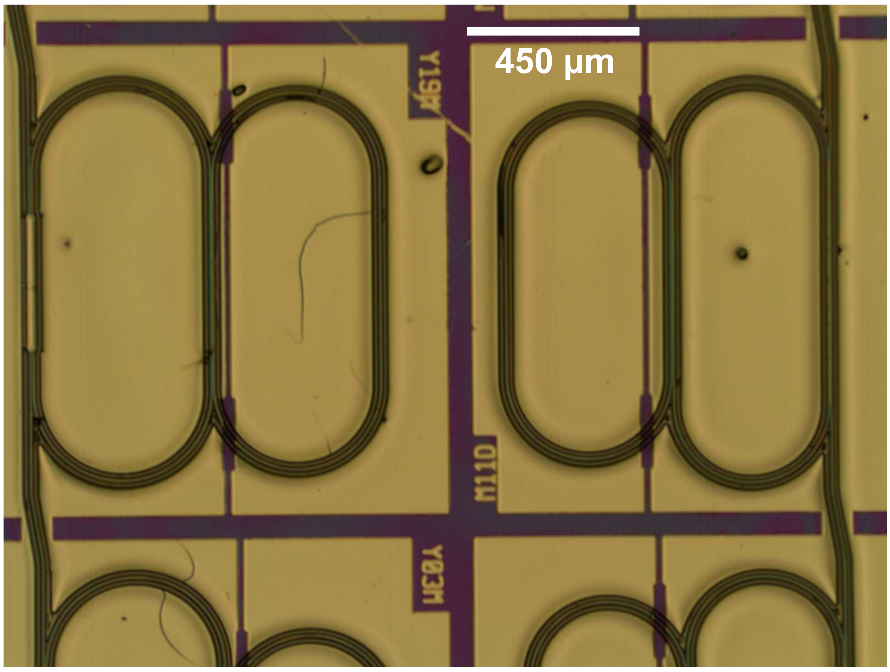

FIGURE 4.9: Micrograph image of metal liftoff on a coupled ring realised using second approach

4.9 Metalisation (Top contact)

Prior to metal deposition on the sample, oxide strip was carried out by dipping the sample in a 1:4 mixture of hydrochloric acid (HCl) and water, for 30 seconds, to remove native oxides that may have formed on the oxide surface. The stripped oxide sample was mounted on a substrate holder ready for metal deposition. Plassys 1, a metal deposition machine in the JWNC was used for this process. Ti(30 nm)/ Pd (20 nm)/ Ti(dummy)/ Au(240 nm) were deposited on the top of the sample. For devices made using the first lift-off patterning approach detailed in 4.8, 200 nm gold was further sputtered on the sample to ensure metal contact continuity on the ring side walls but for devices made using planarisation technique, metal sputtering was not necessary.

4.10 Metal Liftoff

After metallisation, the sample was dipped in a beaker containg SVC-14 developer to lift-off the unwanted metals from the sample. The solution was maintained at 60 ^{o}C while being continually stirred. The sample was left in the solution for 20 minutes before being rinsed in IPA for 20 seconds. SEM images of the lift-off is shown in Fig.4.8 and Fig.4.9

4.10.1 Thinning, Back contact metallisation and Annealing

Substrate thinning was done to facilitate heat extraction from the device to the heatsink whilst in operation. In this case, the substrate was mechanically thinned by rubbing the substrate over a solution of aluminum oxide (Al_3O_2) powder and water, sprinkled on a glass board. The substrate was thinned down to 200 μm using a combination of 9 and 3 μm (Al_3O_2) powder. While the former was used to aggressively reduce the thickness of the substrate, the later was used to smoothen the surface, thus ensuring good metal adhesion.

The sample was giving a thorough solvent cleaning and subsequently mounted upside down on a glass slide for back metallisation. Same metal layers used for the top contact (see section 4.9) was deposited on the back side of the sample.

Rapid thermal annealing (RTA) was done to alloy the metal contacts, thus making it ohmic. The sample was annealed at 360 ^{o}C to enable the intermixing of the layered metals.

4.11 Cleaving, Mounting and Wire-bonding

Using the scriber and cleaver in the JWNC, the sample was separated into individual devices. These devices were mounted on heatsink tiles, specially designed to match the probes on our cryorod, with using indium solder. Using gold wires, the devices were wirebonded to the contact pads on the heatsink. An SEM image of a cleaved device and a wire-bonded coupled ring laser are shown in figure 4.10 and figure 4.11

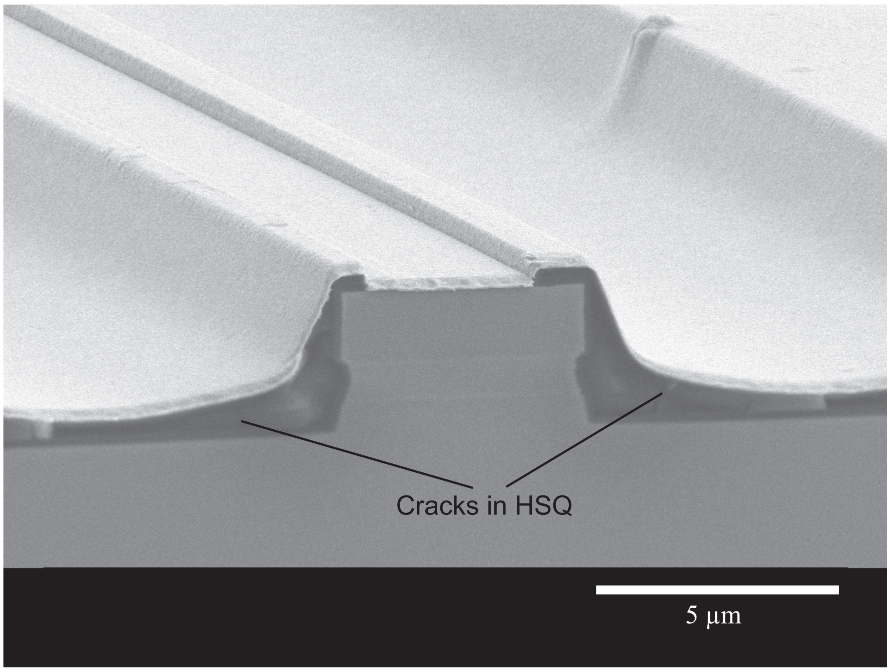

FIGURE 4.10: SEM image showing the cleaved facets of one of the processed devices

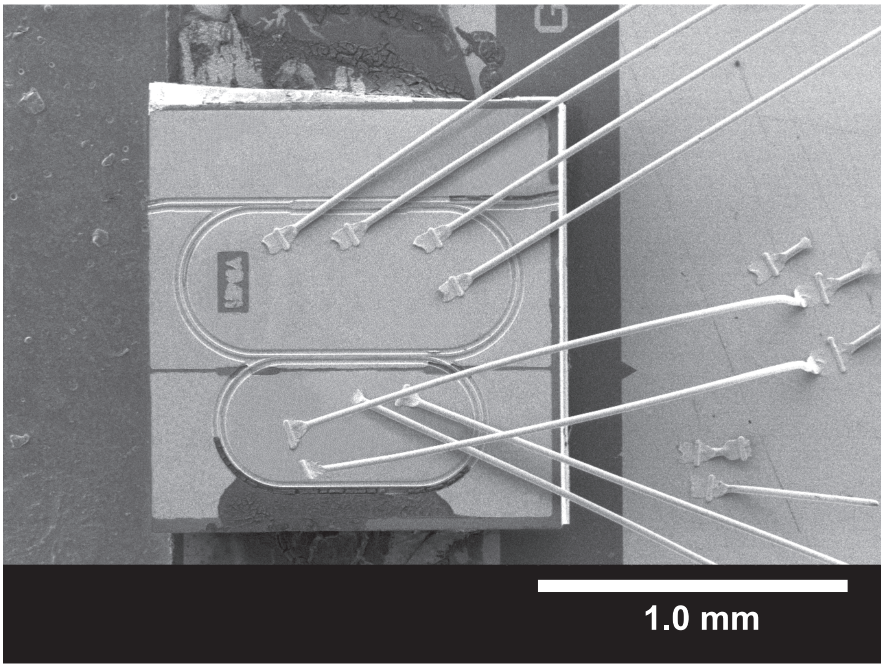

FIGURE 4.11: SEM image showing a wire-bonded coupled ring laser

4.12 Conclusion

This chapter discussed the fabrication techniques employed in this work. The main fabrication challenges were also highlighted. The main fabrication achievements include: utilising RIE lag effect positively for the first time in quantum cascade laser (QCL) processing, QCL waveguide planarisation using HSQ, developing multilayer liftoff recipe for deeply etched waveguides and achieving metal liftoff across a 6.4 μm high ring waveguide. The fabrication techniques discussed here were used to process the quantum cascade rings discussed in chapters 6 and 7.

Chapter 5

Unidirectional Quantum Cascade Ring Lasers

5.1 Introduction

Unidirectional operation in a ring laser is defined as when when greater percentage of light is emitted from one output direction. Semiconductor ring lasers discussed in section 3.6 are inherently bi-directional due to the reciprocity of the gain medium in the ring resonator. Unidirectional emission in semiconductor ring lasers (SRLs) have been achieved by either driving the laser in the unidirectional regime [77], or by introducing both a non-reciprocal loss and gain into the ring cavity (e.g using an active crossover waveguide) [76]. Some of the advantages of unidirectional operation include:

1. stable single mode operation
2. ability to operate in the traveling wave regime
3. absence of spatial hole burning which is a source of noise and has recently been shown to be a limitation on modelocked operation of quantum cascade lasers (QCLs) [92]

4. uniform saturation of gain medium
5. More power extracted in the favoured emission direction [93]
6. higher quantum efficiency in the preferred direction

The work described here was focused on achieving unidirectional operation by incorporating an active S-cross-link waveguide. The nature of the quantum cascade (QC) material gain (inhomogeneously broadened) means that gain competition which is responsible for unidirectional operation was not there. By introducing the S-cross-link waveguide we link the individual gains, thereby introducing gain competition and hence, unidirectional operation. This is the first unidirectional quantum cascade ring laser (QCRL) ever reported and it operates in pulsed mode with good spectral purity.

5.2 Aim

The main aim of the research work described in this chapter was to demonstrate unidirectional emission from a bidirectional QCRL, at all injection currents above threshold. This is achieved by intentionally introducing non-reciprocal loss and gain in the counter-clockwise (CCW) and clockwise (CW) propagating modes, respectively.

5.3 Objective

The target objectives were to demonstrate single mode emission with unidirectionality (i.e. CWSR) greater than 90%

5.4 Literature review on unidirectional ring laser

Unidirectional operation of ring lasers requires the use of a nonreciprocal mechanism which favours the oscillation of the mode moving in one direction around the cavity at the expense of the other. In conventional lasers this behaviour have been reportedly achieved by using Faraday isolator [94] and back reflections from auxiliary mirrors [95]. The absence of monolithically integrable isolators meant no semiconductor unidirectional laser was demonstrated till the early nineties.

In 1991, Sennaroglu and Pollock from Cornell University Ithaca, New York proposed an alternative mechanism for breaking the symmetry in a ring laser by tilting the output facet of the waveguide ring laser by a small angle (1-2 °) to encourage feedback into the system which in turn provides the required non-reciprocity.[96] Barely two months after the proposal, the first unidirectional oscillation in a ring-resonator type semiconductor laser based on feedback mechanism was demonstrated by Oku and colleagues [97] from NTT Opto-electronics Laboratories, Kanagawa, Japan. Unidirectional emission based on facet reflection was also demonstrated by researchers in University of Glasgow, led by Marc Sorel [93].

At the same time, extensive research in the field of SRL, in the early 1990s by Hohimer and fellow workers at the Sandia National laboratories, Albuquerque, New Mexico, led to the demonstration of the first unidirectional operation in a SRL based on the use of active crossover waveguide [76, 83].

In 1997 J. Liang and co-workers reported on unidirectional operation in a triangular ring laser [98]. Their approach was to create a loss asymmetry by introducing a waveguide tapering section that widens the waveguide gradually followed by an abrupt section that connects to the original width. The abrupt section is responsible for the feedback mechanism.

Finally, in the early 2000 a group of researchers led by Marc Sorel, from University of Glasgow, reportedly demonstrated unidirectional operation in a SRL by naturally allowing low feedback from the output facets into the cavity [77]. They also predicted and experimentally demonstrated the operating regimes of SRL as a function of the bias current; the regimes include, bidirectional, alternate oscillation and unidirectional [77, 99].

5.5 Operation of Unidirectional QCRL

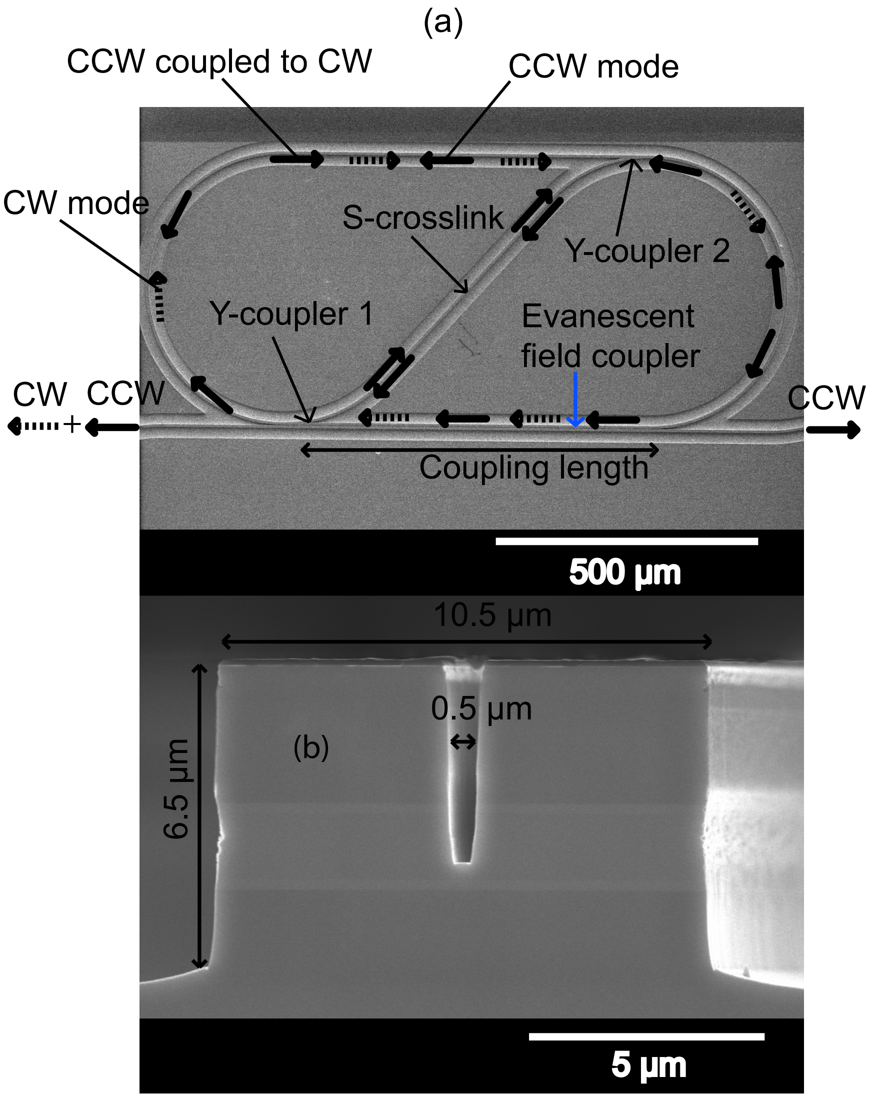

Figure 5.1: (a) SEM image of the top view of unidirectional ring showing the racetrack circumference (2900 μm) with the “S-shaped” cross arm and at the bottom of the figure is the directional coupler; solid and dotted arrow indicate CCW and CW modes, respectively. (b) SEM of the cross-sectional view of the evanescent field coupler part of the laser (point shown by a blue arrow in Figure above), the width of the waveguide is 5 μm and the slot in the centre of the waveguide is 0.5 μm wide and 4.0 μm deep is etched down to the active region of the laser.

Illustrated in Fig.5.1 is the schematics of the operation of an S-crossover unidirectional ring laser and it works as follows: the racetrack ring laser has an S shaped cross arm joined to the racetrack cavity at two points with the aid of two asymmetric Y-couplers which split or combine power through them, depending on the direction of the propagating light. In this design the asymmetric Y-junctions were oriented in a manner that they split light in the CCW direction (solid arrows) but combine light in the CW direction (dotted arrows). This introduces a non reciprocal loss in the CCW direction and gain in the CW direction as the split part of the CCW light passes through the S-shaped waveguide to combine with the CW mode at the next Y-junction. These modes compete for gain in the racetrack but the CW mode is always dominant and therefore as the current injected into the racetrack ring laser is increased the CW increases and suppresses the CCW mode thus the laser becomes more unidirectional as the laser is operated further above the threshold current. Light is coupled out of the ring through the evanescent field coupler.

5.5.1 Rate Equation Model for QCRL

Laser rate equations are employed to model the optical and electrical characteristics of any laser system. These equations relate the photon and charge carrier densities in the device to the injection current and material parameters (eg. optical gain, photon lifetime and carrier lifetime).

In a three-state QCL system, schematically shown in Fig.5.2; electrons injected into n = 3 state from the ground state of the injector of the previous period at a rate equals to J/q_0 may scatter from this state to the n = 2 and and n = 1 states with rates τ_{32}^{-1} and τ_{31}^{-1} respectively and n = 3 lifetime, given by the relation, τ_3^{-1}=τ_{32}^{-1}+τ_{31}^{-1}+τ_{esc}

The rate of change of the population of the three levels and photon density may be expressed as;[100]

$$\frac{dn_3}{dt} = \frac{J}{q_0} - \frac{n_3}{\tau_3} - Sg_c(n_3 - n_2) \tag{5.1}$$

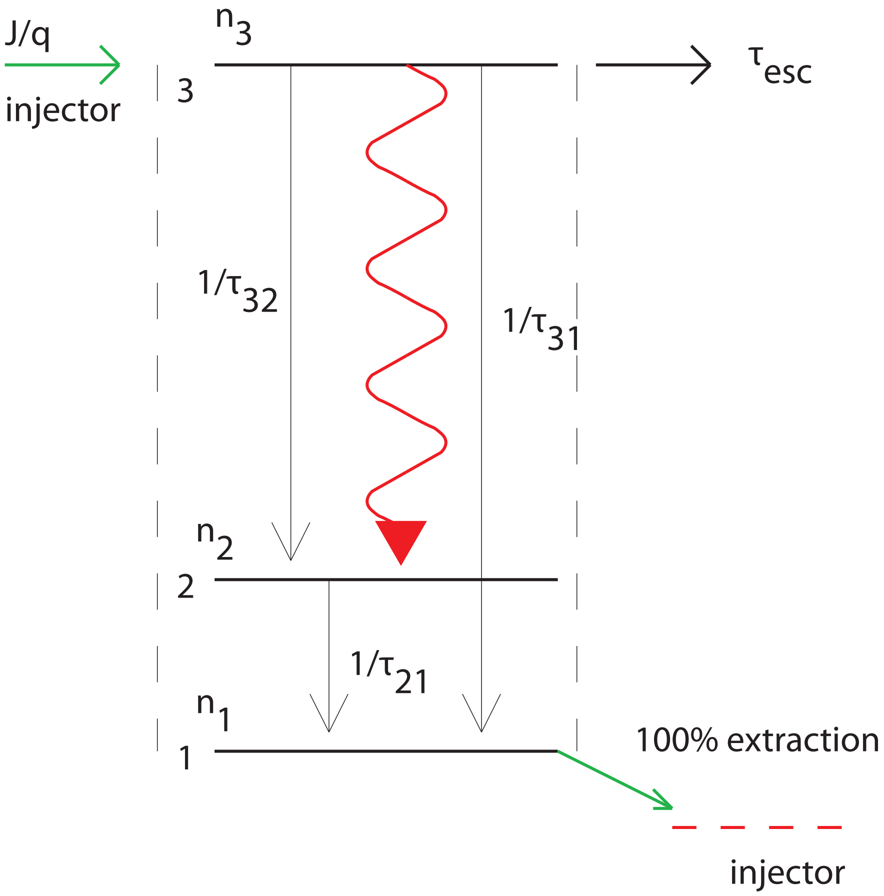

FIGURE 5.2: Schematic representation of the energy level scheme of a three states QCL. The tunneling and relaxation processes are indicated by arrows (green for injectors, wavy red for optical transition and black for interstates transition). Level 1 is rapidly depopulated into the energy level of the next injector.

$$\frac{dn_2}{dt} = \frac{n_3}{\tau_{32}} + Sg_c(n_3 - n_2) - \frac{n_2}{\tau_{21}} \tag{5.2}$$

$$\frac{dS}{dt} = \frac{c}{n_{eff}} \left[\left(g_c(n_3 - n_2)\right) S + \beta \frac{n_3}{\tau_{sp}} - \frac{S}{\tau_c} \right] \tag{5.3}$$

where J is the injected current density, q_0 is the electronic charge and S denotes the photon flux density (per unit length per second) for a certain mode. c is the speed of light in free space, n_{eff} is the effective index of the material, β ~0.001 [101] is the fraction of the spontaneous emission coupled in the lasing mode and τ_{sp} the spontaneous emission lifetime. $\alpha_{tot} = \alpha_m + \alpha_w$ is the total cavity loss; where α_w

is the waveguide loss and mirror loss,α_m, is given by equation 5.4

$$\alpha_m = \frac{1}{2L} ln \frac{1}{R_1 R_2} \tag{5.4}$$

The cavity lifetime or exponential decay time is given as;

$$\tau_c = \gamma_c^{-1} = \frac{\tau_r}{\alpha_{tot}} \tag{5.5}$$

where τ_r round-trip time (i.e $2n_{eff}L/c$). The gain coefficient (cm/kA) of a QCL can be calculated as [26]

$$g = \tau_3 \left(1 - \frac{\tau_{21}}{\tau_{32}}\right) \frac{4\pi q^2}{\epsilon_0 n_{eff} \lambda} \frac{z_{32}^2}{2\gamma_{32} L_p} \tag{5.6}$$

where z_{32} is the dipole matrix element, γ_{32} is the broadening of the transition, λ the wavelength and L_p the length of the period.

Assuming that the gain spectrum of the QCL has a Lorentzian shape and always lase at its gain maximum, the gain cross section, g_c, (unit: cm) can be deduced as

$$g_c = \frac{qg\Gamma}{\tau_{3(1-\tau_{21}/\tau_{32})}} = \Gamma \frac{4\pi q^2}{\epsilon_0 n_{eff} \lambda} \frac{z_{32}^2}{2\gamma_{32} L_p} \tag{5.7}$$

where Γ the total overlap factor. The threshold current density in this type of QCL is given in equation 5.8[26]

$$J_{th} = \frac{1}{\tau_3(1 - \tau_{21}/\tau_{32})} \left(\frac{\epsilon_0 n_{eff} \lambda}{4\pi q \Gamma_p N_p z_{32}^2} (\alpha_m + \alpha_w) \right) \tag{5.8}$$

5.6 Coupled Rate Equation Model For Unidirectional QCRL

The photon density coupled rate equation model for a unidirectional quantum cascade laser can be developed by modifying the rate equations of the QCRL described in section 5.5.1 to include light coupling from the CCW to CW direction (see figure 5.3).

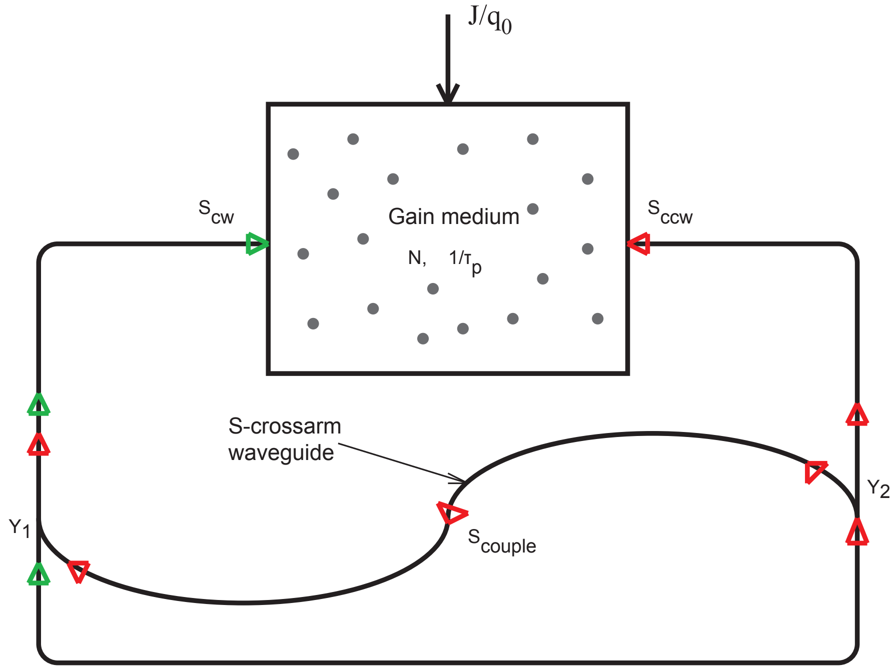

FIGURE 5.3: Conceptual diagram of unidirectional ring laser with a directional coupling, S_{couple}, where both CW and CCW resonators have identical carrier densities and photon lifetimes, τ_p
and dots represent photons

The modified photon density rate equations for CCW and CW are given in equations 5.9 and 5.10, respectively.

$$\frac{dS_{CCW}}{dt} = \frac{C}{n_{eff}}\left[(g_c(n_3 - n_2))\, S_{CCW} + \beta\frac{n_3}{\tau_{sp}} - S_{Couple} - \frac{S_{CCW}}{\tau_c}\right] \tag{5.9}$$

$$\frac{dS_{CW}}{dt} = \frac{C}{n_{eff}}\left[(g_c(n_3 - n_2))\, S_{CW} + \beta\frac{n_3}{\tau_{sp}} + \frac{1}{2}S_{Couple} - \frac{S_{CW}}{\tau_c}\right] \tag{5.10}$$

where S_{Couple} for a unidirectional QCRL, adapted from Ref.[102] can be expressed as;

$$S_{Couple} = (R_{c1} + R_{c2})exp(g_{cs} - \alpha_s)L_s + (R_{c1} + R_{c2})\beta\frac{n_3}{\tau_{sp}} \tag{5.11}$$

where R_{c1} and R_{c2} represent light reflected into the S-cross arm from the top Y-coupler (Y_1)and the bottom Y-coupler (Y_2)respectively and T_{c1} and T_{c2} the transmittance at the two couplers. τ_r is the round trip time and g_{cs} the gain in the S-cross arm.

By comparing eqnuation5.9 and equation 5.10 we come to the conclusion that unidirectional emission in this structure is predominantly controlled by the amount of light we are able to couple from the CCW to the CW direction. Though only about one quarter of the coupled light (S_{Couple}) finally gets to the racetrack waveguide (see equation 5.11). This is as a result of a 3dB radiation loss in each of the asymmetric Y-couplers [103].

However, in this work we developed a simpler mathematical model for calculating photon densities on both directions based on coupled rate equation method.

In the S-crossover ring lasers (i.e unidirectional operation), the intracavity photons of the CCW direction couple to those of the CW direction through two asymmetric Y-couplers in the S-crossover waveguide during each round trip. Here we investigates the intracavity photon density on both sides as function of net modal gain in the material and k1 (i.e cavity-“S” waveguide coupling coefficient). We started by tracing the optical paths of the photons in both directions as shown in figure 5.4

By injecting a normalised photon density, S, into the cavity in the CCW direction we can calculate the fraction of the light that was (1) emitted out (via the output coupler), (2) coupled to the CW direction (via the S-waveguide) and (3) remaining in the CCW direction after the first round trip. These fractions are calculated using coupled rate equation developed for this device, provided the following assumptions:

- no facets reflection back into the cavity
- negligible bending loss
- negligible spontaneous emission

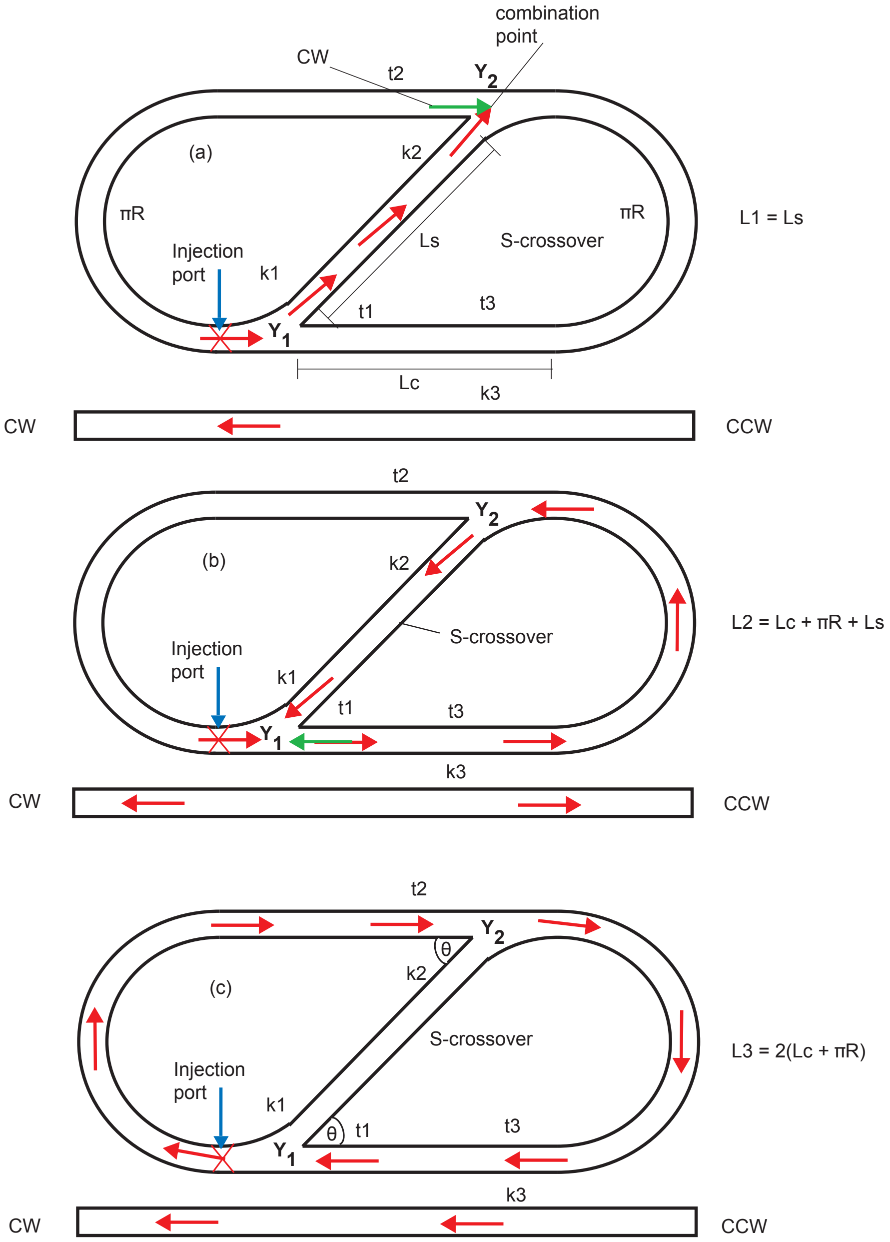

FIGURE 5.4

The fraction of injected photon density remaining in the CCW direction of the ring cavity after the first round trip can be calculated from the expression,

$$S_{CCW}(remain) = St_1t_2t_3exp(g\Gamma - \alpha)L_3 \tag{5.12}$$

where t_1, t_2 and t_3 are the transmission coefficients at Y_1, Y_2 and output coupler, respectively. $L_3 = 2(\pi R + Lc)$ is the cavity path length per round trip as shown in figure 5.4(c). R is the radius of the ring cavity and L_c is the length of the coupler. S is the normalised photon density injected into the ring cavity and α is the waveguide loss in the material.

On the other hand, the photon density remaining in the CW direction of the ring cavity after the first round trip can be calculated from the expression,

$$S_{CW}(remain) = St_3 exp(g\Gamma - \alpha)L_3 S_{couple} \tag{5.13}$$

where,

$$S_{couple} = Sk_1 exp(g\Gamma - \alpha)L_2 exp(g_s\Gamma - \alpha)L_s St_1 k_2 t_3 exp(g\Gamma - \alpha)L_1 exp(g_s\Gamma - \alpha)L_s \tag{5.14}$$

k$_1$, k$_2$ and k$_3$ are the coupling coefficients at point Y$_1$, Y$_2$ and the output coupler, respectively. L$_s$ is the length of the "S"-crossover waveguide, L$_1$ = (πR+ Lc +L$_s$)[see figure 5.4(a)] and L$_2$ = L$_s$ [see figure 5.4(b)] are the path length travelled by the coupled light from CCW to CW before combining in the next Y coupler.

Finally the measure for unidirectionality, otherwise known as the counter propagating wave suppression ratio (CWSR) is obtained by dividing the photon density in the CW direction by the photon density in the CCW direction. The CWSR per round trip is calculated from the expression,

$$CWSR = \frac{St_3 exp(g\Gamma - \alpha)L_3 \frac{1}{2} S_{couple}}{St_1 t_2 t_3 exp(g\Gamma - \alpha)L_3} \tag{5.15}$$

Substituting the data in table 5.1 into equation 5.15 we modeled CWSR as a function of k1. The result is shown in figure 5.5

From the figure, as expected, the CWSR continuously increased with increasing k1. In reality the maximum coupling available when coupling light into a ring cavity from a straight waveguide is set by the angle of inclination (θ) between the "S" waveguide and the straight waveguide (see figure 5.4(c)). In this work we used θ = 42 degrees. The coupling coefficient at Y$_1$ for device reported here, modeled using BEAMPROP is about 40 %.

TABLE 5.1: Parameters used to model unidirectional behaviour in an “S”-crossover ring waveguide cavity

Parameters	Values
k_1	0.1∼0.9
t_1	$1-k_1$
t_2	t_1t_3
k_2	k_1t_3
k_3	$0.5t_1$
t_3	$0.5t_1$
S	1
R	250 μm
Lc	670 μm
Ls	850 μm

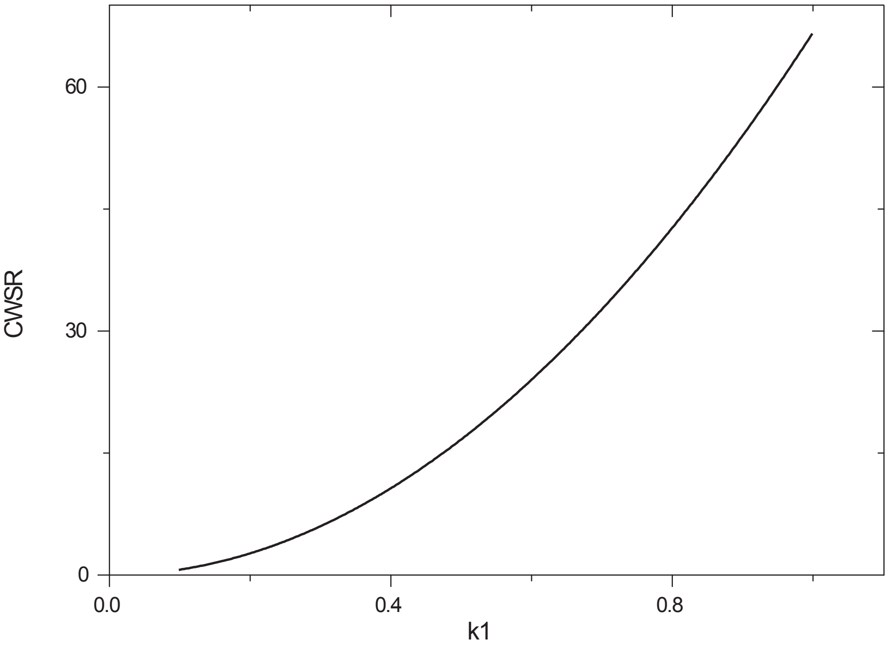

FIGURE 5.5: Computed CWSR as a function of cross-coupling coefficient, k_1, for cavity net modal gain of 3800 m^{-1}

From the modeled result, it is evident that the unidirectional operation in this structure is predominantly controlled by the amount of light we are able to couple from CCW to CW direction. As the net modal gain increases, CW mode claims most of the gain and continuously suppress the CCW mode.

Table 5.2: Design parameters for the unidirectional QCRL with chip id: UR250DC

Parameter	Dimension
Waveguide width (μm)	5
Inner ring radius (μm)	245[a]
Outer ring radius (μm)	250[b]
Effective ring radius (μm)	248[c]
Length of evanescent coupler (μm)	670[d]
Evanescent coupler gap (μm)	0.5[e]
Length of the straight waveguide (μm)	528
Etch-depth of waveguide(μm)	6.5[f]
Etch-depth of coupler (μm)	4.0[g]
Effective length of waveguide (μm)	2614
Output coupling ratio	50:50
Y-coupling ratio	20:80
Output guide tilt angle (degree)	7
Length of S-cross-arm waveguide (μm)	850
Number of electrical contacts	2

---

[a] section3.6.4
[b] section3.6.4
[c] section3.6.4
[d] section3.5.1.1
[e] section3.5.1.1
[f] section4.5.3
[g] section4.5.3

5.7 Design

Based on the modeled data and the constitutional component design considerations discussed in section 3.5, we designed two variants of the unidirectional QCRL. The design parameters for the first (chip id :UR250DC) and second (chip id :UR250MMI) variants are given in tables 5.2 and 5.3, respectively. The only difference between the two devices is the type of output coupler employed.

An SEM image of a processed unidirectional quantum cascade ring laser is shown in figure 5.6

TABLE 5.3: Design parameters for unidirectional QCRL with chip id: UR250MMI

Parameter	Dimension
Waveguide width (μm)	5
Inner ring radius (μm)	245[a]
Outer ring radius (μm)	254[b]
Effective ring radius (μm)	248[c]
MMI length (μm)	374[d]
MMI width (μm)	24[e]
Length of the straight waveguide (μm)	528
Etch-depth of waveguide(μm)	6.5[f]
Etch-depth of coupler(μm)	4.0[g]
Effective length of waveguide (μm)	2614
Output coupling ratio	50:50
Y-coupling ratio	20:80
Output guide tilt angle (degree)	7
Length of S-cross-arm waveguide (μm)	850
Number of electrical contacts	2

---

[a] section3.6.4
[b] section3.6.4
[c] section3.6.4
[d] section3.5.1.2
[e] section3.5.1.2
[f] section4.5.3
[g] section4.5.3

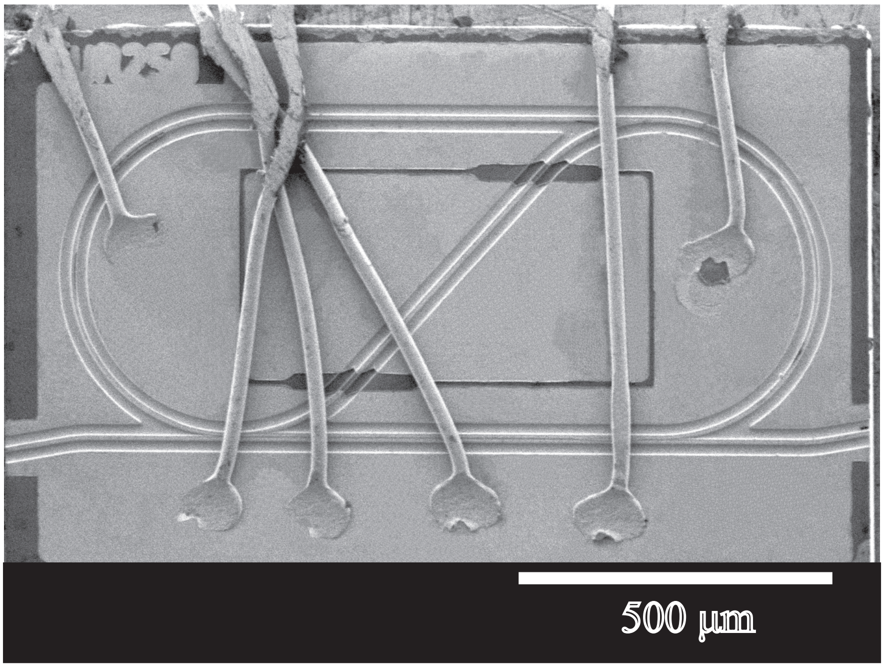

FIGURE 5.6: SEM image of a processed unidirectional quantum cascade ring laser

5.8 Device Characterisation Technique

This section details all the experimental techniques and equipment setup employed to characterise the devices reported in this chapter and the following chapter (chapter 7). The optical and electrical performances of the fabricated devices (QCRLs, unidirectional quantum cascade laser (UQCRL) and coupled ring quantum cascade lasers (CRQCLs)), were probed by measuring their light-current (L-I) and current-voltage (I-V) characteristics and spectra.

5.8.1 Experimental Setup

The schematic of the experimental setup employed to characterise the quantum cascade ring laser devices reported in this work is shown in figure 5.7. It comprises of

- optical systems
- electrical systems
- cryogenic component
- data display/acquisition unit

The optical unit is made up of the Bruker Vertex 70 fourier transform infrared (FTIR) spectrometer, a liquid nitrogen cooled InSb detector, KBr beamsplitter, ZnSe cryostat window and a host of parabolic and plane mirrors.

The electrical unit include voltage pulse generators, low inductance 50 Ohm resistors and current probes. Voltage pulse generators used in this work are (1) Avtech A-V-1011-B dual polarity pulse generator capable of providing pulse widths (~50-100 ns) at repetition rates of 500 Hz - 1 MHz and maximum current output of 2 A (2) Agilent 8114A capable of supply upto 100 V and 2 A when shorted. Also this pulse generator could be used as either a positive or negative pulse generator,

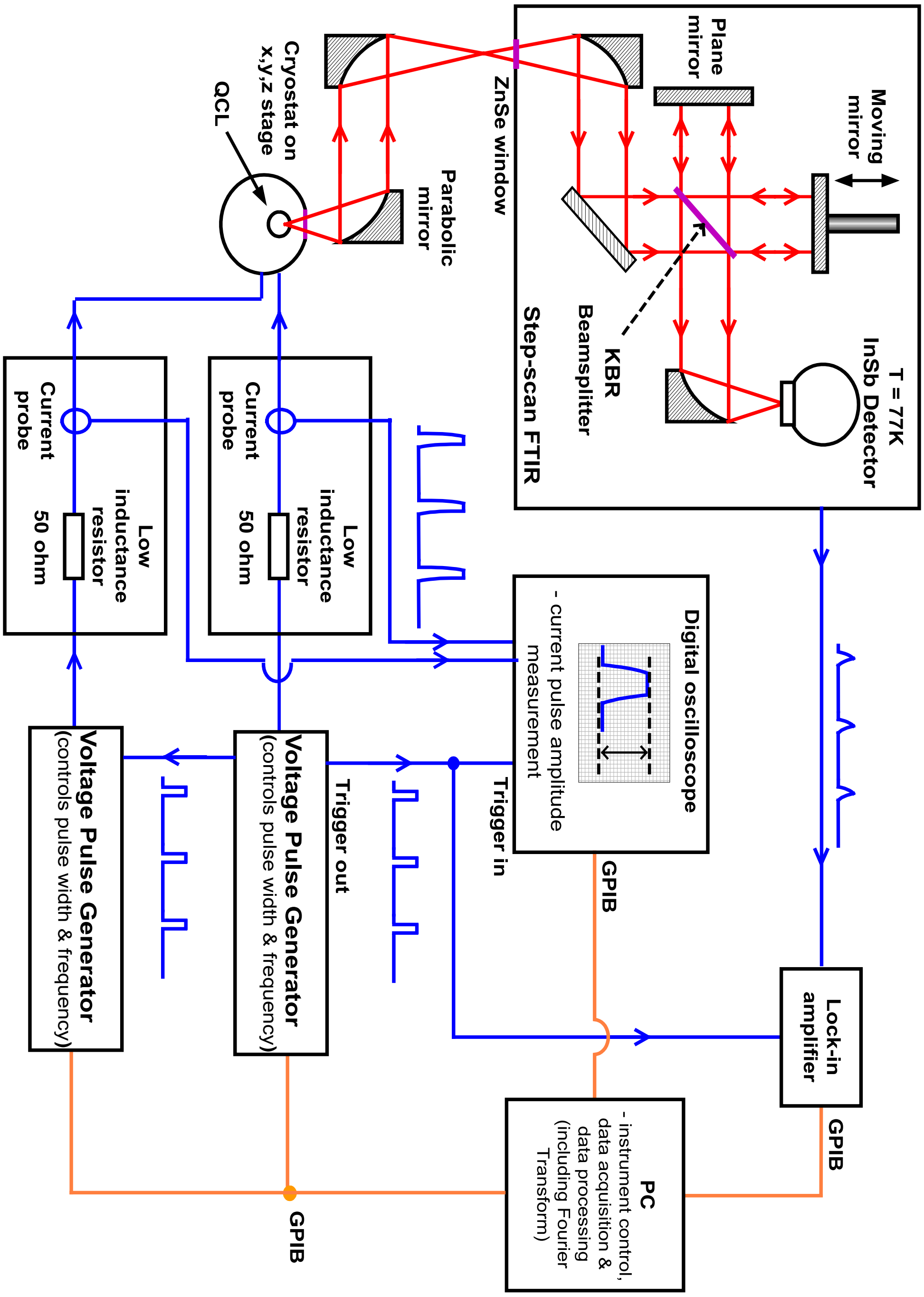

Figure 5.7: Experimental setup used to measure the spectra of the processed quantum cascade lasers
[104]

(3) high voltage (0-1 kV) DEI-HV1000 positive pulser, capable of providing pulse width (50 ns-10 μs) at repetition rates from as low as ~100 Hz to 1 GHz.

The only part of the cryogenic unit captured in the schematic diagram is the Oxford close cycle cooler (CCC1204) cryostat which is used to control the operating temperature of these devices. Two data display and acquisition units were used. They include a personal computer and an oscilloscope.

5.8.2 Spectra Acquisition

Properly wire-bonded devices are epi-layer up mounted in the cold finger of the cryostat and the temperature pumped down to the desired value. Electrical access is made to the device through a 50 Ohm coaxial cable wired into the cryostat rod. Injected current required to drive the devices and voltage needed to bias the devices were provided by connecting a 50 Ohm low-inductance resistor in series with the tested device to a voltage pulse generator; while the voltage pulser controls field across the device, the 50 Ohm resistor controls current through the device. This resistor also provides the necessary load impedance to roughly match the output impedance of the pulse generator. The actual resistor used was a Meggit CGS high-power thick-film, low inductance resistor, chosen to minimise inductive kicks which would be obtained if a standard resistor had been used. Once the device were driven to and above threshold, the emitted light is collected, collimated and transmitted (with the help of the parabolic mirrors) to beamsplitter which generates interference pattern (interferogram). The light from the beam splitter is then focused on the detector. Fourier transform of the time dependent-interferogram gives the spectrum.

All the QCL devices in this thesis were driven in pulsed mode, with a typical pulse width ranging from 50-100 ns at repetition rate of 5-10 kHz. The configuration of device under test determines the number of independent power sources needed; e.g the unidirectional and coupled ring QCLs have two isolated electrical contacts to be powered (thus three-terminal devices), while the single rings and FP QCLs have only one contact (two-terminal devices). In the three terminal devices, the two power sources were sychronised by an external trigger.

5.8.3 Light-Current and Current-Voltage Measurement Setup

The same set-up described in section 5.8 was used for the L-I and I-V characterisation with the exception that the output DC signal from the lock-in detector was fed into an averaging BOXCAR unit, which also has inputs from the injected current and voltage. A PC installed with LABVIEW (a software used to control the drive electronics and record gated measurements of the current and voltage signals obtained) was connected through the GPIB to the BOXCAR averaging.

5.9 Result And Discussion

The fabricated devices were epi-layer up soldered onto a heat sink and mounted onto the cold finger of a closed cycle helium cryostat and driven at 5 kHz with 90 ns pulses at 200 K. Current pulses were injected into the racetrack (note: no current injection into the crossover) waveguide and L-Is from both sides measured using an uncalibrated power meter. Shown in Figure 5.8 are the L-I curves measured from CW and CCW directions . From this figure it is clear that as expected there is more emission in the CW direction. The curves were measured in similar conditions and are therefore comparable.

However, to obtain conclusive evidence of unidirectional operation, made a plot of CWSR (i.e CW/CCW) as a function of injected current and shown in figure 5.9; it then becomes clear that the CCW curve is not just a scaled down version of the CW curve because the ratio of CW to CCW emission increases as the CW power increases and this is what is expected from unidirectional operation. For instance, at a factor of 1.5 above threshold the intensity of light from CW direction is about 9 times greater than that from the CCW direction (i.e 90% of the light is emitted in the CW direction). As the power increases the dominant CW mode claims more

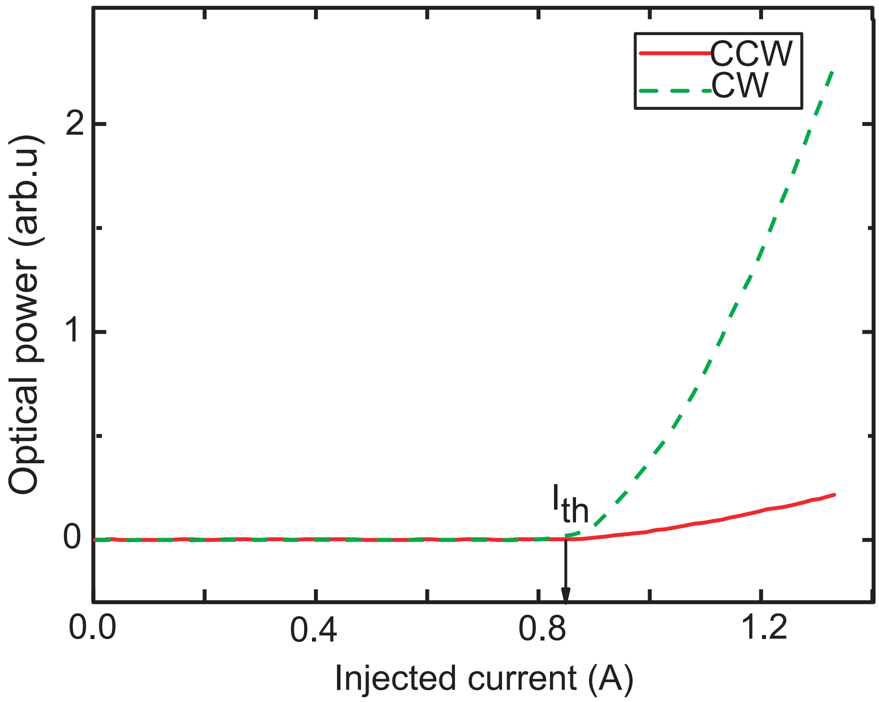

Figure 5.8: Light-current curves from the CW and CCW exit waveguides, both measured at 200 K

of the available optical gain and leaves less gain available for the CCW mode. This type of behaviour was also observed for conventional interband unidirectional ring lasers [76] and corroborated by the modelled result.

The ratio of CW to CCW mode at threshold is very close to unity, which signifies similar collection efficiency from the two sides. Below threshold the ratio is very noisy as a result of low light output.

The spectrum measured from the clockwise direction of the unidirectional ring laser is shown in figure 5.10. A single peak can be observed from the spectrum indicating single mode operation.

Compared to the spectra of the distributed feed back (DFB) made from the same QC material [14], the spectral width of the unidirectional ring laser is twice less. The spectral purity is a clear advantage of the unidirectional operation but the hope for improved efficiency has not yet been realised. Radiative losses at the Y-couplers must be compensated for to improve the efficiency of the device. This can be implemented by actively injecting current into the "S" crossover waveguide.

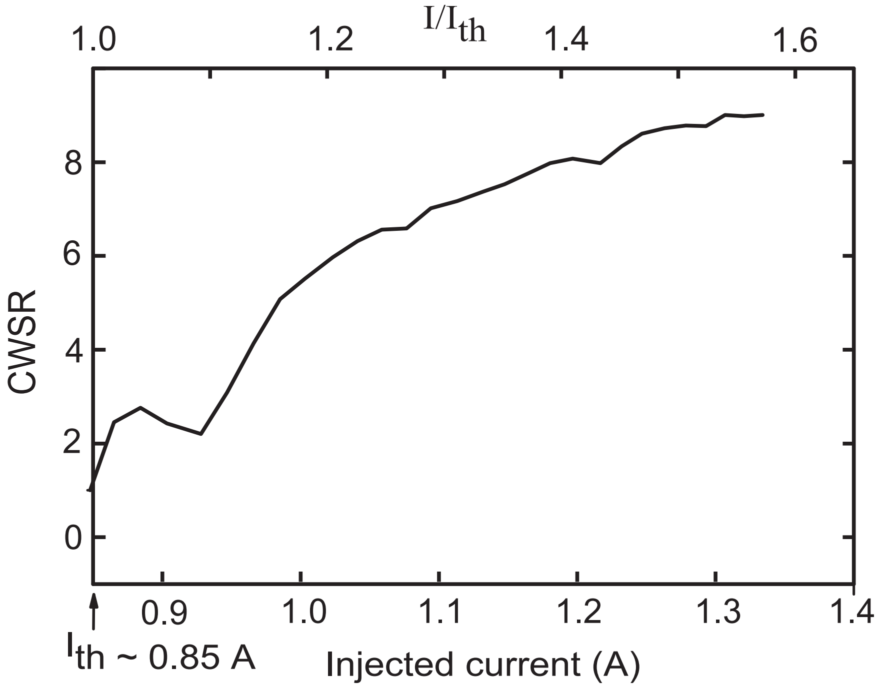

FIGURE 5.9: The plot of CWSR as a function of injection current, shown from laser threshold.

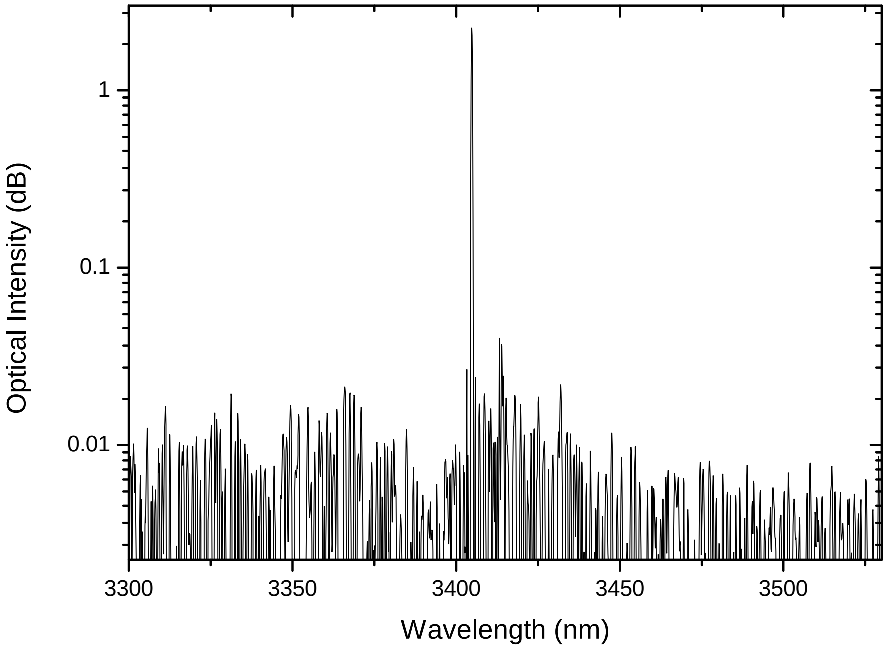

FIGURE 5.10: Acquired spectrum of the unidirectional quantum cascade ring laser at 1.2times the threshold current obtained at 80 K

Coupled photons passing through the cross-over waveguide are amplified prior to combining in the couplers. This improves the gain competition and hence the spectral purity and output power.

5.10 Conclusion

This is the first unidirectional quantum cascade laser reported [105] and showed single mode operation with about 90 % of the emitted light in the desired CW direction. The device performance can be improved by optimising the design reported here. This will have to include (1) optimising the junction connecting the straight and the curved part of the “S” crossover waveguide, (2) finding the optimum coupling coefficient between the ring cavity and the “S” crossover waveguide (3) providing gain to the cross-over waveguide.

Chapter 6

Coupled Rings Quantum Cascade Lasers

6.1 Chapter Introduction

In this chapter, we investigated a new approach to achieving tunable single mode quantum cascade lasers (QCLs). This technique which has been investigated and demonstrated in the communication wavelength (1.55 μm) by Choi *et al* [16], Segawa *et al* [17], Liu *et al* [18] is based on a coupled ring effect. Coupled ring lasers exhibit single mode operation and wide tuning range due to the Vernier effect [19]. Coupled ring quantum cascade lasers (CRQCLs) offer many advantages over distributed feed back (DFB)-QCLs: ultra wide wavelength tuning range [106–108], narrower band-width, low frequency chirp, lower fabrication tolerance and lower fabrication cost as these structures can be patterned with photolithography (in contrast to electron beam lithography (EBL) used for DFB).

6.1.1 Aims

The aim of the work described in this chapter was to design, fabricate and characterise single mode tunable quantum cascade ring lasers (QCRLs) with performances comparable to DFB-QCLs made from the same material system.

6.1.2 Objectives

The objective here was to achieve sidemode suppression ratio (SMSR) of at least 20 dB and tunability of at least 10 cm^{-1} from these devices.

6.2 Principle of coupled racetrack laser

6.2.1 Structure

Racetrack ring structure considered in this work, unlike regular circular rings, offers the advantage of controlling the amount of power coupled from one ring to the other by merely varying the coupler spacing or etch-depth (see section 3.5.1.1 for more details). Shown in figure 6.1, is a micrograph picture of one of the processed coupled ring lasers. It consists of two racetrack cavities (with slightly different dimensions) closely placed in a manner that light propagating in one couples to the other via the evanescent field coupler (EFC). Other components include the output power coupler (multimode interference (MMI)) and the output waveguides, tilted at an angle of 7^o to the waveguide normal to reduce backreflections [83].

Two coupling mechanisms were utilised in this work. The first mechanism is EFC (described in section 3.5.1.1) which controls the degree of coupling between the racetracks. This coupler is critical to the operation of these devices as detailed in section 6.3.

The second mechanism involves an MMI (see section 3.14) which controls the amount of light coupled out of the second racetrack per roundtrip. The coupling

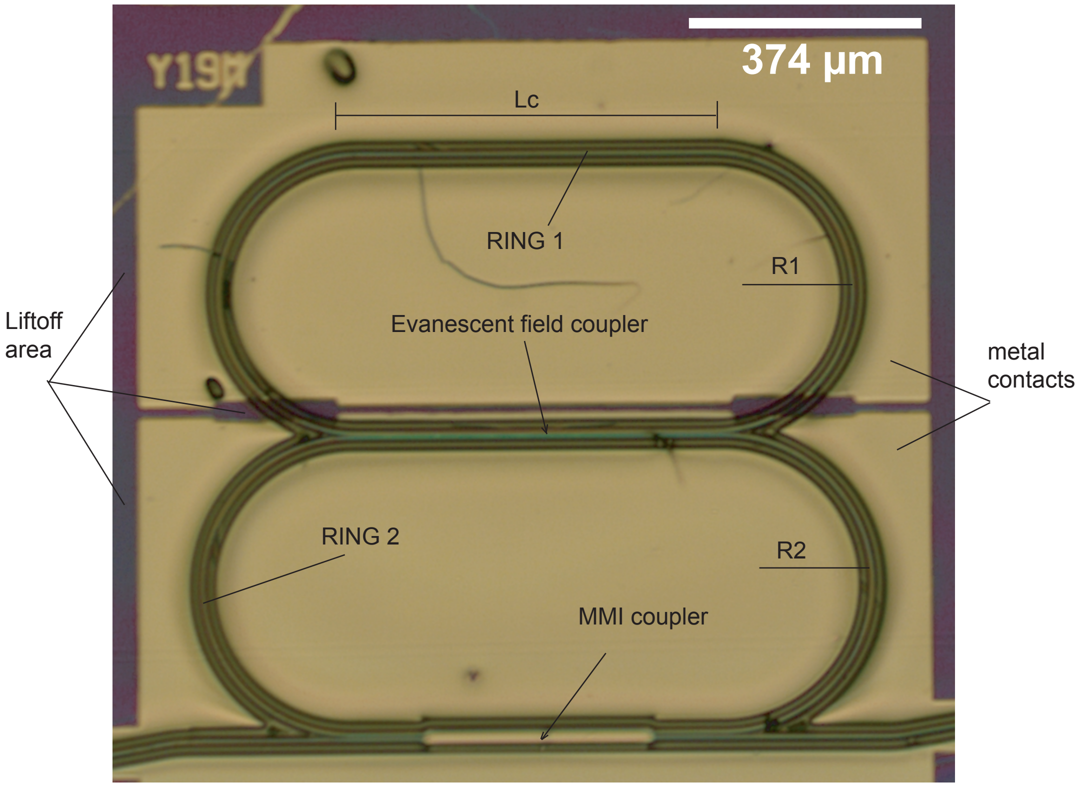

FIGURE 6.1: A micrograph showing one of the processed coupled-ring lasers

strength is not as critical as in inter-racetrack case, but sufficient light must be coupled out in order to characterise the devices.

6.2.2 Operation

Coupled ring lasers have the capabilities of operating in single mode (due to larger free spectral range (FSR) associated with the topology) with wider tuninability (due to Vernier tuning enhancement) compared to DFB lasers. Operation of these lasers can best be described using the illustration in figure 6.1. When the two rings (ring1 and ring2) are in isolation, the FSRs are independently determined by the effective length of the racetracks and group refractive index of the propagating modes in the semiconductor material, as expressed in equation 6.1

$$FSR = \frac{\lambda^2}{n_g L_{eff}} \tag{6.1}$$

TABLE 6.1: Design parameters for coupled ring laser with chip ID Y03MI

n_g	$R_1(\mu m)$	R_2 (μm)	Lc_1 (μm)	$Lc_2(\mu m)$	λ (μm)
3.3	226	241	300	592	3.46

and

$$L_{eff} = 2\pi R + 2L_c \tag{6.2}$$

where R is the radius of the bent part of the racetrack, n_g is the group index of the semiconductor material, L_c is the length of the coupler and λ is the free space wavelength.

Figure 6.2 shows the FSR in the slightly smaller racetrack (ring 1) and figure 6.3 shows the FSR in the slightly bigger racetrack (ring 2) calculated by substituting the design parameters given in table 6.1 into equations 6.1 and 6.2.

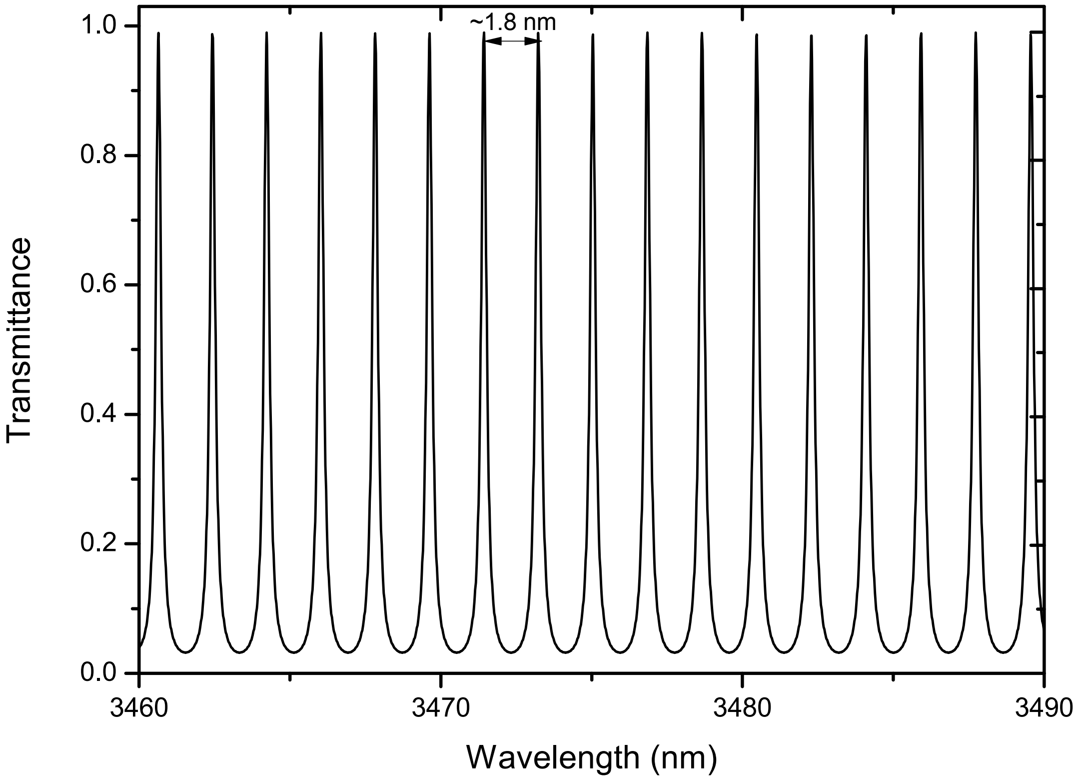

FIGURE 6.2: Calculated free spectral range of ring 1 using data given in table 6.1 in equations 6.1 and 6.2

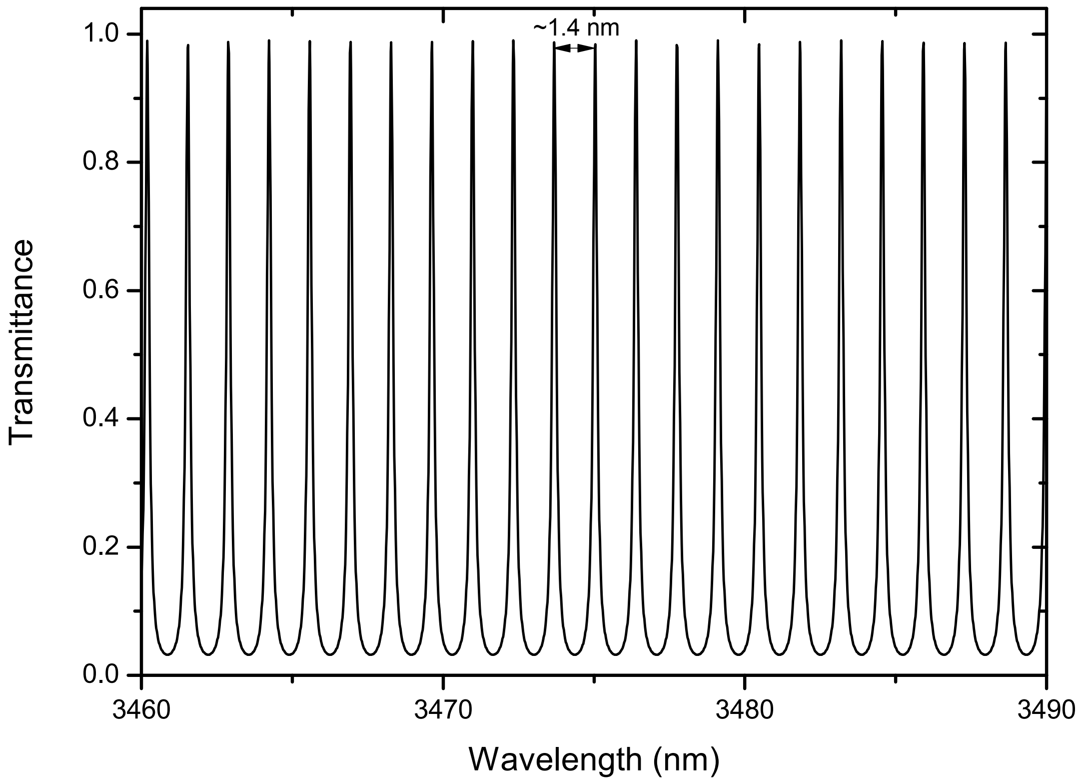

Figure 6.3: calculated free spectral range of ring 2 using data given in table 6.1 in equations 6.1 and 6.2

In the event of bringing the two racetracks into proximity, as is the case with coupled ring topology, the modes in the racetracks overlap (constructively and destructively) leading to a new regime of operation with wider free spectral range (FSR_c) as can be seen in figure 6.4, provided equation 6.3 is satisfied. The wider FSR observed is due to Vernier coupling effect between the rings. The FSR of the coupled rings with two different circumferences, FSR_c is expressed by,

$$FSR_c = M.FSR_1 = N.FSR_2 \tag{6.3}$$

where M and N are natural coprime numbers, FSR_1 and FSR_2 are FSR in racetracks 1 and 2 respectively.

One of several advantages of using a coupled ring topology is the possibility of achieving wider tuning range due to the Vernier tuning enhancement present.

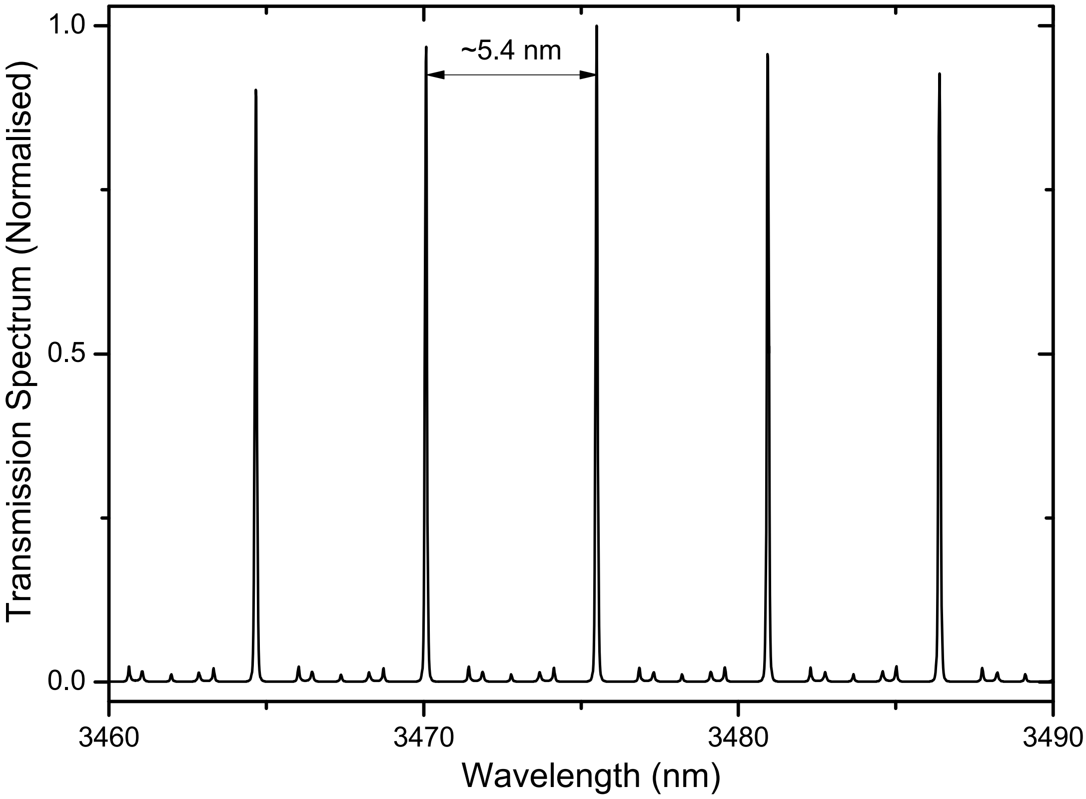

FIGURE 6.4: The coupled free spectral range calculated by superimposing FSR1 over FSR2. The design coprime numbers N and M are 3 and 4 respectively, meaning that every 3rd peak of FSR1 must overlap with every 4th peak of FSR2. The coupled free spectral range in this case is $\sim$ 5.4 nm = 3xFSR1 = 4xFSR2

The tuning enhancement factor is given by [109],

$$\Delta T = \frac{1}{1 - \frac{L_1}{L_2}} \tag{6.4}$$

where L_1 and L_2 are the cavity length of racetracks 1 and 2 respectively. The tuning range of a coupled ring is ΔT times the tuning range of a single ring.

6.2.2.1 Wavelength tuning

Wide tuning range is one of the greatest features of coupled rings. Just like every other semiconductor laser, wavelength tuning can be achieved by changing the material refractive index via, carrier injection into the tuning region (current tuning) or by varying the operating temperature of the device (thermal tuning). While tuning due to carrier injection is commonly preferred over electrothermal tuning, it is important to note that either of these methods are suitable to achieve tuning and have been successfully experimented on [110].

In this work, we opted for current tuning because the refractive index in the two rings can be separately tuned, unlike in thermal tuning where both rings are simultaneously tuned. To achieve this, we electrically isolated the two rings using liftoff technique as can be seen in figure 6.1.

Digital tuning of resonant wavelengths of the fabricated devices was achieved by injecting direct current (DC) into one of the rings (i.e the tuned ring) while driving the active ring with pulsed current. The pulsed current injected into the active ring is held constant and the DC current into ring2 is swept. At low DC current, blue-shifting (i.e shifting to the shorter wavelength) of the resonant wavelength of the cavity is observed but at higher injection current, red-shifting (i.e shifting to the longer wavelength) is observed due to current heating in the active region.

Depending on the ring tuned, two different tuning steps can be achieved according to the theoretical simulation result shown in figures 6.5 and 6.6. The theoretical tuning was achieved by varying the refractive index of one of the rings in equation 6.11. In the case of tuning ring 1 (see figure 6.5), the wavelength jump in steps of 1.4 nm which corresponds to the FSR of ring 2. Also from the figure, the refractive index change (Δn) required to achieve one complete tuning range (i.e the coupled ring FSR), is about 0.06.

On the other hand, tuning ring 2 (see figure 6.6) causes wavelength jump of about 1.8 nm which corresponds to the FSR of ring 1. The index change required to achieve a complete tuning range here is about 0.05 i.e 1.2 times less than 0.06 required in the case of tuning ring 1.

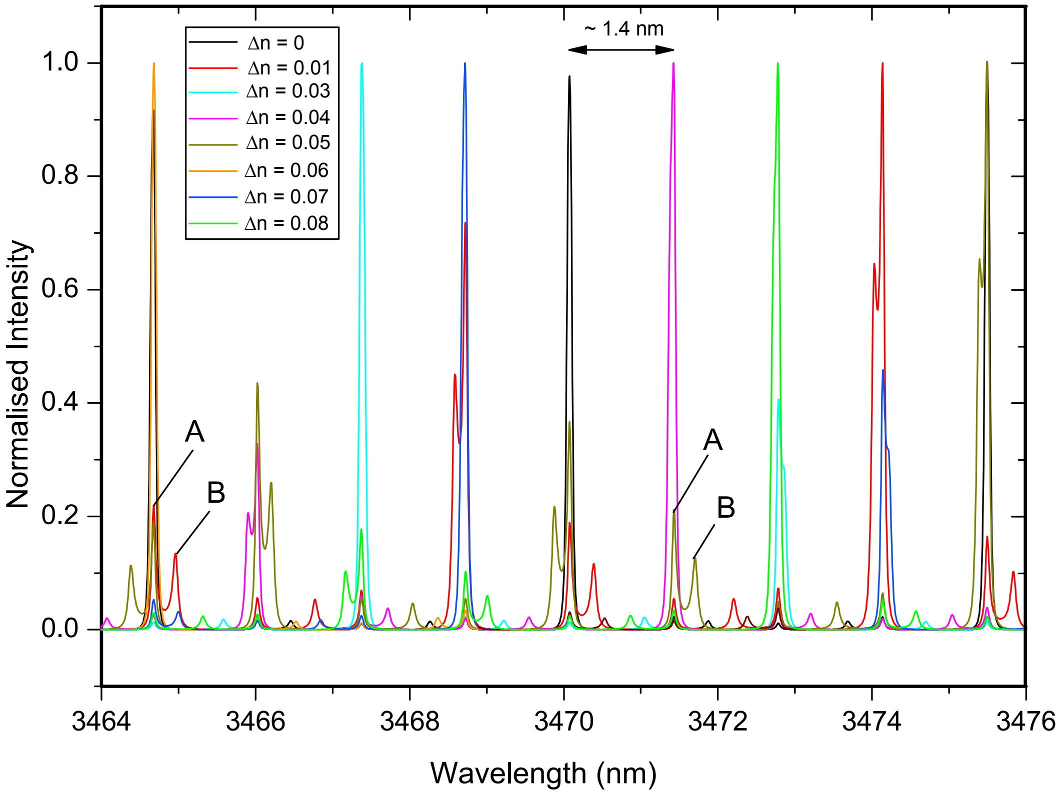

FIGURE 6.5: Theoretical tuning of the coupled ring (FSR1 = ∼ 1.8 nm and FSR2 = ∼ 1.4 nm) obtained by varying the refractive index of ring 1, in equation 6.11, from Δn = 0.01 to 0.08. A and B are the subpeaks shown in figure 6.8. Wavelength jump by 1.4 nm i.e FSR2 and the tuned peaks overlapped consistently with subpeak A

6.3 Coupled Ring Model

The theoretical characteristics of a coupled ring resonator and its mathematical model have been detailed in ref.[111] and summarised in this section. Shown in figure 6.7 is the schematic diagram used for modeling the devices.

To make the analysis less complicated, the coupled ring resonator was split into three sections by two broken lines. In the figure 6.7, the input and output lightwaves are labeled a_{ij} and b_{ij} respectively, where i = (the port number) and j = (section number); K1, K2 and K1 are amplitude coupling coefficients of couplers 1,2 and 3 respectively. R_1 and R_2 are the radii of rings 1 and 2. φ_1 and φ_1 are half the round trip phase delay in the rings respectively.

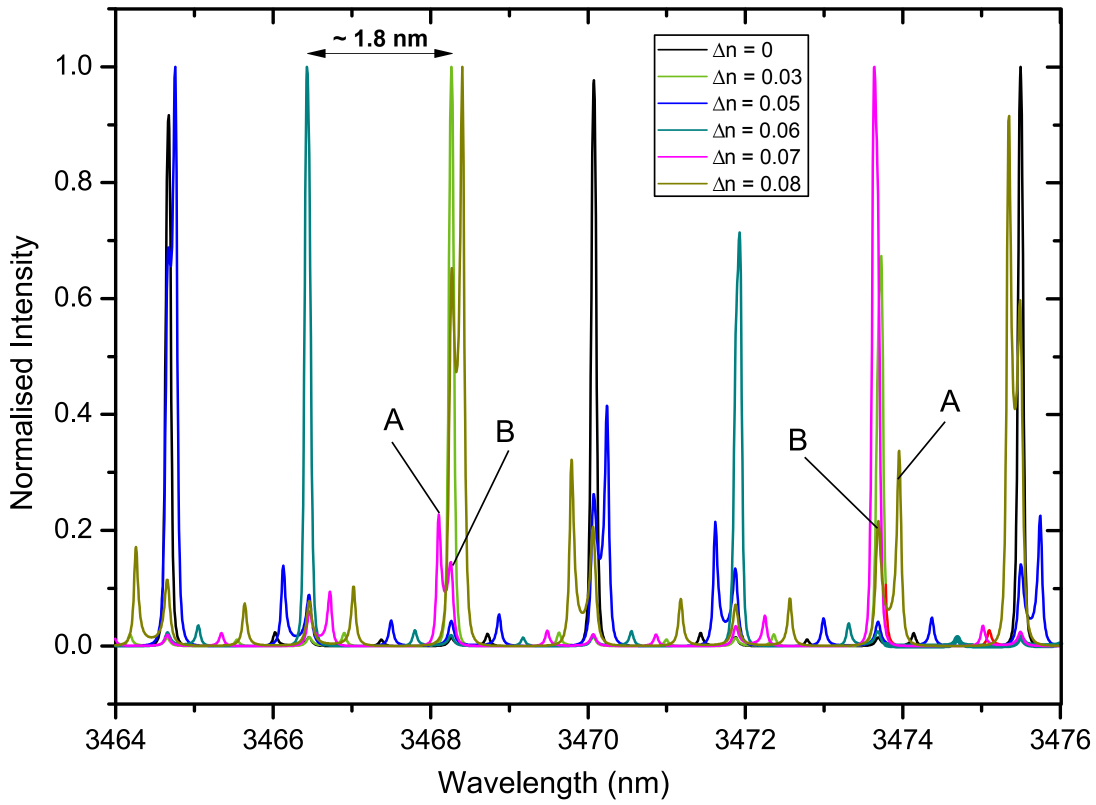

FIGURE 6.6: Theoretical tuning of the coupled ring (FSR1 = ∼ 1.8 nm and FSR2 = ∼ 1.4 nm) obtained by varying the refractive index of ring 2, in equation 6.11, from Δn = 0.01 to 0.08. A and B are the subpeaks shown in figure 6.8. Wavelength jump by 1.8 nm i.e FSR1 and the tuned peaks overlapped consistently with subpeak B

Assuming no coupling loss in the couplers and no facet reflections from the two access waveguides, then

$$a_{21} = a_{41} = a_{22} = a_{42} = a_{23} = a_{43} = b_{11} = b_{31} = b_{12} = b_{32} = b_{13} = b_{33} = 0 \quad (6.5)$$

Based on these assumptions, the transmission equations for the three sections are derived using **S** matrix. For section 1 the amplitudes of output lightwaves b_{21} and b_{41} can be derived as follows;

$$\begin{pmatrix} b_{11} \\ b_{21} \\ b_{31} \\ b_{41} \end{pmatrix} = [\mathbf{S}]_{K=K1} \cdot \begin{pmatrix} a_{11} \\ a_{21} \\ a_{31} \\ a_{41} \end{pmatrix} = [\mathbf{S}]_{K=K1} \cdot \begin{pmatrix} a_{11} \\ 0 \\ a_{31} \\ 0 \end{pmatrix} \quad (6.6)$$

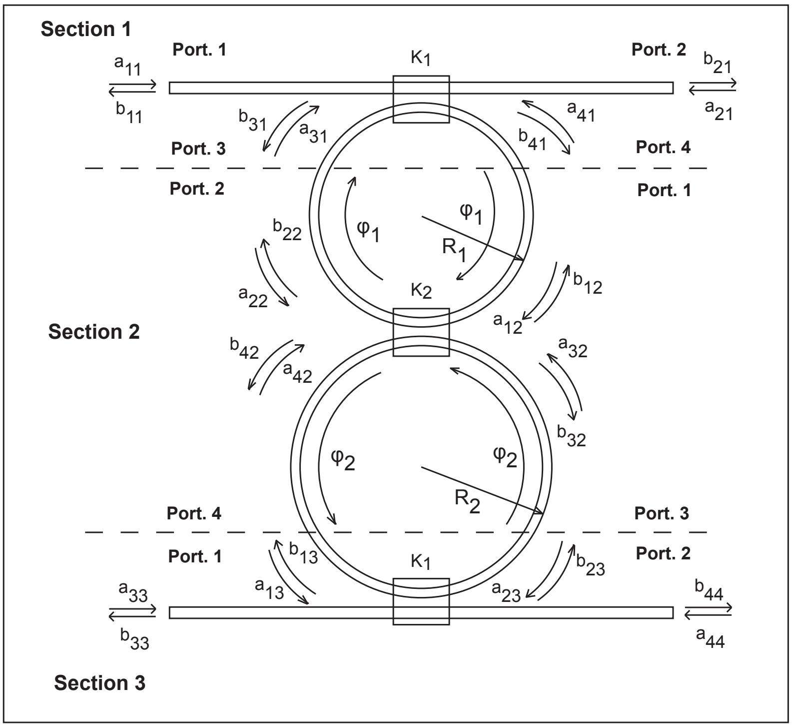

FIGURE 6.7: Schematic diagram of a double coupled ring laser [111]

where **S** is given as

$$[\mathbf{S}] = \begin{pmatrix} 0 & \sqrt{1-K^2} & 0 & -jK \\ \sqrt{1-K^2} & 0 & -jK & 0 \\ 0 & -jK & 0 & \sqrt{1-K^2} \\ -jK & 0 & \sqrt{1-K^2} & 0 \end{pmatrix} \tag{6.7}$$

The transmission equations for sections 2 and 3 are given in equations 6.8 and 6.9,

$$\begin{pmatrix} b_{12} \\ b_{22} \\ b_{32} \\ b_{42} \end{pmatrix} = [\mathbf{S}]_{K=K2}. \begin{pmatrix} a_{12} \\ a_{22} \\ a_{32} \\ a_{42} \end{pmatrix} = [\mathbf{S}]_{K=K2}. \begin{pmatrix} b_{41}e^{-j\varphi_1} \\ 0 \\ b_{23}e^{-j\varphi_2} \\ 0 \end{pmatrix} \tag{6.8}$$

$$\begin{pmatrix} b_{13} \\ b_{23} \\ b_{33} \\ b_{43} \end{pmatrix} = [\mathbf{S}]_{K=K1}. \begin{pmatrix} a_{13} \\ a_{23} \\ a_{33} \\ a_{43} \end{pmatrix} = [\mathbf{S}]_{K=K1}. \begin{pmatrix} b_{42}e^{-j\varphi_2} \\ 0 \\ 0 \\ 0 \end{pmatrix} \tag{6.9}$$

where φ_i is half the round trip phase delay of a ring resonator with radius r$_i$. The expression for the phase delay is given in equation 6.10; β is the propagation constant in the ring waveguides and α, the propagation loss.

$$\varphi_i = (\beta - j\alpha).\pi r_i \qquad (i = 1, 2) \tag{6.10}$$

Using equations 6.6-6.10, the transmission equation from the input port (port.1 of section 1) to the drop port (port.4 of section 3) can be derived as

$$\left|\frac{b_{43}}{a_{11}}\right|^2 = \left|\frac{jK_1^2K_2e^{-j(\varphi_1+\varphi_2)}}{1-\sqrt{(1-K_1^2)(1-K_2^2)}(e^{-j2\varphi_1+e^{-j2\varphi_2}})+(1-K_1^2)e^{-j2(\varphi_1+\varphi_2)}}\right|^2 \tag{6.11}$$

at the same time the transmission equation of the coupled ring laser from input port (port.1 of section 1) to the through port (port.2 of section 1) is given as

$$\left|\frac{b_{21}}{a_{11}}\right|^2 = \left|\frac{1}{\sqrt{1-K_1^2}}\left[1-\frac{K_1^2 1-\sqrt{(1-K_1^2)(1-K_2^2)}e^{-j(\varphi_1+\varphi_2)}}{1-\sqrt{(1-K_1^2)(1-K_2^2)}(e^{-j2\varphi_1+e^{-j2\varphi_2}})+(1-K_1^2)e^{-j2(\varphi_1+\varphi_2)}}\right]\right|^2 \tag{6.12}$$

In this work, the through port access waveguide was removed from the final design (see figure 6.1) because the rings are active (i.e photons are internally generated in the rings). Based on this, equation 6.12 becomes zero i.e no transmittance at the through port. Using equation 6.11 in MATLAB, the transmittance characteristics of coupled ring (chip ID Y03MI) including the effect of propagation loss was simulated at various inter-ring coupling coefficient (K$_2$) with output coupling coefficient (K$_1$) = 0.5. The simulation result is plotted in figure 6.8. From this plot we deduced that the coupled free spectral range (FSR_c) is equal to ∼5.4 nm thus corresponds to the value calculated using equation 6.3. Two observations are made from the plot. The first is that the major transmission peaks are split into two sub-peaks (A and B) and the second observation is on the variation of the FSR with increasing K_2, to the extent of being 1/6 of the initial value at $K_2 =$ 1.0.

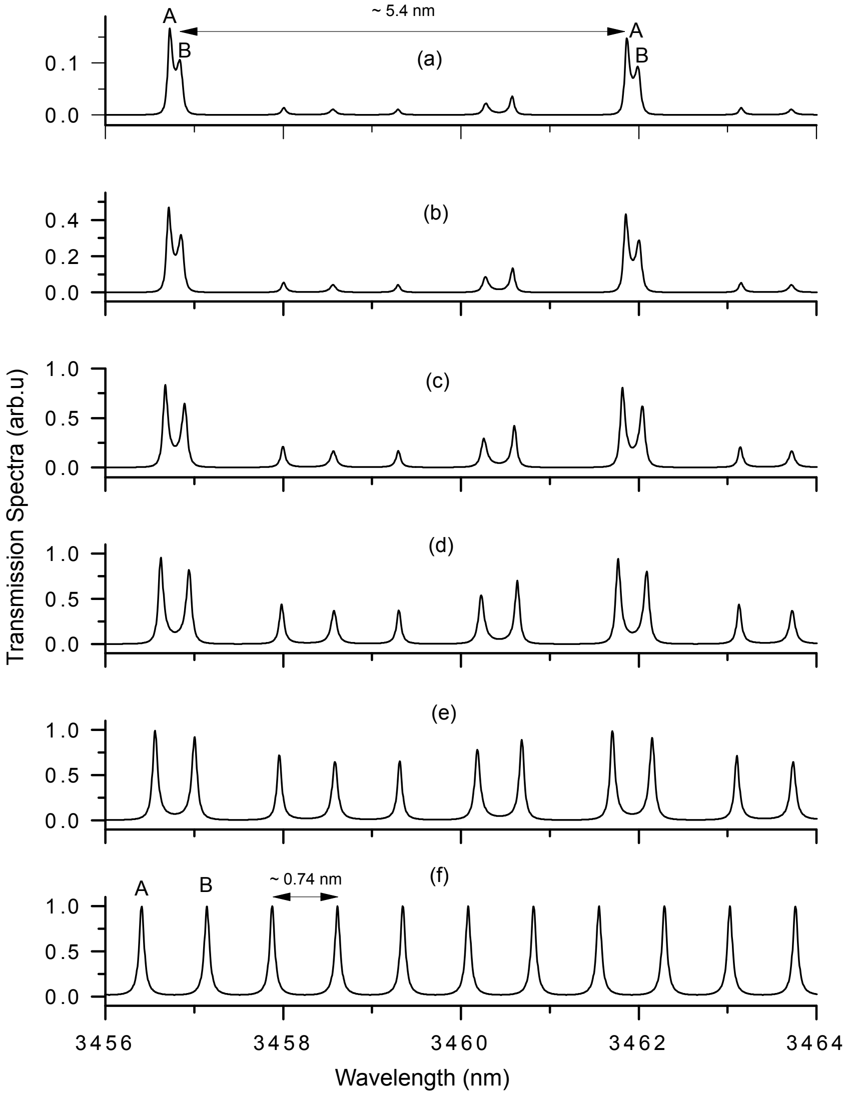

FIGURE 6.8: Simulated transmission spectrum of coupled rings (Chip ID Y03MI) at coupling coefficients (a) k2 = 0.1, (b) k2 = 0.2, (c) k2 = 0.4, (d) k2 = 0.6, (e) k2 = 0.8, (f) k2 = 1.0. FSR1 = ∼ 1.8 nm and FSR2 = ∼ 1.4 nm, N=3 and M=4

To understand the splitting (coupling) behaviour observed in figure 6.8, we simulated the transmission characteristics of two identical rings coupled together (i.e FSR1 = FSR2 = 1.8 nm). The result shown in figure 6.9 indicates that the number of subpeaks is determined by the number of coupled rings. Also the intensity of the subpeaks, unlike in figure 6.8, are the same due the uniformity of the coupled rings. The change in operating FSR due to increasing inter-ring coupling strength, for the coupled identical rings shown in figure 6.10, indicates a combination of linear and exponential relationship. Also shown in the figure, is a 3rd order polyfit of the simulated data with the fit equation given as

$$\Delta FSR = B_0 + B_1K2^1 + B_2K2^2 + B_3K2^3 \tag{6.13}$$

where B_0, B_1, B_2 and B_3 are -9.65, 103.18, -163.26 and 118.81 respectively.

To further understand the relationship between the sub-peaks, which is imperative in understanding the behaviour of coupled ring lasers, we theoretically tuned the refractive index of the rings in the simulation program. In the case of tuning ring 1 (see figure 6.5) the tuned peaks jump by 1.4 nm i.e the FSR of ring2 and the tuning overlapped consistently with sub-peak A. On the other hand, tuning ring 2 causes wavelength jump of about 1.8 nm i.e the FSR of ring1 and the wavelength jump consistently overlapped with sub-peak B (see figure 6.6). From the two figures we conclude that subpeak A is associated with ring 2 and sub-peak B to ring 1.

Based on the coupled ring simulations, most of the devices reported here were designed with very low interring coupling coefficients to avoid over coupling the rings.

6.4 Design

In coupled ring lasers, the maximum tuning range is limited by the available gain bandwidth in the material and maximum index change attainable [108]. To obtain the gain bandwidth of the quantum cascade (QC) material used in this thesis,

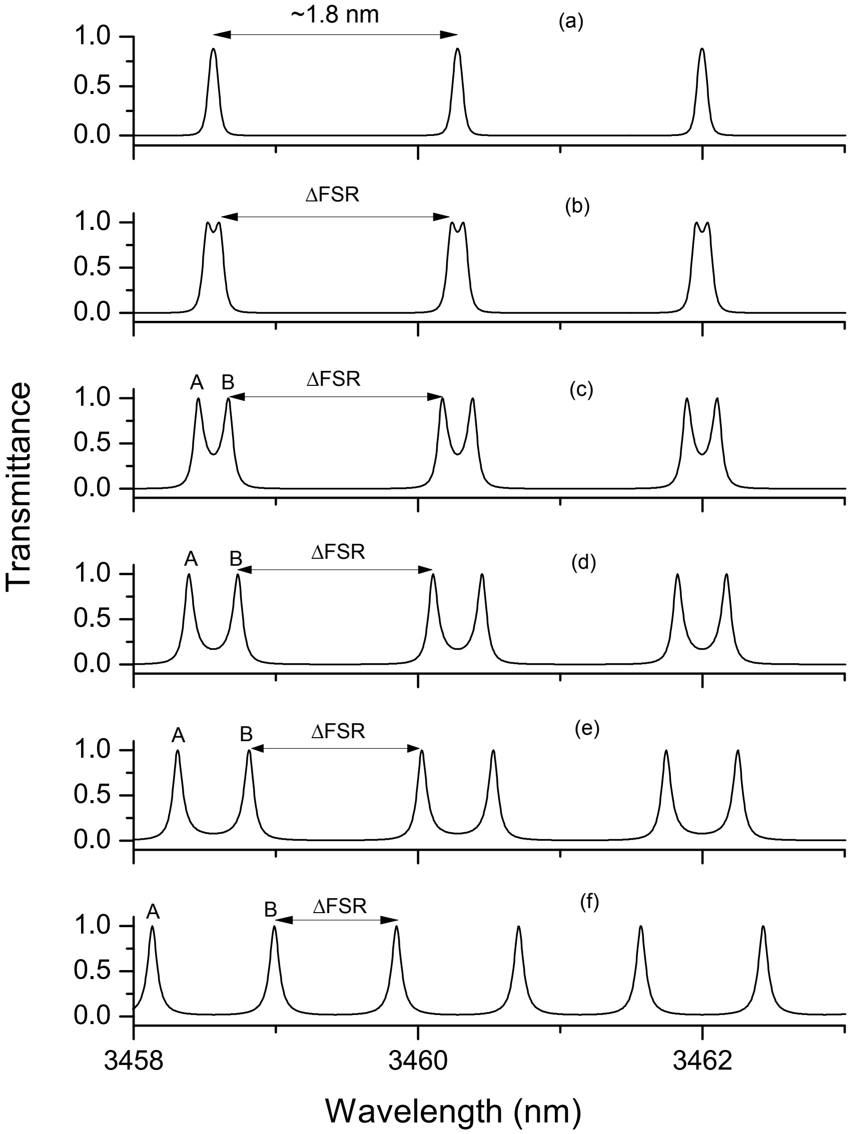

FIGURE 6.9: Transmission spectrum of coupled uniform rings (i.e Ring = Ring 2) at coupling coefficients (a) k2 = 0.1, (b) k2 = 0.2, (c) k2 = 0.4, (d) k2 = 0.6, (e) k2 = 0.8, (f) k2 = 1.0. FSR1 = FSR2 = 1.8 nm

we processed some Fabry Perot (FP) lasers from the material. These lasers were mounted onto the cold finger of the cryostat and driven below threshold with 90 ns pulses at 5 kHz repetition rate at 200 K. Using fourier transform infrared (FTIR) in step-scan mode, with lock-in detection technique, the amplified spontaneous emission (ASE) spectra shown in figure 6.11 was acquired. For the detailed spectra measurement setup and technique, the reader is referred to section 5.8. The measured gain bandwidth at full width at half maximum (FWHM) is $\sim$ 400 nm.

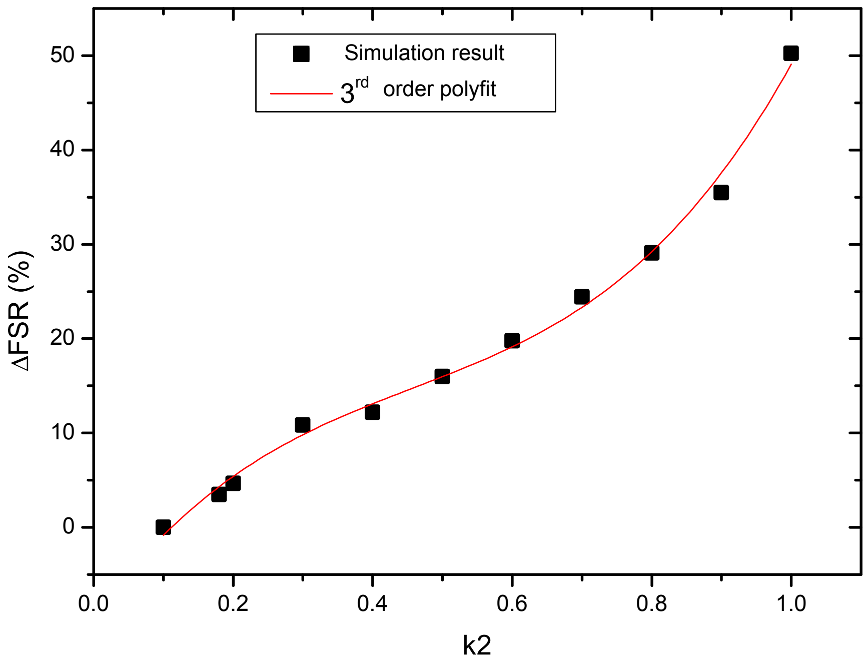

FIGURE 6.10: Simulation data plot of change in FSR of identical coupled rings as a function of inter-ring coupling coefficient (k2)

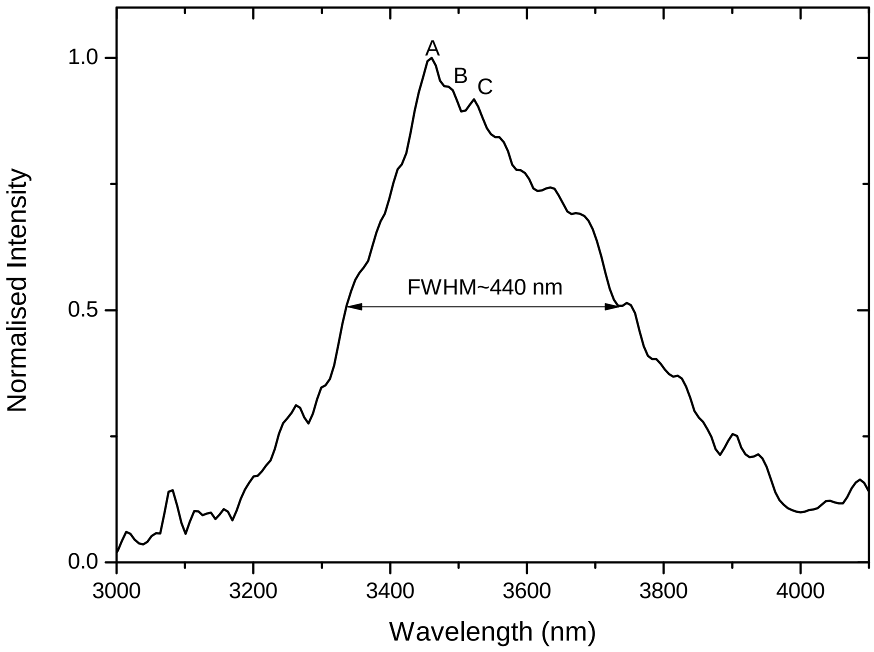

FIGURE 6.11: Amplified spontaneous emission spectrum from a FP processed from quantum cascade material used in this research. Measurement was taken at 200 K with FTIR resolution of 4 nm, using step-scan lock-in detection technique

Multiple peaks (A at 3460 nm, B at 3491 nm and C at 3522 nm) can be observed in the gain (i.e ASE) spectrum shown in figure 6.11 instead of single central peak (e.g A at 3460 nm). The implication of using materials with multiple gain peaks for coupled ring lasers are;

- single mode selection is frustrated
- Continuous wavelength tuning is not attainable

In figure 6.12, we compared the ASE acquired from coupled ring laser with chip ID M15DC (see table 6.2) to that from an FP shown above. The two spectra were individually normalised to enable comparison. The spectrum of the coupled ring shows Vennier effect coupling with FSR of ∼ 22 nm i.e 15 x 1.5 nm (see device M15DC in table table 6.2). Apart from the filter characteristics introduced by the rings, the peaks also coincides with the three peaks (A, B and C) of the FP. This further confirms that the QC material utilised in this work is not ideal for this research. But being the only material available at the time of my research we made do with it.

6.4.1 Designed Chips

This section details all the design parameters for every device covered in this chapter. These parameters and the chip ID are given in table 6.2

The devices were processed using the steps discussed in chapter 5. An scanning electron microscope (SEM) of a wirebonded coupled ring laser is shown in figure 6.13.

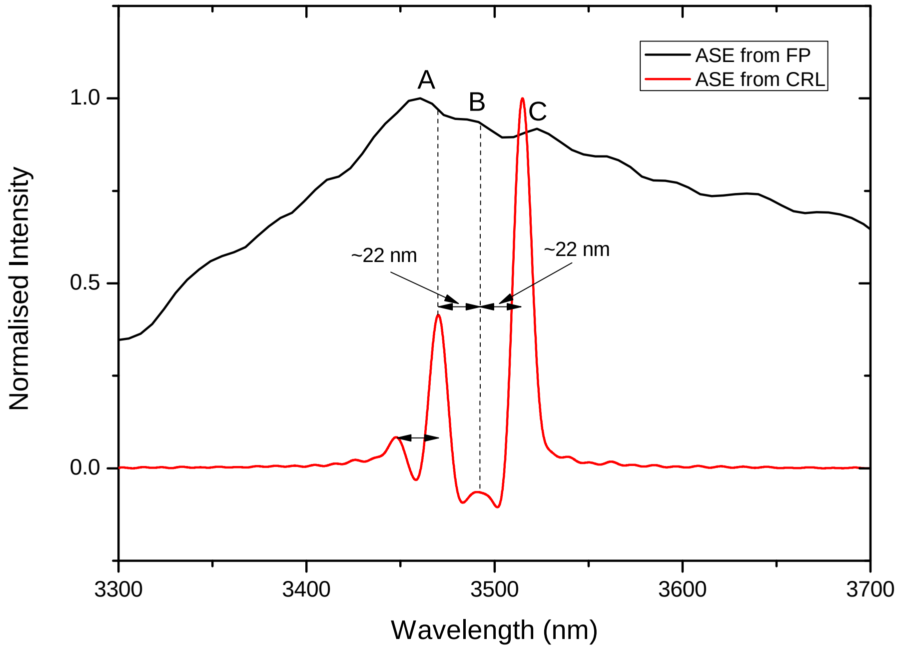

FIGURE 6.12: Comparison between ASE from a FP and ASE from coupled ring laser (M15DC). The spectra were individually normalised and both measured with the same FTIR resolution (4 nm), using step-scan lock-in detection technique

TABLE 6.2: Design parameters for devices reported in this chapter

Chip ID	Y03MI	Y06DC	M9DC	M05MI	Y15DC	Y19MI
R_1 (μm)	226	230	204	216	223	228
R_2 (μm)	241	241	211	254	241	241
Lc_1 (μm)	300	433	550	528	564	565
Lc_2 (μm)	592	592	600	500	592	592
K_1 (%)	50	50	50	50	50	50
K_2 (%)	5	12	16	1.0	3	18
Inter-ring Coupler	EFC	EFC	EFC	EFC	EFC	EFC
Output Coupler	MMI	EFC	EFC	MMI	EFC	MMI
n_g	3.3	3.3	3.3	3.3	3.3	3.3
FSR_{R1} (nm)	~1.8	~1.6	~1.5	1.5	~1.44	1.4
FSR_{R2} (nm)	~1.4	~1.4	1.4	1.4	~1.36	1.35
FSR_c (nm)	~5.4	~10	~13	~8	~22.0	27
M	3	6	9	5	15	19
N	4	7	10	6	16	20

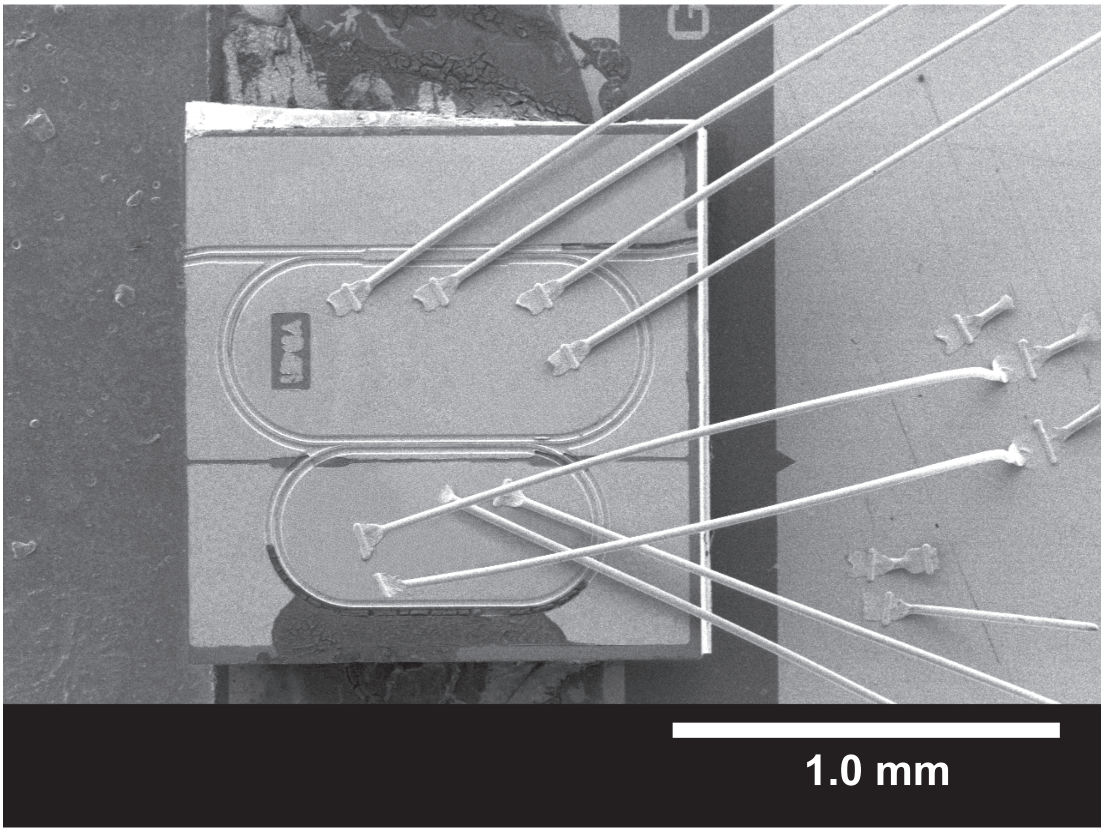

Figure 6.13: An SEM image of one of the processed coupled ring laser)

6.5 Characterisation

6.5.1 Measurement Challenges

Most devices were shorted after being operated at temperatures less than 100 K. Although the devices can operate at room temperature, we did not have the right power sources to operate at or near this temperature. The power sources available and discussed in section 5.8.1 could barely drive some of the devices to threshold. To attain at least twice the threshold currents, we operated the devices at low temperatures. But after driving these devices at low temperatures, most of them became short-circuited. On the contrary, the devices that were never operated at low temperatures were not shorted.

We believe that the planarisation layer (HSQ) which cracked (see figure 4.10) in the 180 ^{o}C oven during curing, exhibited non uniform contraction (at low temperature) and relaxation (at ∼ room temperature), thereby creating channels for current leakage and hence short-circuiting.

6.5.2 Results

The devices reported in this section were characterised using the technique described in sections 5.8.2 and 5.8.3. All the devices were characterised with 90 ns pulses at 5 kHz repetition rate (except where the ring is tuned). Also all measurements, except where stated otherwise, were carried out at 200 K. In this work, I_{R1} and I_{R2} signifies current injected into ring1 and ring2 respectively. Ring1 and Ring2 in the coupled ring configuration are identified in figure 6.1.

6.5.2.1 Device M05MI

The emission spectrum of this device acquired at I_{R1} =0 and $I_{R2} = 3.2\text{x}I_{R1th}$ (where I_{R1th} = 250 mA) is shown in figure 6.14. There appears a single mode peak with SMSR∼22 dB at wavelength = 3530 nm (i.e point C). The distance between points A-B, B-C, C-D and D-E equal the designed coupled ring FSR i.e $FSR_c \sim 8.0$ nm

Ring1 could not be activated because it was electrically shorted. Optically, the ring was alright as the measured FSR equals the calculated FSR_c for this device (see table 6.2). The measurement of this chip was inconclusive as we could not optically tune Ring1, by current injection.

6.5.2.2 Device Y19MI

Shown in figure 6.15, is the acquired emission spectrum for this device, at I_{R1} = 0 and $I_{R2} = 2.6\text{x}I_{th}$, where I_{th} = 300 mA. Three peaks (A, B and C) at 3448 nm (SMSR∼ 10 dB), 3475 nm (SMSR∼ 15 dB) and 3502 nm (SMSR∼ 15 dB) respectively, are observed. The distance A-B = B-C = 27 nm which corresponds to the designed coupled ring FSR i.e $FSR_c \sim 27.0$ nm (see table 6.2).

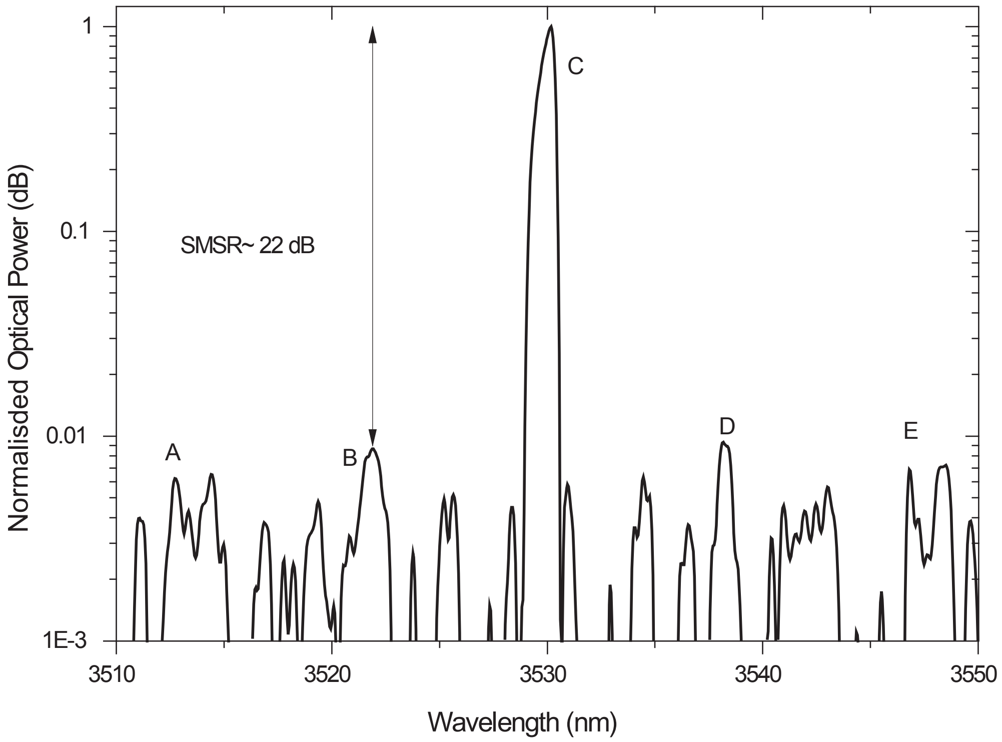

FIGURE 6.14: Emission spectrum of the Y05MI CRQCL acquired at $I_{R1} = 0$ and $I_{R2} = 3.2xI_{R2th}$, where $I_{R2th} = 250$ mA. The distance between points A-B, B-C, C-D and D-E equal the designed coupled ring FSR i.e $FSR_c \sim 8.0$ nm

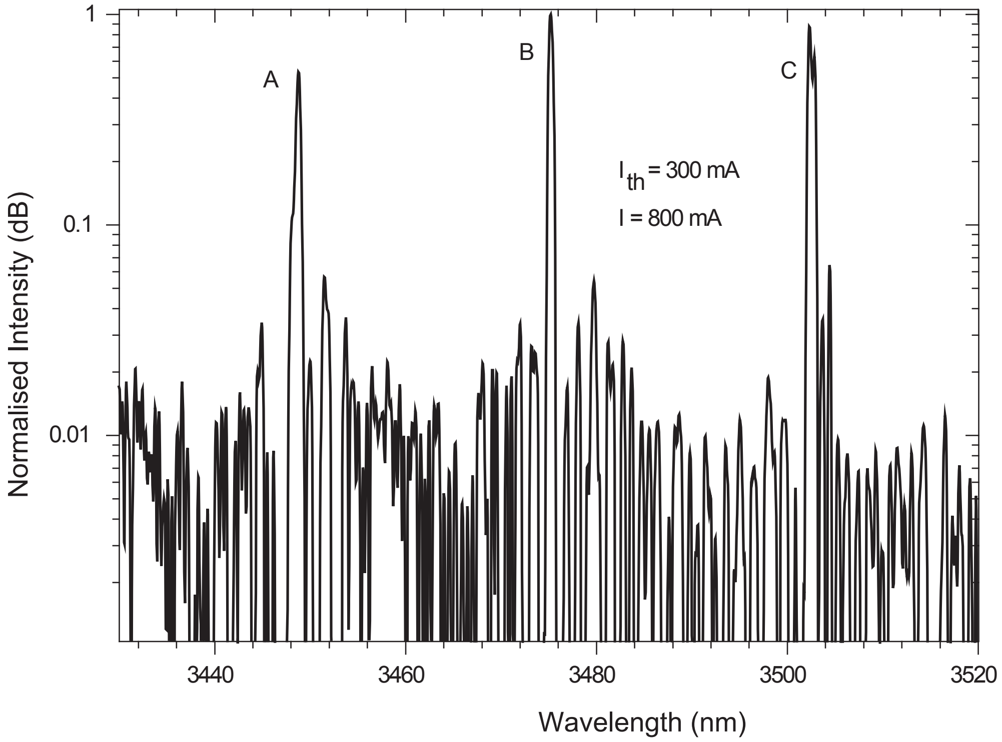

FIGURE 6.15: Emission spectrum of the Y019MI CRQCL measured at $I_{R1} = 0$ and $I_{R2} = 2.6xI_{th}$, where $I_{th} = 300$ mA. The distance A-B = B-C = 27 nm and corresponds to the designed FSR_c (see table 6.2)

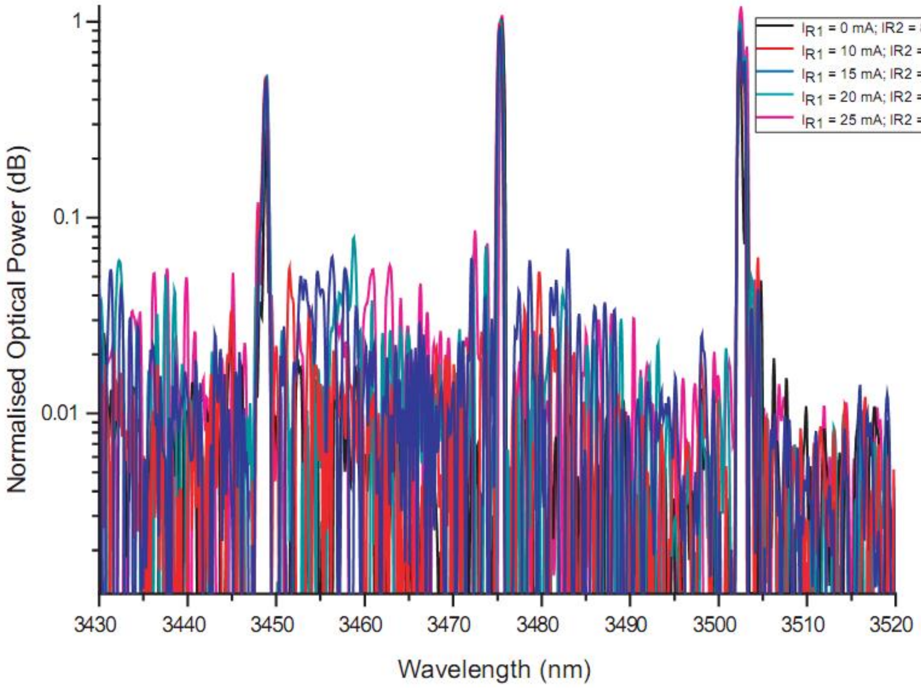

FIGURE 6.16: Acquired emission spectra for Y019MI CRQCL at $I_{R2} = 2.6xI_{th}$, where $I_{th} = 300$ mA. Refractive index of ring1 was tuned by injecting DC current in the range of 0-25 mA. No tuning was observed

Two methods of tuning were attempted here. The first involved injecting DC current into ring1 while actively pumping ring2 and the second is vice versa. Shown in figure 6.16 is the spectra measured when ring1 was tuned. 800 mA pulsed current was constantly injected into ring2 while DC current injected into ring1 was varied from 0-25 mA. No wavelength tuning was observed as the peaks remain unshifted with increasing injection current into ring2.

In the second method, we constantly injected 400 mA ($I_{th} = 100$ mA) pulsed current into ring1 while varying the DC current injected into ring2 from 0-35 mA. The acquired spectra is shown in figure 6.17 and wavelength tuning was observed.

The calculated rate of change of wavelength with current, $d\lambda/dI = 0.4$ nm/mA. This value is in good agreement with other reported values for QCLs emitting around this wavelength [28].

The spectra is very noisy because the power output from the device was very low, even when ring1 was operated at 4 times the threshold current of the ring. We

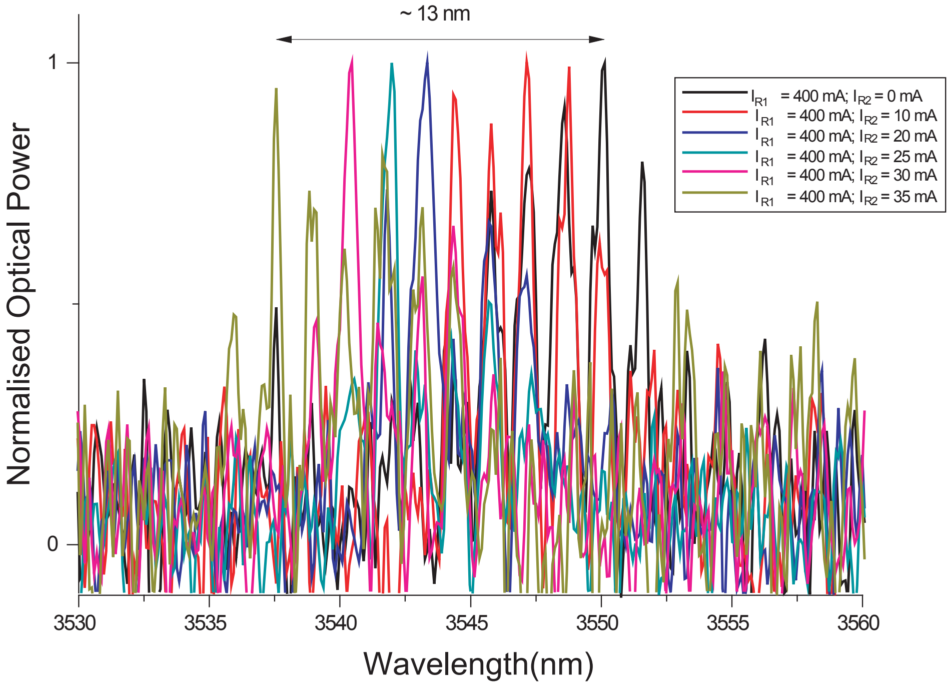

FIGURE 6.17: Acquired emission spectra for Y019MI CRQCL at $I_{R2} = 4xI_{th}$, where $I_{th} = 100$ mA. Refractive index of ring2 was varied by injecting DC current in the range of 0-35 mA into the ring. Wavelength tuning $\sim$ 13 nm can be observed (from 3550-3537 nm)

believe that the low inter-ring coupling adopted in this work in order to avoid over-coupling of the rings was responsible for the low output power.

The emission wavelength was continuously tuned from 3550 nm to 3537 nm (i.e blue shifting) by injecting between 0-35 mA of DC current into ring2.

To deduce the refractive index change as a result of the injected currents, we simulated the transmittance of the coupled ring (using equation 6.11) at emission wavelength = 3550 nm (i.e wavelength at which I_{R2}=0) and n_g =3.4. Subsequently the n_g in ring2 was varied at steps of Δn_g = 0.0001 which continuously tuned the wavelength till 3537 nm. By comparing the two results as shown in figure 6.18, the index change as a result of current injection can be deduced. From this, the total index change required to tune this device from 3550 - 3537 nm (i.e 13 nm) is $\sim$0.017%

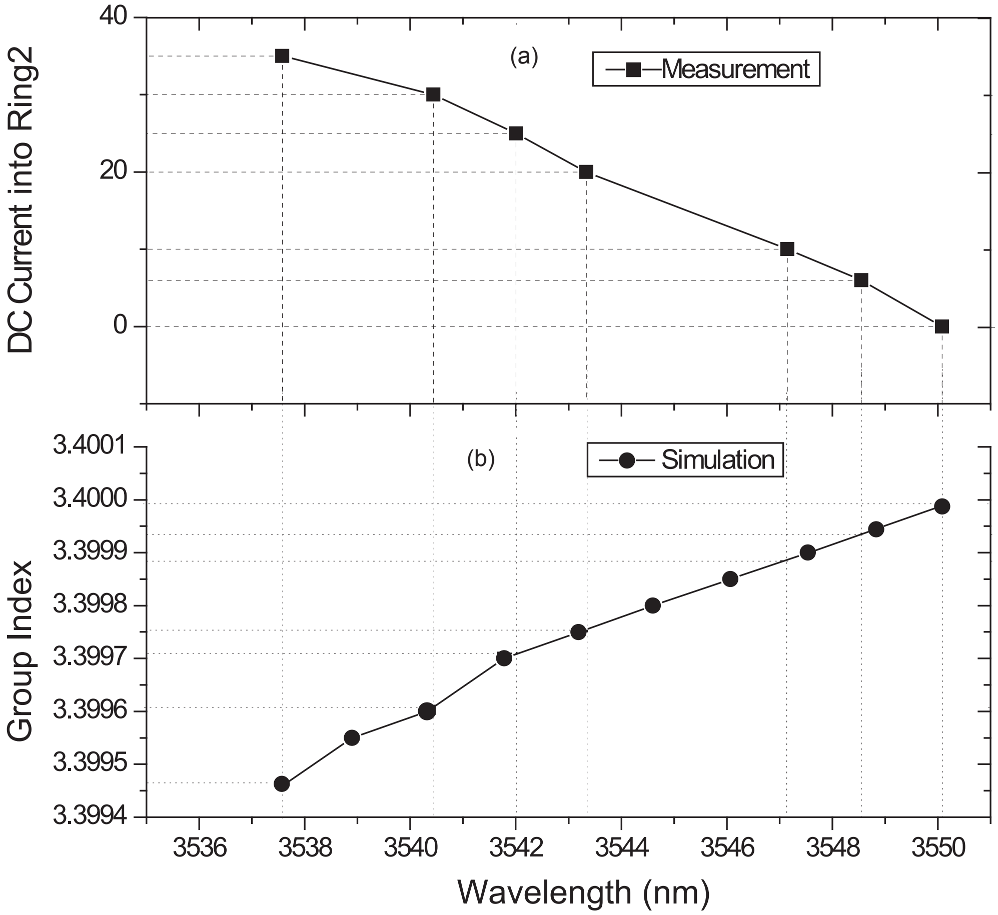

Figure 6.18: (a) plot of measured wavelength versus DC current into ring2 for device Y19MI, (b) Simulation plot of wavelength versus group index for device Y19MI, calculated using equation 6.11

6.5.2.3 Device Y06DC

Shown in figure 6.19 are the spectra acquired from device Y06DC. The red line indicates spectrum measured at I_{R1} = 100 mA and I_{R2}=0 mA. On the other hand, the black line indicates the spectrum acquired at I_{R1}=0 mA and I_{R2} = 300 mA. Both spectra showed evidence of coupled ring behaviour. The distance A-B = B-C = D-E = E-F = ∼10 nm, corresponds to the designed FSR_c (see table 6.2)

The Y06DC device, just like the M05MI device reported in section 6.5.2.1 could not be tuned by current injection. Possible reason: lower inter-ring coupling than the designed values. There was no material to investigate this so we leave it as a future work

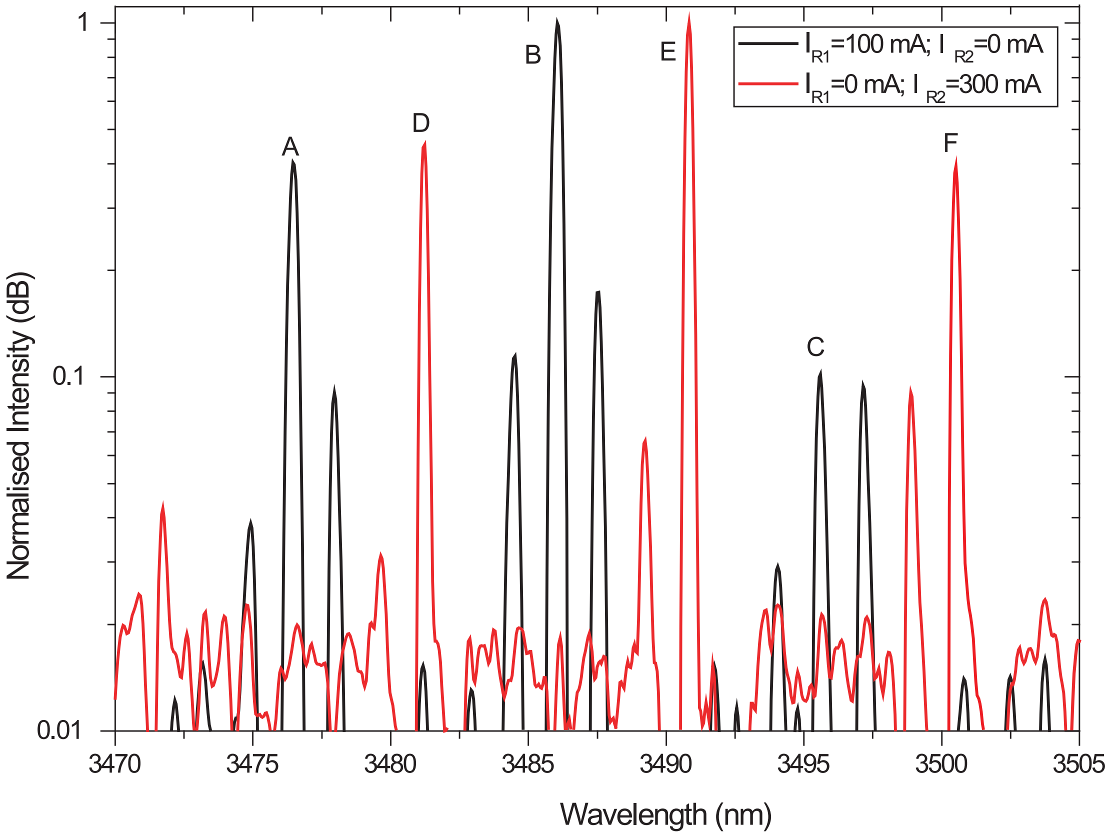

FIGURE 6.19: Emission spectrum of the Y06DC CRQCL acquired at $I_{R1} = 100$ mA and $I_{R2} = 0$ (black line); $I_{R1} = 0$ mA and $I_{R2} = 300$ mA (red line). The distance between points A-B, B-C, D-E and E-F equal the designed coupled ring FSR i.e $FSR_c \sim 10.0$ nm

6.6 Conclusion

The devices reported in this chapter are to the best of my knowledge, (1) the first coupled ring quantum cascade lasers operating in the hydrocarbon absorption region (i.e 3-4 μm), (2) the first ring lasers reported on this new strain compensated $AlAs_{0.56}Sb_{0.44}/In_{0.53}Ga_{0.47}As$ /InP material system.

The coupled rings reported here demonstrated clear evidence of Vernier coupling effect. Single mode operation was also demonstrated by one of the devices (M05MI) while continuous wavelength tuning was observed from device Y19MI from 3550 - 3537 nm. Interestingly, the measured wavelength tuning step corresponds to the tuning step predicted by the coupled ring model described in section 6.3. However, the tuning range (13 nm) is only half of the expected tuning range

(27 nm). The limitation is due to current heating in the active region at I_{R2} greater than 35 mA.

These devices were the first batch to be processed so there is plenty of chance of being optimised. Areas to optimise include finding the optimum inter-ring coupling coefficient between the two rings and replacing the evanescent field couplers (used for inter-ring coupling) with multimode interference couplers which are less sensitive to etch depth variation.

Given enough material and time we would make better coupled ring devices that would, compete with DFBs made from the same quantum cascade materials.

Chapter 7

SuperTune

7.1 Introduction

Portable and field deployable chemical and biological agent detection systems based on optical detection methods need compact, robust, widely tunable mid-infrared region (MIR) light sources. Current commercial systems use complex external cavity lasers schemes [112, 113], arrays of quantum cascade lasers (QCLs) [114, 115], or bulky optical parametric oscillator (OPO) sources [116, 117]. The system proposed here is a vastly mechanically simpler, cheaper and compact semiconductor MIR source especially suitable for use in high sensitivity Photoacoustic spectroscopy systems.

The proposed device has a highly tunable output wavelength ($\lambda \sim 5 - 13\mu$m) that would enable detection of many molecules of interest in, gas sensing, environmental monitoring, defence and home security applications, as shown in figure 1.1. The SuperTune device is a highly tunable MIR semiconductor emitter, based on intersubband transitions in a semiconductor superlattice (SSL) -thus SuperTune. In this research work, we propose a development of preliminary SuperTune work by Rizzi *et al* [118] to produce devices suitable as sources for spectroscopy and gas sensing.

In a periodic SSL consisting of closely coupled quantum wells, the application of electric field in the growth direction causes the localisation of electronic states to the quantum wells. These localised intersubband states form a so-called Wannier-Stark ladder (WSL) with regularly spaced energy levels. Varying the applied electric field changes the spacing of the energy steps in the WSL (see figure 7.9). It is this feature that gives the voltage tunable electroluminescence observed in Ref. [118]. Though this has been observed before, they showed that by using a three terminal device, the interdependence of injected current and the applied field in the active SSL region can be avoided, thus making it possible to obtain a widely tunable ($\lambda \sim 5 - 13\mu$m) emission by varying the reverse bias on the base-collector junction from 7-14 V.

The device was an $n - p - i - n$ heterostructure bipolar transistor (HBT) in which the SSL active region is inserted into the intrinsic region between the base and the collector regions. The key challenges in the idea proposed here is to overcome the present limitation of lower power emission (a few nW) low temperature operation ($\sim 20K$). Large gains in performance can be obtained by simply changing the physical layout of the device. The device reported in [118] were circular mesas, but by using a ridge waveguide with edge emission, then increased power can be obtained. The edge emitting ridge waveguide layout will give a considerable increased volume of active material and thereby increased optical output power. In this research work, we have redesigned the wafer to include, waveguide layers for optical confinement, by replacing the lower-bandgap, GaAs collector in table 7.1 with a wider gap material (AlGaAs), as shown in tables 7.2 and 7.3, thus introducing index difference between the undoped GaAs spacer layer and the moderately doped collector. Also the cap layer was excessively doped (2x10^{19} cm^{-3}) to encourage plasma assisted waveguiding, especially in the longer wavelength [119]. And finally, the semi-insulating substrate was replaced with a conducting substrate to compliment light confinement in the active region, while also promoting easier fabrication and a more efficient thermal extraction.

7.2 Project Aim

The project aim was to reproduce an earlier work by Rizzi *et al* [118] with improved optical power output.

7.3 Project Objectives

The main objective of this work was to fabricate and characterise SuperTune devices that could be tuned from $\sim$ 5-13 μm region, with higher power (i.e in $\sim \mu$Watts) compared to nWatts reported in the original work (see Ref. [118]).

To achieve the stated aims and objectives, we redesigned the original wafer structure to include:

1. waveguides. This was accomplished by replacing the low-bandgap collector (GaAs) with a wider gap material (AlGaAs) which introduces index difference in the region, thereby helping confine emitted light and reducing modal overlap with the moderately doped substrate. Electrically, having a wider-gap collector increases the reverse breakdown voltage [120], thus giving us wider operation regime for these devices.
2. a thicker and more heavily doped cap layer for plasmon assisted waveguiding especially at longer wavelengths ($\gtrsim 6\mu$m).
3. a conducting substrate in contrast to semi-insulating substrate used in the original structure. Using a conducting substrate simplifies the fabrication as only one etch step is needed, i.e to define the base; the collector contact is deposited on the bottom of the substrate (see figure 7.1).
4. the device was fabricated as a ridge waveguide structure to increase the optical power output.

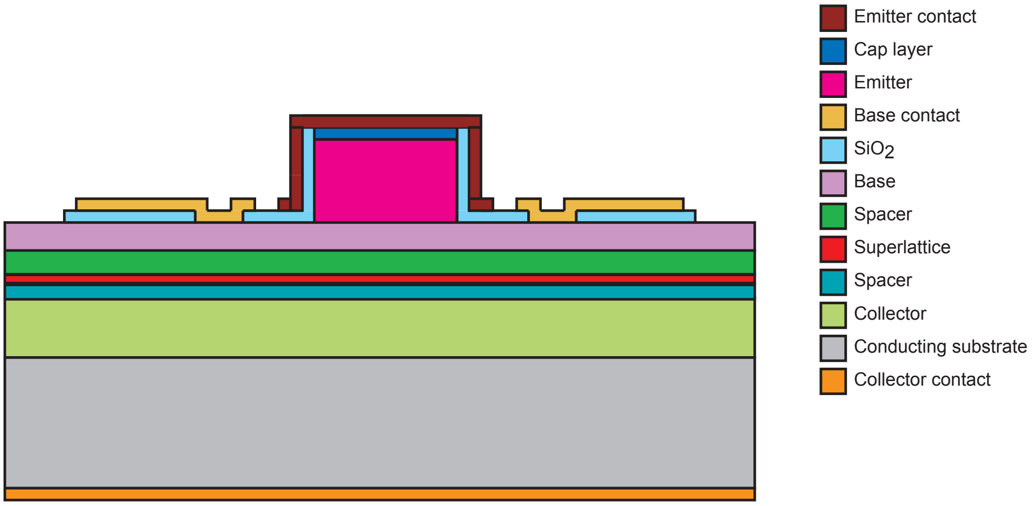

FIGURE 7.1: Cross-sectional view of the processed SuperTune device

7.4 Components of SuperTune

Structurally, SuperTune consists of two main parts, an active region (undoped SSL) inserted in the base-collector junction of an *npn* (AlGaAs/GaAs/AlGaAs) HBT. Rizzi *et al* [118] proposed the HBT, a three terminal device, as a solution to the formation of high field domains in the two terminal SSL structures caused by the interdependence of carrier (electrons) mobility on the applied field. The three terminal device gives separate control over the injected current and field across the SSL (in the base collector region). The two terminal devices suffer from instabilities due to the negative differential resistance (NDR) in some regions of its current-voltage (I-V) curve. For a more detailed explanation, see reference [118].

7.4.1 Semiconductor Heterostructures

Semiconductor heterojunction, a building block in optoelectronics, are formed when two semiconductors with similar lattice constants but different bandgaps (i.e energy difference between the conduction and the valence bands) are placed into contact. The bandgap difference between the two materials results in conduction and valence bands offsets as can be seen in figure 7.2(a)

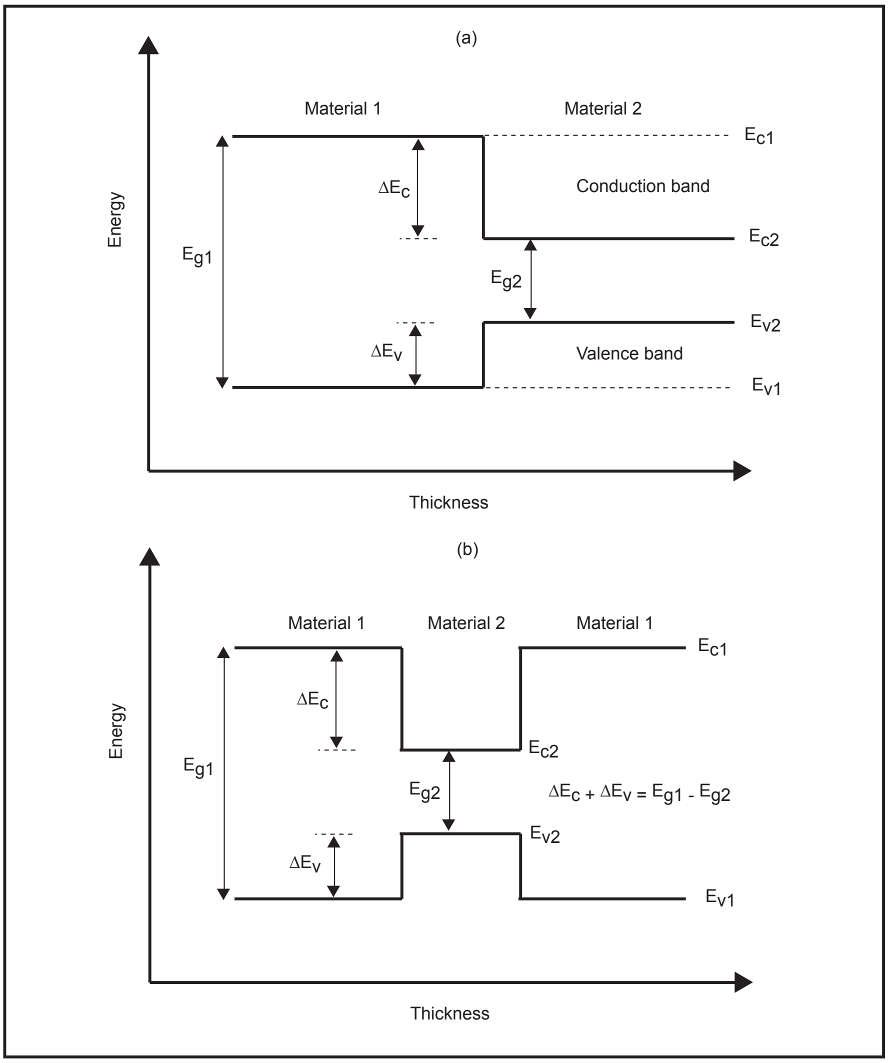

FIGURE 7.2: Bandstructure diagram of (a) Single heterojunction (b) quantum well (double heterojunction). E_{g1} and E_{g2} are respectively the bandgap of materials 1 and 2.

7.4.2 Quantum well

Quantum wells (QWs) are potential energy well formed by sandwiching an ultrathin lower gap semiconductor material between two larger gap semiconductors, as can be seen in figure 7.2(b). The discontinuity formed due to a heterojunction creates a potential well of depth ΔE_c and ΔE_v in the conduction and valence band respectively. Henceforth, we will only concentrate on quantum wells (QWs) in the conduction band since SuperTune and QCL operations only occur within subband energy levels in the conduction band. Within this potential well, electrons can be confined quantum mechanically at discrete energy levels which can be be found by solving the Schrödinger equation for a one dimensional potential well with finite barriers [41].

7.4.3 SSLs

SSLs are a type of solid state semiconductor material with additional periodic potential incorporated into the original lattice structure. They are a regular periodic structure of two alternating types of semiconductor material, usually a wider bandgap semiconductor material, called *barrier* (eg AlAs) and a narrow bandgap material, known as QW (eg GaAs). The schematic structure of a typical SSL is shown in Fig. 7.3, where A(barrier) and B(well) are two different semiconductor materials of respective layer thicknesses a and b (period: $d = a + b$). The period of the additional one-dimensional potential must significantly exceed the lattice period, as shown in fig 7.3, in order for SSLs to be formed. And when this occurs, and also because the QWs are degenerate and the barriers very thin, the QWs couple leading to formation of *minibands* and associated *minigaps*.

7.4.4 Minibands in SSLs

Minibands in SSLs are formed as result of interwell coupling in these structures [121]. Tunneling, the phenomenon behind the formation of minibands and their associated gaps, is observed as the thicknesses of the grown layers approach the quantum regime ($\lesssim$ 10 nm for typical III-V semiconductors). In this regime, the quantized electronic states (wavefunctions) associated with individual wells disperse into bands of energy (minibands); with finite energy widths [122], due to

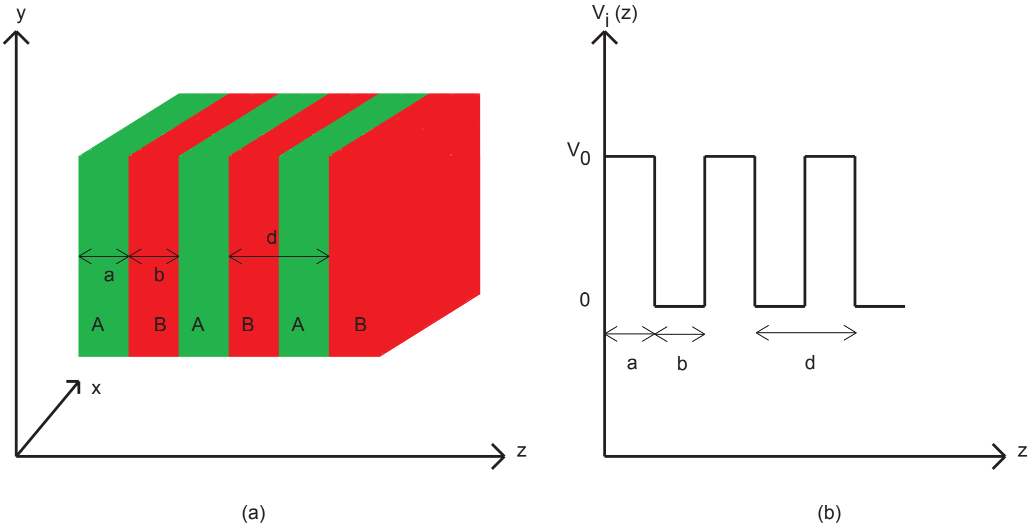

FIGURE 7.3: (a) Schematic structure of a superlattice made of alternated materials A and B grown along the z-axis .(b) The effective potential experienced by electrons in the growth direction

delocalization of wavefunctions along the SSL growth direction (z-axis). This can be seen in Fig.7.4(b) where minibands 1 and 2 can be thought as a superposition of the states (E_1 and E_2) of the individual wells, in the same way electron states of a crystal can be considered as a superposition of the atomic states. In Fig.7.4(a) the electronic states E_1 and E_2 can be seen localised within the well. This is what happens when the wells become completely decoupled. The miniband width (Δ), a linear function of interwell coupling, determines the electrical and optical behavior of SSL devices. Thus the miniband width can be tailored to suit its application by varying the thickness of the barrier. On the other hand, the position of the minibands in the quantum well can be controlled by the well thickness and its effective mass.

The calculated energy/wavefunction diagram of $\mathrm{GaAs}_{(6.1nm)}$ / $\mathrm{AlAs}_{(2.4nm)}$ superlattice showing minibands at 0 kV/cm applied field is shown in figure 7.5. The width of the first and second miniband is calculated to be ∼4 and ∼10 meV respectively. At the same time, the energy spacing between the minibands (minigap) was calculated to be 220 meV. These values are in good agreement with those reported by Scamarcio *et al* [4]. The third miniband do not contribute to the electron transport through the SSLs and, consequently, to optical emission from the active region.

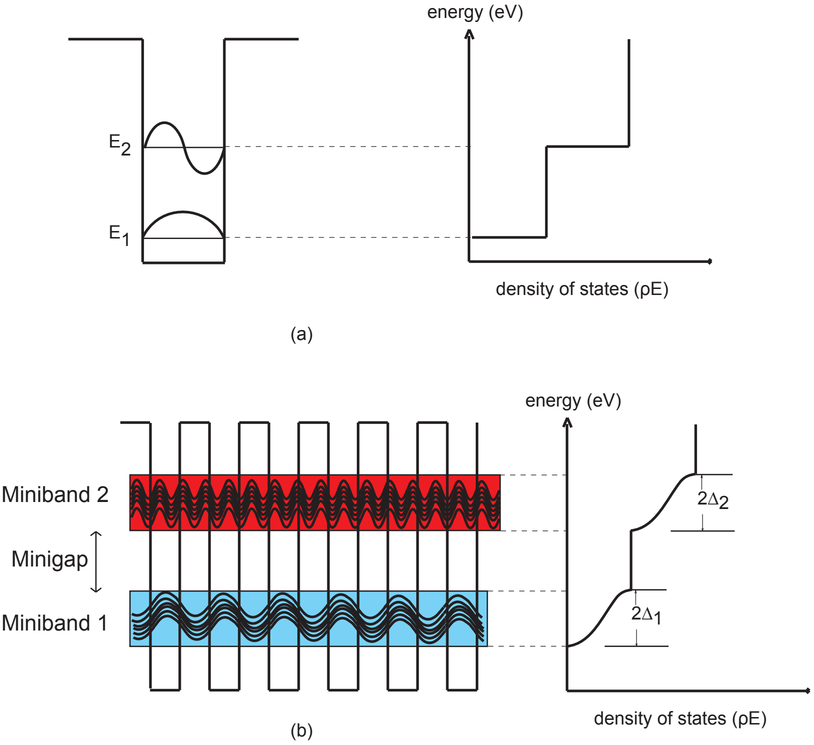

FIGURE 7.4: (a) Conduction band-diagram of an isolated quantum well and corresponding energy vs density of states plot (b) Conduction band-diagram of coupled quantum wells (formation of minibands and minigaps) and corresponding energy vs density of states plot

7.4.5 Wannier-Stark ladders in Semiconductor Superlattices

Application of a constant electric field in the direction perpendicular to the layer planes introduces an electrostatic potential that detunes the interwell resonance and tilts the miniband. This localises the state within a distance known as *localisation length*, λ (see equation 7.3) and the process is known as *Wannier-Stark localisation* [123, 124]. At large fields this leads to the splitting of SSL minibands into WSLs; with energy separation given by,

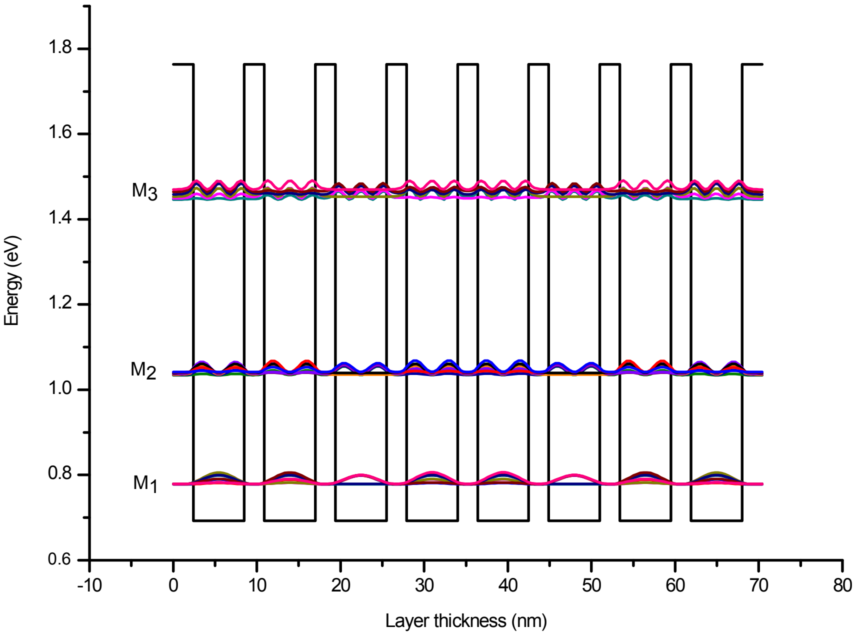

FIGURE 7.5: Calculated energy/ wavefunction diagram of GaAs$_{(6.1nm)}$ / AlAs$_{(2.4nm)}$ superlattice showing minibands at 0 kV/cm applied field. This calculation was done by solving the one-dimensional Schrdinger equation using nextnano [51]

$$\Delta E = eFd, \tag{7.1}$$

where F is the applied field, e is the electronic charge and d is the SSL period. Each electronic state level is localised on a number of periods given by,

$$n = \Delta / eFd, \tag{7.2}$$

$$\lambda = \Delta / eF, \tag{7.3}$$

At high applied field, the localisation length approaches a single superlattice period (i.e. complete localisation regime) and the miniband splits into a discrete series of levels: *Wannier-Stark ladders*. The computed WSLs formed in GaAs$_{(6.1nm)}$ / AlAs$_{(2.4nm)}$ SSLs at F = 140 kV/cm is shown in figure 7.6; in the figure, two WSLs can be observed; the top ladder which is a collection of E_2 energy states and the bottom ladder which is a collection E_1 energy states in the respective wells.

7.4.6 Wavelength Tunability in GaAs/AlAs superlattice

Observation of MIR electroluminescence associated with WSL transitions in intrinsic GaAs/AlAs strongly-coupled SSLs has been reported by Scamarcio *et al* [4]. Two types of optical transitions are observed in these structures: inter-WSL (2→1) and intra-WSL (1→1) transitions. In the former, injected electrons transit from the excited ladder (composed of E_2 states) to the ground ladder (composed of E_1 states) emitting photons (see figure 7.6), while in the latter, injected electrons

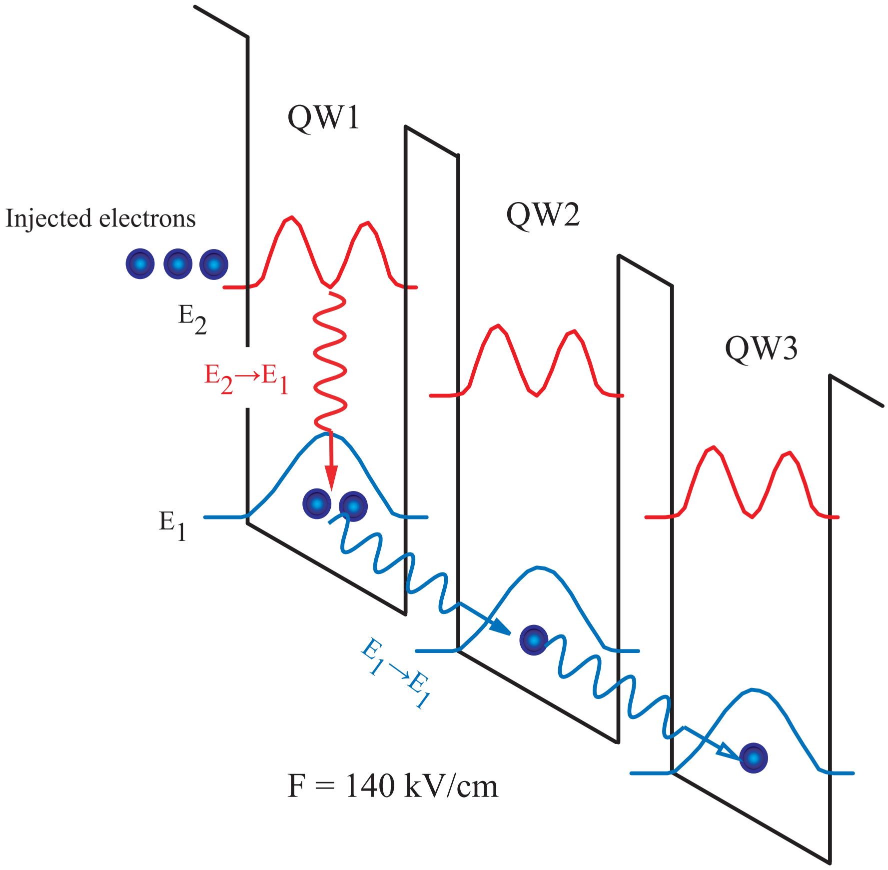

FIGURE 7.6: Schematic illustration of the operation of SuperTune in the first three wells from the left, at applied field of 140 kV/cm: the injected electrons into the upper state (i.e E_2) of QW1 scatters only to the ground state (i.e E_1) of the same well via optical or non- radiative transition. However, electrons in E_1 of QW1 either scatters via resonant tunneling into E_2 of QW3 or via radiative/non-radiative transition into E_1 of QW2 and so on and so forth.

transit from a higher energy state in the bottom ladder (E_1) to a lower state (E_1) in the adjacent well, still in the same ladder. This transition type is responsible for the wavelength tuning widely observed in these structures. Application of electric field as discussed in section 7.4.5 leads to equal energy separation between states, in the same ladder, according to equation 7.1. The energy separation increases with applied field, unlike the emission wavelength. The emission wavelength blue shift with increased field until it merges with transitions due to 2→1 which is fixed (see figure 7.7). From this figure, as the applied field is varied in the range of 100-260 kV/cm, the transition peak corresponding to the 1→1 transition is continuously blue shifted from $\lambda \sim 14$ μm (i.e 90 meV transition energy) to $\lambda \sim 5$ μm (i.e 235 meV). At 260 kV/cm, the energy difference between E_1 in QW1 and E_2 in QW2 approaches one optical phonon energy (i.e 36 meV in GaAs) in the well. The electrons in the former are rapidly scattered to the latter, thereby making it almost impossible for a 1→1 transition. At this point the 2→1 intersubband transition dominates the spectrum.

Finally a comparison of the computed result is made to the measurement result reported in Ref. [4]. The result shown in figure 7.8 are in good agreement.

7.5 Wafer Design

Central to the SuperTune wafer design was the structure reported in reference [118], and shown in table 7.1.

7.5.1 SuperTune Wafer Structure

Two wafer structures (ST2547 and ST2548) were respectively grown by molecular beam epitaxy (MBE) for this experiment. The only difference between the two wafers is the aluminium composition (x) in the collector. In ST-2547 wafer, shown in table 7.2, 10 % aluminium was used while in ST-2548 (see table 7.3) 25 % aluminium composition was used.

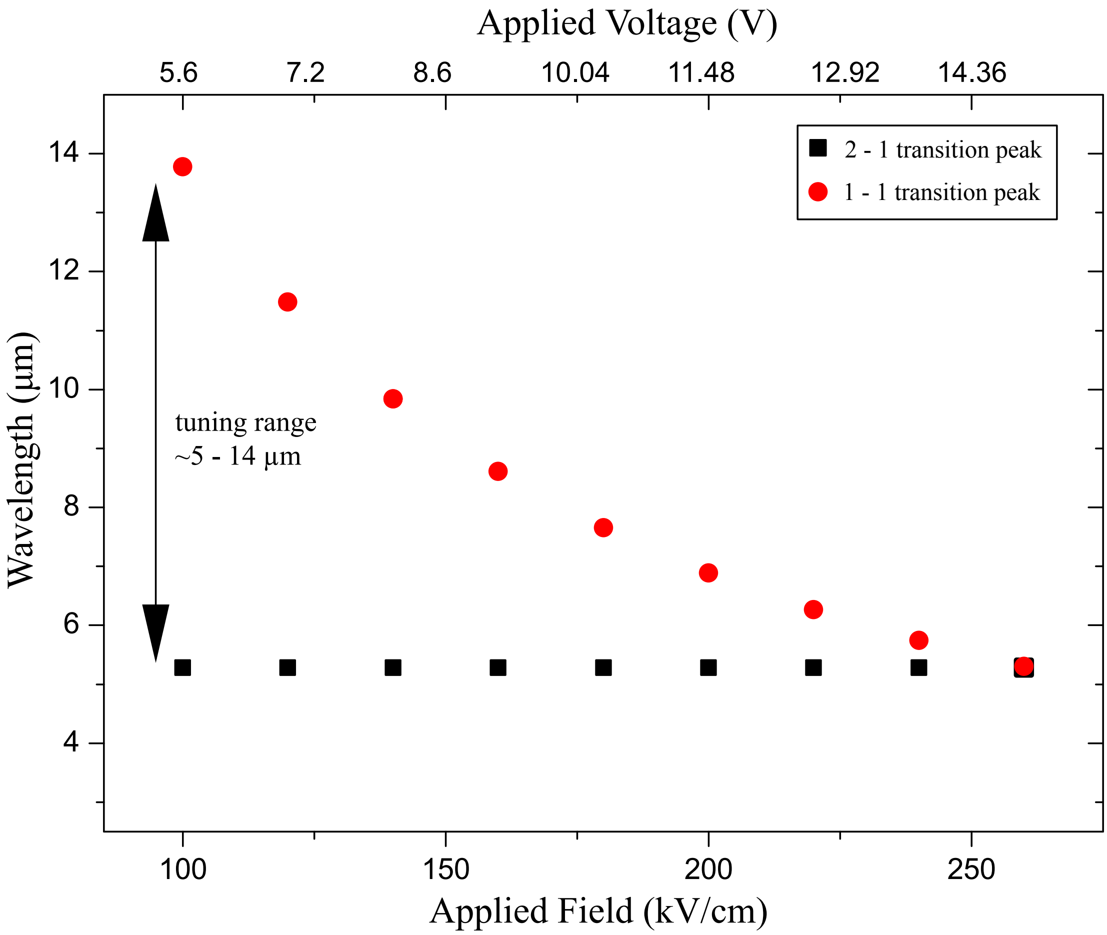

FIGURE 7.7: Computed wavelength of operation of SuperTune device as a function of applied field.

7.5.2 Wavefunction calculation

Calculating the electronic wavefunctions in the superlattice at fields greater or equal to zero requires solving the time-independent Schröedinger equation given by,

$$\left(-\frac{\hbar^2}{2m^*}\frac{d^2}{dz^2}+V(z)\right)\chi_{k_z}^{(i)}(z)=E^{(i)}\chi_{k_z}^{(i)}(z) \tag{7.4}$$

. The applied electric field F_{ap} is related to the applied voltage V_{ap} through

$$F_{ap}=(V_{bi}-V_{ap})/L_{in} \tag{7.5}$$

where V_{bi} denotes the built-in voltage (typically ∼1.5 V for GaAs/AlGaAs p-i-n junction at low temperatures) and L_{in} the width of the intrinsic region of the p-i-n diode (typically ∼1 μm) [125](p. 160).

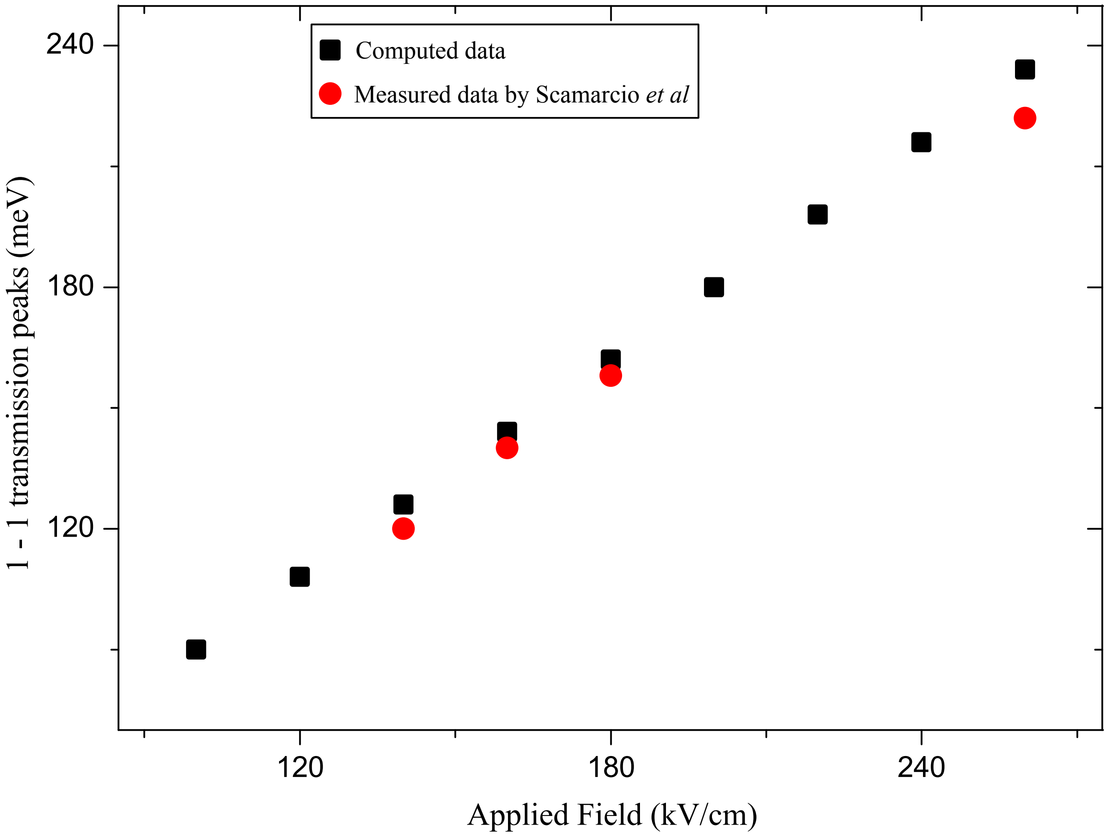

FIGURE 7.8: Continuous tuning of the Electroluminescence spectra peak associated with intra-WS ladder (1-1) transition as reported by Scamarcio *et al* [4] and confirmed by the calculated wavefunction result; using nextnano^3

Figures 7.9, 7.10 and 7.11 show wavefunctions and transition energes computed using equations 7.4 and 7.5 for applied fields $F = 140\ kV/cm$, $F = 180\ kV/cm$, and $F = 240\ kV/cm$ respectively, using nextnano^3 [51].

7.6 Optical Confinement in SuperTune

In designing an intersubband light emitter in the mid-infrared region, special attention must be paid to the optical losses present in the structure, which can have detrimental effect on device performance. In this region of the spectrum, free carrier absorption is a significant loss mechanism. To these effect, the core region is sandwiched between two semiconductor cladding layers with a lower refractive index, forming an optical waveguide in the transverse direction.

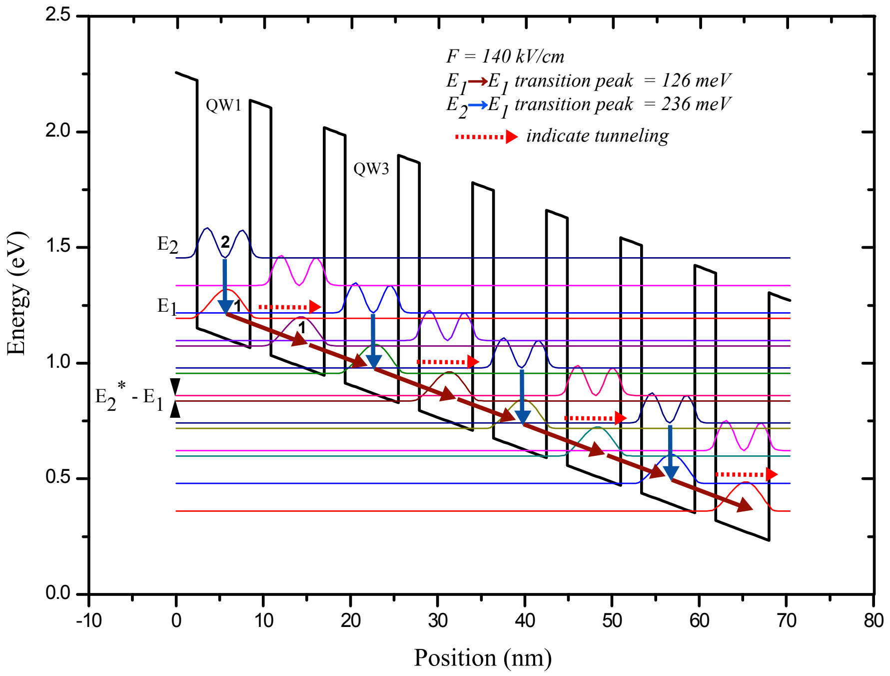

FIGURE 7.9: Computed wavefunctions and transition energies at $F = 140\ kV/cm$

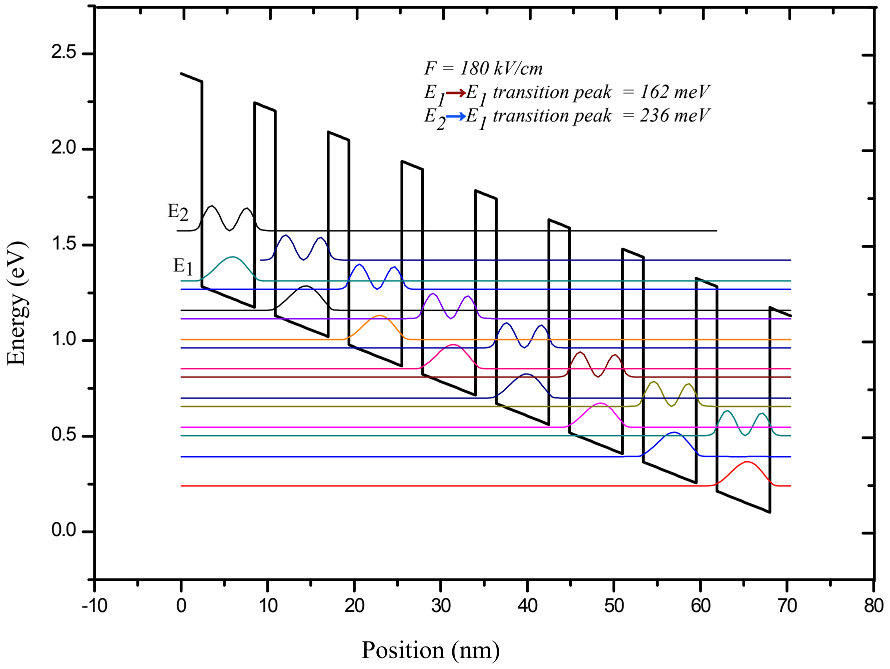

FIGURE 7.10: Computed wavefunctions and transition energies at $F = 180\ kV/cm$

Table 7.1: Wafer structure as reported in the original work

Semiconductor	Thickness (nm)	Doping (cm^{-3})	Layer function
GaAs	30	n^+=5e18	Contact layer
$Al_xGa_{1-x}As$ (x:0 to 0.23)	50	n^+=5e18	Graded alloy
$Al_{0.23}Ga_{0.77}As$	1000	n=5e17	Emitter
GaAs	500	p=5e18	Base
GaAs	50	undoped	Space layer
AlAs	2.5	undoped	Input barrier
GaAs	6.5	undoped	Superlattice
AlAs	2.5	undoped	repeated 8x
GaAs	550	undoped	Spacer layer
GaAs	1000	n=5e17	Collector
GaAs	30	n=5e18	contact layer
GaAs		Semi-insulating	Substrate

Table 7.2: Epilayer structure of wafer ST2547

Semiconductor	Thickness (nm)	Doping (cm^{-3})	Layer function
GaAs	100	n^+=5e19	Contact layer
$Al_xGa_{1-x}As$ (x:0 to 0.23)	30	n^+=5e17	Graded alloy
$Al_{0.23}Ga_{0.77}As$	1000	n=5e17	Emitter
GaAs	500	p=5e18	Base
GaAs	50	undoped	Space layer
AlAs	2.4	undoped	Input barrier
GaAs	6.1	undoped	Superlattice
AlAs	2.4	undoped	repeated 8x
GaAs	500	undoped	Spacer layer
$Al_{0.1}Ga_{0.9}As$	1000	n=5e17	Collector
GaAs		n^{++}	Substrate

In the SuperTune structure design, a lower waveguide cladding was incorporated by replacing the higher-index collector (GaAs) with a lower-index material (AlGaAs). Also By heavily doping the contact layer we benefit from plasmon assisted waveguiding which is expected to compliment the ridge waveguide structure in confining the emitted photons. The biggest threat to optical confinement and possible operation of the proposed device was the proximity of the heavily p-doped base (GaAs(p$\sim$5e18 cm^{-3})) to the active region. This layer has high absorption coefficient in the Mid-infrared region due to free carrier absorption.

TABLE 7.3: Epilayer structure of wafer ST2548

Semiconductor	Thickness (nm)	Doping (cm^{-3})	Layer function
GaAs	100	n^+=5e19	Contact layer
$Al_xGa_{1-x}As$ (x:0 to 0.23)	30	n^+=5e17	Graded alloy
$Al_{0.23}Ga_{0.77}As$	1000	n=5e17	Emitter
GaAs	500	p=5e18	Base
GaAs	50	undoped	Space layer
AlAs	2.4	undoped	Input barrier
GaAs	6.1	undoped	Superlattice
AlAs	2.4	undoped	repeated 8x
GaAs	500	undoped	Spacer layer
$Al_{0.25}Ga_{0.75}As$	1000	n=5e17	Collector
GaAs		n^{++}	Substrate

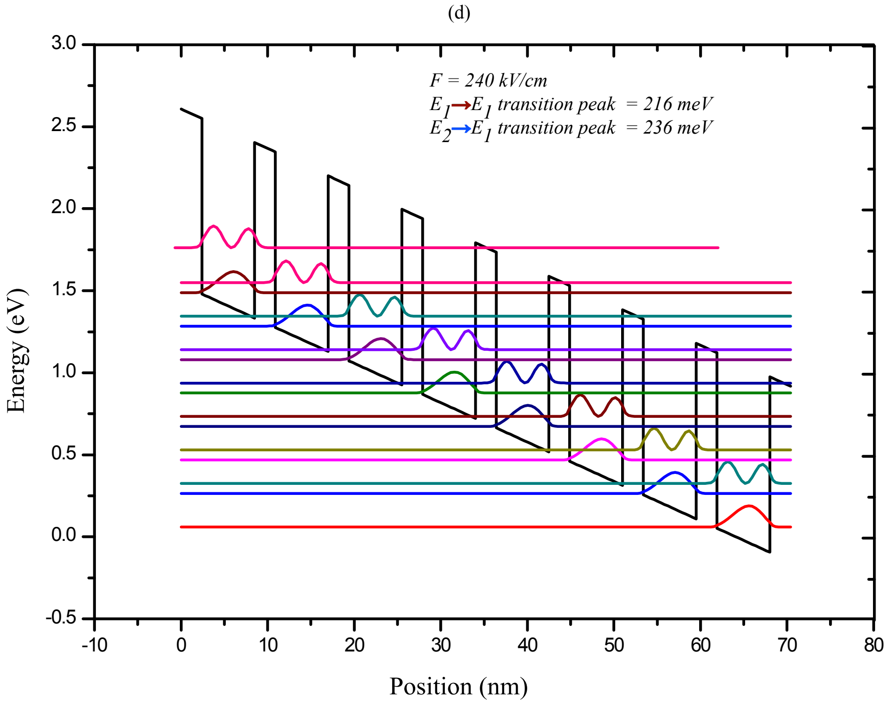

FIGURE 7.11: Computed wavefunctions and transition energies at $F = 240\ kV/cm$

7.6.1 Optical Parameter Modeling

To predict the optical behaviour of these devices, an insight into the optical responses (i.e refractive indices and absorption coefficients) of the layers to the various wavelengths propagating through, is imperative. Obtaining accurate values of the refractive index n and absorption coefficient α (cm-1) is a prerequisite to modelling and optimising the optical modes of the waveguide.

7.6.1.1 Dielectric Permittivity of a Medium

The complex dielectric function which describes the optical properties of a medium at all photon energies (ω), taken into account the phonon [126, 127] and free carrier contribution [128], is given by the expression [128],

$$\varepsilon(\omega) = \varepsilon_\infty \left(1 + \left(\sum_j \frac{\omega_{LO_j}^2 - \omega_{TO_j}^2}{\omega_{TO_j}^2 - \omega^2 - i\omega\gamma_{ph_j}}\right) - \frac{\omega_p^2}{\omega(\omega + i\gamma_{pl}j)}\right) = \varepsilon_1(\omega) - i\varepsilon_2(\omega) \tag{7.6}$$

where γ_{ph_j}, ω_{LO_j} and ω_{TO_j} are, respectively, the phonon damping constant, the long-wavelength longitudinal-optical and transverse-optical phonon frequencies of the j^{th} oscillator. ε_∞ is the high-frequency permittivity of the layers. The plasma frequency, ω_p, is given by, [128]

$$\omega_p = \sqrt{\frac{n_e e^2}{m^* \varepsilon_\infty \varepsilon_0}} \tag{7.7}$$

where ε_0, n_e, e and m^* are the free space permittivity, electron doping density, electron charge and the effective mass of the material respectively.
Also, the Plasmon damping coefficient, γ_{pl}, is calculated from, [129].

$$\gamma_{pl} = \frac{e}{\mu m^*} \tag{7.8}$$

where μ is the mobility of electrons in the semiconductor.

Similarly, the real refractive index $n(\omega)$ and the extinction coefficient $k(\omega)$ can be calculated from,

$$n(\omega) = \left(\frac{[\varepsilon_1(\omega)^2 + \varepsilon_2(\omega)^2]^{1/2} + \varepsilon_1(\omega)}{2}\right)^{1/2}, \tag{7.9}$$

and

$$k(\omega) = \left(\frac{[\varepsilon_1(\omega)^2 + \varepsilon_2(\omega)^2]^{1/2} - \varepsilon_1(\omega)}{2}\right)^{1/2}. \tag{7.10}$$

The frequency dependent absorption coefficient $\alpha(\omega)$ in the material is given by,

$$\alpha(\omega) = \frac{4\pi}{\lambda} k(\omega), \tag{7.11}$$

where λ is the free-space wavelength.

7.6.2 Waveguide modeling

The choice of fabricating SuperTune as a ridge waveguide structure was to enhance the optical output power. Also by using ridge structure we have a wider surface semiconductor area to pump, yielding higher optical gain but at the same time increases the optical loss. The optimum length should strike a balance between low gain and high losses expected from these devices. Ridge waveguide modeling

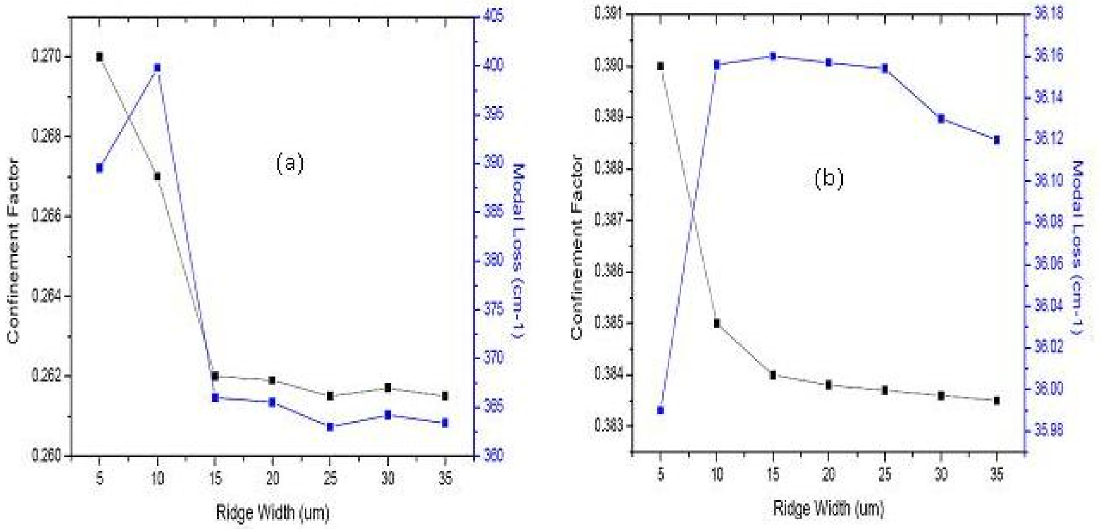

FIGURE 7.12: Confinement factor and Modal loss vs. Ridge width plot, for the TM fundamental mode at (a) $\lambda = 10$ μm, (b) $\lambda = 5$ μm. Modeling is based on parameters given in Ref. [130]

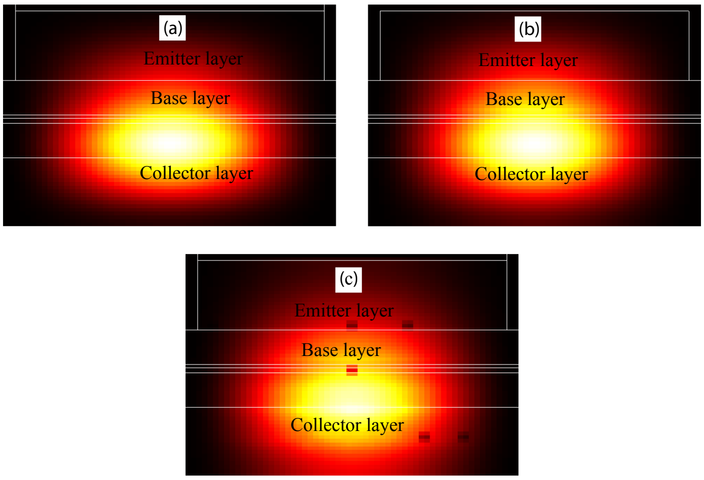

FIGURE 7.13: Cross-sectional view of the fundamental TM mode at (a) 5 μm wavelength, (b) 7 μm wavelength and (c) 10 μm wavelength

was done to ascertain the position of the modes in the waveguide and also to calculate the modal overlap with the heavily p-doped base, which is a source of concern. The percentage of overlap will give us a clue as to the possibility of light emission from these devices; high overlap means low optical output and vice versa. FIMMWAVE [131], a photonic CAD software, based on vectorial 3D mode solver, was used for the modeling. The results are shown in figure 7.12. Wider ridge waveguides (20-40 μm) were selected for this work because they have higher confinement factor for the modes and lesser overlap with the base. Shown in figure 7.13 are the cross-sectional view of the fundamental transverse magnetic (TM) modes at $\lambda \sim 5\ \mu m$, $\lambda \sim 7\ \mu m$ and $\lambda \sim 10\ \mu m$. From the diagram, it can be seen that the fundamental mode, the least lossy mode in the structure, has great overlap with the heavily p-doped base; 24, 27 and 42% overlap was deduced for the $\lambda \sim 5\ \mu m$, $\lambda \sim 7\ \mu m$ and $\lambda \sim 10\ \mu m$ respectively.

7.7 SuperTune Processing

All the devices reported in this work were processed in CST. The devices we processed in (JWNC) were electrically unstable.

7.8 SuperTune Characterisation

The characterisation was carried out in two phases. The first phase, detailed in section 7.8.2, was to measure the dc electrical characteristics of SuperTune. The second phase, explained in section 7.8.3, was centered on the optical emission characterisation.

7.8.1 Experimental setup for SuperTune dc characterisation

The experimental setup for SuperTune dc characterisation is shown in figure 7.14. It comprises three components; a probe station, Agilent 4155c semiconductor parameter analyser (SPA) and a personal computer (PC). The probe station mechanically holds the device in position during the measurement and also provides electrical access from the SPA to the device under test, via probes. The SPA communicates to the probe station via four BNC cables and to the PC through GPIB interface.

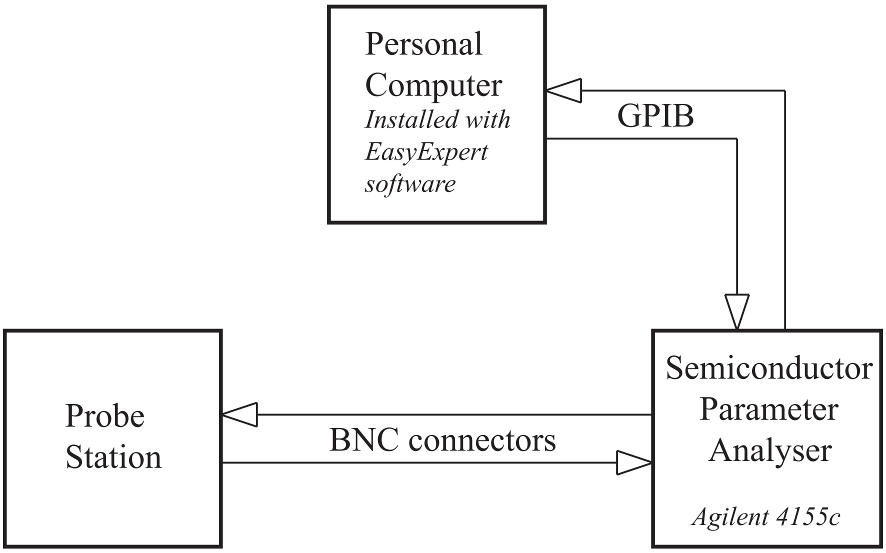

FIGURE 7.14: Schematic diagram of the SuperTune experimental setup

The SPA is a fully automated, high performance and versatile instrument capable of measuring, analysing and graphically displaying dc characteristics of a wide range of semiconductor devices. The Agilent 4155c SPA used in this particular measurement has in inclusion a Desktop EasyEXPERT software for PC-based graphical user interface (GUI) instrument control.

7.8.2 SuperTune electrical characterisation

The electrical measurements carried out include; base-collector and base-emitter turn-on voltages, common-base transistor output characteristics and the reverse breakdown voltage for devices (F07 and I03) fabricated from wafers ST2547 and ST2548 respectively. Both devices have the same dimension (20 x 500 μm)

The bonded devices were mounted on a probe station for the electrical characterisation at room temperature. Common base configuration was adopted for the measurement since the base-collector voltage (V$_{bc}$) equals the voltage drop across the superlattice active region. In this configuration, the base was grounded while negative and positive voltages were applied to the emitter and collector respectively, as shown in Fig. 7.15

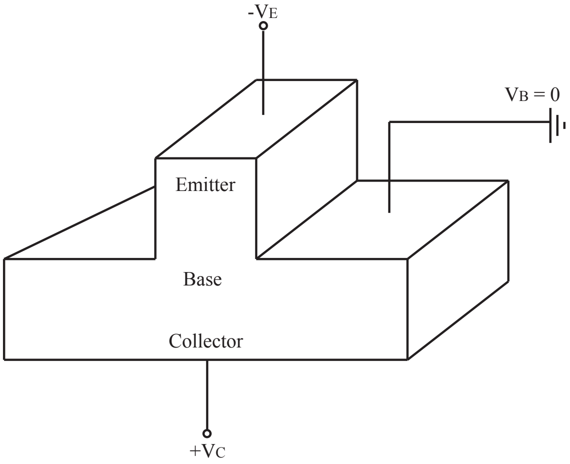

FIGURE 7.15: SuperTune connected in common base configuration

7.8.2.1 Turn-on Voltage

This was the first of the measurement to be carried out. This measurement was done to ascertain the quality of the junctions by measuring the voltage at which the base-emitter and base-collector junction starts conducting in forward bias condition. This voltage is the point at which applied voltage exceeds the junction barrier height. The result of these measurements are shown in Figs.7.16 for F07 and I03 devices.

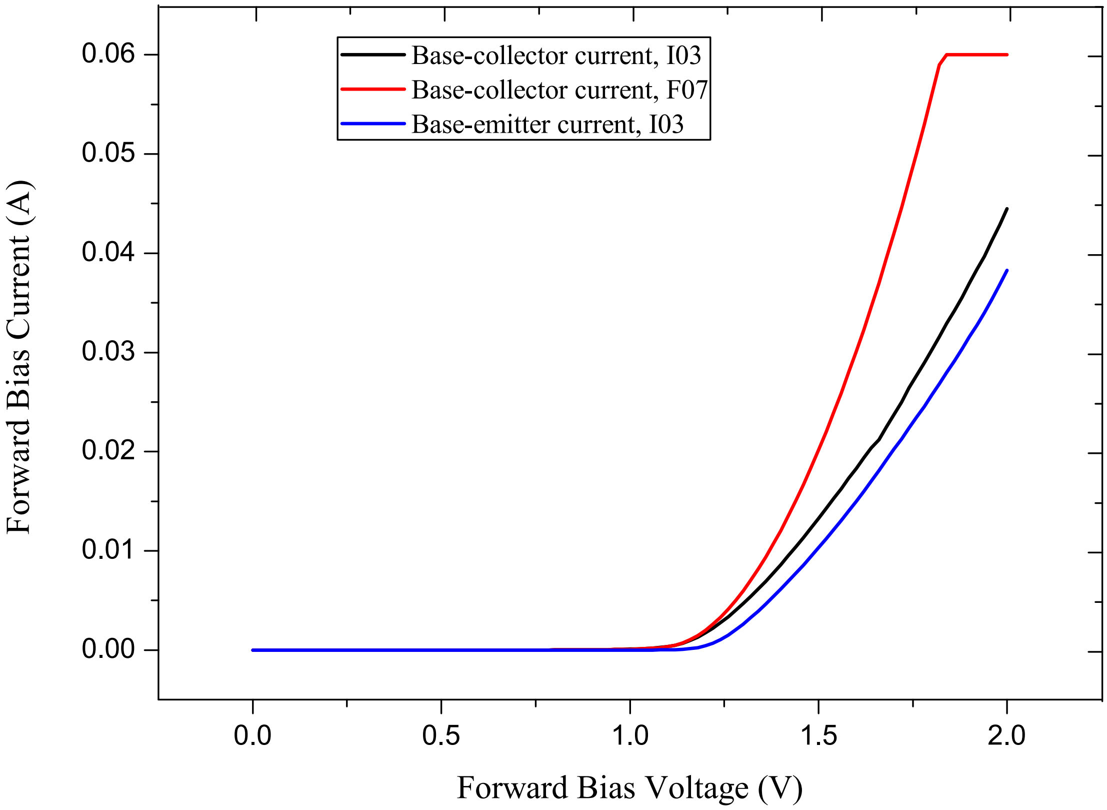

Figure 7.16: Forward bias turn-on voltages for the base-collector junctions of F07 and I03 devices. Also shown is the forward bias base-emitter turn-on voltage for I03 device. F07 and I03 devices were fabricated from wafers ST2547 and ST2548 respectively

The base-emitter and base-collector junctions shown in figure 7.16 exhibit good I-V curve of a typical diode in forward bias. Base-emitter turn-on voltage of 1.24 V was measured for both devices, while 1.16 and 1.18 V were measured for the base-collector junctions of F07 and I03 respectively, at 300 K. The difference in the base-collector turn on voltages is due to the difference in the aluminium composition of the collectors (10 % for F07 and 25 % for I03 device). Typically at low temperatures ($\lesssim$ 20 K), ~1.5 V turn-on voltage have been reported for GaAs/AlGaAs $p-i-n$ junctions [125].

In addition, linear resistances of ~7.5 Ohm and ~15 Ohm were calculated for the base-collector junctions of F07 and I03 respectively.

7.8.2.2 Negative Differential Resistance measurement

Negative differential resistance observed in the I-V curves of undoped superlattice at very low temperature was used to probe the presence of superlattices in the grown wafer.

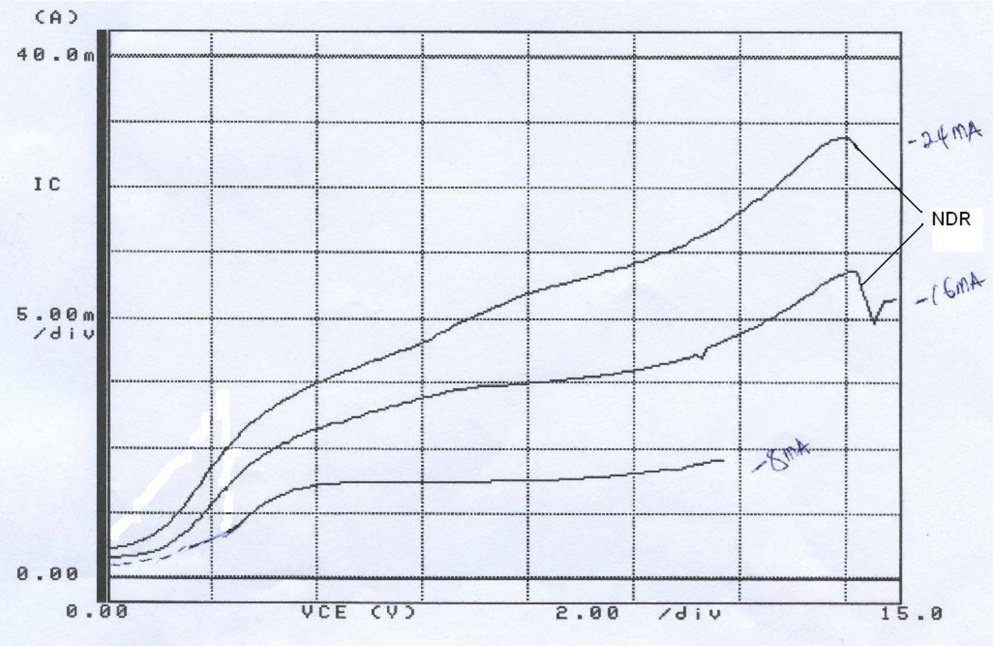

FIGURE 7.17: SuperTune I-V curve showing regions of negative differential resistance (NDR) at 77K

In this experiment, we measured the transistor output characteristics using the method described in section 7.8.2 but at liquid nitrogen temperature (77K). The I-V curve for this measurement is shown in Fig.7.17. In the plot NDR is observed at ~14 V. This is in good agreement with the value reported by Rizzi *et al* [118].

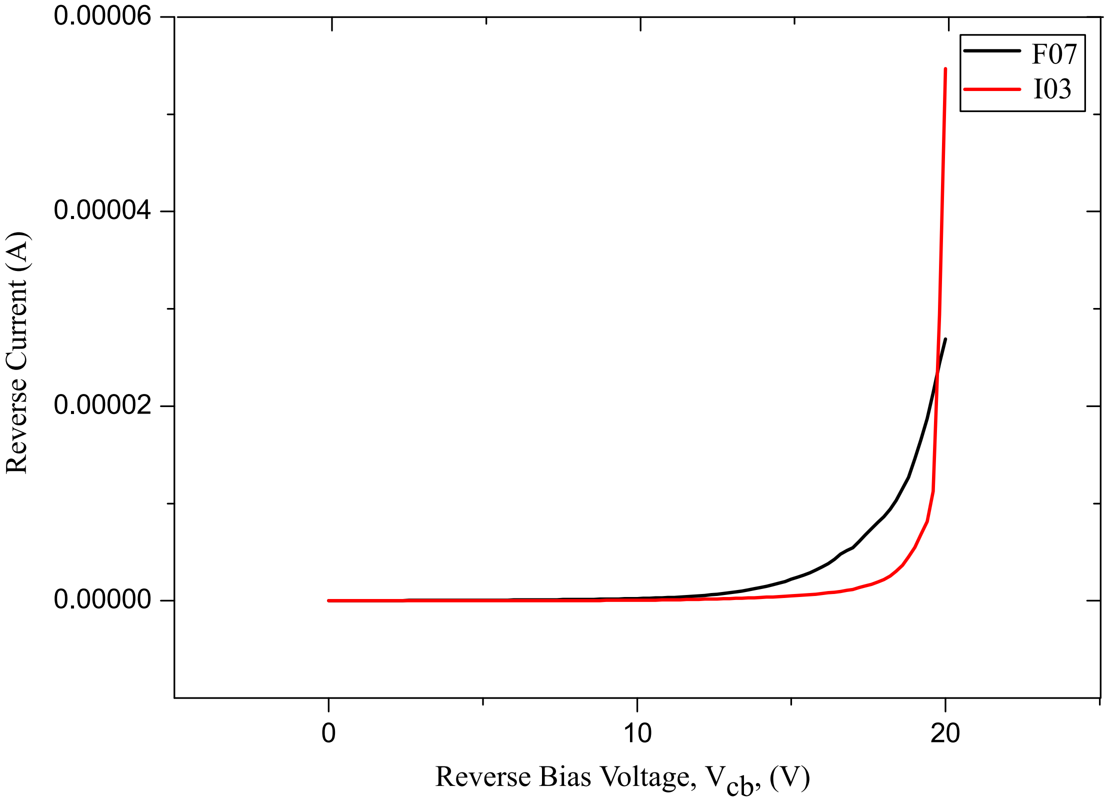

FIGURE 7.18: Reverse breakdown voltage for the base-collector junction

7.8.2.3 Reverse Breakdown Voltage

This is the voltage at which a reverse biased p-n junction, breaks and starts conducting. In this measurement, using the setup described in section 7.8.2, a positive bias was applied to the collector with reference to the base and current through the collector (I_{CE0}), was measured. The I-V plot, shown in Fig. 7.18, shows breakdown voltages at 18.2 and 19.5 V for F07 and I03 devices. This is very close to the value (18 V) reported in reference [118]. The difference is due to higher breakdown voltages associated with wide-gap collector (AlGaAs) HBTs [132].

7.8.2.4 Common-base output Characteristic

This is a series of plots of the collector current (I_C) as a function of collector-base voltage (V_{CB}), at various emitter current (I_E). The output characteristic (i.e V_{CB}-I_C curve) for F07 and I03 devices are shown in Figs. 7.19 and 7.20 respectively

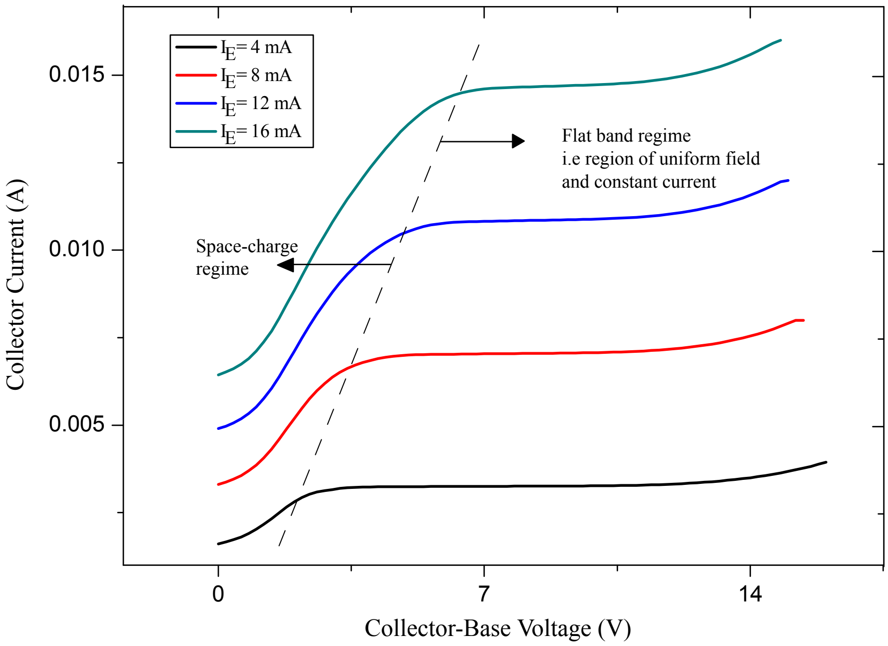

FIGURE 7.19: Common-base output characteristics of F07 SuperTune device. Two regimes of operation are identified; space-charge and flatband regimes separated by the dotted line

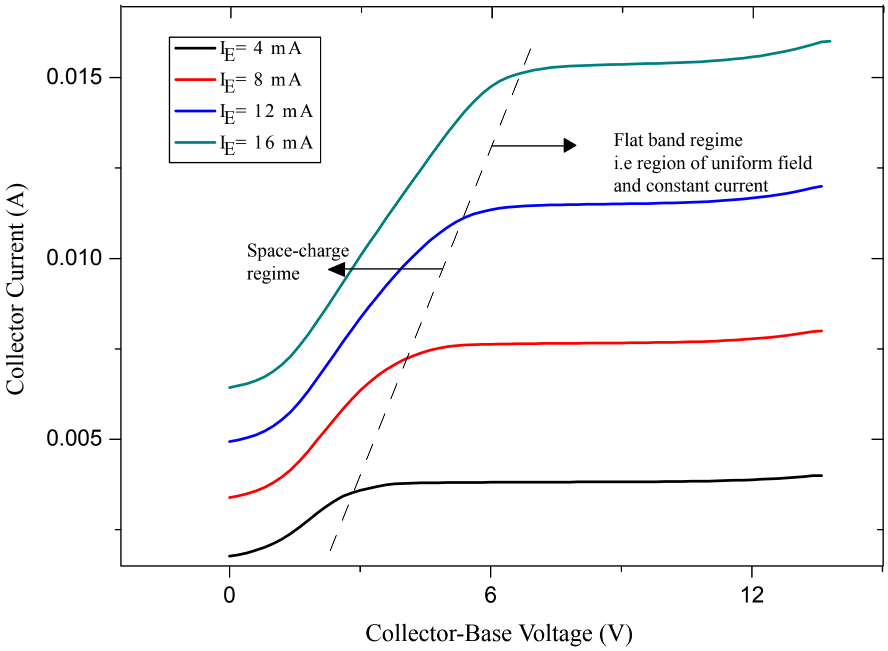

FIGURE 7.20: Common-base output characteristics of I03 SuperTune device. Two regimes of operation are identified; space-charge and flatband regimes separated by the dotted line

The HBT's output characteristic curves, shown in figures 7.19 and 7.20 show parabolic behaviour at low voltages (e.g 0-3 V for I_E=4 mA); this behaviour is expected because of the space-charge effect in this region. The rounded (bent) region indicates transition from the space-charge regime (i.e non-uniform electric field region) to the flat-band regime (i.e region of uniform electric field and constant current across and through the superlattice). In this region, the transfer coefficient, α = IC/IE, is very close to unity (∼0.9) at every emitter current injected. The region is flat because almost all the electrons injected from the emitter pass to the collector, through the superlattice. This region is very important for finding tunable emission in our device.

7.8.3 SuperTune Optical characterisation

The measurement setup used for the optical characterisation of SuperTune is shown in figure 7.21.

The fabricated devices were epilayer up soldered onto heat sink and mounted onto the cold finger of a closed cycle helium cryostat and pumped down to 20 K. Constant emitter current IE = 9 mA was injected into the device while varying the collector-base voltage (VBC). Figure 7.22 shows the spectra acquired at VBC = 10 and 13 V. The spectra were measured with a Vertex 70 fourier transform infrared (FTIR) spectrometer using a step-scan and lock-in detection technique and a liquid nitrogen cooled MCT detector.

The optical measurement of the devices were not as successful as the electrical characterisation. As can be seen from figure 7.22, the acquired spectra are basically thermal noise. Also shown in the spectra are the expected peak positions of the emitted optical power, based on data from Ref.[118]. The emitted optical signal appeared to be masked by the thermal emission. In the original work (Ref.[118]), the measured optical power was in nano-Watts scale i.e slightly above noise level. The replacement of the (GaAs) collector with AlGaAs material in this work introduced additional resistance to current flow through the collector.

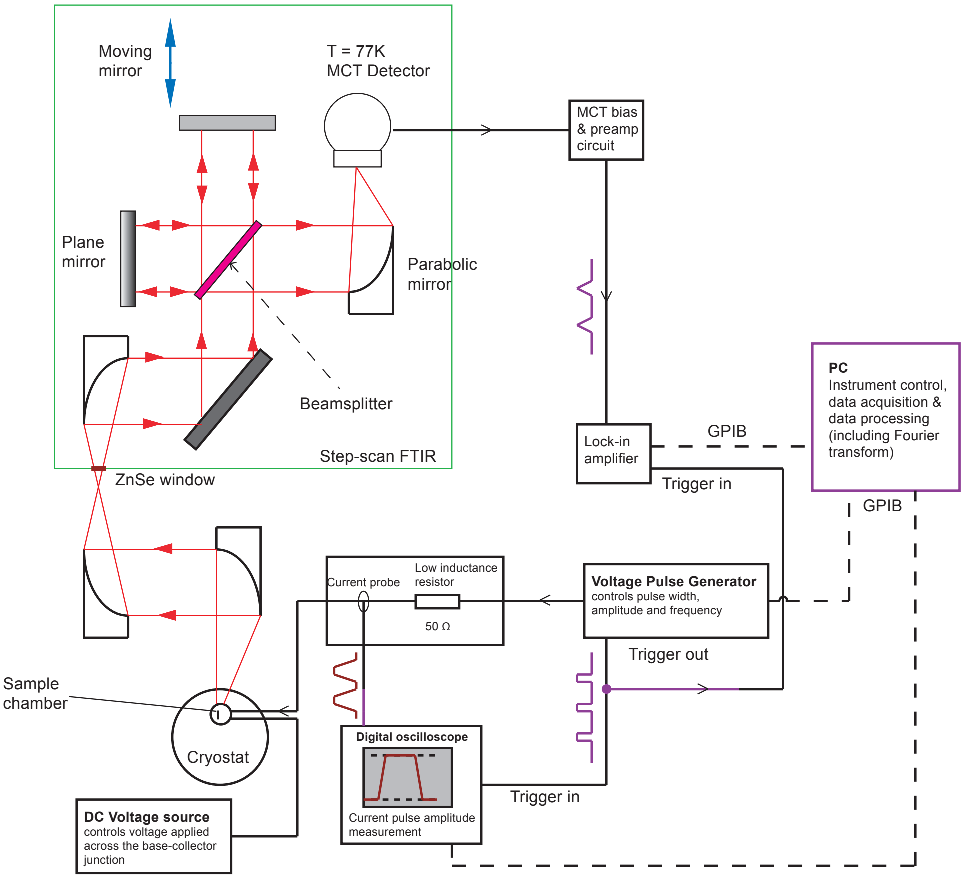

FIGURE 7.21: Measurement setup for optical characterisation SuperTune

Thereby increasing the thermal heating. The resistance reported in the original (Ref.[118]) work was 13 ohms at 20 K. We could not acquire the I-V curves of the SuperTune devices reported in this work at 20 K because we did not have the appropriate LabView set-up for this type of measurement. Therefore the devices were electrically characterised at 300 K using the set-up discussed in section 7.8.1.

The resistance deduced from the base-collector I-V characteristic for F07 and I03 devices are 7.5 and 15 Ohm respectively. Though this values can not be compared to 13 Ohm obtained at 20 K by Rizzi and co (Ref.[118]), It did show that by increasing the aluminum composition in the collector from x = 0.1 (F07 device) to x = 0.25 (I03 device), the measured resistance increased by 50 %. Meaning that thermal emission due to current heating doubles by increasing the aluminum fraction by 60%. So by replacing the GaAs collector with $Al_xGa_{1-x}As$, we may

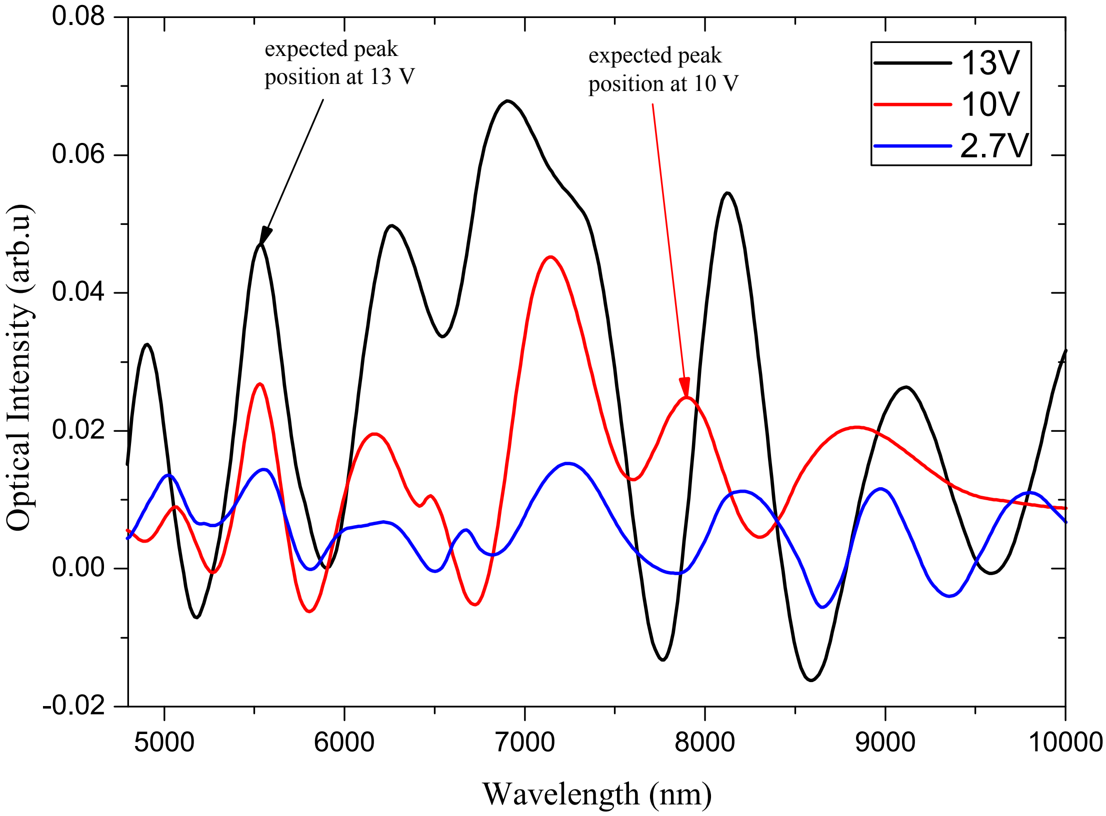

FIGURE 7.22: Acquired spectra of SuperTune, using lock-in detection step-scan technique, at applied voltages of 2.7, 10 and 13 V at 20 K and 9 mA injection current. Expected peak position is based on data from Ref.[118]

have increased the base-collector resistance by ∼30 % (in F07 device) and by ∼83 % in (in I03 device).

7.9 Conclusion

The SuperTune project, though very promising, remains inconclusive. The electrical characteristics of the devices show good electrical behaviour but no appreciable optical signal was observed. The possible reasons for the poor optical behaviour include: additional thermal emission introduced by replacing the GaAs collector with AlGaAs material and the proximity of the of the heavily p-doped GaAs base layer to the active region. To these effects, future work on this project should be focused on alternative means of suppressing domain formation in the intrinsic superlattice active region. HBT employed for this purpose in this work helped eliminate domain formation in the operational field regime but introduced great optical losses due to the position of the heavily doped base.

Chapter 8

Conclusion

We have described how for the first time, unidirectional operation and coupled ring tuning were realised in quantum cascade (QC) material; specifically in a new strain compensated material containing antimony and operating in the 3-4 μm hydrocarbon absorption region. The presence of antimony made the fabrication more complicated than ordinary AlInAs/InGaAs or AlGaAs/GaAs materials. Also the nature of metal liftoff required to electrically isolate the “S” crossover waveguide and the racetrack cavity (for the unidirectional ring laser) and the two ring cavities (for the coupled ring lasers) meant that a special liftoff recipe was developed. This recipe was described in section 4.8 and detailed in Appendix A.

The devices discussed in this thesis were investigated as alternative approach to realising (1) single mode operation (2) wide tunability and (3) high power output compared to distributed feed backs (DFBs) in this wavelength region.

The unidirectional quantum cascade ring lasers discussed in chapter 5 were particularly interesting for the following reasons:

1. stable single mode operation
2. operates in the traveling wave regime
3. no spatial hole burning

4. uniform saturation of gain medium
5. more power extracted in the favoured emission direction
6. quantum efficiency in the favoured direction is up to twice that of the bi-directional lasers

The nature of the gain in the material (i.e inhomogenous broadening) meant that gain competition necessary for unidirectional operation was very weak, as explained in section 3.6.1. To improve gain competition in the material and finally unidirectional behaviour, we improved the cross-coupling coefficients between the counter-propagating modes by incorporating an active cross-over waveguide in a manner that introduces non reciprocal gain and loss to the desired and undesired modes respectively. The active cross-over waveguide continuously couple light from the counter-clockwise (CCW) direction to the clockwise (CW) direction, leading to increased photon density in the later. The CW mode claims more of the available gain until it completely suppresses the CCW mode, leading to a single mode operation.

The measured L-I curves for the unidirectional laser (see figure 5.9) show that both the CW and CCW attained threshold at the same current, signifying similar collection efficiency from both sides. Also, as expected, the former dominated the later as the injection current was increased beyond threshold. In fact at 1.5 times the threshold current, 90 % of the emitted light was in the desired CW direction. This satisfied the project aim. We could not inject the “S” crossover waveguide at this time because the heat sink on which the device was mounted could only support two electrical contacts.

The spectrum from the unidirectional quantum cascade shown in figure 5.10 exhibits unidirectional operation with side mode suppression ratio ∼20 dB.

The emitted power from the CW could not be compared to that from the DFB, though this was part of the project aim, because we did not have access to calibrated power meter. The L-I measurements were carried out with un-calibrated power detector but measurements from both sides were taken under the same condition.

Future works on the unidirectional quantum cascade ring lasers have been discussed in section 5.10.

Coupled ring quantum cascade lasers discussed in chapter 6 were investigated because they have the potential to operate in single mode. Other advantages of these devices over DFB include:

1. Wider tunability due to Vernier coupling effect
2. faster wavelength tuning because they employ plasma effect tuning which is faster than thermal tuning employed in most DFB devices
3. narrower linewidth (1.2nm) compared to DFB (2.0 nm)
4. Lower fabrication cost

80 % of the characterised coupled ring quantum cascade lasers showed Vernier coupling effect as expected with M05MI device exhibiting sidemode suppression ratio (SMSR)$>\sim$ 20 dB. Wavelength tuning behaviour was only observed from one device (M19MI). Continuous wavelength tuning over the range of about 13 nm was measured with tuning rate of about 0.4 nm/mA. The tuning spectra was very noisy due to low inter-ring coupling employed in the design. Also the high current injected to boost the optical output power increased the thermal noise.

Although the performances of the coupled ring quantum cascade lasers reported in this work is quite inferior to devices using similar wavelength selection/ tuning techniques reported in Ref. [133] and Ref. [134] at the longer wavelengths, they can still be improved as discussed in section 6.6.

The SuperTune project remains incomplete as the devices were not emitting significant optical signal, despite the good electrical characteristics. The emitted optical power was masked by thermal emission and the signal level, we believe, was below the sensitivity of the MCT detector. To improve the signal to noise level, we tried techniques like; lowering the thermal signature of the signal by reducing the pulse width of the injected current, while maintaining the duty cycle through increasing the repetition rate (2) chopping the optical signal and locking its frequency to the lock-in detector (3) Mounting a polariser in the optical path to reduce the noise level which is randomly polarised and allowing the signals which are polarised in the growth direction (TM) to pass through (4) using step-scan lock-in detection method in the FTIR to measure the devices.

Possible reasons for insignificant optical power output and the way forward have been discussed in section 7.9.

Finally, the highlights of this research are;

1. The first unidirectional ring quantum cascade ever reported [105]
2. The first tunable coupled ring quantum cascade lasers ever reported

Appendix A

Multilayer Lift-off Recipe

Listed below is the special lift-off process developed for devices reported in this thesis. This process was only successfully applied after waveguide planarisation.

1. Solvent cleaning (see 4.5.1)
2. 2 minutes oxygen ashing at 100 W
3. Deoxidation: 30 seconds dip in 1:4 $HCl{:}H_2O$. Rinse in deionised water and blow-dry.
4. Dehydrate 200 ^{o}C for 5 minutes on a hot plate
5. Dispense LOR10A at 500 revolution per minute (RPM) for 5 seconds followed by a 3000 RPM for 45 seconds. This gives LOR10A layer thickness of about 1 μm
6. Bake sample at 90 ^{o}C for 20 minutes, followed by 10 minutes bake in an 180 ^{o}C oven
7. Repeat steps 5 and 6 four times. This gives over all LOR10A layer thickness of about 4 μm
8. Spin S1818 photoresist at 4000 RPM for 30 seconds
9. Pre-bake on a vacuum hot plate at 115 ^{o}C for 50 seconds

10. Expose the lift-off pattern using photolithography technique.
11. Develop S1818 in 1:1 mixture of microchem microposit developer
12. Inspect under microscope to ensure proper development
13. 5 minutes oxygen ashing at 100 W
14. Hard-bake S1818 on a hotplate at 125 ^{o}C for 5 minutes
15. Develop LOR10A in CD26 developer solution for 7 minutes to produce the required undercut (development rate is 10 nm/s)
16. Inspect under microscope to check for undercut
17. 60 seconds oxygen ashing at 100 W
18. De-oxidise sample for 30 seconds in 1:4 $HCl:H_2O$, rinse in deionised water and blow dry
19. Evaporate metal layers
20. Dip in warm SVC-14 (60 ^{o}C) for 10 minutes
21. Transfer into another beaker of warm SVC-14 for another 10 minutes
22. Rinse SVC-14 with Isopropyl alcohol (IPA) for 5 minutes and blow dry
23. 2 minutes oxygen ashing at 100 W
24. Inspect lift-off under microscope

Bibliography

[1] L. C. West and S. J. Eglash, "First observation of an extremely large-dipole infrared transition within the conduction band of a GaAs quantum well," *Applied Physics Letters*, vol. 46, no. 12, pp. 1156–1158, 1985. [Online]. Available: http://link.aip.org/link/?APL/46/1156/1

[2] A. Kosterev and F. Tittel, "Chemical sensors based on quantum cascade lasers," *Quantum Electronics, IEEE Journal of*, vol. 38, no. 6, pp. 582 –591, Jun. 2002.

[3] [Online]. Available: http://www.laser2000.co.uk

[4] G. Scamarcio, M. Troccoli, F. Rizzi, and I. M. Catalano, "Widely tunable mid-infrared emission from coupled Wannier-Stark ladders in semiconductor superlattices," *Physica B: Condensed Matter*, vol. 314, no. 1-4, pp. 332 – 335, 2002. [Online]. Available: http://www.sciencedirect.com/science/article/B6TVH-44KPPWT-25/2/798258c79fe7381cc192606c8a531f08

[5] C. Sirtori, J. Faist, F. Capasso, D. L. Sivco, A. L. Hutchinson, and A. Y. Cho, "Quantum cascade laser with plasmon enhanced waveguide operating at 8.4 μm wavelength," *Applied Physics Letters*, vol. 66, no. 24, pp. 3242 –3244, Jun. 1995.

[6] J. Faist, F. Capasso, D. L. Sivco, C. Sirtori, A. L. Hutchinson, and A. Y. Cho, "Quantum cascade laser," *Science*, vol. 264, no. 5158, p. 553, 1994. [Online]. Available: http://dx.doi.org/10.1126/science.264.5158.553

[7] [Online]. Available: http://www.cfa.harvard.edu/HITRAN/

[8] J. P. Commin, D. G. Revin, S. Y. Zhang, A. B. Krysa, K. Kennedy, and J. W. Cockburn, "High peak power lambda 3.3 and 3.5 μm InGaAs/AlAs(Sb) quantum cascade lasers operating up to 400 K," *Applied Physics Letters*, vol. 97, no. 3, p. 031108, 2010. [Online]. Available: http://link.aip.org/link/?APL/97/031108/1

[9] B. Lane, Z. Wu, A. Stein, J. Diaz, and M. Razeghi, "InAsSb/InAsP strained-layer superlattice injection lasers operating at 4.0 mu m grown by metal-organic chemical vapor deposition," *Applied Physics Letters*, vol. 74, no. 23, pp. 3438–3440, 1999. [Online]. Available: http://link.aip.org/link/?APL/74/3438/1

[10] M. Tacke, "New developments and applications of tunable ir lead salt lasers," *Infrared Physics and Technology*, vol. 36, no. 1, pp. 447–463, 1995, proceedings of the Sixth International Conference on Infrared Physics. [Online]. Available: http://www.sciencedirect.com/science/article/B6TJ9-3YN9FNJ-3Y/2/71a6d75bbd8d0b07ffc520ab406b477e

[11] G. Springholz, T. Schwarzl, M. Aigle, H. Pascher, and W. Heiss, "4.8 mu m vertical emitting pbte quantum-well lasers based on high-finesse eute/pb[sub 1 - x]eu[sub x]te microcavities," *Applied Physics Letters*, vol. 76, no. 14, pp. 1807–1809, 2000. [Online]. Available: http://link.aip.org/link/?APL/76/1807/1

[12] C. Sirtori, J. Faist, F. Capasso, and A. Y. Cho, "The quantum cascade laser. a device based on two-dimensional electronic subbands," *Pure and Appl. Opt.*, vol. 7, no. 2, p. 373, 1998.

[13] R. F. Curl, F. Capasso, C. Gmachl, A. A. Kosterev, B. McManus, R. Lewicki, M. Pusharsky, G. Wysocki, and F. K. Tittel, "Quantum cascade lasers in chemical physics," *Chemical Physics Letters*, vol. 487, no. 1-3, pp. 1 – 18, 2010. [Online]. Available: http://www.sciencedirect.com/science/article/B6TFN-4Y35TMD-5/2/5e2e1b7f24caa705d1b0a607777382ac

[14] J. P. Commin, K. Kennedy, D. G. Revin, S. Y. Zhang, A. B. Krysa, and J. W. Cockburn, “lambda   3.36 mu m room temperature ingaas/alas(sb) quantum cascade lasers with third order distributed feedback grating,” *Applied Physics Letters*, vol. 97, no. 11, p. 111113, 2010. [Online]. Available: http://link.aip.org/link/?APL/97/111113/1

[15] K. Nill, A. Strauss, and F. Blum, “Tunable cw pb[sub 0.98] cd[sub 0.02]s diode lasers emitting at 3.5 μm: Applications to ultrahigh-resolution spectroscopy,” *Applied Physics Letters*, vol. 22, no. 12, pp. 677–679, 1973. [Online]. Available: http://link.aip.org/link/?APL/22/677/1

[16] S. Choi, Z. Peng, Q. Yang, S. J. Choi, and P. Dapkus, “Tunable narrow linewidth all-buried heterostructure ring resonator filters using vernier effects,” *Photonics Technology Letters, IEEE*, vol. 17, no. 1, pp. 106 –108, jan 2005.

[17] T. Segawa, S. Matsuo, T. Kakitsuka, T. Sato, Y. Kondo, and H. Suzuki, “Tunable double-ring-resonator-coupled laser over full c-band with low tuning current,” in *Indium Phosphide Related Materials, 2007. IPRM ’07. IEEE 19th International Conference on*, may 2007, pp. 598 –601.

[18] B. Liu, A. Shakouri, and J. Bowers, “Wide tunable double ring resonator coupled lasers,” *Photonics Technology Letters, IEEE*, vol. 14, no. 5, pp. 600 –602, may 2002.

[19] K. Oda, N. Takato, and H. Toba, “A wide-fsr waveguide double-ring resonator for optical fdm transmission systems,” *Lightwave Technology, Journal of*, vol. 9, no. 6, pp. 728 –736, Jun. 1991.

[20] C. C. Nshii, C. N. Ironside, M. Sorel, T. J. Slight, S. Y. Zhang, D. G. Revin, and J. W. Cockburn, “A unidirectional quantum cascade ring laser,” *Applied Physics Letters*, vol. 97, no. 23, p. 231107, 2010. [Online]. Available: http://link.aip.org/link/?APL/97/231107/1

[21] V.-M. Gkortsas, C. Wang, L. Kuznetsova, L. Diehl, A. Gordon, C. Jirauschek, M. A. Belkin, A. Belyanin, F. Capasso, and F. X. Kärtner, *Opt. Express*, vol. 18, no. 13, pp. 13 616–13 630, 2010.

[22] J. P. Hohimer and G. A. Vawter, *Applied Physics Letters*, vol. 63, no. 18, pp. 2457–2459, 1993.

[23] R. F. Kazarinov and R. A. Suris, "Amplification of electromagnetic waves in a semiconductor superlattice," *Sov. Phys. Semicond.*, vol. 5, p. 707, 1971.

[24] L. Esaki and R. Tsu, "Superlattice and negative differential conductivity in semiconductors," *IBM J. Res. Dev.*, vol. 14, p. 61, 1970.

[25] J. Faist, C. Sirtori, F. Capasso, D. L. Sivco, A. L. Hutchinson, and A. Y. Cho, "Continuous wave operation of a vertical transition quantum cascade laser above t=80 k," *Applied Physics Letters*, vol. 67, no. 21, pp. 3057–3059, 1995. [Online]. Available: http://link.aip.org/link/?APL/67/3057/1

[26] J. Faist, C. Gmachl, M. Striccoli, C. Sirtori, F. Capasso, D. L. Sivco, and A. Y. Cho, "Quantum cascade disk lasers," *Applied Physics Letters*, vol. 69, no. 17, pp. 2456–2458, 1996. [Online]. Available: http://link.aip.org/link/?APL/69/2456/1

[27] M. Beck, D. Hofstetter, T. Aellen, J. Faist, U. Oesterle, M. Ilegems, E. Gini, and H. Melchior, "Continuous Wave Operation of a Mid-Infrared Semiconductor Laser at Room Temperature," *Science*, vol. 295, no. 5553, pp. 301–305, 2002. [Online]. Available: http://www.sciencemag.org/content/295/5553/301.abstract

[28] C. Gmachl, F. Capasso, D. L. Sivco, A. L. Hutchinson, and A. Y. Cho, "Recent progress in quantum cascade lasers and applications," *Rep. Prog. Phys.*, vol. 64, pp. 1533–1601, 2001. [Online]. Available: http://dx.doi.org

[29] J. Faist, F. Capasso, C. Sirtori, D. L. Sivco, J. N. Baillargeon, A. L. Hutchinson, S.-N. G. Chu, and A. Y. Cho, "High power mid-infrared (lambda 5 mu m) quantum cascade lasers operating above room

temperature," *Applied Physics Letters*, vol. 68, no. 26, pp. 3680–3682, 1996. [Online]. Available: http://link.aip.org/link/?APL/68/3680/1

[30] M. R. Soulby, "Mid-infrared spectroscopic studies of quantum cascade lasers," Ph.D. dissertation, University of Sheffield, 2010.

[31] J. Faist, F. Capasso, C. Sirtori, D. L. Sivco, A. L. Hutchinson, and A. Y. Cho, "Vertical transition quantum cascade laser with bragg confined excited state," *Applied Physics Letters*, vol. 66, no. 5, pp. 538–540, 1995. [Online]. Available: http://link.aip.org/link/?APL/66/538/1

[32] J. Faist, F. Capasso, D. L. Sivco, C. Sirtori, A. L. Hutchinson, and A. Y. Cho, "Laser action by tuning the oscillator strength," *Nature*, vol. 387, no. 6635, pp. 777–782, 1997.

[33] C. Sirtori, P. Kruck, S. Barbieri, P. Collot, J. Nagle, M. Beck, J. Faist, and U. Oesterle, "Gaas/al[sub x]ga[sub 1 - x]as quantum cascade lasers," *Applied Physics Letters*, vol. 73, no. 24, pp. 3486–3488, 1998. [Online]. Available: http://link.aip.org/link/?APL/73/3486/1

[34] C. Gmachl, F. Capasso, D. L. Sivco, and A. Y. Cho, "Recent progress in quantum cascade lasers and applications," *Reports on Progress in Physics*, vol. 64, no. 11, p. 1533, 2001. [Online]. Available: http://stacks.iop.org/0034-4885/64/i=11/a=204

[35] J. Faist, M. Beck, T. Aellen, and E. Gini, "Quantum-cascade lasers based on a bound-to-continuum transition," *Applied Physics Letters*, vol. 78, no. 2, pp. 147–149, 2001. [Online]. Available: http://link.aip.org/link/?APL/78/147/1

[36] F. Capasso, A. Tredicucci, C. Gmachl, D. Sivco, A. Hutchinson, A. Cho, and G. Scamarcio, "High-performance superlattice quantum cascade lasers," *Selected Topics in Quantum Electronics, IEEE Journal of*, vol. 5, no. 3, pp. 792 –807, 1999.

[37] D. Hofstetter, M. Beck, T. Aellen, and J. Faist, "High-temperature operation of distributed feedback quantum-cascade lasers at 5.3 mu m,"

Applied Physics Letters, vol. 78, no. 4, pp. 396–398, 2001. [Online]. Available: http://link.aip.org/link/?APL/78/396/1

[38] C. Sirtori, F. Capasso, J. Faist, A. Hutchinson, D. Sivco, and A. Cho, "Resonant tunneling in quantum cascade lasers," *Quantum Electronics, IEEE Journal of*, vol. 34, no. 9, pp. 1722 –1729, Sep. 1998.

[39] J. Faist, F. Capasso, D. L. Sivco, C. Sirtori, A. L. Hutchinson, and A. Y. Cho, "Quantum Cascade Laser," *Science*, vol. 264, no. 5158, pp. 553–556, 1994. [Online]. Available: http://www.sciencemag.org/content/264/5158/553.abstract

[40] I. Vurgaftman, J. R. Meyer, and L. R. Ram-Mohan, "Band parameters for iii–v compound semiconductors and their alloys," *Journal of Applied Physics*, vol. 89, no. 11, pp. 5815–5875, 2001. [Online]. Available: http://link.aip.org/link/?JAP/89/5815/1

[41] P. Harrison, *Quantum Wells, Wires and Dots: Theoretical and Computational Physics of Semiconductor Nanostructures*, 3rd ed. John Wiley and Sons, Ltd, Publication, September 2010.

[42] J. Faist, F. Capasso, D. L. Sivco, A. L. Hutchinson, S.-N. G. Chu, and A. Y. Cho, "Short wavelength (lambda 3.4 mu m) quantum cascade laser based on strained compensated ingaas/alinas," *Applied Physics Letters*, vol. 72, no. 6, pp. 680–682, 1998. [Online]. Available: http://link.aip.org/link/?APL/72/680/1

[43] S. Y. Zhang, D. G. Revin, J. W. Cockburn, K. Kennedy, A. B. Krysa, and M. Hopkinson, "lambda 3.1 mu m room temperature ingaas/alassb/inp quantum cascade lasers," *Applied Physics Letters*, vol. 94, no. 3, p. 031106, 2009. [Online]. Available: http://link.aip.org/link/?APL/94/031106/1

[44] D. G. Revin, J. W. Cockburn, M. J. Steer, R. J. Airey, M. Hopkinson, A. B. Krysa, L. R. Wilson, and S. Menzel, "Ingaas/alassb/inp quantum cascade lasers operating at wavelengths close to 3 mu m," *Applied*

Physics Letters, vol. 90, no. 2, p. 021108, 2007. [Online]. Available: http://link.aip.org/link/?APL/90/021108/1

[45] J. Matthews and A. Blakeslee, “Defects in epitaxial multilayers: I. misfit dislocations,” *Journal of Crystal Growth*, vol. 27, pp. 118 – 125, 1974. [Online]. Available: http://www.sciencedirect.com/science/article/B6TJ6-4NGKJHD-F/2/c9bcce50b19aab3fbf05faab6e647e7c

[46] S. Blaser, D. A. Yarekha, L. Hvozdara, Y. Bonetti, A. Muller, M. Giovannini, and J. Faist, “Room-temperature, continuous-wave, single-mode quantum-cascade lasers at lambda = 5.4 mu m,” *Applied Physics Letters*, vol. 86, no. 4, p. 041109, 2005. [Online]. Available: http://link.aip.org/link/?APL/86/041109/1

[47] J. Faist, M. Beck, T. Aellen, and E. Gini, “Quantum-cascade lasers based on a bound-to-continuum transition,” *Applied Physics Letters*, vol. 78, no. 2, pp. 147–149, 2001. [Online]. Available: http://link.aip.org/link/?APL/78/147/1

[48] G. X., D. M., B. D., and K. I., “Design and optimization of a gaas-based sub-7- um quantum cascade laser based on multivalley monte carlo simulation,” in *Numerical Simulation of Optoelectronic Devices, 2007. NUSOD ’07. International Conference on*, sept 2007, pp. 17 –18.

[49] X. Gao, M. D’Souza, D. Botez, and I. Knezevic, “Design and simulation of deep-well gaas-based quantum cascade lasers for 6.7 mu m room-temperature operation,” *Journal of Applied Physics*, vol. 102, no. 11, p. 113107, 2007. [Online]. Available: http://link.aip.org/link/?JAP/102/113107/1

[50] H. Page, C. Becker, A. Robertson, G. Glastre, V. Ortiz, and C. Sirtori, “300 k operation of a gaas-based quantum-cascade laser at lambda [approximate] 9 mu m,” *Applied Physics Letters*, vol. 78, no. 22, pp. 3529–3531, 2001. [Online]. Available: http://link.aip.org/link/?APL/78/3529/1

[51] S. Birner, S. Hackenbuchner, M. Sabathil, G. Zandler, J. Majewski, and T. Andlauer, “Modeling of semiconductor nanostructures with nextnano3,” *ACTA PHYSICA POLONICA A*, vol. 110, no. 2, pp. 111–124, 2006.

[52] C. Sirtori, F. Capasso, J. Faist, and S. Scandolo, “Nonparabolicity and a sum rule associated with bound-to-bound and bound-to-continuum intersubband transitions in quantum wells,” *Phys. Rev. B*, vol. 50, no. 12, pp. 8663–8674, Sep 1994.

[53] K. Ohtani, H. Sakuma, and H. Ohno, “Inas-based quantum cascade light emitting structures containing a double plasmon waveguide,” *Journal of Crystal Growth*, vol. 251, no. 1-4, pp. 718 – 722, 2003, proceedings of the Twelfth International Conference on Molecular Beam Epitaxy. [Online]. Available: http://www.sciencedirect.com/science/article/B6TJ6-47RBR83-1/2/771aa36b8a3f8fc5f4c8ad8388bda618

[54] R. Teissier, D. Barate, A. Vicet, D. Yarekha, C. Alibert, A. Baranov, X. Marcadet, M. Garcia, and C. Sirtori, “Inas/alsb quantum cascade lasers operating at 6.7 mu;m,” *Electronics Letters*, vol. 39, no. 17, pp. 1252 – 1254, 2003.

[55] R. Teissier, D. Barate, A. Vicet, C. Alibert, A. N. Baranov, X. Marcadet, C. Renard, M. Garcia, C. Sirtori, D. Revin, and J. Cockburn, “Room temperature operation of inas/alsb quantum cascade lasers,” *Applied Physics Letters*, vol. 85, no. 2, pp. 167–169, 2004. [Online]. Available: http://link.aip.org/link/?APL/85/167/1

[56] J. Devenson, R. Teissier, O. Cathabard, and A. N. Baranov, “Inas/alsb quantum cascade lasers emitting below 3 mu m,” *Applied Physics Letters*, vol. 90, no. 11, p. 111118, 2007. [Online]. Available: http://link.aip.org/link/?APL/90/111118/1

[57] S. A. Aliev, A. Y. Nashelskii, and S. S. Shalyt, *Sov. Phys. Solid State*, vol. 7, September 1965.

[58] Q. Yang, C. Manz, W. Bronner, K. Köhler, and J. Wagner, “Room-temperature short-wavelength (lambda 3.7–3.9 mu m) gainas/alassb quantum-cascade lasers,” *Applied Physics Letters*, vol. 88, no. 12, p. 121127, 2006. [Online]. Available: http://link.aip.org/link/?APL/88/121127/1

[59] D. G. Revin, J. W. Cockburn, M. J. Steer, R. J. Airey, M. Hopkinson, A. B. Krysa, L. R. Wilson, and S. Menzel, "Ingaas/alassb/inp strain compensated quantum cascade lasers," *Applied Physics Letters*, vol. 90, no. 15, p. 151105, 2007. [Online]. Available: http://link.aip.org/link/?APL/90/151105/1

[60] Q. Yang, R. Lösch, W. Bronner, S. Hugger, F. Fuchs, R. Aidam, and J. Wagner, "High-peak-power strain-compensated gainas/alinas quantum cascade lasers (lambda 4.6 mu m) based on a slightly diagonal active region design," *Applied Physics Letters*, vol. 93, no. 25, p. 251110, 2008. [Online]. Available: http://link.aip.org/link/?APL/93/251110/1

[61] J. P. Commin, D. G. Revin, S. Y. Zhang, A. B. Krysa, K. Kennedy, and J. W. Cockburn, "High peak power lambda 3.3 and 3.5 mu m ingaas/alas(sb) quantum cascade lasers operating up to 400 k," *Applied Physics Letters*, vol. 97, no. 3, p. 031108, 2010. [Online]. Available: http://link.aip.org/link/?APL/97/031108/1

[62] B. Reid, R. Maciejko, and A. Champagne, "Absorption and index of refraction for modeling of ingaasp/ inp photonic devices," *Can. J. Phys.*, vol. 71, p. 410, 1993.

[63] G. P. Agrawal and N. K. Dutta, *Long- Wavelength Semiconductor Lasers*. Van Nostrand Reinhold Company Inc., 1986.

[64] [Online]. Available: http://www.rsoftdesign.com

[65] P. Hansen, G. Raybon, M.-D. Chien, U. Koren, B. Miller, M. Young, J.-M. Verdiell, and C. Burrus, "A 1.54- mu;m monolithic semiconductor ring laser: Cw and mode-locked operation," *Photonics Technology Letters, IEEE*, vol. 4, no. 5, pp. 411 –413, may. 1992.

[66] A. S.-H. Liao and S. Wang, "Semiconductor injection lasers with a circular resonator," *Applied Physics Letters*, vol. 36, no. 10, pp. 801–803, 1980. [Online]. Available: http://link.aip.org/link/?APL/36/801/1

[67] T. Krauss, R. M. DeLaRue, I. Gontijo, P. J. R. Laybourn, and J. S. Roberts, "Strip-loaded semiconductor ring lasers employing multimode interference output couplers," *Applied Physics Letters*, vol. 64, no. 21, pp. 2788–2790, 1994. [Online]. Available: http://link.aip.org/link/?APL/64/2788/1

[68] T. Krauss, R. De La Rue, and P. Laybourn, "Impact of output coupler configuration on operating characteristics of semiconductor ring lasers," *Lightwave Technology, Journal of*, vol. 13, no. 7, pp. 1500 –1507, jul. 1995.

[69] D. L. Lee, *Electromagnetic principles of integrated optics.* John Wiley and sons, 1986.

[70] L. B. Soldano and E. C. M. Pennings, "Optical multi-mode interference devices based on self-imaging : Principles and applications," *Lightwave Technology, Journal of*, vol. 13, no. 4, p. 615, April 1995.

[71] G. Kokkoris, E. Gogolides, and A. G. Boudouvis, "Etching of sio[sub 2] features in fluorocarbon plasmas: Explanation and prediction of gas-phase-composition effects on aspect ratio dependent phenomena in trenches," *Journal of Applied Physics*, vol. 91, no. 5, pp. 2697–2707, 2002. [Online]. Available: http://link.aip.org/link/?JAP/91/2697/1

[72] E. Pennings, R. van Roijen, M. van Stralen, P. de Waard, R. Koumans, and B. Verbeck, "Reflection properties of multimode interference devices," *Photonics Technology Letters, IEEE*, vol. 6, no. 6, pp. 715 –718, jun. 1994.

[73] R. Hanfoug, L. Augustin, Y. Barbarin, J. van der Tol, E. Bente, F. Karouta, D. Rogers, S. Cole, Y. Oei, X. Leijtens, and M. Smit, "Reduced reflections from multimode interference couplers," *Electronics Letters*, vol. 42, no. 8, pp. 465 – 466, apr. 2006.

[74] T. Krauss and P. Layboum, "Very low threshold current operation of semiconductor ring lasers," 1992, pp. 66 –67.

[75] A. E. Siegman, *Lasers*, A. Kelly, Ed. Oxford University Press, 1986.

[76] J. P. Hohimer and G. A. Vawter, "Unidirectional semiconductor ring lasers with racetrack cavities," *Applied Physics Letters*, vol. 63, no. 18, pp. 2457–2459, 1993. [Online]. Available: http://link.aip.org/link/?APL/63/2457/1

[77] M. Sorel, G. Giuliani, A. Scire, R. Miglierina, S. Donati, and P. Laybourn, "Operating regimes of gaas-algaas semiconductor ring lasers: experiment and model," *Quantum Electronics, IEEE Journal of*, vol. 39, no. 10, pp. 1187 – 1195, oct. 2003.

[78] G. Giuliani, R. Miglierina, M. Sorel, and A. Scire, "Linewidth, autocorrelation, and cross-correlation measurements of counterpropagating modes in gaas-algaas semiconductor ring lasers," *Selected Topics in Quantum Electronics, IEEE Journal of*, vol. 11, no. 5, pp. 1187 – 1192, sep. 2005.

[79] V. Subramaniam, G. De Brabander, D. Naghski, and J. Boyd, "Measurement of mode field profiles and bending and transition losses in curved optical channel waveguides," *Lightwave Technology, Journal of*, vol. 15, no. 6, pp. 990 –997, jun. 1997.

[80] D. L. Lee, *Electromagnetic principles of integrated optics.* John Wiley and Sons, Inc. USA, 1986.

[81] K. Thyagarajan, M. R. Shenoy, and A. K. Ghatak, "Accurate numerical method for the calculation of bending loss in optical waveguides using a matrix approach," *Opt. Lett.*, vol. 12, no. 4, pp. 296–298, 1987. [Online]. Available: http://ol.osa.org/abstract.cfm?URI=ol-12-4-296

[82] I. Kiyat, A. Aydinli, and N. Dagli, "High-q silicon-on-insulator optical rib waveguide racetrack resonators," *Opt. Express*, vol. 13, no. 6, pp. 1900–1905, 2005. [Online]. Available: http://www.opticsexpress.org/abstract.cfm?URI=oe-13-6-1900

[83] J. P. Hohimer, G. A. Vawter, D. C. Craft, and G. R. Hadley, "Improving the performance of semiconductor ring lasers by controlled reflection feedback," *Applied Physics Letters*, vol. 61, no. 9, pp. 1013–1015, 1992. [Online]. Available: http://link.aip.org/link/?APL/61/1013/1

[84] [Online]. Available: http://www.oxinst.com

[85] [Online]. Available: http://www.nanophys.kth.se/nanophys/facilities/nfl/resists/zep520a-7-2.pdf

[86] J. A. Bondur, "Dry process technology (reactive ion etching)," *Journal of Vacuum Science and Technology*, vol. 13, no. 5, pp. 1023 –1029, Sep. 1976.

[87] [Online]. Available: http://www.oxinst.com

[88] H. Jansen, M. de Boer, R. Wiegerink, N. Tas, E. Smulders, C. Neagu, and M. Elwenspoek, "Rie lag in high aspect ratio trench etching of silicon," *Microelectronic Engineering*, vol. 35, no. 1-4, pp. 45 – 50, 1997, micro- and Nano- Engineering 96. [Online]. Available: http://www.sciencedirect.com/science/article/B6V0W-3X0M7M9-31/2/d58b7cb0bedf67bef262b5ecce3bf56e

[89] [Online]. Available: http://www.dowcorning.com

[90] M. Zegaoui, N. Choueib, P. Tilmant, M. Franois, C. Legrand, J. Chazelas, and D. Decoster, "A novel bondpad report process for iii-v semiconductor devices using full hsq properties," *Microelectronic Engineering*, vol. 86, no. 1, pp. 68 – 71, 2009. [Online]. Available: http://www.sciencedirect.com/science/article/B6V0W-4TPPDVM-1/2/b36ec50b83e04c8dd13888e7037552f4

[91] [Online]. Available: http://www.microchem.com/products/pdf/PMGI-Resists-data-sheetV-rhcedit-102206.pdf

[92] V.-M. Gkortsas, C. Wang, L. Kuznetsova, L. Diehl, A. Gordon, C. Jirauschek, M. A. Belkin, A. Belyanin, F. Capasso, and F. X. Kärtner, *Opt. Express*, vol. 18, no. 13, pp. 13 616–13 630, 2010.

[93] M. Sorel and P. Laybourn, "Control of unidirectional operation in semiconductor ring lasers," in *Lasers and Electro-Optics Society, 2001. LEOS 2001. The 14th Annual Meeting of the IEEE*, 2001.

[94] C. L. Tang, H. Statz, and G. deMars, “Spectral output and spiking behaviour of solid-state lasers,” *Journal of Appl. Phys.*, vol. 34, pp. 2289–2295, August 1963.

[95] M. Hercher, M. Young, and C. B. Smoyer, “Travelling wave ruby laser with a passive optical isolator,” *Journal of Appl. Phys.*, vol. 36, p. 3351, October 1965.

[96] A. Sennaroglu and C. Pollock, “Unidirectional operation of rectangular dielectric single-mode ring waveguide lasers,” *Lightwave Technology, Journal of*, vol. 9, no. 9, pp. 1094 –1098, Sep. 1991.

[97] S. Oku, M. Okayasu, and M. Ikeda, “Control of unidirectional oscillation in semiconductor orbiter lasers,” *Photonics Technology Letters, IEEE*, vol. 3, no. 12, pp. 1066 –1068, Dec. 1991.

[98] J. J. Liang, S. T. Lau, M. H. Leary, and J. M. Ballantyne, “Unidirectional operation of waveguide diode ring lasers,” *Applied Physics Letters*, vol. 70, no. 10, pp. 1192–1194, 1997. [Online]. Available: http://link.aip.org/link/?APL/70/1192/1

[99] M. Sorel, P. J. R. Laybourn, A. Scirè, S. Balle, G. Giuliani, R. Miglierina, and S. Donati, “Alternate oscillations in semiconductor ring lasers,” *Opt. Lett.*, vol. 27, no. 22, pp. 1992–1994, 2002. [Online]. Available: http://ol.osa.org/abstract.cfm?URI=ol-27-22-1992

[100] J. Faist, F. Capasso, C. Sirtori, D. L. Sivco, and A. Y. Cho, *Semiconductors and Semimetals Quantum cascade laser.* Academic, San Diego, 2000, vol. 66.

[101] Q. K. Yang, B. Hinkov, F. Fuchs, W. Bronner, K. Köhler, J. Wagner, R. Maulini, and J. Faist, “Rate equations analysis of external-cavity quantum cascade lasers,” *Journal of Applied Physics*, vol. 107, no. 4, p. 043109, 2010. [Online]. Available: http://link.aip.org/link/?JAP/107/043109/1

[102] S.-H. Cho, “Laser micromachining of active and passive photonic integrated circuits,” Ph.D. dissertation, MASSACHUSETTS INSTITUTE OF TECHNOLOGY, December 2003.

[103] T. Krauss and P. Laybourn, “Very low threshold current operation of semiconductor ring lasers,” *Optoelectronics, IEE Proceedings J*, vol. 139, no. 6, pp. 383 –388, Dec. 1992.

[104] C. D. Farmer, “Fabrication and evaluation of In0.52Al0.48As/In0.53Ga0.47As/InP,” Ph.D. dissertation.

[105] C. C. Nshii, C. N. Ironside, M. Sorel, T. J. Slight, S. Y. Zhang, D. G. Revin, and J. W. Cockburn, “A unidirectional quantum cascade ring laser,” *Applied Physics Letters*, vol. 97, no. 23, p. 231107, 2010. [Online]. Available: http://link.aip.org/link/?APL/97/231107/1

[106] R. Todt, T. Jacke, R. Laroy, G. Morthier, and M.-C. Amann, “Demonstration of vernier effect tuning in tunable twin-guide laser diodes,” *Optoelectronics, IEE Proceedings* -, vol. 152, no. 2, pp. 66 – 71, 2005.

[107] G. Barbarossa and A. Matteo, “Novel double-ring optical-guided-wave vernier resonator,” *Optoelectronics, IEE Proceedings* -, vol. 144, no. 4, pp. 203 –208, Aug. 1997.

[108] B. Liu, A. Shakouri, and J. Bowers, “Wide tunable double ring resonator coupled lasers,” *Photonics Technology Letters, IEEE*, vol. 14, no. 5, pp. 600 –602, May 2002.

[109] D. Rabus, Z. Bian, and A. Shakouri, “A gainasp-inp double-ring resonator coupled laser,” *Photonics Technology Letters, IEEE*, vol. 17, no. 9, pp. 1770 –1772, 2005.

[110] T. Wolf, S. Illek, J. Rieger, B. Borchert, and M.-C. Amann, “Tunable twin-guide (ttg) distributed feedback (dfb) laser with over 10 nm continuous tuning range,” *Electronics Letters*, vol. 29, no. 24, pp. 2124 –2125, 1993.

[111] K. Oda, N. Takato, and H. Toba, “A wide-fsr waveguide double-ring resonator for optical fdm transmission systems,” *JOURNAL OF LIGHTWAVE TECHNOLOGY*, vol. 9, no. 6, p. 728, June 1991.

[112] R. Maulini, A. Mohan, M. Giovannini, J. Faist, and E. Gini, “External cavity quantum-cascade laser tunable from 8.2 to 10.4 mu m using a gain element with a heterogeneous cascade,” *Applied Physics Letters*, vol. 88, no. 20, p. 201113, 2006. [Online]. Available: http://link.aip.org/link/?APL/88/201113/1

[113] G. Hancock, J. H. van Helden, R. Peverall, G. A. D. Ritchie, and R. J. Walker, “Direct and wavelength modulation spectroscopy using a cw external cavity quantum cascade laser,” *Applied Physics Letters*, vol. 94, no. 20, p. 201110, 2009. [Online]. Available: http://link.aip.org/link/?APL/94/201110/1

[114] B. Lee, H. Zhang, C. Pflugl, L. Diehl, M. Belkin, M. Fischer, A. Wittmann, J. Faist, and F. Capasso, “Broadband distributed-feedback quantum cascade laser array operating from 8.0 to 9.8 m,” *Photonics Technology Letters, IEEE*, 2009.

[115] B. G. Lee, M. A. Belkin, R. Audet, J. MacArthur, L. Diehl, C. Pflugl, F. Capasso, D. C. Oakley, D. Chapman, A. Napoleone, D. Bour, S. Corzine, G. Hofler, and J. Faist, “Widely tunable single-mode quantum cascade laser source for mid-infrared spectroscopy,” *Applied Physics Letters*, vol. 91, no. 23, pp. 231 101 –231 101–3, Dec. 2007.

[116] H. C. Guo, S. H. Tang, Z. D. Gao, Y. Q. Qin, S. N. Zhu, and Y. Y. Zhu, “Multiple-channel mid-infrared optical parametric oscillator in periodically poled mgo:linbo3,” *Journal of Applied Physics*, vol. 101, no. 11, pp. 113 112 –113 112–5, Jun. 2007.

[117] D. Reid, G. Kennedy, A. Miller, W. Sibbett, and M. Ebrahimzadeh, "Widely tunable, near- to mid-infrared femtosecond and picosecond optical parametric oscillators using periodically poled linbo3 and rbtioaso4," *Selected Topics in Quantum Electronics, IEEE Journal of*, vol. 4, no. 2, pp. 238 –248, 1998.

[118] F. Rizzi, G. Scarmarcio, and G. Strasser, "Three therminal mid-ir tunable emitters based on wannier-stark ladder transitions in semiconductor superlattices," *Semicond. Sci. Technol.*, vol. 19, pp. S87–88, 2004.

[119] C. Sirtori, J. Faist, F. Capasso, D. L. Sivco, A. L. Hutchinson, and A. Y. Cho, "Quantum cascade laser with plasmon-enhanced waveguide operating at 8.4 mu m wavelength," *Applied Physics Letters*, vol. 66, no. 24, pp. 3242–3244, 1995. [Online]. Available: http://link.aip.org/link/?APL/66/3242/1

[120] Y. S. Lin, "Breakdown characteristics of inp/ingaas composite-collector double heterojunction bipolar transistor," *Applied Physics Letters*, vol. 83, no. 26, pp. 5545–5547, 2003. [Online]. Available: http://link.aip.org/link/?APL/83/5545/1

[121] R. Dingle, A. C. Gossard, and W. Wiegmann, "Direct observation of superlattice formation in a semiconductor heterostructure," *Phys. Rev. Lett.*, vol. 34, no. 21, pp. 1327–1330, May 1975.

[122] A. Salin, "Semiconductor superlattices," *Sov. Phys. Usp*, vol. 29, p. 892, 1986.

[123] J. Bleuse, G. Bastard, and P. Voisin, "Electric-field-induced localization and oscillatory electro-optical properties of semiconductor superlattices," *Phys. Rev. Lett.*, vol. 60, no. 3, pp. 220–223, Jan 1988.

[124] E. E. Mendez, F. Agulló-Rueda, and J. M. Hong, "Stark localization in gaas-gaalas superlattices under an electric field," *Phys. Rev. Lett.*, vol. 60, no. 23, pp. 2426–2429, Jun 1988.

[125] H. Grahn, *Semiconductor Superlattices, Growth and Electronics Properties*, H. Grahn, Ed. World Scientic Publishing Co, Pte. Ltd, 1995.

[126] B. Ancker-Johnson, R. K. Williardson, and A. C. Beer, Eds., *Semiconductors and Semimetals - Physics of III-V Compounds*, vol. I. Academic Press Inc, London, 1966.

[127] T. Yuasa, S. Naritsuka, M. Mannoh, K. Shinozaki, K. Yamanaka, Y. Nomura, M. Mihara, and M. Ishii, "Raman scattering from coupled plasmon–lo-phonon modes in n-type al_xga_{1-x}as," *Phys. Rev. B*, vol. 33, no. 2, pp. 1222–1232, Jan 1986.

[128] S. Adachi, *Physical properties of III-V semiconductor compounds - InP, InAs, GaAs, GaP, InGaAs, and InGaAsP.* Wiley, New York, 1992.

[129] P. Spencer and K. Shore, "Surface plasmon effects and waveguide properties of quantum cascade lasers," *Optoelectronics, IEE Proceedings -*, vol. 144, no. 1, pp. 48 –52, feb 1997.

[130] W. G. Spitzer and J. M. Whelan, "Infrared absorption and electron effective mass in n-type gallium arsenide," *Phys. Rev.*, vol. 114, no. 1, pp. 59–63, Apr 1959.

[131] [Online]. Available: http://www.photond.com/products/fimmwave.htm

[132] H. Kroemer, "Heterostructure bipolar transistors and integrated circuits," *Proceedings of the IEEE*, vol. 70, no. 1, pp. 13 – 25, jan. 1982.

[133] J. Semmel, W. Kaiser, H. Hofmann, S. Hofling, and A. Forchel, "Single mode emitting ridge waveguide quantum cascade lasers coupled to an active ring resonator filter," *Applied Physics Letters*, vol. 93, no. 21, pp. 211 106 –211 106–3, Nov. 2008.

[134] P. Fuchs, J. Seufert, J. Koeth, J. Semmel, S. Hofling, L. Worschech, and A. Forchel, "Widely tunable quantum cascade lasers with coupled cavities for gas detection," *Applied Physics Letters*, vol. 97, no. 18, pp. 181 111 – 181 111–3, Nov. 2010.